CONSTRUCTION OF PHOTOSENSITISED SEMICONDUCTOR CATHODES

MOHD ASRI MAT TERIDI

A DOCTORAL THESIS

SUBMITTED IN PARTIAL FULFILMENT OF THE REQUIREMENTS FOR THE AWARD OF

DOCTOR OF PHILOSOPHY OF LOUGHBOROUGH UNIVERSITY

4/09/2012

Loughborough University

Construction of Photosensitised Semiconductor Cathodes

Abstract

Recent studies suggest that the performance of dye-sensitised solar cells (DSC) has appeared to have reached a limit, therefore solar cells based on semiconductor materials, such as extremely thin absorber (ETA) solar cells and tandem solar cells are currently the subject of intense research in the framework of low-cost photovoltaic devices as sources of harvesting sunlight to generate electricity. Generally, semiconductor solar cells have been divided into two different types, namely anodic and cathodic type solar cells. Extensive research and development work has been focused on anodic semiconductor sensitised solar cells to date. In contrast, the cathodic semiconductor sensitised solar cells have received no attention which is very surprising. Developing the cathodic semiconductor sensitised solar cell concept is very important in the development of tandem solar cells as well as other new solar cell configurations. The main reason for the lack of research in this area was due to the rarity of *p*-type semiconductor materials, which made it difficult to find suitable materials to match the energy band edges for cathodic semiconductor sensitised solar cells (CSSC) as well as solid-state cathodic semiconductor solar cells (SS-CSSC). The primary aim of this thesis was to construct cathodic semiconductor sensitised solar cells as well as their solid-state analogues (SS-CSSC). The work conducted within this doctoral study presents state-of-art materials and thin film processing/preparation methods, their characterisation and developing CSSCs and SS-CSSCs employing such films in cascade configurations. No reports have been published in the literature on SS-CSSC to date.

The first stage of this thesis is focused on optimising the morphology and the texture (porosity) of the CuI and NiO semiconductor photocathode, by the introduction of new deposition methods – namely, pulsed-electrodeposition (PED) and Aerosol-Assisted Deposition (AAD) and Aerosol-Assisted Chemical Vapour Deposition (AACVD). The electrodes prepared by employing the methods mentioned above and controlling the deposition parameters systematically, we have achieved significant improvement in the film morphology and the texture of the deposited films. The resulting electrodes showed excellent improvement in the photoelectrochemical performance which made it suitable for application in construction of both CSSC and SS-CSSC. The photoelectrochemical performance of the

electrodes can be seen clearly through the photocurrent density data. For the case of bare CuI, the PEC performance of electrode prepared by the AAD and PED compared against that of continuous-electrodeposition (ED) electrodes. The photocurrent density achieved for the electrodes prepared by AAD and PED was reported around 175 and 75 μAcm^{-2} respectively which are way higher than the ED case.

At the second stage of this study, the work focused on fabrication and characterisation of the CSSCs. Cathodic sensitised PEC solar cells ($CuI/Cu_2S/(Eu^{2+}/Eu^{3+})$ and $NiO/Cu_2S/(I_3^-/I^-)$) were fabricated by deposition of *p*-Cu_2S on the texture controlled CuI and NiO photocathodes. The morphological properties of the photocathode, in particular layer thickness, particle size and film porosity, play an important role in the PEC performance of CSSCs. Optimisation of these parameters led to increased adsorption of the Cu_2S light harvester on the photocathode's surface. As a result, the charge injection from Cu_2S to the wide band gap photocathode material (CuI and NiO) was significantly improved. Due to this, the CSSC performance showed significant improvement as semiconductor sensitised cathodic solar cells (CSSC). The IPCE and photocurrent density of the CSSC achieved in this study was around (19 and 7 %) and (1 and 0.5 $mAcm^{-2}$) for the CuI/Cu_2S and NiO/Cu_2S electrodes respectively.

Finally, the SS-CSSC has been fabricated by employing *n*-Fe_2O_3 electron transport layer. The construction of SS-CSSC for the first time using the *n*-Fe_2O_3 electron transport layer ($CuI/Cu_2S/Fe_2O_3$ and $NiO/Cu_2S/Fe_2O_3$) allowed us to study the materials, optical and photoelectrochemical properties of this device. Under AM 1.5 illumination, the SS-CSSC shows a photocurrent density of 6 and 9 μAcm^{-2} for $CuI/Cu_2S/Fe_2O_3$ and $NiO/Cu_2S/Fe_2O_3$ solar cells, respectively. The results of this work indicated low performance for both SS-CSSC compared to CSSC results, due to the lack of adsorption between the absorber and Fe_2O_3 electrode. However, this study proved the concept of SS-CSSC based on semiconductor material, which is valuable for the future work of cathodic semiconductor sensitised solar cells as well as solid-state tandem solar cells.

Acknowledgements

I would first like to thank Dr. Upul Wijayantha who was the supervisor for my thesis. I appreciated his vast scientific knowledge and valuable suggestions in many instructive discussions. The financial support of the National University of Malaysia, Ministry of Higher Education of Malaysia and Loughborough University are greatly acknowledged.

I want to thank to all my friends and colleagues who have accompanied helping me in this work; Dr. Asif Ali Tahir, Dr. Senthilarasu Sundaram, Dr. Sina Saremi Yarahmadi, Dr. Ruvini Dharmadasa, Jagdeep Singh Sagu, Thomas David Smith, Henry Arthur Burch, Thelge Anton Nirmal Peiris, Anish Patel, Mohammet Kose and Zeeshan Sielvi.

Finally I wish to thank my parents, my fiancée and my friends in Malaysia for all their help throughout my studies.

Contents

List of figures

List of Tables

Abbreviations

AACVD – Aerosol Assisted Chemical Vapour Deposition

AAD – Aerosol Assisted Deposition

ALD – Atomic layer Deposition

AM 1.5 – The solar spectrum in the surface of the Earth

APCVD – Atmospheric Pressure Chemical Vapour Deposition

c – The speed of light

CB – Conduction Band

CBD – Chemical Bath Deposition

CSSC – Cathodic Semiconductor Sensitised Cells

CVR – Chemical Vapour Reaction

CVD – Chemical Vapour Deposition

DSC – Dye Sensitised Solar Cell

E_g – Energy band gap

ETA – Extremely Thin Absorber

FF – Fill Factor

FWHM – Full Width of Half Maximum

h – The Planck constant

HOMO – Highest Occupied Molecular Orbital

$h\upsilon$ – Photon energy

ILGAR – Spray-ion Layer Gas Reaction

J_{sc} – Short Circuit Current Density

LUMO – Lowest Unoccupied Molecular Orbital

MOCVD – Metal Organic Chemical Vapour Deposition

mpp – Maximum Power Point

p-DSC – *p*-type Dye Sensitised Cell

PEC – Photoelectrochemical

P_{in} – Incident light

PLD – Pulse Laser Deposition

P_{out} – The electric power generated by the cell

PV – Photovoltaic

SILAR – Successive Ionic Layer Adsorption and Reaction

SP – Spray Pyrolysis

SS-CSSC – Solid-State Cathodic Semiconductor Sensitised Cells

USP – Ultrasonic Spray Pyrolysis

VB – Valence Band

V_{oc} – Open Circuit Voltage

η – Efficiency

λ –Wavelength

Chapter 1: Introduction

1.0 Introduction

1.1 Status of PV technology

Currently, many countries around the world are dependent on fossil fuels as their main energy source. The fossil fuels are formed by natural processes and are depleting at an unsustainable rate. These types of energy sources include petroleum, natural gas and coal [1]. Although these energy sources have made our everyday life much easier, they have proven to be one of the main causes of our environmental problems. The environmental impacts of energy consumption produced by fossil fuels have been known for some time and unfortunately the climate change associated with the CO_2 emission from fossil fuels has become a major issue [1]. These phenomena have encouraged the search for cleaner and more efficient alternative energy sources to eventually replace fossil fuels.

Humans have been tapping into many different renewable energy sources such as solar, wind, geothermal and water for thousands of years for their needs. However, to date, they are not being employed for large scale uses. This is mainly due to the extraordinarily cheap price of fossil fuels, disregarding the consequential environmental damage caused by its production and consumption. However, there is a strong belief that the renewable energy sector will become a key source of energy by replacing fossil fuels in the 21^{st} century leading the way out of the energy crisis that the world is facing today [2].

Among the available renewable energy generation technologies, photovoltaic (PV) devices have the potential to play a significant role in the future. This is due to the large abundance of solar radiation on Earth. The earth receives 1.2×10^{17} W (or 3×10^{24} Joules of energy per year) from the sun, meaning that if only 0.13% of the earth's surface was covered with 10% efficient solar cells, the energy generated by PV would easily satisfy our present energy needs [3]. Apart from the abundance of potentially exploitable solar energy, PV cells also have other competitive advantages such as environmental friendliness, relatively low maintenance cost and off-grid operation which make them ideal for usage in a range of territories and applications [4].

Up to now this field is totally dominated by conventional PV technologies such as silicon or thin film solar cells. Great improvements in device construction have enhanced the

overall solar energy conversion efficiency and thus have significantly reduced the cost of fabrication [4]. However, due to certain fundamental properties of classical inorganic PV solar cells, such devices will always require the use of extremely pure starting materials which therefore results in the use of more expensive and sophisticated production procedures competing with other semiconductor technologies, such as Si wafers. A very promising alternative to classical, silicon *p*-*n* junction solar cells is the concept of nanocrystalline photoelectrochemical (PEC) dye-sensitized solar cells (DSC), which was first introduced by O'Regan and Grätzel in 1991 [5], who were inspired by the energy and electron transfer mechanisms the natural photosynthesis process in plants. The DSC consists of a nanocrystalline wide band gap semiconductor such as TiO_2, sensitized with a light absorbing dye, with an electrolyte as a redox mediator and a counter-electrode to complete the cell.

By following a similar concept, in 1996, Konenkamp introduced the extremely thin absorber-layer (ETA) solar cell [6]. The ETA cell has a more promising future since the organic dye molecule absorber in DSC has been replaced by a strongly light absorbing inorganic semiconductor material in ETA cell. Nevertheless, until now the overall efficiency of ETA solar cells is still far behind those of the DSC as well as other solar cells. This is due to many reasons such as poor energy band match and non-ideal contact between each inorganic semiconductor phase in the ETA cell structures. Today, the DSC and ETA solar cells have reported impressive efficiencies of up to 11.4% and 4%, respectively [7,8]. The production cost of such cells is only a fraction of that of conventional solar cells, as they are constructed from cheap starting materials using simple fabrication techniques [9]. In principle, both DSC and ETA cells have similar charge generation, separation and collection mechanisms, and the only difference between both types is that the light harvesting dye in the DSC is replaced by a semiconductor absorber in ETA solar cells.

The ETA solar cells are based on single-junction solid-state solar cells. The use of solvent free electrolytes (i.e. gel-based electrolytes) in the ETA solar cells has renewed the expectations of developing very stable high performance cells. A solid-state *p*-type hole conducting phase (*p*-type semiconductor materials or conducting polymers) was introduced to replace the ionic liquid electrolyte in ETA solar cells. They seem to have a significant potential for the development of highly efficient and flexible devices compared to the traditional silicon based solar cells because of the advantages listed below [10]:

1. The device performance is less sensitive to the defects in anodic or cathodic semiconductor phases (in contrast to Si-based PV) due to efficient charge separation into adjacent phases.
2. The high surface area semiconductor/electrolyte interface is easy to fabricate and cost effective.
3. The ETA cell efficiency in indoor light conditions is better than that of existing silicon based solar cells, because the semiconductor/absorber interface is effective in diffuse sunlight as well as in indoor lightings (i.e. fluorescent lighting).

The ETA solar cells can be divided into two main types. The first is *n*-type (anodic) semiconductor based ETA solar cell, of which a significant amount of work has been done in order to understand the working principle and to improve the performance of this type of solar cell [8,11,12]. Such cells can be made with ease and are cheap due to a variety of *n*-type materials, with different range band gaps, being readily available [13-15]. The fact that the preparation methods of *n*-type thin film solar cells are widely available has also significantly contributed to this situation [16-19].

The second ETA cell concept can be described as *p*-type (cathodic) semiconductor based ETA solar cell. Constructing cathodic semiconductor based ETA solar cell is very challenging, and until now there are no reports available in the literature on such devices. This is mainly due to the limited choice of materials available and the fact that research in this area is at very early stage compared to the *n*-type counter-part today. Even if such cells were constructed as working devices, there would still be further challenges remaining which would need to be resolved (i.e. the contact between different adjacent phases in the device's structure), short-circuiting (shunting issues) and mass transport limitations of the ions resulting in low conversion efficiencies compared with liquid junction solar cells [20].

The objectives of the present work were to investigate, construct and optimise the photoelectrochemical cathodic semiconductor sensitised solar cells (CSSCs) as well as the solid-state analogues of cathodic semiconductor sensitised solar cells (SS-CSSCs). It is anticipated that such work will lead to the construction of tandem solar cells in the future. The work presented in this thesis focuses on the PV performance of CSSCs and SS-CSSCs prepared using Cu_2S as the cathodic light absorbing semiconductor material. In order to

complete the fabrication of SS-CSSC solar cells, Fe_2O_3 is employed as the anodic phase as its energetic properties are favourable. The individual components in the device and the complete solar cell were then characterised for material, optical and photoelectrochemical properties using a range of techniques such as XRD, UV-Visible, FEGSEM, capacitance, *J-V* and IPCE measurements.

1.2 History of PV

The history of PV began in 1839 when A.E. Becquerel discovered that platinum or silver chloride electrode in contact with an electrolyte generates a voltage under illumination [21]. The next significant development of PV took place when Adams and Day investigated the photoconductive effect in selenium in 1876. They noted anomalies when Platinum contacts were pushed into a Selenium bar. This led them to demonstrate that it was possible to induce a current in selenium merely by the action of light [22]. This study was extended by the finding of the photoelectric effect by Albert Einstein in 1921 [3]. Einstein's finding was the theoretical framework for all PEC effect in all semiconductors and subsequent photovoltaic devices. In a typical semiconductor, the photons excite electrons from the valence band into the higher-energy levels (i.e. the conduction band), where they undergo recombination unless separated, transported and then collected through appropriate contacts. The first semiconductor PV solar cell was constructed by Russel Ohl of Bell Laboratories in 1941 [22]. Exploration of their properties led to further understanding of the role of dopants in *p*- and *n*-type semiconductor phases in controlling semiconductor properties and hence the microelectronic revolution [22].

The first silicon solar cell was thereafter developed by Chapin *et al.* [23], at Bell laboratories in 1954 and the best reported device performance was about 6% overall energy conversion efficiency at that time. It is 50 times more efficient than the selenium based solar cells reported in the 1930s [23]. This device marked a major development of the area as it was the first photovoltaic structure that converted light to electricity with appreciable efficiency. In the following years, PV solar cells employing new materials such as CdS, GaAs, InP and CdTe emerged. These cells found initial applications such as power sources in spacecraft as early as 1958 [21]. By the early 1960s, the design of cells for space use had stabilized, and over the next decade, became the major application of solar cells. The early 1970s saw an innovative

period in silicon cell development due to the oil crisis of the 1970s. Since then the research of PV has accelerated significantly and has undergone different stages to date. A complete table detailing the history of solar cells is shown in Table 1-1 describing early discoveries by well-known scientists such as Becquerel (in 1839) and various development stages since then. It also shows that the cumulative worldwide installation of PV reached 2000 MW in the year 2002, which was a significant milestone.

Table 1-1: Notable events in the history of photovoltaics [4].

Year	Event
1839	• Becquerel (FR) discovered the photogalvanic effect in liquid electrolytes
1873	• Smith (UK) discovered photoconductivity of solid Se
1877	• Adams and Day (UK) discovered photogeneration of current in Se tubes; the first observation of PV effect in solids
1883	• Fritts (US) makes first large area solar cell using Se film
1954	• First 6% efficient solar cells reported: Si (Bell Lab, USA) and Cu_2S/CdS (Air Force, USA)
1955	• Hoffman Electronics (USA) offers 2% efficient Si PV cells at $1500/ W
1958	• NASA Vanguard satellite with Si backup solar array
1959	• Hoffman Electronics (USA) offers 10% efficient Si PV cells
1963	• Sharp Corp (JP) produces first commercial Si modules
1966	• NASA Orbiting Astronomical Observatory launched with 1 kW array
1970	• First GaAs heterostructure solar cells by Alferov, Andreev *et al*. in the USSR
1972	• First PV conference to include a session on terrestrial applications (IEEE)
1973	• A big year in photovoltaics: Worldwide oil crisis spurs many nations to consider renewable energy including photovoltaics; Cherry Hill Conference in USA (established photovoltaics' potential and legitimacy for government research funding); World's first solar powered residence (University of Delaware, USA) built with Cu_2S (not c-Si!) solar modules
1974	• Project Sunshine initiated in Japan to foster growth of PV industry and applications; Tyco (USA) grows 2.5 cm wide Si ribbon for photovoltaics, first alternative to Si wafers
1975	• First book dedicated to PV science and technology by Hovel (USA)
1980	• First thin-film solar cell >10% using Cu_2S/CdS (USA)
1981	• 350 kW Concentrator array installed in Saudi Arabia
1982	• First 1 MW utility scale PV power plant (CA, USA) with Arco Si modules on 2-axis trackers
1984	• 6 MW array installed in Carrisa Plains CA, USA
1985	• A big year for high-efficiency Si solar cells: Si solar cell >20% under standard sunlight (UNSW, Australia) and >25% under 200X concentration (Stanford Univ. USA)
1986	• First commercial thin-film power module, the a-Si G4000 from Arco Solar (USA)
1987	• Fourteen solar powered cars complete the 3200 km World Solar Challenge race (Australia) with the winner averaging 70 Rmph
1994	• GaInP/$GaAs_2$-terminal concentrator multijunction>30% (NREL, USA)
1995	• "1000 roofs" German demonstration project to install photovoltaics on houses, which triggered the present favourable PV legislation in Germany, Japan and other countries
1996	• Photoelectrochemical "dye-sensitized" solid/liquid cell achieves 11% (EPFL, Switzerland)
1997	• Worldwide PV production reaches 100 MW per year
1998	• Cu(InGa)Se_2 thin-film solar cell reaches 19% efficiency (NREL, US) comparable with multicrystalline Si. First concentrating array for space launched on Deep Space 1 by US (5 kW using high efficiency GaInP/GaAs/Ge triple junction cells)
1999	• Cumulative worldwide installed photovoltaics reaches 1000 MW
2000	• Olympics in Australia highlight wide range of PV applications, and the awarding of the first Bachelor of Engineering degrees in Photovoltaics and Solar Engineering (UNSW, Australia)
2002	• Cumulative worldwide installed photovoltaic reaches 2000 MW. It took 25 years to reach the first 1000 MW and only 3 years to double it; production of crystalline Si cells exceeds 100 MW per year at Sharp Corp. (Japan). BP Solar ceases R&D and production of a-Si and CdTe thin-film modules in USA ending >20 years of effort

Modern research in the area of PV technologies has led to the creation of a variety of solar cells, which are commonly classified in to three generations, differing from one another based on the material and the processing technology used to fabricate the solar cells. The first generation of solar cells (also known as silicon wafer-based photovoltaics) were first developed in the beginning of the 1870 s [3] are the dominant technology for global applications today, accounting for more than 85% of the solar cell market. Single-crystalline and multi-crystalline wafers, used in commercial production, give power conversion efficiencies up to 31% under 1 sun illumination (AM 1.5 global intensity). This upper limit is known as the Shockley-Queisser limit [24], although the challenges in device construction and incompatible materials limit the experimental value to about 20 to 25% at present [25].

The study therefore, predicts the lowest cost for high-efficiency in material and processing for solar cell application. The second generation solar cells were introduced around 1958 [21]. From the early 1980s, it appeared that the PV industry was on the verge of switching to the next generation of thin film solar cell technology (the so called 2^{nd} generation). The second generation PV materials were based on the use of thin-film deposits of semiconductors, such as amorphous silicon (a-Si), cadmium telluride (CdTe), copper indium gallium diselenide ($CuInGaSe_2$) or copper indium disulfide ($CuInS_2$). The thin film technology offers prospects for large reduction in material costs by eliminating the costs of using crystalline silicon wafers. Thin film technology also offers other advantages, such as the increased size of the unit of manufacturing. This increases the area of a silicon wafer (~ 100 cm^2) to that of a glass sheet (~ 1 m^2), about 100 times larger [26]. The efficiencies of thin film solar cells tend to be lower compared to conventional solar cells, around 6% to 10% [25], but manufacturing costs are also lower, such that the price of electrical output can be reduced.

In order to increase the light to electricity conversion efficiency beyond the Shockley-Queisser limit, new approaches have been studied, and are generally referred to as the third generation of PV cells. The third generation of PV cells is a research goal towards a dramatic increase in efficiency whilst maintaining the cost advantage of second-generation materials. Other approaches also have been introduced in order to achieve this target. These approaches include dye sensitized nanocrystalline solar cells (also known as the Gratzel cell), extremely thin absorber-layer solar cells, organic polymer-based solar cells, tandem (or multi-junction) solar cells, hot carrier solar cells, multi-band and thermophotovoltaic solar cells. All of the

above developments are focused on multi-junction solar cells that use a combination of semiconductor materials to capture a wide range of photon energies efficiently. Multi-junction solar cells have the highest theoretical limit of conversion efficiency compared to other photovoltaics. In principle, in multi-junction solar cells, sunlight can be converted to electricity at efficiencies close to the limit of 95% for the sun modelled as a black-body at 6000 K. This suggests the performance of solar cells could be improved up to 2-3 times if fundamentally different underlying concepts were used in the design, ultimately to produce a third generation of high performance, low-cost photovoltaic cell. A present record efficiency of 43.5% was achieved with a multi-junction solar cell by Solar Junction Company in April 2011 [27]. Table 1-2 shows the performance of solar cells dominated by the Silicon (wafer) based solar cells. However, since the volumes of silicon-based approaches are decreasing, the thin-film solar cell technology is becoming increasingly attractive.

Table 1-2: A brief summary of the latest data of the energy conversion efficiencies of PV.

Classifications	**Efficiency (%)**	V_{oc} **(V)**	J_{sc} **(mA/cm^2)**	***FF*** **(%)**
Silicon				
Si (crystalline)[25]	25.0	0.706	42.7	82.8
Si (multi-crystalline)[29]	20.4	0.664	38.0	80.9
III-V cells				
GaAs (crystalline)[30]	27.6	1.111	29.4	85.9
GaAs (multi-crystalline)[27]	18.4	0.994	23.2	79.7
InP (crystalline)[27]	22.1	0.878	29.5	85.4
Thin Film Chalcogenide				
CIGS [31]	19.6	0.713	34.8	79.2
CdTe/CdS[27]	16.7	0.845	26.1	75.5
Amorphous/Nanocrystalline Si				
Si (amorphous)[27]	10.1	0.859	16.75	67.0
Si (nanocrystalline)[27]	10.1	0.539	24.4	76.6
Photochemical				
Dye sensitised[27]	10.9	0.736	21.7	68.0
Extremely thin absorber[32]	1.52	0.447	11.1	31.0
Organic				
Organic polymer[27]	8.3	0.816	14.46	70.2
Multijunction Devices				
GaInP/GaAs/Ge[27]	32.0	2.622	14.37	85.0
Tandem[33]	1.91	1.079	2.40	74.0

1.3 Relevant work reported by others to date

Very recently, CSSC and SS-CSSC have received wide attention because of the potential application of photoactive semiconductor cathodes in tandem solar cells. It was first introduced in dye sensitised solar cells by Peng Qin *et al.* [34] who studied the PEC photoactive cathodes for tandem cell applications. The study achieved ~17% efficiency which proves that the *p*-type materials can be used to construct Tandem cells. This led to the introduction of SS-CSSC by J. Bandara and H. Weerasinghe [35] which achieved a photocurrent density of 0.15 mA cm^{-2}. Until now, no research has been reported regarding SS-CSSC. This is due to the difficulty in finding energetically matching cathodic semiconductors for SS-CSSC which are stable. Later, the focus of research was turned towards fully inorganic solar cells such as ETA solar cells. More research and development is required for photoactive cathodic materials in tandem cells. Our study is focused on construction and studies of CSSC and SS-CSSC based on ETA solar cells. In general, CSSC and SS-CSSC solar cells comprise of a nanocrystalline, *p*-type semiconductor with a wide band gap material. This is attached to a *p*-type light absorber material. If an electrolyte is used to construct the cell, it'll become CSSC whereas if an *n*-type semiconductor material or electron conducting polymer is employed the device will become the SS-CSSC. Like any other PEC cell, a platinum counter electrode and a redox electrolyte can be employed instead of the electron conducting phase in the CSSC cell.

1.4 Scope of this thesis

The initial objective of this work was to construct SS-CSSC cells directly. This is mainly due to the short life-times of PEC cells, which contain a corrosive and volatile electrolyte, which can corrode other cell components and evaporate over time. Solid-state devices based on cathodic study, were originally designed to be applied in tandem solar cell applications to avoid such electrolyte-specific problems. However, to date, solid-state analogues of photosensitised solar cells are still far from competing with their PEC counterparts in terms of their performance. The other objectives of the present work were to perform a systematic study of the performance limiting factors associated with the photosensitised photocathodes. However, due to the difficulty of construction of SS-CSSC

directly, CSSC solar cells were initially constructed and studied. At the final stage of this work, attempts were made to construct SS-CSSC. The study is mainly of an experimental nature, supported by different spectroscopic and electrochemical characterisation techniques.

The thesis is divided into seven main chapters: chapter 1 summarizes the fundamentals of photovoltaics, history of photovoltaics and the latest performance of photovoltaic devices. The second chapter gives the theoretical background of single-junction solar cell designs/architectures and the limitations of CSSC and SS-CSSC, ending with key parameter requirements for such cells. Chapter 3 presents the materials used for photosensitising the wide band gap photocathodes in the present work, and practical issues that are encountered and the attempts that were taken to overcome them. Chapter 3 also considers the device preparation and experimental characterisation techniques. Chapter 4 presents the characterization of photosensitised photocathodes such as CuI and NiO that are sensitised with Cu_2S using different methods. Chapter 5 shows the performance of CSSCs and the influence of the electrolyte on the devices. Chapter 6 addresses the influence of the electron collector replacing redox couple electrolyte in the solid-state analogues (SS-CSSC). The final section, chapter 7 of this thesis presents the conclusions and suggestions for future work.

Chapter 2: Theoretical

2.0 Theoretical Background

Semiconductors are essential components in solar cells. They come in organic and inorganic forms and play a key role in the solar cell operation. For example, they play active roles in light absorption and charge generation, charge separation, transport and subsequent collection in all types of solar cells known today. Therefore, a brief introduction is given to semiconductors at the beginning of this chapter. This is followed by the limitations of present solar cells, emerging solar cell configurations such as Tandem solar cells. The final section of this chapter will deal with cathodic semiconductor based solar cells which is one of the key objectives of this doctoral research project.

2.0.1 Basics of semiconductors

Generally, there are three types of materials, and they can be classified as metal, semiconductor and insulator based on their energetics as illustrated in Fig 2.1.

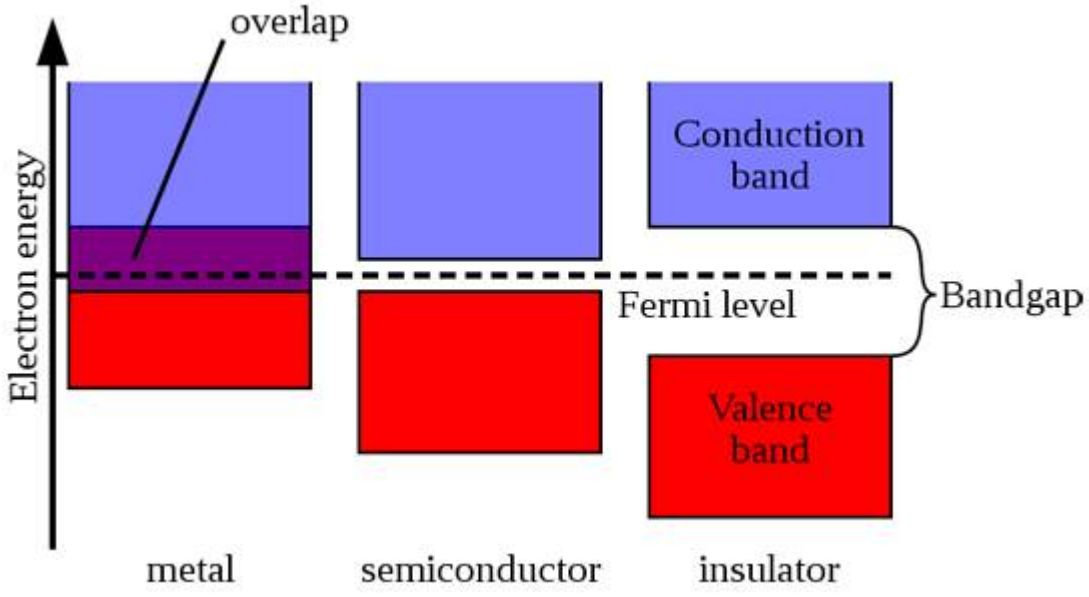

Fig. 2-1: Comparison of energetics for a metal, a semiconductor and an insulator.

As shown in Fig 2-1, the highest occupied energy band in a semiconductor, which contains the electrons, is known as the valence band (VB) and the lowest unoccupied energy band is called the conduction band (CB). The difference in energy between the valence and conduction bands is defined as the band gap (E_g). For an intrinsic semiconductor, the probability of an energy level being occupied by an electron is half and is called the Fermi level (E_F). If the valence band and the conduction band naturally overlap each other, the solid is a conductor (i.e. a metal). Such materials are able to carry charge current under any condition [36,37]. In other words, the availability of empty states with similar energies makes it easy for electrons in the VB to become excited into the CB and act as a carrier to conduct heat and electric current. For insulator materials, the VB is fully occupied by electrons and there is a large energy gap between this band and the CB. Due to this large energy gap, the electrons do not promote from VB to CB in such materials. This class of materials therefore do not conduct heat or electric current easily.

A semiconductor is a type of insulator which has a narrow band gap compared to that of an insulator. Typical band gap ranges from 0.5 to 3 eV [21,38]. At low temperatures, a semiconductor acts as an insulator which does not conduct electricity but at higher temperatures the electrons in the VB will gain enough energy to excite across the band gap to an available unoccupied level (i.e. CB). Then, the electrons in the excited state (i.e. CB) can conduct charge resulting in a current flow. Semiconductors also have low conductivity in dark conditions at room temperature because a small number of electrons in the VB have enough kinetic energy at room temperature to be excited to the CB level [38].

Semiconductors can be generally classified into two types, namely intrinsic and extrinsic semiconductors [39]. An intrinsic semiconductor material is chemically very pure and possesses low conductivity. It has equal numbers of negative carriers (electrons) and positive carriers (holes) in the conduction and valence bands and the E_F is located in the middle of the band gap as shown in Fig 2-2 (a). Whereas an extrinsic semiconductor is an improved intrinsic semiconductor with a small amount of impurities added by a process, known as doping, which alters the electrical properties and improves its conductivity. Introducing impurities into the semiconductor materials (i.e. doping process) can control their conductivity [39]. Doping processes produce two groups of semiconductors: the negative

charge conductor (*n*-type) and the positive charge conductor (*p*-type). In *n*-type doping, the addition of donor impurities (e.g. group V materials such as phosphorous are used for *n*-type doping of silicon) shifts the E_F closer to the conduction band as illustrated in Fig 2-2 (b). For *p*-type doping, the addition of electron acceptor impurities (e.g. group III materials such as boron are used in silicon) shifts the E_F closer to the valence band as shown in Fig 2-2 (c) [39].

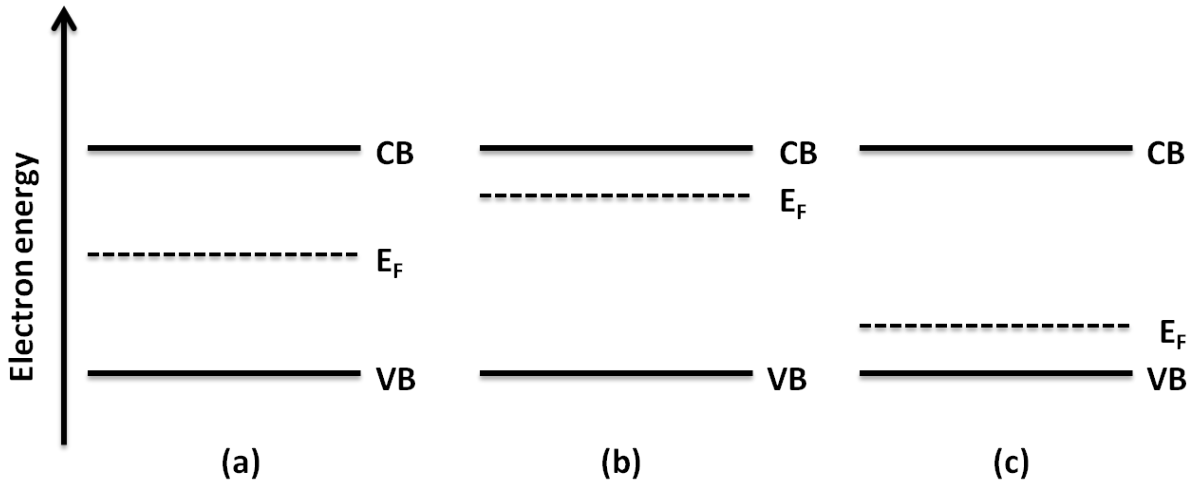

Fig. 2-2: Energy level diagrams for various conduction types of semiconductor a) an intrinsic semiconductor, b) an extrinsic *n*-type semiconductor and c) an extrinsic *p*-type semiconductor.

2.0.2 Semiconductor materials for solar cell application

The solar cell devices based on semiconductor materials mainly operate via two separate mechanisms: Firstly, an electron in the valence band is excited across the band gap by an incident photon of sufficient energy, leading to the formation of an electron-hole pair. Secondly, the electron-hole pair must then be separated by an electric field before the charges recombine, in order for a photocurrent to be generated and collected. The effect that light has when incident on an ideal semiconductor principally depends upon the band gap of the material, E_g, and the energy of incident photons, hv. The possible outcomes of this interaction are listed below and illustrated in Fig 2-3 [3,40]:

- For photons with energy less than the material band gap ($hv < E_g$), no excitation across the band gap may occur as the photons have insufficient energy.

- For photons of energy, $hv = E_g$, an electron from the valence band is excited across the band gap leading to the formation of an electron-hole pair
- For photons of energy, $hv > E_g$, the photon can raise the electron to the conduction band but any excess energy is quickly lost as heat as the carriers relax to the band edge.

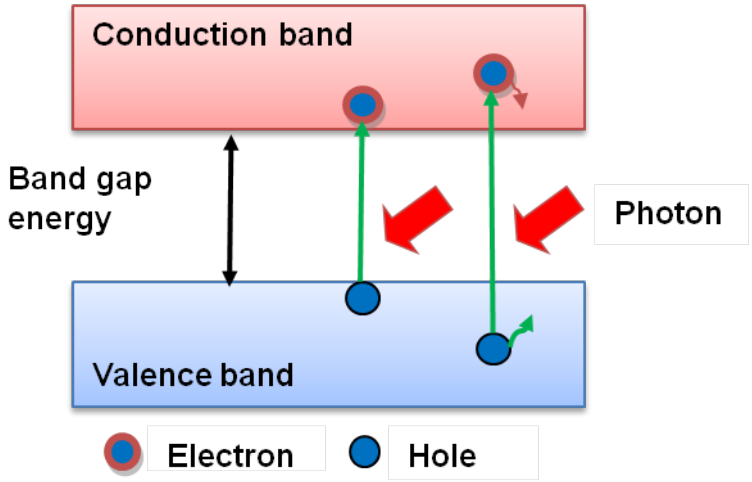

Fig. 2-3: A diagram that shows light absorption and charge generation within a semiconductor.

2.1 Single-junction solar cell designs and their limitations

A single-junction by definition will have a single band gap as it employs only one semiconductor [41]. In principle, a semiconductor with the smallest band gap should yield the highest photocurrent as such a material can absorb the entire solar spectrum (i.e. absorption of the maximum number of photons from the sunlight). Still, the photons with higher energy will waste most of their energy in collisions with the lattice. The opposite scenario is not satisfactory either. Having a large band gap implies that the photons at the lower energy end of the solar spectrum will not be absorbed, and therefore only a small portion of the solar spectrum will be used and hence, the resulting photocurrent will be significantly low [3,21,40]. In order to design a highly efficient solar cell based on a single-junction, attention should be paid to the solar spectrum factor (band gap engineering of the semiconductor materials) as shown in Fig. 2-4.

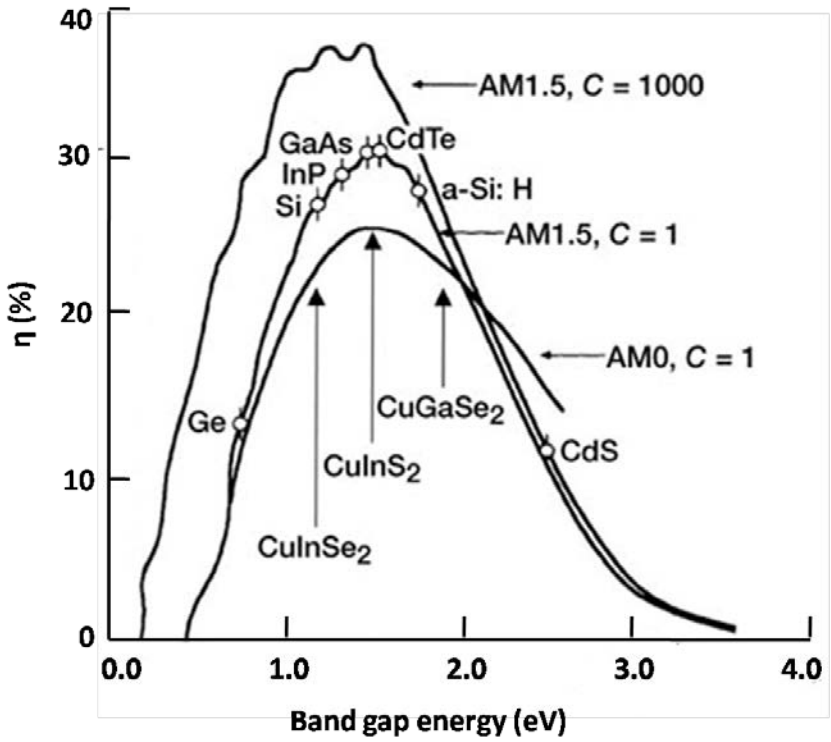

Fig. 2-4: Efficiency vs. band gap for thin-film photovoltaic materials for the solar spectrum in space air mass zero (AM 0), on the surface of the Earth air mass 1.5 (AM 1.5) at 300 °K and C is concentration ratio corresponding to the air mass [42].

Knowing that the greatest number of electrons is emitted in the visible range, the band gap of the prospective semiconductor should align with the visible region. Nevertheless, it appears that the greatest balance between the current and the voltage is achieved by using semiconductors with band gaps in the mid region of the solar spectrum [3]. The main problem of the single-junction based solar cells arises from its single band gap. There will be a lot of unused photons that will be wasted [3,21,40]. Fig. 2-4 also shows the Shockley-Queisser ideal efficiency limit. Shockley and Queisser called this limit the nominal efficiency, to be compared with ultimate efficiency (estimated for the limiting efficiency solar cell label as air mass 1.5 (AM 1.5, C = 1000 (concentration ratio corresponds to AM 1.5)). The other two curves are namely air mass zero (AM 0, C=1 (concentration ratio corresponds to the AM 0, solar intensity as observed outside the earth atmosphere) and AM 1.5, C=1 (concentration ratio corresponds to the AM 1.5, light focus on the cell by a mirror or a lens). The area above

the label AM 1.5, C=1 is equal to the loss of current due to the inability of the semiconductor to absorb below the band gap. The area above the band gap represents energy losses due to thermalisation (the losses of energy by the photoexited electron-hole pair in excess of the band gap [43]) of the electron-hole pairs only the area below the label AM 1.5, C=1 represents the maximum efficiency that can obtained for a single junction solar cell constructed from a semiconductor [3]. In addition, the air mass is the path length which takes light through the atmosphere normalized to the shortest possible length. The air mass quantifies the reduction in the power of light as it passes through the atmosphere and is absorbed by air and other atmospheric objects such as dust. The air mass is defined as [21]:

$$AM = \frac{1}{\cos\theta} \qquad (2-1)$$

Where θ, is the angle from the vertical (Zenith angle). Zenith angle is how far away from directly overhead the sun is.

For the limitation of short-circuit current (J_{sc}), under the ideal condition (AM 1.5, C = 1000), each incident photon on the cell with energy greater than the band gap gives rise to one electron flowing in the external circuit, provided that all loss mechanisms are prevented [21]. Hence, the maximum J_{sc}, can be estimated from the monochromatic energy distribution of sunlight by dividing the energy content at a given wavelength (λ) by the energy of an individual photon ($h\upsilon$ or hc/λ) of this wavelength. The maximum J_{sc} is then found by integrating these distributions across the concerning wavelength window for a given semiconductor. The relationship between photon energy E (in eV) and its wavelength λ (in micro meters) is given in Eq. 2-2: [40]

$$E\ (\text{eV}) = 1.24/\lambda\ (\mu\text{m}) \qquad (2-2)$$

As a result, when the band gap is decreased, the maximum short-circuit photocurrent density is increased and more photons have sufficient energy to promote an electron from VB to the CB.

The fundamental limitations on the open-circuit voltage (V_{oc}) of a single-junction solar cell is given by Eq. 2-3: [44]

$$\mathrm{V_{oc}} = \frac{kT}{q} ln\left(\frac{I_L}{I_o}\right) + 1 \qquad (2-3)$$

Where k is the Boltzmann constant, T is the temperature, q is the elementary charge, I_L is the light-generated current and I_o is the diode saturation current density. A reasonable estimation of the minimum value of the saturation current density as a function of band gap (E_g) is given by Eq. 2-4; [21]

$$\mathrm{I_o} = 1.5 \times 10^5 \exp\left(-\frac{E_g}{kT}\right) A/cm^2 \qquad (2-4)$$

The above relationship ensures that the maximum value of V_{oc} decreases with decreasing band gap. It can be concluded that the optimum band gap (1.1 eV) gives relatively high efficiency.

In the Shockley-Queisser analysis for a single junction solar cell, the major limiting factor is the maximum energy conversion efficiency (31%) and that the absorbed photon energy above the semiconductor band gap is lost as heat through electron-phonon scattering and subsequent phonon emission (thermalisation) [40,44]. In order to overcome this limitation, a number of approaches have been taken. Construction of multiple *p-n* junctions (cascades) and developments of tandem cells are notable among them [45-49].

The ability to absorb a wide range of the solar spectrum more effectively by utilising a multi-junction structure is the key to construction of highly efficient solar cells. The achievable efficiency of such cells exceeds beyond the Shockley Queisser limit of about 31% for a single-junction device [50]. The multiple junctions are layered upon one another and are connected optically, electrically and are stacked in series. Ideally, the multi-junction approach requires that incident photons be directed on to the first junction, and then cascade through the subsequent layers. These layers have been made in the decreasing order of their band gaps, where the light travels through the semiconductor with the largest band gap, before passing through to the lower band gap materials progressively. This arrangement makes use of the fact that junctions act as low-pass photon energy filters, transmitting only the sub–band gap light. In this way, the light absorption onset of the complete device is shifted to longer wavelengths. In addition, high energy photons are converted more efficiently since thermalization losses of the generated electron-hole pairs are reduced with the graded band gap structure. Firstly, photons with $h\upsilon > E_g3$ get absorbed by the E_g3 junction, $E_g2 < h\upsilon < E_g3$ absorbed by the E_g2 junction and so on as shown in Fig 2-5. In other words, the junctions themselves act as optical elements to distribute the spectrum to the appropriate junctions for multi-junction

photoconversion. Theoretically, the photovoltaic conversion efficiency of a multi-junction cell approaches the thermodynamic limit of about 85% if an infinite number of subcells and maximum solar concentration is used [51,52]. The highest photovoltaic power efficiency is reached with multi-junction concentrator solar cells based on III-V semiconductors. Stunning record conversion efficiencies of over 40% at concentrated sunlight have been measured with epitaxial grown triple-junction GaInP/GaInAs/Ge devices [53]. Though this expensive technology may be interesting for space and terrestrial concentrator applications, it plays a marginal role in the large-scale PV market.

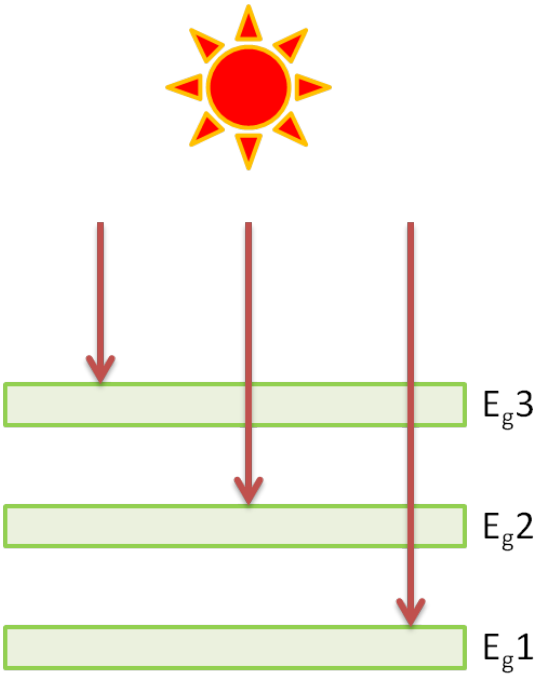

Fig. 2-5: A schematic diagram of stacked-configuration approaches to distributing light to the multi-junction cells from the high band gap material to the lower band gap material.

The tandem cell concept utilizes high-quality inorganic semiconductor materials, for this application materials with different band gaps have been studied, but the focus to date is on dye sensitised tandem solar cells (DSC) rather than extremely thin absorber-layer Tandem (ETA) solar cells. A feature that makes the DSC and ETA solar cells particularly attractive for tandem cell application is that their optical transmission and short-circuit photocurrent can be readily adjusted by changing the film thickness, pore size, the nature of the dye/light-absorber

and its loading. In theory, tandem solar cells based on the DSC and ETA cells can reach up to 45% efficiency which depends on the optimal band gaps for the top and bottom cells being around 1.65 eV and 1 eV respectively [54]. To assemble tandem solar cells for these two types of solar cells, the dye/light-absorber can be separated into two compartments namely the photoanode and a photocathode in a simple sandwich configuration with a redox electrolyte occupying the space in between as illustrated in Fig. 2-6. In the photoanodic compartment which is closer to the light source, with the highly efficient dye/light-absorber absorbing in the shorter wavelength region are attach to the highly transparent *n*-type wide band gap semiconductor material such as TiO_2 particles. In the lower compartment, the photocathode, dye/light-absorber molecules absorbing in the longer wavelength region which is the low energy photons are not absorbed by the dye/light-absorber in the first compartment, may be harvested in the second compartment. Note, in order to optimise the device performance, the photocathode should be at least equally efficient in term of absorbance or electron injection because it contributes to the number of photons converted to electrical current. A simple mechanism can be used to explain the operation of a tandem dye-sensitised or an ETA solar cell. The absorption of light by the two sensitizers, causes generation of an excited state, in which an electron is injected into the conduction band (CB) of the anode and a hole is injected into the valence band (VB) of a *p*-type semiconductor at the cathode. These charges are transported through the respective semiconductor photoelectrodes and are collected at the respective FTO substrate. To complete the overall photo-induced charge transfer reaction, the oxidized and reduced forms of the redox mediator regenerates the dye/light-absorber at the cathode and the anode, respectively. This is schematically presented in Fig. 2-6. As mentioned above, in order to achieve high performance tandem cells, first it is important to optimise the performance of individual photoelectrodes which have complimentary light harvesting characteristics. The cell structure must be designed by matching photocurrent density at each photoelectrode. For this, each photoelectrode should be considered separately. However, until now such efforts have yielded relatively poor device performance mainly due to the limited availability of desired materials and preparation techniques that are compatible.

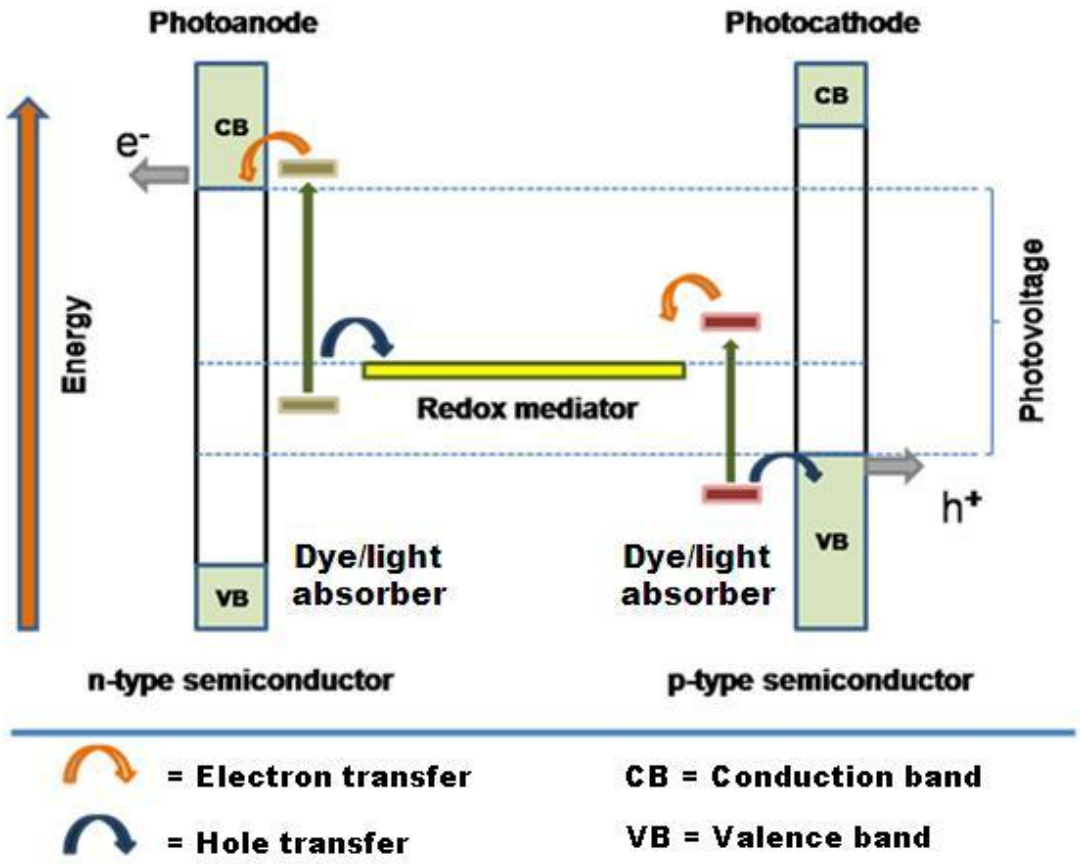

Fig. 2-6: Scheme for the electron transfer processes occurring in the tandem DSC and ETA solar cell.

2.2 Cathodic semiconductor sensitised solar cells (CSSCs)

The issues of single junction solar cells have been briefly discussed in previous sections of this chapter. In order to move beyond the current efficiency records, novel solar cell structures with new materials that improve the light harvesting efficiency and photovoltage need to be explored. Furthermore, it was discussed that light harvesting cathodic half –cells play a key role in the development of successful Tandem solar cells. Unfortunately, the progress of cathodic semiconductor sensitised solar cells (CSSC) has been painstakingly slow during the last decade. This is due to the fact that the CSSC is inversing the working principle of *n*-type solar cell where the semiconductor materials play the important role in development of solar cells. It is well known that *p*-type semiconductor materials are very rare and not highly stable under solar cell operational conditions which make it difficult to

construct Tandem cells when the band gap energetics matching has to be considered. Wide band gap *p*-type semiconductor materials are transparent to visible light, and only absorb in the UV region of the solar spectrum. The majority charge carriers in *p*-type materials are holes whereas the minority charge carriers are electrons. Many known and affordable cathodic semiconductor materials have wide band gaps, hence only a small amount of electrons are excited to the unoccupied band leading to poor light harvesting properties. Another drawback is the crystal structure mismatch leading to defect rich solid-solid heterojunctions. High defect densities at heterojunctions increase the losses leading to poor contact between the materials which lead to the poor light to electricity conversion efficiency.

A schematic diagram of a CSSC based on the photosensitisation concept is displayed in Fig 2-7.

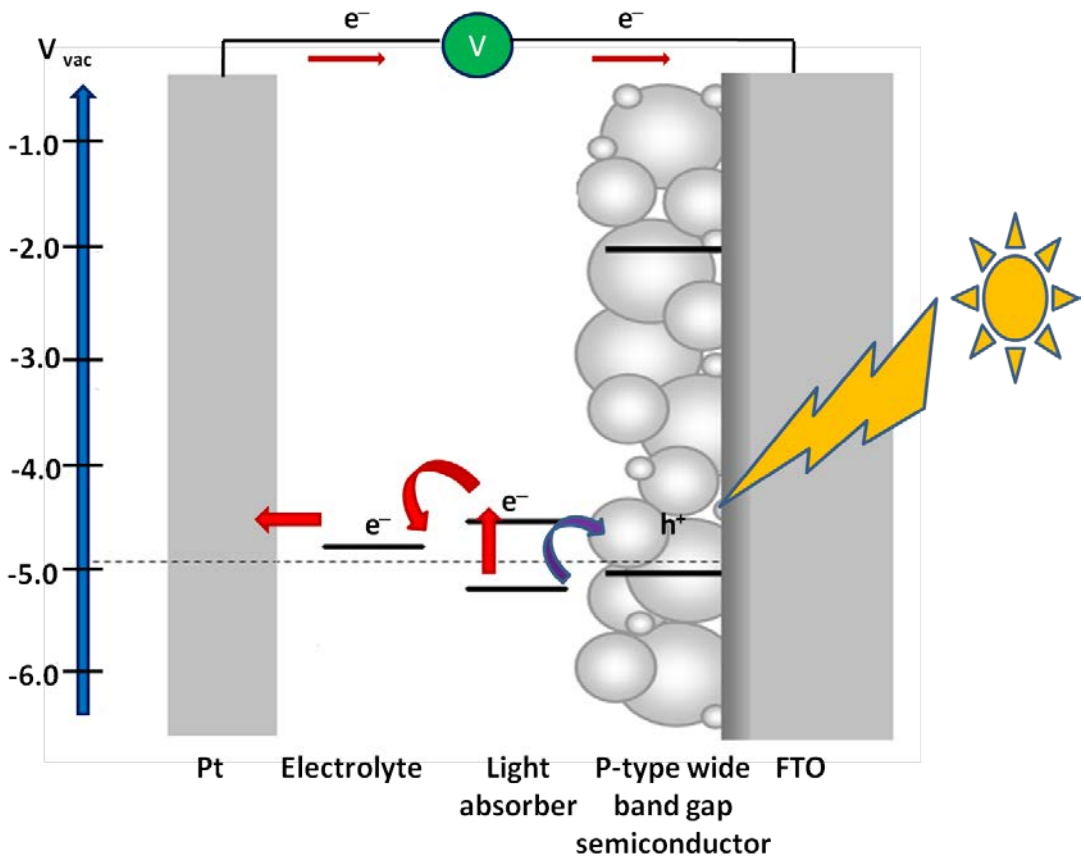

Fig. 2-7: A schematic diagram of a cathodic semiconductor solar cell based on the photosensitisation concept.

In a typical cathodic semiconductor sensitised solar cell (CSSC) the hole transporting layer consists of wide band gap photocathodic semiconductor materials. Generally, it is not expected that this material be a light harvesting component. It acts as a support for a thin layer of light absorbing material over a large internal surface area. Hence, this wide band gap cathodic semiconductor layer is preferred to be in a textured form (i.e. microstructured or nanostructured). The light absorber material (often a narrow band gap cathodic semiconductor) is then deposited on the surface of the wide band gap semiconductor photocathodic material. The nature of attachment between light absorber and textured cathodic wide band gap window material can be either chemisorption or physisorption type. For chemisorption type attachment, organic linkers are required to provide the chemical bond. Chemisorption of the light absorbing material on the wide band gap material makes it easy for the charge transfer to occur [55]. Therefore, a chemisorption linker between the wide band gap material and the absorber is necessary to establish the electronic communication. By improving the hole transfer rate, the electrons can easily be injected in the opposite direction (from light absorbing material to the electrolyte and ensure regeneration of light absorbing material thereby preventing the material degradation (i.e. oxidation). If the adsorption of the light absorber material on the wide band gap material is physisorption type, the interaction is weak (i.e. Van der Waals). The obvious consequence of such electrostatic interaction is the inefficient charge transfer rate [55]. In such a situation it is possible that the light absorber looses the contact due to poor bonding. Bonding of such weakly attracted materials will not be sustained for a prolonged period of time under illumination. This is due to the nature of the weak interaction between these two materials.

As shown in Fig. 2-7, the CSSC was made from the simple sandwich structured device composed of a visible light-sensitised photoelectrode (photocathode), Pt counter electrode (anode), and a redox electrolyte. The main components in the making of a CSSC type solar cell are fluorine-doped SnO_2 (FTO) glass substrate, nanostructured (or microstructured) *p*-type wide band gap semiconductor thin film electrode, light absorber semiconductor material layer, counter electrode (i.e. Pt) and the electrolyte containing a redox couple. In this study, CuI and NiO have been used as the wide band gap *p*-type semiconductors, Cu_2S as the light absorber material and iodide/tri-iodide and europium nitrate solution as redox electrolytes.

The operational mechanism of CSSCs can be explained as follows; after generation of an electron-hole pair upon illumination, hole injection from the light absorber material to the valence band of the wide band gap semiconductor material takes place. The light absorber material is then regenerated by electron transfer to the reduced absorber from the oxidized species in the electrolyte (from tri-iodide species if I^-/I_3^-)) before light absorber material undergoes degradation. If the reduced light absorber material is not capable of transferring electrons to the electrolyte at sufficient rate, electrons may recombine with the holes in the valence band of the wide band gap semiconductor. In the absence of such recombination, the hole in the semiconductor material moves to the hole collector layer (i.e. FTO substrate). This charge collection gives rise to a cathodic photocurrent in the external circuit.

In order for charge transfer to take place in the CSSC, the valence band of the light absorber semiconductor should be below the energy level of that of the wide band gap *p*-type semiconducting material, whereas the conduction band of absorber should be located above the potential of the redox system and far below the bottom of the conduction band of a *p*-type semiconductor material (Fig. 2-7). In other words, the conduction and valence bands of a wide band gap semiconductor must be higher than absorbers conduction and valence band but the potential energy of the redox system in between the two materials. The open circuit voltage (V_{oc}) can be measured in between the potential energy level of the redox system and the conduction band level of the *p*-type semiconductor material which is normally small compared to *n*-type solar cells. There are two possible ways for electron transfer to occur after the absorber is excited by the illumination of the light. The first way is electron transfer from the valence band of the *p*-type semiconducting material to the valence band of the absorber, followed by electron transfer from the reduced absorber to the oxidized species of the redox couple in the electrolyte. The second way is that the excited electron in the conduction band of the absorber transfers to the oxidized species in the electrolyte, followed by electron transfer from the valence band of the *p*-type semiconductor material to the oxidized absorber.

2.4 Solid-state cathodic semiconductor sensitised solar cells (SS-CSSC)

The novel solid-state cathodic semiconductor sensitised solar cell (SS-CSSC) as illustrated in Fig. 2-8 is a new approach and until now published work especially in the field of ETA solar cells are scarce. However, this challenge has been fulfilled in dye sensitized solar cell successfully by constructing solid-state DSC cells successfully. Table 2-1 and 2-2 shows the work conducted by others on the development of cathodic solar cells to date.

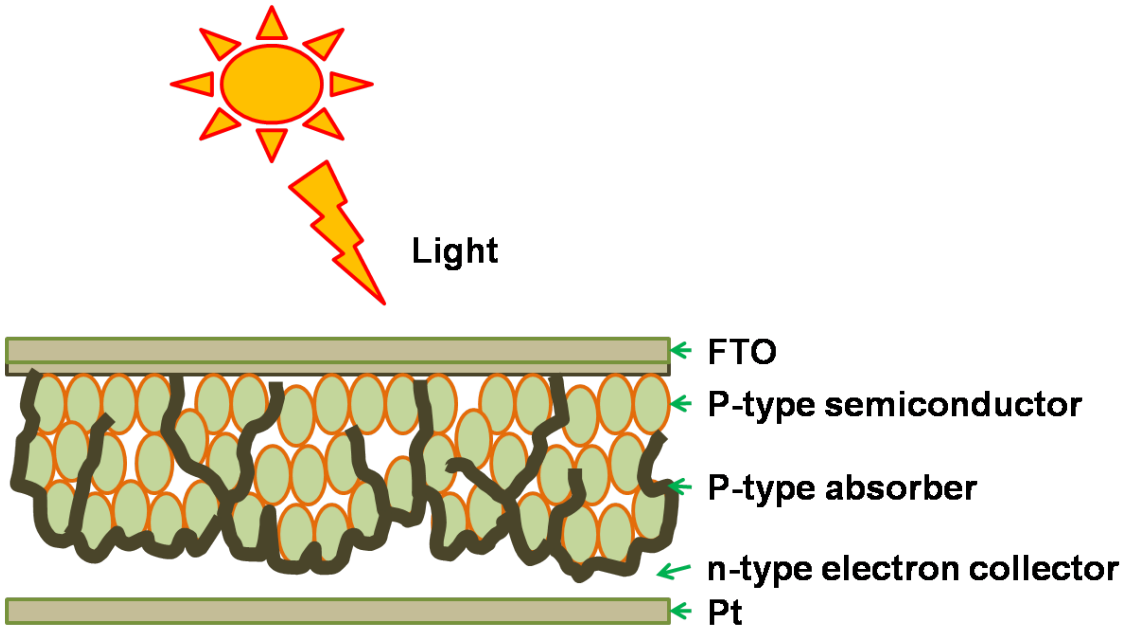

Fig. 2-8: Schematics of solid state cathodic semiconductor sensitised solar cell.

The concept of SS-CSSC is an extension of CSSC. In this solar cell type, the electrolyte is replaced by the electron-collector and the function of it is to collect electrons from the absorber. This can be a polymer (electron conducting polymer, PCBM, P3HT and P3OT) or an *n*-type inorganic semiconductor material (i.e. TiO_2, In_2S_3, Fe_2O_3, WO_3, ZnO and SnO_2). In this study, Fe_2O_3 was used as the electron collector n-type semiconductor material.

The working principle of SS-CSSC is very similar to that of solid-state DSCs, when the light is absorbed, electron hole pairs are generated inside the absorber layer. Hole is injected into the valence band of the wide band gap photocathode semiconductor material and the resulting excited electron in the conduction band of the absorber material is injected to the

electron collector material. The hole reaches the working electrode (WE) via charge percolation mechanism inside the porous photocathode matrix. On the other side, the electron is transferred to the Pt electrode through a hopping type charge transfer mechanism. Whilst the photogenerated electrons are being transferred to the collector contact of the wide band gap photocathode they can be still lost through the recombination with the electrons (that still exist inside the photocathode), so the lifetimes of both carriers have to be substantially longer than the time they require to reach the contacting electrode in order to convert light to electricity efficiently. In order to draw large photocurrent densities, the charge transport capacities of the two interpenetrating networks need to be sufficiently high so that the cell efficiency is not limited due to their high Ohmic resistances. These properties will mainly be governed by material properties such as charge mobility and charge carrier concentration. A further important prerequisite for a functioning SS-CSSC is finding suitable contact between the materials and the window conductor (FTO). This is due to the internal short circuits (Ohmic contact) between the charge transport material and the FTO. The charge transfer schematics of an SS-CSSC and the corresponding energy diagram are shown in Fig. 2-9 and Fig. 2-10 respectively.

As shown in the desired energetic diagram (Fig. 2-10) the difference between the valence band energies of the *p*-type semiconductor and the absorber, as well as the difference between the conduction band energy of the absorber and electron acceptor, need to be minimised in order to avoid energy losses in the solar cell. Such energy losses will reduce the photovoltage, efficiency and overall performance of the solar cell.

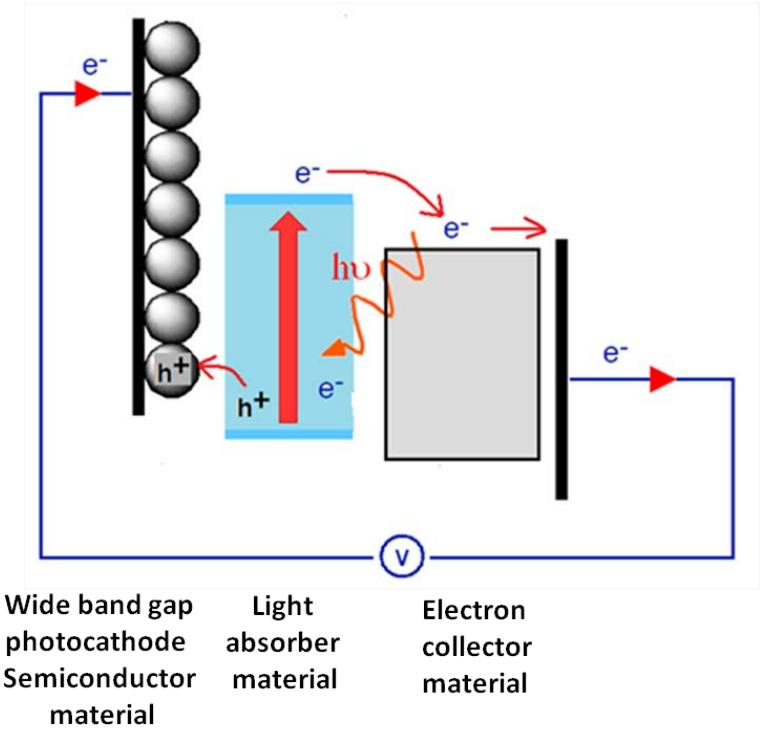

Fig. 2-9: The charge transfer schematic of solid-state cathodic semiconductor solar cells (SS-CSSC).

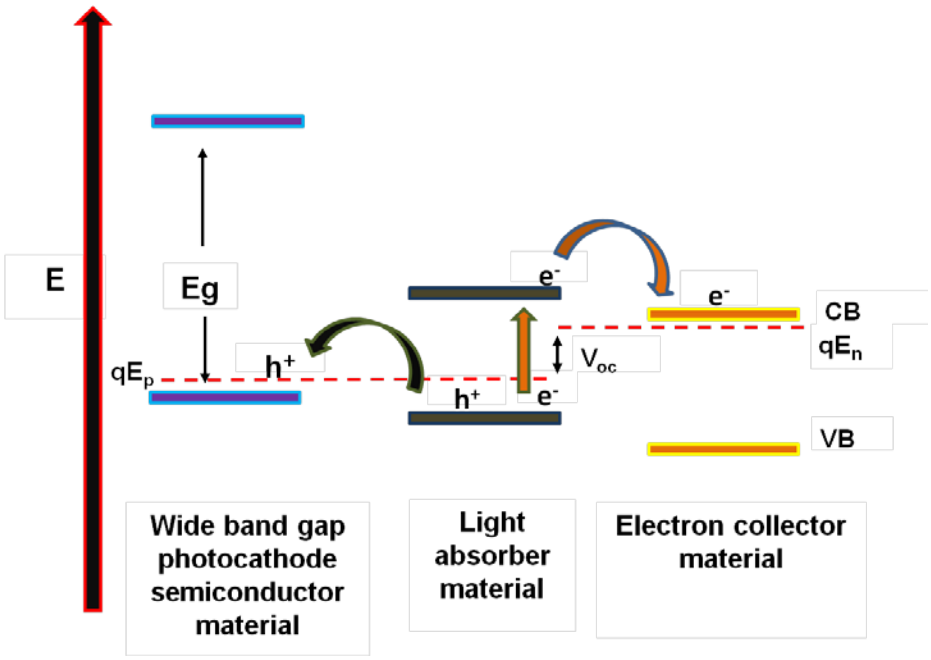

Fig. 2-10: Desired energy band diagram of a solid-state cathodic semiconductor solar cell (SS-CSSC).

Table 2-1: Review of photoelectrochemical cathodic solar cells reported in the literature.

Cell structure	PEC cells electrolyte	J_{sc} / $mAcm^{-2}$	V_{oc} / V	FF	η %	Year	Ref
Cu / CuSCN / Rhodamine-C18	I^-/I_3^-	0.40	-	-	0.09	1994	[56]
NiO/ Erythrosin B	I^-/I_3^-	0.23	0.08	0.27	0.03	1999	[57]
NiO/Eosin B	I^-/I_3^-	0.80	-	-	-	2005	[58]
NiO/Coumarin 343	I^-/I_3^-	0.55	0.09	0.29	0.02	2008	[59]
NiO/Fast green	I^-/I_3^-	0.14	0.09	0.32	0.04	2008	[60]
NiO/N_3	I^-/I_3^-	0.15	0.11	0.31	0.18	2008	[61]
CuO/NK-2612	I^-/I_3^-	0.36	0.10	0.22	0.08	2008	[62]
NiO/Cu_2S	I^-/I_3^-	0.36	0.95	-	0.18	2009	[63]
NiO/C343	I^-/I_3^-	0.88	0.12	0.28	0.04	2009	[64]
NiO/PINDI	I^-/I_3^-	1.70	0.35	-	-	2009	[65]
NiO/ Bithiophene	I^-/I_3^-	4.64	0.19	0.35	0.30	2010	[33]
NiO/ P1dye	I^-/I_3^-	5.48	0.84	0.33	0.15	2010	[66]
NiO/CdS	I^-/I_3^-	0.38	0.35	0.21	0.027	2011	[67]

Table 2-2: Review of solid-state cathodic solar cells reported in the literatures.

Cell structure	J_{sc} / mAcm^{-2}	V_{oc} / V	FF	η %	Year	Ref
TiO_2/cyanidin/CuI	0.25	0.38	-	0.80	1995	[68]
TiO_2/Selenium/CuSCN	3.00	-	-	0.13	1998	[69]
TiO_2/ Rhodamine /CuSCN	0.50	0.6	-	0.02	2002	[70]
TiO_2/N719/PEDOT-PSS/CuI	0.15	0.44	0.48	0.03	2005	[35]
TiO_2 / Ruthium(II)trisbipyridyl /NiO	0.50	0.48	0.43	0.01	2007	[71]

2.4.1 Device components and materials

A typical SS-CSSC consists of several layers of different materials as thin films in textured cascade form. Generally, a SS-CSSC consists of a transparent conducting substrate (i.e. FTO, ITO), porous wide band gap cathodic semiconductor window layer, narrow band gap light absorber layer (i.e. a narrow band gap *p*-type inorganic semiconductor) and an electron conducting phase (i.e. an electron conducting polymer or an *n*-type semiconductor). Each component material should have specific energetic, physical and chemical properties to play the desired role in the device. They must be complementing each other spectroscopically and the deposition method of each layer should be compatible with other components within the device. Each phase affects the overall performance of the device in some form or another. A critical understanding of the behaviour of these individual components is essential for designing and successfully constructing a SS-CSSC. The nature of interfaces of different components is also equally important. For example, each layer of material has it's own crystal structure, microstructure, lattice constants, electron affinity/work function, thermal expansion coefficient, diffusion coefficient, chemical affinity, mechanical adhesion and charge mobility. Due to this, the interfaces can cause stresses, defects and interface states, surface recombination centers, photon reflection/transmission/scattering, inter-diffusion and chemical changes that directly influence the SS-CSSC device performances [72]. A brief review of the current understanding of different SS-CSSC components is given in the following section.

The knowledge of the energy band diagram of a solar cell is essential for a fundamental understanding of their function and mechanism. In other words the perfect match in the energy gaps is one of the key and essential criteria for selecting materials in the construction of SS-CSSC. In this study several materials were chosen by thorough consideration of their properties to construct SS-CSSCs. The discussion of these components is primarily limited to the major SS-CSSC technologies based on CuI and NiO as the wide band gap *p*-type semiconductor, Cu_2S as the light absorber and Fe_2O_3 as the electron collection and transporting media from the reduced state of the light absorber material. The conduction and valence band edges and band gaps of materials used in SS-CSSC device structure in the present study are shown in Table 2-3. The redox potentials of the electrolytes used in CSSC are presented in Table 2-4. All values presented in Tables 2-3 and 2-4 are against the vacuum energy scale.

Table 2-3: Conduction and valence band values of the materials used to construct SS-CSSC as reported in the literatures.

Material/	Conduction band eV vs. vacuum	Valence band eV vs. vacuum	Band gap *Eg* vs. vacuum	Reference
CuI	-2.2	-5.3	3.1	[73]
NiO	-1.4	-5.0	3.4	[74]
Cu_2S	-4.44	-5.70	1.26	[75]
Fe_2O_3	-4.78	-6.98	2.3	[76]

Table 2-4: Redox potentials of electrolytes used in CSSC in the present study.

Electrolyte	Redox Potential eV vs. Vacuum	Reference
$Eu^{2}+/Eu^{3+}$	-4.55	[77]
I^-/I_3^-	-4.85	[74]

Therefore, the CSSC and SS-CSSC solar cells constructed in this work has been referred as $CuI/Cu_2S/(Eu^{2+/}Eu^{3+})$, $NiO/Cu_2S/(I^-/I_3^-)$, $CuI/Cu_2S/Fe_2O_3$, $NiO/Cu_2S/Fe_2O_3$, respectively.

2.4.1.1 Hole conducting materials

The porous wide band gap semiconductor photocathode is a key component of both CSSC and SS-CSSC. Due to the rarity of *p*-type semiconductor materials, there is a significant challenge in finding a suitable cathodic semiconductor that fulfils the stringent requirements demanded by such devices. These requirements are listed below [78-80];

- Significant hole conductivity.

- Small size nanocrystalline particles which support built-in electric field.
- Transparent to visible light.
- Chemically stable.
- High porosity and large internal surface area (avoid pin holes).
- Photoelectrochemically active.
- Resistance to photocorrosion.
- Appropriate band energetics (the upper edge of the valence band of *p*-type semiconductors must be located above the ground state level of the absorber, i.e. negative in energy) and
- A suitable method of material deposition while preserving the properties of other components during the construction of the rest of the device (compatibility of the process).

Several semiconductor materials such as NiO, CuI, Cu_2S and Fe_2O_3 satisfy most of these requirements.

2.4.1.2 Light absorbing materials

Similar to the light harvesting molecular dyes in DSCs, the light absorber material plays a central role in CSSC and SS-CSSC. Ideally this material is required to absorb the entire solar spectrum in order to harvest the maximum number of photons from sunlight. The second important aspect of this material is associated with the internal surface area of the wide band gap *p*-type semiconductor. The wide band gap *p*-type semiconductor hosts the light absorbing material in the form of a thin film (layer) on its surface which allows light absorption and charge transfer. Hence, a large internal surface area is desirable for the wide band gap *p*-type semiconductor. The light harvesting efficiency can be increased by having many thin film cross sections of the light absorbing material. Such structures facilitate the increase of the number of light absorber layers that encounter light. This effectively allows reduction of the thickness of each light absorber layer that encounters light. The reduction of light absorber layer thickness may significantly improve the charge separation and suppress the charge recombination as a result of relatively short transport path length that photogenerated charge carriers travel within the light absorber layer before arriving at the

adjacent *n*- and *p*-type semiconductor phases. However, the reduction in the absorber thickness also reduces the number of photons harvested. In order to solve this problem the absorbing material should possesses very high light absorption coefficient (i.e. in the order of 10^5 cm^{-1}).

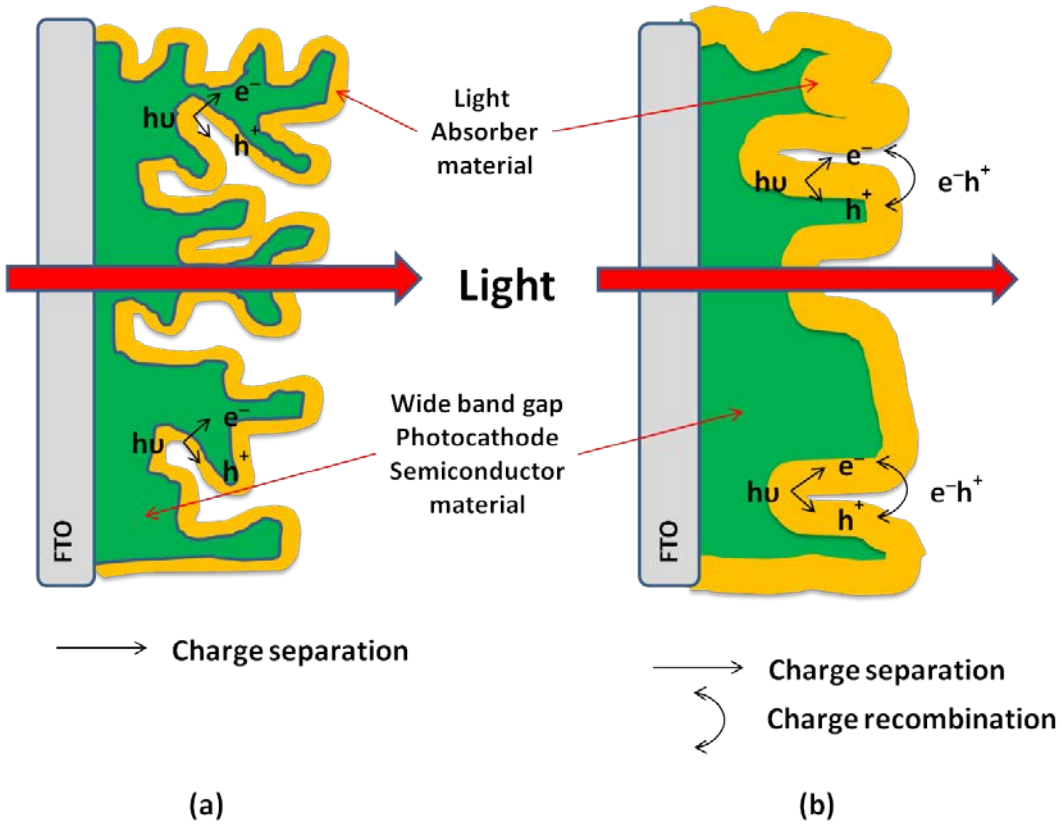

Fig. 2-11: Schematic representation of the surface structure of light absorbing and wide band gap photocathode semiconductor effected by the different thickness of (a) Ideal structure solar cell where the electron/hole pair generation and separation and (b) High thickness of the light absorbing and wide band gap photocathode semiconductor lead to charge recombination.

Light absorber semiconductors can be either *n*-type or *p*-type in nature. In this study, a *p*-type semiconductor absorber material was preferred to construct the CSSC. There only a limited number of *p*-type narrow band gap light absorber semiconductors available which are suitable to be employed for the preparation CSSCs and SS-CSSCs. Cu_2O, Cu_2S, CdTe, $CuInS_2$ and $CuInGaSe_2$ are among them. For this work, Cu_2S has been chosen. The Cu_2S has a

relatively high absorption coefficient (in the order of 10^4 cm^{-1}) and a narrow band gap (about 1.2 eV) therefore it will absorb photons towards the infrared region of the solar spectrum. The deposition method of Cu_2S is also compatible with the other components of CSSC and SS-CSSC.

2.4.1.3 Electron conducting materials

As already discussed previously, this study deals with the construction of CSSCs and SS-CSSCs. If the device is CSSC, an electron acceptor redox media can be employed. Such regenerative redox couple containing electrolyte is typically used to shuttle the electrons to the counter electrode. A prospective redox electrolyte must fulfil the following requirements:

- ❖ Does not absorb photons in the visible region (400-800 nm) to avoid screening the available photons to the absorber layer.
- ❖ Fast electron self-exchange rate with conduction band of absorber and high electron diffusion coefficient to ensure a fast electron transport to the counter electrode.
- ❖ The redox potential must be more positive than the conduction band energy of the absorber to afford the required driving force for the regeneration reaction.
- ❖ The redox potential needs to be more negative than the valence band energy of the hole collector (*p*-type semiconductor) to ensure a good open circuit voltage.

In this study Eu^{2+}/Eu^{3+} and the well-known iodide/tri-iodide have been used as fast redox couples in CSSC configuration.

An electron transporting material used in fabrication of SS-CSSC is required to meet a number of key requirements. They are listed below:

- ➢ The electron transport material must be able to accept electrons at a sufficient rate from the light absorber material, after the light absorber material injected holes into the cathodic wide band gap material.

- It should have sufficient electron mobility (i.e. in the order of several hundred $cm^2(Vs)^{-1}$.
- A deposition method must be available to coat a conformal layer of the electron transport material over the light absorber layer.
- The deposition method of it must be compatible with the light absorber material (i.e. this method should not cause degradation/decay of the light absorber material).
- Light must be able to penetrate the porous structure of the light absorber/wide band gap cathodic semiconductor material heterostructure.
- It should be able to form a good contact with the charge collector material (i.e. Pt, Au, C)

The electron transporting materials can be divided into two main types, namely *n*-type inorganic semiconductor materials (i.e. ZnO, Fe_2O_3 and SnO_2) and electron conducting polymer (i.e. C60, PDI-FCN_2 and PCBM). In the present study, Fe_2O_3 has been used as an electron conducting media for the construction of SS-CSSC.

2.5 Key solar cell parameters

Current density-voltage (*J-V*) analysis is an important technique to study solar cell characteristics. In fact, it is the most common method by which the overall cell efficiency can be determined. In this case, the current generated by a solar cell is measured as a function of applied bias potential in either dark, or under illumination (typically the illumination source provides AM 1.5 spectra, ~1000 Wm^{-2}). In addition to determination of the device efficiency, standard device performance parameters such as the fill factor *(FF),* the open circuit voltage *(V_{oc})* and the short circuit current density *(J_{sc})* may also be determined from *J-V* measurements.

2.5.1 Equivalent circuit

The equivalent circuit diagram for a solar cell is shown in Fig 2-12. The circuit consists of a diode representing the *p-n* junction, as well as series and shunt resistances to account for the resistivity of the layers and any leakage currents, respectively.

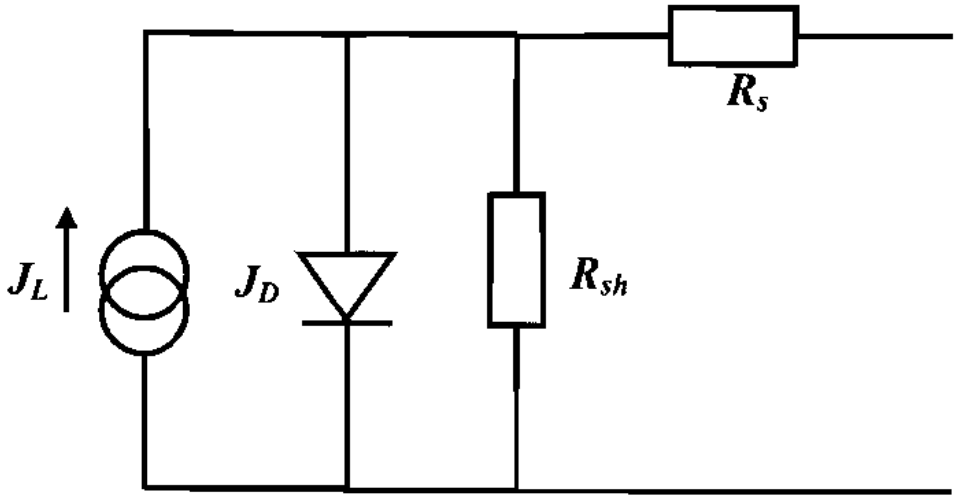

Fig. 2-12: Equivalent circuit for a solar cell, including a current generator with light generated current density J_L, a diode with dark current density J_D, shunt resistance R_{sh} and a series resistance R_s.

However, for an ideal device the resistances are deemed to have no impact on performance and it is thus assumed that $R_s = 0$ and $R_{sh} = \infty$. In the case of an ideal device, and when the device is in the dark, the diode current density (J) may be determined as a function of voltage using the Schockley diode equation [3,21,38]:

$$J = J_o\left(e^{qV/AkT} - 1\right) \qquad (2-5)$$

Where J_o is the reverse saturation current density (a constant related to material properties), q is the charge of an electron, k is Boltzman's constant, T is the temperature and A is the diode ideality factor. When the device is placed under a light source a light generated current density term (J_L) is added to the equation [3,21,38]:

$$J = J_o\left(e^{qV/AkT} - 1\right) - J_L \qquad (2-6)$$

Typical light and dark *J-V* curves for an ideal device are shown in Fig.2-13, these represent direct plots of equations 2-5 and 2-6.

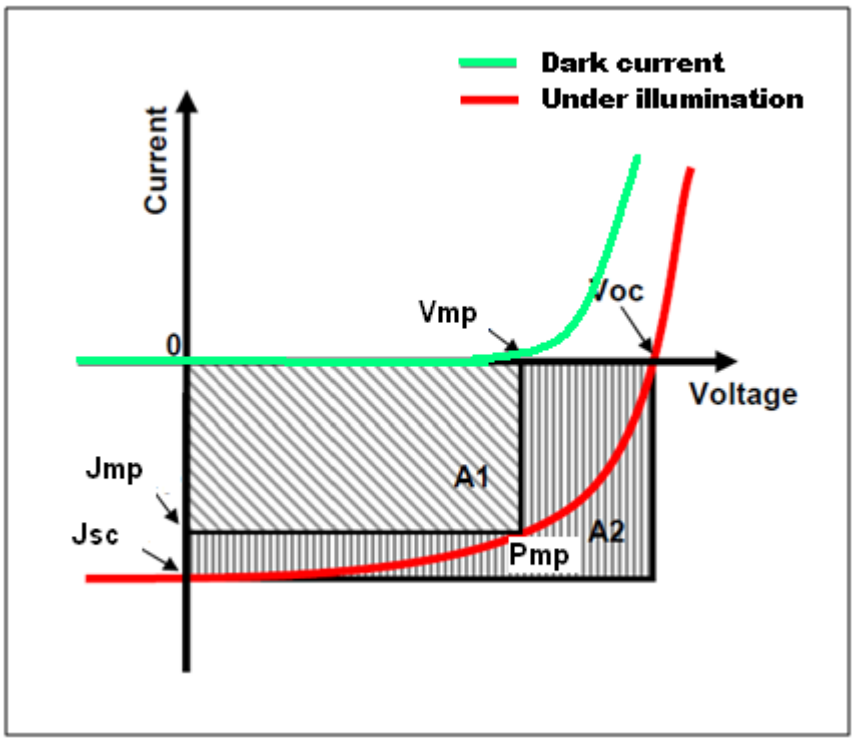

Fig. 2-13: Current density-voltage (*J-V*) curve of a solar cell, displaying the main characteristics of a solar cell. Green line colour showed the dark current and red line colour illustrated the under illumination with AM 1.5 spectrum using solar simulator.

The SS-CSSC solar cells constructed in this study can be treated as a form of thin film solar cells due to its device configuration. The calculation of each of these parameters has been discussed below.

2.5.1.1 Short circuit current density (J_{sc})

The short circuit current density (J_{sc}) is the current generated by the device under no applied bias, seen as the y-intercept in Fig. 2-13. From Eq. 2-6 for an ideal diode, when no bias is applied ($V = 0$) the J_o term become zero and the short circuit current density is equivalent to J_L. An upper limit for the short circuit current density J_{sc} can be computed by considering the normalized AM 1.5 spectrum and assuming that all photons with $h\upsilon >$

E_g(where h is the Planck constant, $v = c/\lambda$ with c the speed of light and λ the wavelength, and E_g is the energy gap of the semiconductor material considered) are absorbed and converted into electron-hole pairs that can, in principle, be collected at short circuit conditions.

2.5.1.2 Open circuit voltage (V_{oc})

The open circuit voltage (V_{oc}) of a device is defined as the applied bias at which no current flows through the device. The V_{oc} can be determined from the x-intercept of the light *J-V* curve as shown in Fig. 2-13. The V_{oc} for an ideal cell may also be determined from Eq. 2-6 by setting the condition $J = 0$, and rearranging Eq. 2-6 [3,21,38].

$$V_{oc} = \frac{AkT}{q} ln\left[\frac{J_L}{J_o} + 1\right] \qquad (2-7)$$

Where J_L is the light generated current density, It can be seen from Eq. 2-7 that V_{oc} is a function of both dark and light generated current density terms, as well as the diode quality factor A.

2.5.1.3 Fill Factor (*FF*)

The Fill factor (*FF*) is defined as a ratio of the size of the maximum power rectangle, to the power rectangle formed by the product of the short circuit current density and open circuit voltage (the ratio between two areas, namely A1 and A2 in Fig.2-13). It describes the quality of the diode behaviour of the solar cell. For an ideal solar cell, these two areas should be similar; this means the fill factor should be nearest to 1 in good solar cells. The fill factor is described by the following equation [3,21,38]:

$$FF = \frac{P_{mp}}{J_{sc}V_{oc}} = \frac{J_{mp}V_{mp}}{J_{sc}V_{oc}} \qquad (2-8)$$

2.5.1.4 Power Conversion Efficiency (η %)

The device efficiency (η) is defined as the ratio of the maximum power generated by the device (P_{out}), to the power of the radiation incident upon it (P_{in}). It can be explained as follows [3,21,38]:

$$\eta = \frac{P_{out}}{P_{in}} = \frac{V_{oc} J_{sc} FF}{P_{in}} \qquad (2-9)$$

The incident light power is usually standardized to AM 1.5 spectrums (e.g. illumination ~1000 Wm^{-2}) by employing a solar simulator as shown in Fig. 2-14.

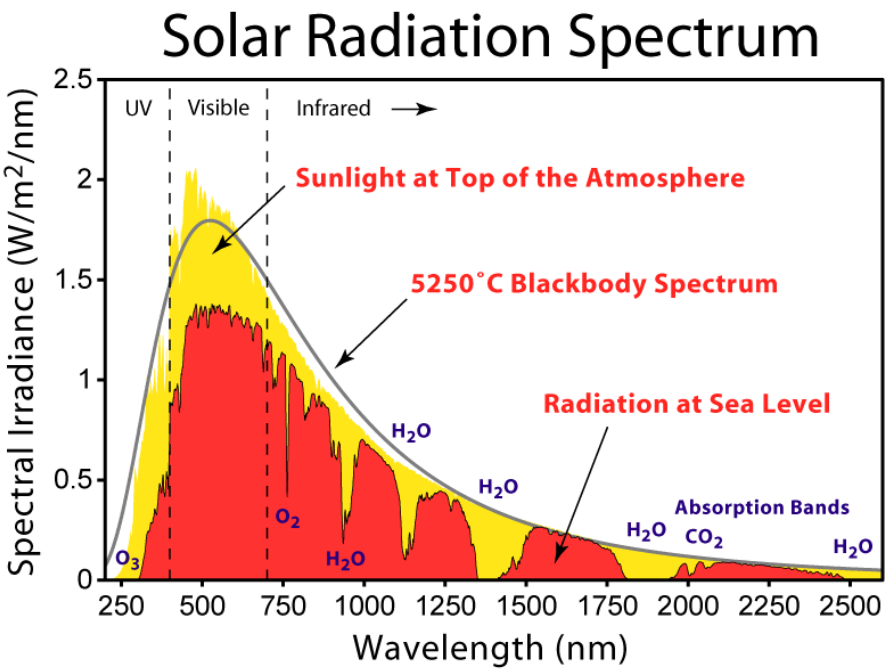

Fig. 2-14: The AM 1.5 solar spectrum which indicated the estimation light can be absorbed in different wavelength of light according to Shockley Queisser limit [81].

Chapter 3: Experimental and Techniques

3.0 Experimental and techniques

This chapter describes the methods used for electrode preparation, characterisation and analysis in this study. Details of the electrode growth techniques are presented in the first part of this chapter. In the second part, the details of cleaning the fluorine-doped tin oxide coated glass substrate are given. It also describes the assembling procedure of the CSSCs and SS-CSSCs. In the final part, the experimental details of component/device characterisation are described. Methods such as XRD and FEGSEM have been used to characterise the materials. The optical and electrical methods used to study the individual components and devices. Photoelectrochemical methods such as current-voltage plots and incident photon-to-electron conversion efficiency have been used to study the light harvesting properties of individual components and devices. In order to proved that the results are reproducible, all the preparation and measurement have been repeated at least 3 times under the similar condition.

3.1 Electrode growth techniques

A number of methods have been used for sample preparation to match the requirements of different characterization methods. In this study, electrodeposition, aerosol assisted chemical vapour deposition and aerosol assisted deposition have been used in order to produce high quality and uniform thin films to prepare CSSCs and SS-CSSCs.

3.1.1 Electrodeposition

Electrodeposition is a very promising and well established method which can be used to deposit thin film semiconductor materials to be used in a range of devices including solar cells. There are a number of key advantages of the electrodeposition technique. It is simple, fast, can be used for the synthesis of multinary precursors for subsequent processing and most importantly it is easy to scale-up for commercial applications. Fig. 3-1 shows a schematic diagram of the electrodeposition system for the deposition of thin films used in this study.

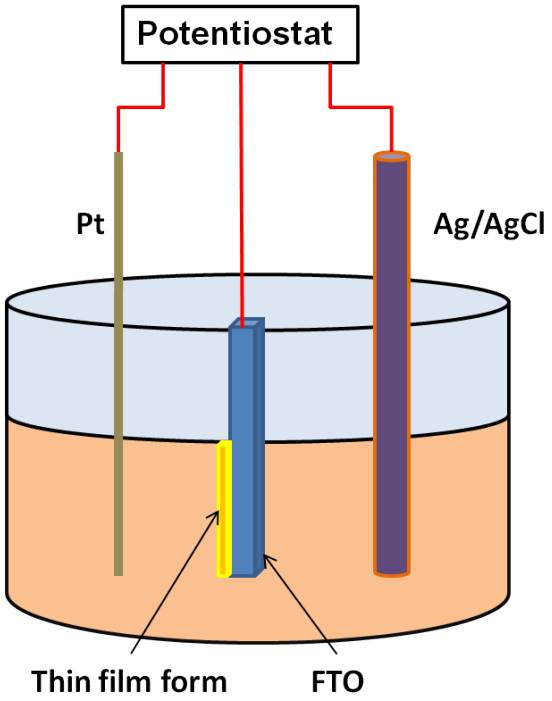

Fig. 3-1: Schematic diagram of the electrodeposition set up used in this study. The sample is connected to the working electrode, and a Pt counter electrode and an appropriate reference electrode (i.e. Ag/AgCl electrode) have been employed.

A typical electrolytic solution (used in the electrodeposition) contains positively charged (cations) and negatively charged (anions). Under the applied external electric field, the cations migrate to the cathode where they are discharged and deposited as a thin film [82]. In practical electrodeposition processes, the chemical reaction around the electrode area occurs in a more complicated way than that shown in Fig. 3-2. Under the influence of an applied potential, rearrangement of ions near the electrode surface results in an electrical double layer called the Helmholtz double layer, followed by the formation of a diffusion layer as shown in Fig 3-2. These two layers are referred to as the Gouy-Chapman layer.

The process can be explained as follows [83]:

- Migration: The hydrated metal ions in the solution migrate towards the cathode under the influence of impressed current as well as by diffusion and convection.

- Electron transfer: At the cathode surface, a hydrated metal ion enters the double layer, where the water molecules of the hydrated ion are aligned. Then the metal ion enters the Helmholtz double layer where it is deprived of its hydrate envelope.
- The dehydrated ion is neutralized and adsorbed onto the cathode surface.
- The adsorbed atom then migrates or diffuses to the nucleation point where the growth starts on the cathode surface.

The thickness of the electrodeposited layer on the substrate is determined by the duration of the electrodeposition.

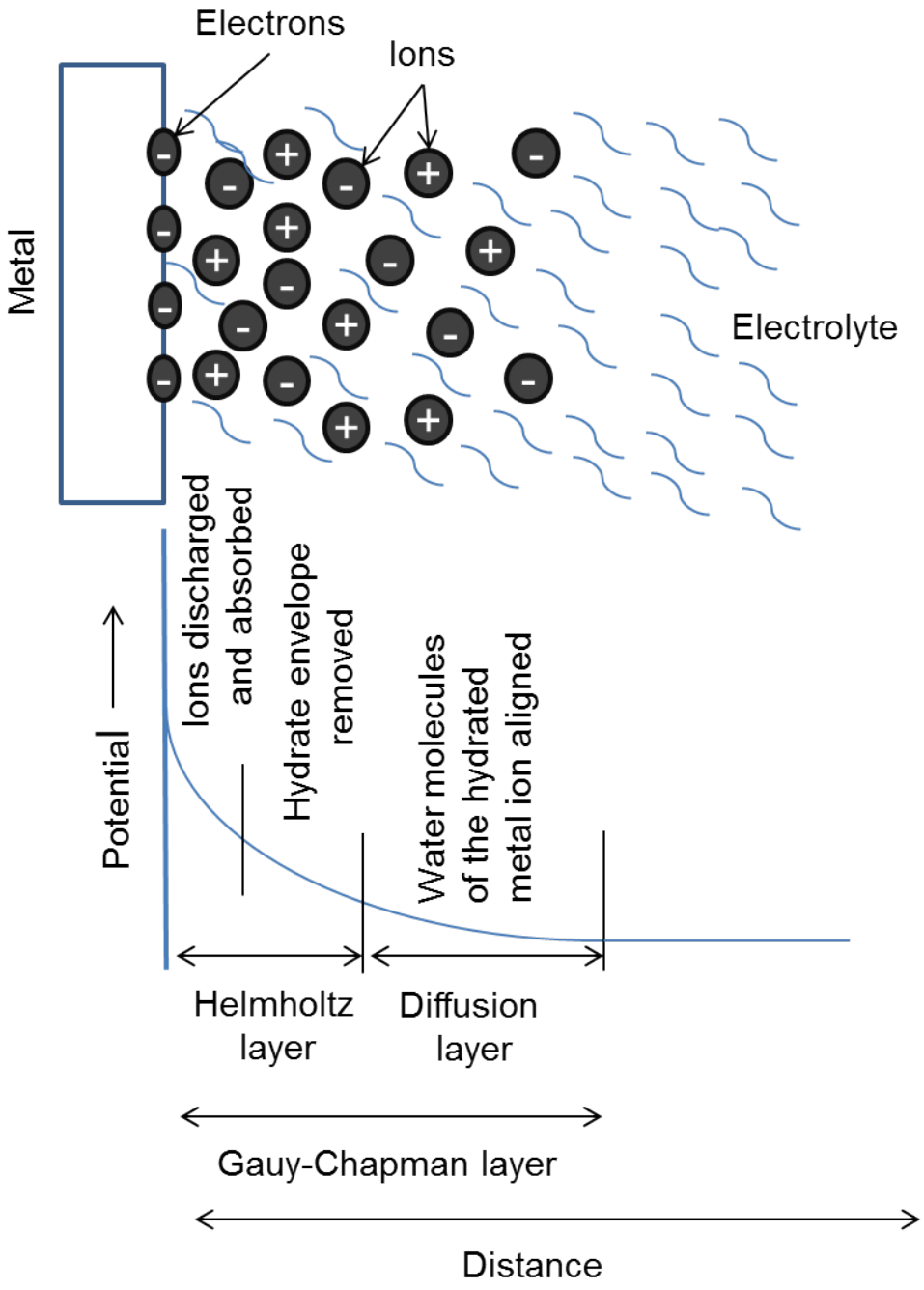

Fig. 3-2: The influence of an applied potential, rearrangement of ions near the electrode surface results in an electrical double layer called the Helmholtz double layer, followed by the formation of a diffusion layer.

3.1.2 Aerosol Assisted Chemical Vapour Deposition (AACVD)

Aerosol delivery of precursors provides a viable alternative route to currently available widely used thin film preparation methods. Aerosol Assisted Chemical Vapour Deposition (AACVD) is an attractive method of depositing metal films for solar cell applications. The film produced can be grown to the desired thickness, uniformity, the particle size can be modify (compact to porous thin film), and it is possible to modify the particle growth direction [84]. The AACVD method involves the atomization of a precursor solution into fine, sub-micrometer-sized aerosol droplets which are delivered to a heated reaction zone undergoing evaporation, decomposition, and homogeneous and/or heterogeneous chemical reactions to form the desired products [85]. A schematic diagram of AACVD is shown in Fig.3-3 and the deposition mechanism is illustrated in Fig 3-4.

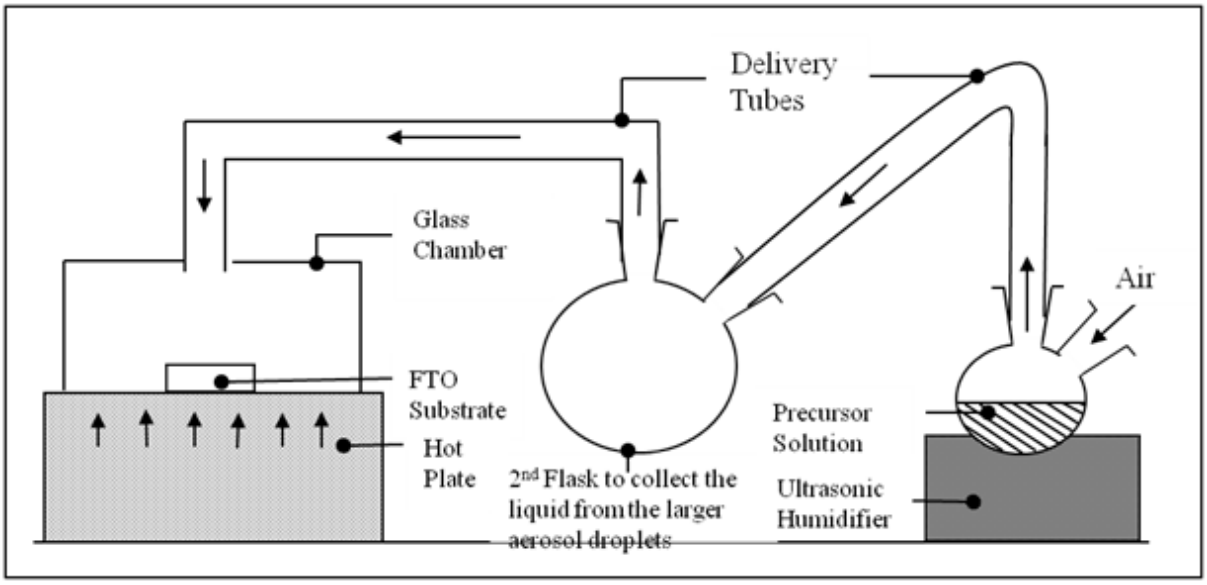

Fig. 3-3: The Aerosol-Assisted Chemical Vapour Deposition (AACVD) set up. The arrow shows the gas carrier flow through the system before entering the heating chamber where the aerosol decomposes to form thin film.

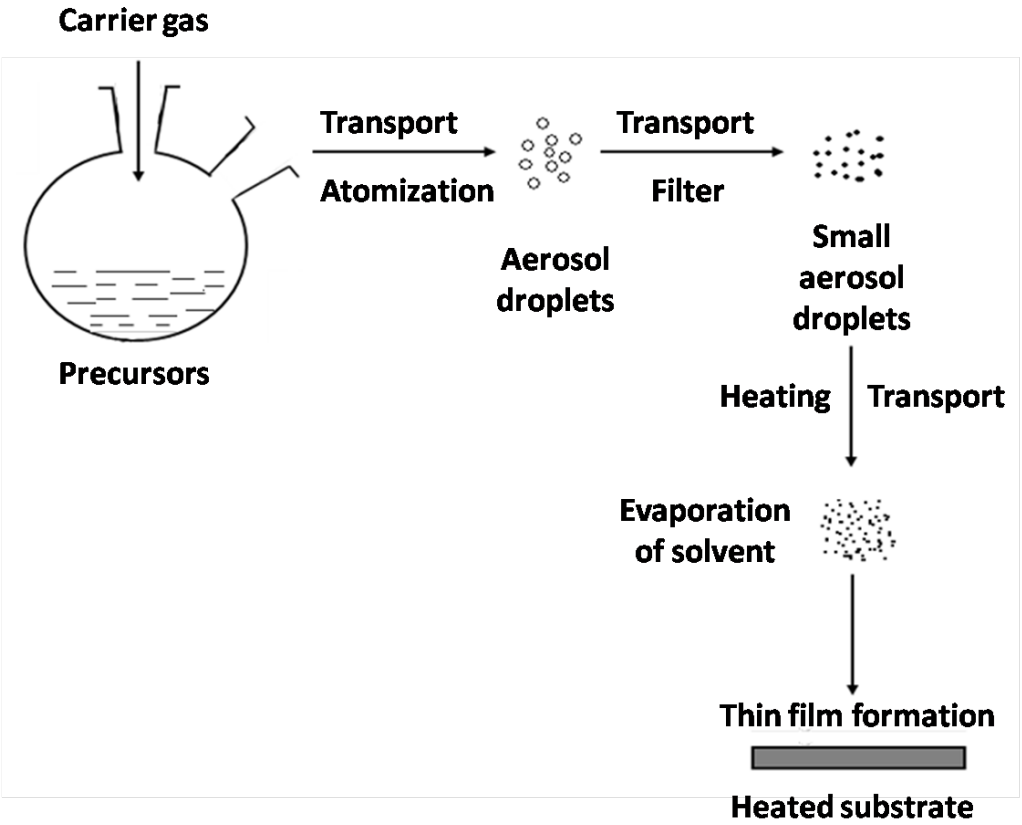

Fig. 3-4: Schematic diagram of the AACVD process for the deposition of films.

In this method the precursor is first dissolved in a solvent which can be easily evaporated and decomposed. The solution is then placed in a round bottom flask and is positioned above an aerosol generator (ultrasonic humidifier). Then, micron sized aerosol droplets containing small particles are generated and transported by a carrier gas into a chamber, where both the solvent and precursor are evaporated and decomposed forming the films. The aerosol droplets generated by the ultrasonic humidifier have a range of sizes. In this instance, for thin film preparation, it is preferable that only small aerosol droplets (in order of several micrometers) are used for the fabrication of thin films so as to obtain highly porous film structures. For this reason, the larger aerosol droplets must be filtered out. In order to filter out the large droplets from the aerosol a trap was used. Such a trap is illustrated by the 2nd flask in Fig 3-3. After passing through the trap, the aerosol reaches the heated substrate surface where thermally induced reactions and film deposition take place. The efficiency of

aerosol delivery and subsequent decomposition enables a high mass transport rate of the precursor to the substrate which can result in a high deposition rate without requiring a high precursor vapour pressure at room temperature or long-term thermal stability of the precursor at elevated temperature. In addition, this system also has the potential to be operated under conditions where the precursor delivery rate and the composition of precursor in solution and droplets do not change with time, which allows reproducible deposition of multi component films, such as complex inorganic semiconductor materials [86].

The most interesting feature in the AACVD is chemical precursors need not necessarily be volatile, but merely soluble in any solvent from which the aerosol can be generated and thermally stable for sensitising the specific materials [87]. Because of that reason, the AACVD method has a high possibility to produce high-quality thin films at a lower cost. The key advantages of AACVD can be described as follows [85,87,88]:

- a wider choice and availability of precursors for high quality chemical vapour deposition (CVD) products at low cost, which is a critical issue for mass production.
- simplification of the delivery and vaporization of precursors via the generation of a precursor aerosol.
- high deposition rate, which may be obtained from a high mass-transport rate of the precursor, and the possible improvement of precursor selection.
- a more flexible reaction environment, since AACVD can be operated under low pressure, atmospheric pressure, or even in an open atmosphere.
- simplification of the synthesis of multicomponent products with precise stoichiometric control.

As a result of the aerosol transport of precursor and the associated CVD deposition mechanism, AACVD can combine the advantages of both conventional CVD and spray-pyrolysis processes. The thickness of the film can be controlled by the deposition time and the rate of aerosol delivery.

3.1.3 Aerosol Assisted Deposition (AAD)

Aerosol Assisted Deposition is almost similar to the AACVD method. AAD also involves the atomization of a liquid precursor solution into fine sub-micrometer-sized aerosol

droplets that are distributed throughout a gaseous medium. The aerosol is subsequently transported into a heated reaction zone, where the solvent undergoes rapid evaporation and/or decomposition, leaving the solid particles on the substrate as a thin film at the increased temperature. The key difference between these two methods is that the precursor made for the AAD technique is obtained by dispersing the desired material as very small particles (i.e. WO_3 and CuI nanoparticles) but for AACVD requires a complex as a precursor which is involved in a chemical reaction in the heated zone. In other words, the difference between the two is that in AACVD, the precursor undergoes a chemical change upon film formation; whereas in AAD, the precursor is already in the desired chemical form, so in this case, the aerosol simply assists in the transportation of the small particles of material containing solvent to the chamber. A schematic diagram of AAD used in this study shows the similarity to the AACVD setup as shown in Fig. 3-3 and Fig. 3-4 but the difference is that AAD is done in a furnace in which the aerosol flows in a horizontal manner rather than using a hot plate with a vertical aerosol flow as shown in Fig. 3-5.

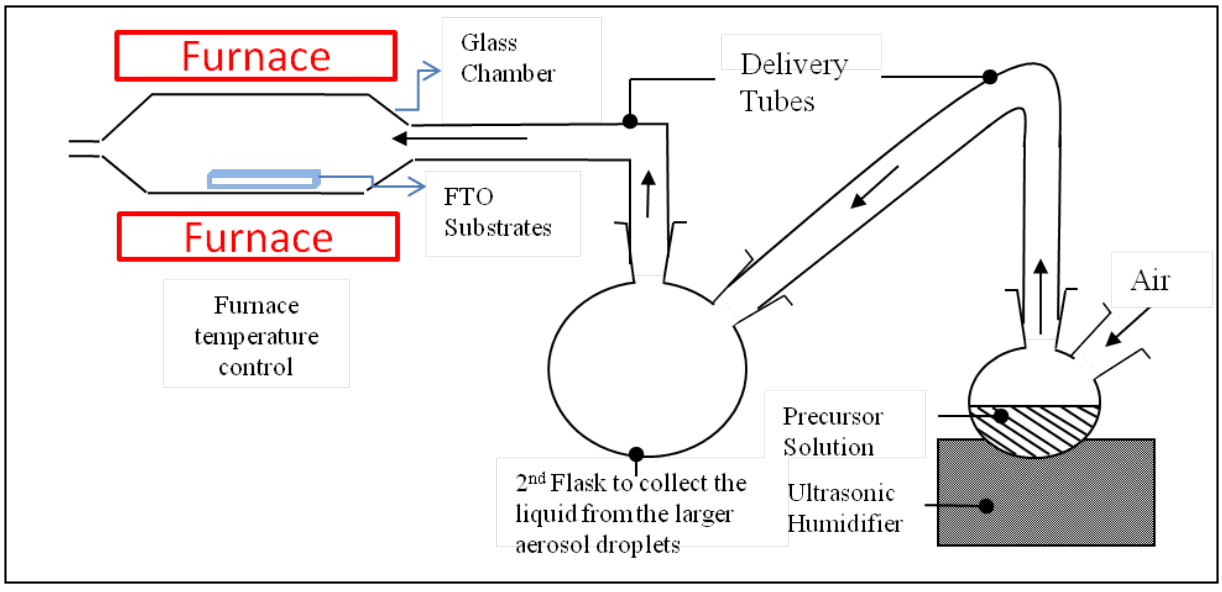

Fig. 3-5: The Aerosol assisted deposition set up.

The temperature can be easily controlled using a tube furnace and this method will also avoid the aerosol falling straight to the substrate. In other words, by using the horizontal deposition method, unnecessary product formation (such as powder or carbon trap) on the

substrate can be avoided, especially when deposition is taking place at relatively low temperatures. Another advantage of AAD is that the precursor can be dissolved or suspended in an appropriate carrier solvent [89]. This shows that the AAD method can avoid unnecessary compound formation on the substrate during deposition and particle aggregation to large clusters.

3.1.4 Preparation of CuI by electrodeposition

A simple electrochemical process has been employed to grow γ-CuI thin films on FTO through a reversible reaction using a copper iodide (CuI) powder in aqueous solution at room temperature. The deposition was performed in a three-electrode cell with FTO as the working electrode, platinum wire as the counter electrode and Ag/AgCl (3 M KCl) as the reference electrode. Prior to electrodeposition, the FTO substrate was cleaned by the same method as discussed in section 3.1.7. The CuI powder (98%) was purchased from Aldrich and potassium iodide (KI, 99%) was purchased from Alfa Aesar.

The CuI complex solution was prepared by dissolving 1.5 g potassium iodide (KI) in 90 ml of acetone and 2 ml of deionised water. A presence of small amount of water into the solution provides increased solubility of KI solution. First, a saturated solution of KI was made up. Then the saturated KI solution was used to dissolve 0.2 g of CuI powder. It is well known that CuI can be dissolved only in a saturated solution of I^- ions. The mixture of the solution will produce a low complex ion CuI_2^-, which will be used for the deposition of CuI on the FTO substrate through electrodeposition. In the present work, γ-CuI was deposited by galvanostatic electrodeposition (~30 $mAcm^{-2}$) by continuous and pulsed electrodeposition for various deposition times as shown in Table 3-1 below.

Table 3-1: Deposition conditions for different samples. Here, the PED stands for pulsed electrodeposition.

Sample Name	Current applied	Deposition cycle (x = 2) (s)
ED	30 mA cm^{-2}	15
PED-1		5x5x5
PED-2		3x6x6
PED-3		1x3x5x6
PED-4		3x3x3x3x3

The electrodeposition was conducted on the FTO substrate provided by Pilkington (dimensions, 1 cm X 2 cm; sheet resistance, 15 Ω/□) and in each case, the deposition area of the electrode was kept constant (1 cm^2). The amount of charge passed during the electrodeposition (in both continuous and pulsed electrodeposition) was maintained at a constant level (0.45 Ccm^{-2}).

When the electrodeposition was conducted in galvanostatic mode the following reduction and oxidation reactions take place in each electrode.

$$Anode: I^- \rightarrow I_2 + 2e^- \qquad (3-1)$$

$$Cathode: [CuI_2]^- + e^- \rightarrow Cu + 2I^- \qquad (3-2)$$

$$Overall: [CuI_2]^- \rightarrow CuI + I_2 + 2e^- \qquad (3-3)$$

As shown in the reaction scheme suggested above, films of CuI and I_2 will form on the substrate during the deposition. As a result, CuI film is formed onto the FTO substrate under the influence of the applied electric filed. The amount of charge passed during the electrodeposition (in both continuous and pulsed electrodepositions) was maintained at a constant level (0.45 Ccm^{-2}) as can be seen in Fig. 3-6. The nucleation of particle growth takes place just after applying the current and is stopped when the current is turned off. The same amount of charge is passed in each case and this was further confirmed by the analysis of the film thickness. After the deposition, each film was washed with distilled water several times to

remove any remaining adsorbed salts. Then, the samples were annealed at 200°C for 2 hrs under N_2 atmosphere to improve the adherence onto the FTO substrate. The iodine is also removed during the annealing process.

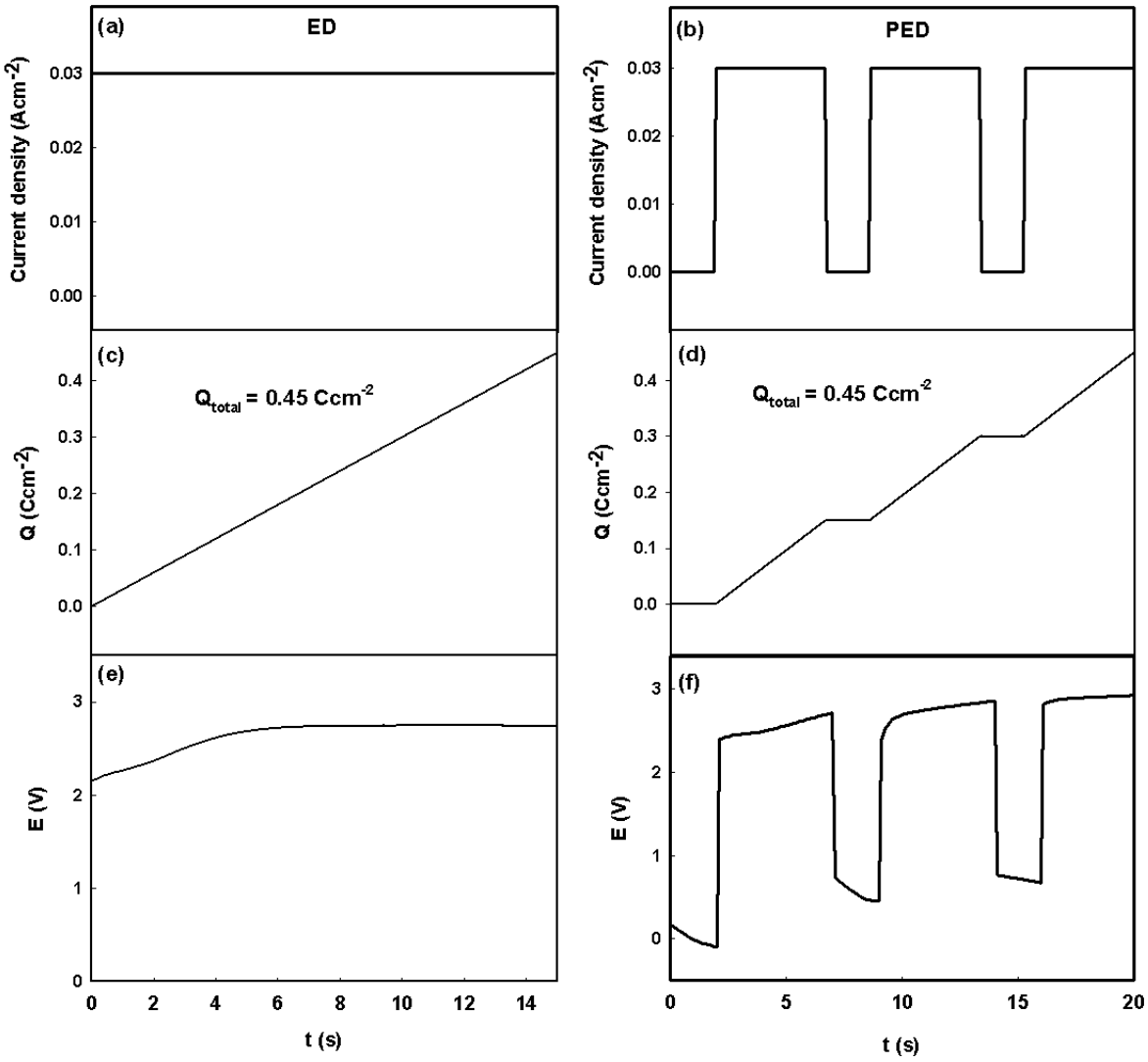

Fig. 3-6: Current, charge, and voltage profiles of continuous and pulsed electrodeposition.

3.1.5 Preparation of CuI by Aerosol Assisted Deposition (AAD)

CuI thin films were also prepared by AAD onto FTO glass substrates. A 0.1 M solution of CuI (powder purchased from Aldrich) prepared in acetonitrile was used as the precursor and the thin films were deposited at 75°C over a period of 10 minutes. All chemicals were used without any further purification. Argon was used as the carrier gas and the flow rate was maintained at 175 ml/min. Then the films were washed by distilled water several times to remove salts accumulated on the films. The AAD of CuI thin films can be described as follows:

$$CuI(solid) + acetonitrile(solvent) \rightarrow CuI(aerosol) \qquad (3-4)$$

$$CuI(aerosol) \xrightarrow{75^{\circ}C} CuI(film) + solvent\ vapors \qquad (3-5)$$

The final product contains only CuI as a thin film and the solvent will evaporate due to the high temperature in the deposition zone.

3.1.6 Preparation of NiO by Aerosol Assisted Chemical Vapour Deposition (AACVD)

NiO electrodes were fabricated from a single source precursor solution. The NiO films were deposited using Nickel (II) acetylacetonate [$Ni(acac)_2$] (95%, Aldrich) as a precursor. A detailed precursor solution procedure can be described; 0.05 M $Ni(acac)_2$ was dissolved in 100 ml toluene for 20 min whilst stirring. The chemical was used without further purification. Heating during the dissolving process helps the $Ni(acac)_2$ to dissolve faster [90], increasing stability and volatility [91] of the precursor solution. Volatility is a prerequisite for conventional CVD methods. Volatility of a compound is a function of intermolecular forces (Van der Waals interactions, hydrogen bonds), which are affected to the lattice structure of the solid [91]. By increasing the solubility, stability and volatility of the precursor better control of structure and crystallization of the thin film results as major benefits [91].

In a typical deposition, 20 ml of 0.05 M solution of $Ni(acac)_2$ was added to a 50 ml round-bottom flask. The aerosols of the precursor solution were formed by keeping the round bottom flask in a water bath above the piezoelectric modulator of an ultrasonic humidifier.

The generated aerosol was transferred to another flask by carrier gas to trap the large aerosol droplets and the aerosol was diluted by introducing more gas. Then the aerosol was transferred into the reactor vertically above the FTO substrate. Decomposition of the precursor occurred in the deposition chamber resulting in nanostructured NiO film formation on the FTO substrate. The deposition can be described as follows:

$$Ni(acac)_2(solid) + Toluene(solvent) \rightarrow [Ni(acac)_2](solution) \quad (3-6)$$

$$[Ni(acac)_2](solution) \rightarrow [Ni(acac)_2](aerosol) \quad (3-7)$$

$$[Ni(acac)_2](aerosol) \xrightarrow{475℃} NiO(film) + volatile\ by-products \quad (3-8)$$

The thickness of NiO electrodes was controlled by varying the deposition times.

3.1.7 Preparation of Cu_2S by Aerosol Assisted Chemical Vapour Deposition (AACVD)

First, the $[Cu(en)_2]Cl_2$ complex was prepared by drop wise addition of 2 ml of ethylenediamine (en) (1.8 g, 0.03 mol) (99%, Alfa Aesar) to a 5 ml ethanolic solution of $CuCl_2$-$2H_2O$ (1.7 g, 0.1 mol) (99%, Acros Organic) while constantly stirring. All chemicals were used as received. A deep blue precipitate was obtained on evaporation in air. The product was filtered, washed with aqueous ethanol, and dried over silica gel. This precursor has been prepared as reported in the literature [92].

A mixture of 10 mM $[Cu(en)_2]Cl_2$ and 30 mM thiourea ($CS(NH_2)_2$, >99%, Fisons) in ethanol (100 ml) was used as the precursor and the films were deposited at 330°C for various deposition times using the AACVD technique. In order to avoid transformation of Cu_2S into CuO, argon was used as the carrier gas and its flow rate was maintained at 175 ml/min. Here, the thiourea was used to supply the sulphur to form Cu_2S film. The thickness was varied by varying the deposition time. The deposition can be described as follow:

$$CuCl_2\,2H_2O(solid) + ethylenediamine\ (en)(liquid) + ethanol(solvent) \rightarrow [Cu(en_2)]Cl_2\ (complex\ solution) \quad (3-9)$$

The reaction suggests that the thiourea is used as the sulphur source during the preparation of Cu_2S films. By mixing thiourea into the $[Cu(en_2)]Cl_2$ complex solution, the precursor has been used for AACVD method. Finally, the aerosol is transported using argon as a carrier gas and is decomposed in the chamber to form a Cu_2S thin film. The undesirable products were removed from the heated zone by carrier gas.

3.1.8 Preparation of Fe_2O_3 by Aerosol Assisted Chemical Vapour Deposition (AACVD)

Iron oxide (Fe_2O_3) thin films were prepared by employing a precursor solution consisting of ethanolic iron chloride. The precursor solution was prepared by dissolving 0.2 M iron (III) chloride hexahydrate powder (> 98%, Aldrich) in ethanol at room temperature. This precursor solution was used as a precursor for aerosol assisted transport to form Fe_2O_3 films on FTO substrate or on light-absorber surface. A thin film of Fe_2O_3 was deposited on the light absorber Cu_2S surface when SS-CSSCs are constructed.

A typical deposition procedure is as follows: The precursor mixture was transferred to the aerosol chamber, a customized silicate glass. A flow of air (rate ~ 175 ml/min) was passed through the apparatus at all time as a carrier gas. The chamber temperature was maintained at 330°C during deposition. Once the temperature was stabilized, an aerosol was generated using an ultrasonic humidifier and air passed through the aerosol mist, directing the aerosol into the chamber. The aerosol entered into the chamber/reactor was decomposed to form a thin film of Fe_2O_3. At the end of the process, the coated films were cooled down to the room temperature.

$$FeCl_3(solid) + ethanol(solvent) \rightarrow FeCl_3(aerosol) \qquad (3-10)$$

$$FeCl_3(aerosol) \xrightarrow{330℃} Fe_2O_3(film) + solvent\ vapors \qquad (3-11)$$

3.2 Materials/electrodes preparation

The general idea behind the development of SS-CSSC is to solve the difficulties caused by construction and operation of CSSCs. CSSC is a liquid based device and possesses numerous challenges in the construction and operation stages. Furthermore, construction of SS-CSSCs is anticipated to reduce the device production cost significantly compared to that of CSSC counterpart. The conventional semiconductor sensitised solar cell based on anodic

sensitisation consists of a nanocrystalline anodic wide band gap semiconductor electrode decorated by a conformal coating of an anodic semiconductor absorber layer and a hole conducting phase which is transparent to visible light. Typically, the first layer fabricated in such devices is the nanocrystalline metal oxide wide band gap anodic semiconductor electrode which is optically transparent to visible light (i.e. TiO_2, ZnO, SnO_2). However, in this study the cell construction follows in the reverse order, such that the first deposited layer was a transparent textured cathodic semiconductor layer. This was followed by the deposition of a cathodic light absorber layer. Construction of the cell was completed by depositing an *n*-type semiconductor material or electron conducting polymer as an electron acceptor.

3.2.1 Materials

3.2.1.1 Substrate cleaning

The substrate used in this study was fluorine-doped tin oxide conductive glass (FTO), supplied by Pilkington Group Ltd. There are two main substrate types, namely TEC 8 and TEC 15, which have sheet resistances of 8 and 15 Ω/□, respectively. The substrates were cut to the desired size (typically 1 x 2 cm^2 in our case) and cleaned according to the following protocol.

- Wash the substrates with distilled water for 15 minutes in ultrasonic bath.
- Rinse with distilled water 10-15 times.
- Wash the substrates with isopropanol for 15 minutes in ultrasonic bath.
- Wash with distilled water 10-15 times.
- Wash the substrates with distilled water for 15 minutes in ultrasonic.
- Wash in ultrasonic bath for 15 minutes in acetone.
- Lastly, clean in ultrasonic bath for 15 minutes in ethanol and stored in ethanol until used.

3.2.1.2 Cuprous iodide (CuI)

Copper (I) iodide (cuprous iodide) is a *p*-type inorganic semiconductor and is a versatile candidate for a wide band gap material. CuI is a water insoluble solid and exists in three stable crystalline phases in different temperature regions, namely α, β and γ [93-96]. The high temperature (above 440°C) α-phase cubic structure is a mix conductor, where the charge carrier is predominantly Cu^{2+} ions [94]. The wurtzite β-phase structure exists at temperatures between 390°C and 440°C is an ionic conductor as reported in the literature [96]. At low temperatures below 390°C, γ-phase CuI is formed as a zinc blende structure of wide band gap (~3.1 eV) *p*-type semiconductor and the conductivity depends on the presence of iodine in stoichiometric excess [97-99]. The iodine atom acts as an electron acceptor that creates holes in the valence band. The different crystalline phases of CuI are illustrated in Fig. 3-7.

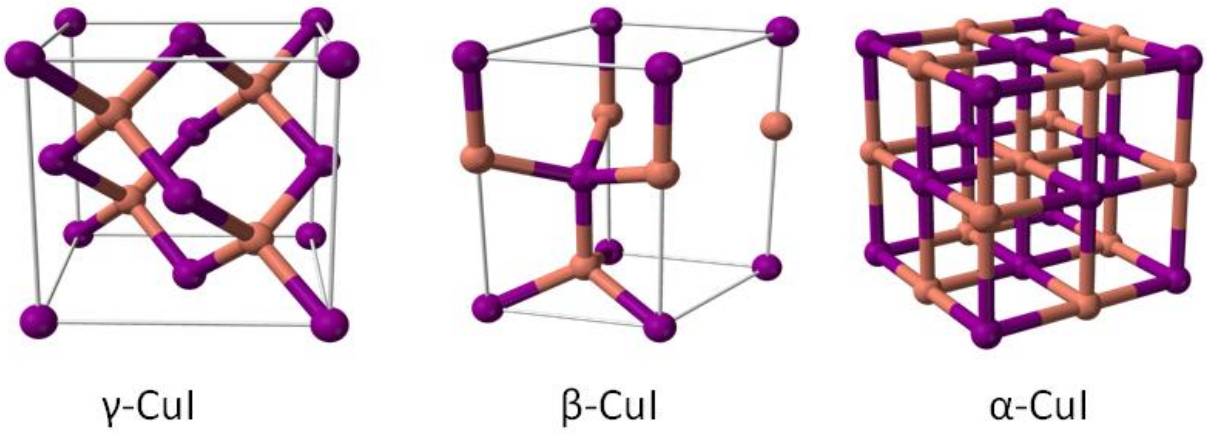

Fig. 3-7: The different crystal structures of CuI at different phases [100].

Recently, γ-phase of CuI prepared at low temperature attracted great attention because it is a fast-ion conductor with low electronic conductivity, and is a wide band gap semiconductor and easy to prepare as a thin film [101]. These properties make γ-phase CuI thin films very useful in dye sensitised solid state solar cells [102-104] as a hole collecting and transporting component [105]. It is also potentially applicable in the fabrication of blue-light emitting devices [106-108], field emission displays and vacuum fluorescent [109]. CuI also be used as a catalyst in organic synthesis [110,111] and also in the formation of both inorganic and biochemical supramolecular compounds [112,113].

Various techniques have been employed for the preparation of CuI thin films such as ionisation [114], radio frequency/direct current (rf-dc) coupled magnetron sputtering [115], pulse laser deposition (PLD) [116], hybrid electrochemical/chemical synthesis [117], electrodeposition [118], chemical bath deposition (CBD)[119], dip-coating [94], successive ionic layer adsorption and reaction (SILAR) [119] and vacuum evaporation [120]. However, some of the film preparation methods mentioned above require high temperature, high vacuum, complex facilities and rigid experimental procedures, which would greatly hinder their universal applications and would increase the cost. These reasons make it necessary to explore alternative techniques to grow more reproducible and better quality films which are simple to use and cost-effective.

3.2.1.3 Nickel oxide (NiO)

Nickel oxide is among the most widely investigated transition metal oxide *p*-type semiconductor. It is a transparent semiconducting, electro-chromic and antiferromagnetic material having a wide range of technological applications on the nanoscale [121,122]. NiO is an interesting candidate material for this class with a wide band gap of 3.6 – 4.0 eV [121,123]. It is well known that bulk NiO has a cubic (NaCl-type) structure (see Fig. 3-8) with low conductivity typically in the order of 10^{-13} - 10^{-11} Ω at room temperature [123-126].

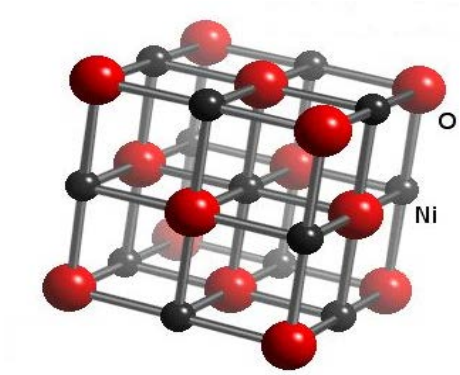

Fig. 3-8: The crystal structure of NiO [127].

However, the conductivity is drastically increased when prepared in the form of thin films or consolidated nanoparticles due to the holes generated by Ni vacancies in the lattice

[128,129]. The electrical conduction is primarily ascribed to the hopping of holes associated with the Ni^{2+} vacancies [124,129]. Although stoichiometric NiO is an insulator, its resistivity can be lowered by an increase of Ni^{3+} ions resulting from addition of monovalent atom or by the introduction of nickel vacancies and/or interstitial oxygen in NiO crystallites [130]. Having excellent durability and electrochemical stability, low material cost, being a promising ion storage material in terms of cyclic stability, having a large span optical density, and the possibility of manufacturing by a variety of techniques make NiO extremely attractive material [121].

These attractive properties of NiO make it suitable to be applied in a range of devices including dye sensitized solar cells [131], chemical sensors [132], electrochromic devices [133], antiferromagnetic layers [134], *p*-type transparent conducting films [135], smart windows [136], electrochemical supercapacitors [137], negative electrode of lithium-ion batteries [138] and catalysts [139].

To date, various methods have been employed to synthesize nanostructured NiO such as thermal decomposition [140], evaporation [141], sputtering [133,142], electrodeposition [143], sol-gel [144], metal organic chemical vapour deposition (MOCVD) [145], chemical vapour deposition (CVD) [146], atomic layer deposition (ALD) [147], pulsed laser deposition (PLD) [148], spray pyrolysis [149], hydrothermal [150], reactive pulsed laser ablation [151], the solution method followed by calcinations [152,153], the tape casting and sintering process [154] and chemical bath deposition (CBD) [155,156].

3.2.1.4 Copper sulphide (Cu_2S)

Copper sulphide can be considered in some ways an ideal absorber material because it combines a number of important characteristics including being non-toxic, low cost, in high abundance (along with silicon) and excellent light absorption properties [157]. There are several stable phases of copper sulphides at room temperature with different stoichiometry (Cu_xS, $1 \leq x \leq 2$) [158]. The stoichiometry depends on the temperature [159], with the extremes being Cu_2S (chalcosite) and CuS (covellite), intermediate phases include $Cu_{1.97}S$ (djurleite), $Cu_{1.8}S$ (digenite), and $Cu_{1.4}S$ (anilite) [159,160]. Among them, Cu_2S is considered

to be an ideal light absorber due to its high absorption coefficient (~ 10^4 cm^{-1}) and narrow enough band gap (1.2 eV) [161-163]. These compounds are *p*-type semiconductors with copper vacancy defects as acceptors [164]. The crystal structure of Cu_2S is illustrated in Fig. 3-9.

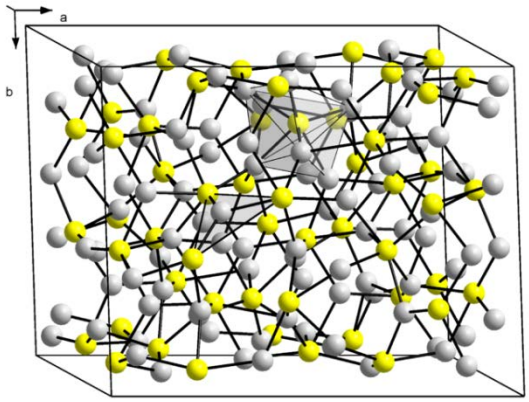

Fig. 3-9: The crystal structure of Cu_2S [165].

Copper sulphide as thin films has been used in a wide range of applications such as photothermal conversion [166], photovoltaic [167,168], solar control coatings [169], lithium batteries [170], gas sensors that functioning at temperatures tending to room temperature [171], polarizers of infrared radiation [172] and active absorbents of radio waves [173].

Many methods have been developed to prepare Cu_2S thin films for various applications such as chemical bath deposition (CBD) [174], solid state reaction [175], chemical vapour deposition (CVD) [176], spray pyrolysis [177], successive ionic layer adsorption and reaction (SILAR) [158], microwave assisted chemical bath deposition [178], the liquid–liquid interface reaction [179], chemical vapour reaction (CVR) [180], electrochemical methods [181], atomic layer deposition (ALD) [182], and spray-ion layer gas reaction (ILGAR) [183].

3.2.1.5 Iron Oxide (Fe_2O_3)

Iron oxide is the fourth most common material in the earth's outer layer as iron is readily oxidized in the air to form the ferrous (Fe^{+2}) and ferric (Fe^{+3}) states [184,185]. At ambient temperature, the common stoichiometric forms of iron oxides are magnetite (Fe_3O_4),

maghemite (γ-Fe_2O_3), and hematite (α-Fe_2O_3); in addition they form hydroxides [93]. Among these, α-Fe_2O_3 or hematite photoanodes have received considerable attention on account of its abundance, stability and environmental compatibility, as well as its suitable band gap (~2.2 eV) [184,186] valence band edge (~ -4.78 eV) and conduction band (~ -6.98 eV) position [187,188]. The structure of hematite is illustrated in Fig. 3-10.

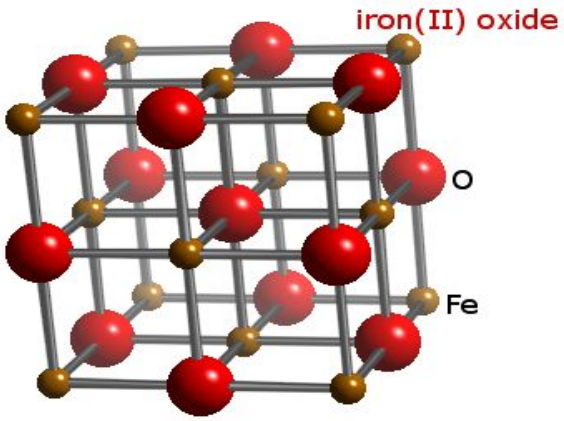

Fig. 3-10: The crystal structure of hematite [189].

Hematite is an interesting material due to its catalytic, magnetic and semiconducting properties, and because it is produced during corrosion [190]. An important feature of hematite which makes it suitable for many optoelectronic devices, including photovoltaic solar cells, are sufficient light absorption, high chemical stability, favourable energetic positions of the band edges with respect to the oxidation potential of water and low cost [191].

It has been intensively investigated for potential applications including gas sensors [192,193], rechargeable lithium ion batteries [193], catalysts [194,195], pigments [194], photoanode for efficient water splitting by sunlight [196], waste-water treatment [197] and biological and medical fields [198].

The preparation of hematite thin films was first reported by Bard and Hardee using the CVD method [199,200]. Then, many studies were done using different techniques such as, sputtering [201] and thermal oxidation [202], ultrasonic spray pyrolysis (USP) and conventional spray pyrolysis (SP) [196,203], atmospheric pressure chemical vapour deposition (APCVD) [204], DC reactive magnetron sputtering [205], sol–gel method [206], potentiostatic anodization [207], sintered disks [208] and single crystals [209,210], aerosol assisted chemical

vapour deposition (AACVD) [211] which results in excellent quality thin films, and is cost effective.

3.2.2 Device preparation

The SS-CSSC configuration containing solar cells have been fabricated using both CuI and NiO wide band gap cathodic semiconductor electrodes. In this study, two different SS-CSSC structures have been investigated namely FTO/CuI/Cu_2S/Fe_2O_3/Pt and FTO/NiO/Cu_2S/Fe_2O_3/Pt.

3.2.2.1 FTO/CuI/Cu_2S/Fe_2O_3/Pt cell

CuI electrode was deposited on clean FTO glass substrates following the method described in Section 3.1.2. During the deposition, the distance between nozzle and the substrate was maintained at about 2 cm inside the glass chamber. The CuI film thickness was recorded to be about 1 µm after 15 minutes deposition time. Then the films were washed using distilled water several times to remove unnecessary salts accumulated on the films. A narrow area of one end of the FTO substrate was kept uncoated (with CuI) in order to provide electrical contact. This was done by masking this specific area of the electrode during the CuI deposition. Then, the absorber Cu_2S was deposited on the textured CuI surface by AACVD method (see the Section 3.1.7 for details). The variation in the thickness of Cu_2S was achieved by varying the deposition time. The effect of Cu_2S thickness on PEC properties was studied. Europium nitrate was used as an electrolyte in the photoelectrochemical characterisation of photosensitised electrodes. This produces high photocurrent due to the fast electron transfer of europium. Finally, in order to complete the fabrication of the solid state cell, a Fe_2O_3 layer was deposited by AACVD method as discussed in Section 3.1.8. The effects of Fe_2O_3 thickness investigated in order to optimize the cell performance. The cells fabricated were stored in air under room temperature and dark conditions. The active area of the cell was 1 cm^2.

3.2.2.2 FTO/NiO/Cu_2S/Fe_2O_3/Pt cell

The SS-CSSC cells based on NiO as hole collector were constructed using similar techniques. The NiO photocathode was deposited by AACVD at 475°C for 40 min as discussed in Section 3.1.2. This was followed by Cu_2S film deposition on the NiO surface. Cu_2S functions as an absorber layer which will absorb photons and generate and separate electron-hole pair. The photoelectrochemical properties of FTO/NiO/Cu_2S electrode in I^-/I_3^- electrolyte was also studied for different Cu_2S thicknesses deposited on the porous NiO layer. The fabrication was then completed by depositing a Fe_2O_3 film on the Cu_2S layer as an electron collector in order to construct SS-CSSC device.

3.3 Characterization

In order to study the structural, surface and optical properties of the prepared electrodes, XRD, FEGSEM and UV-Visible techniques were employed. Finally, the photoelectrochemical properties of electrodes were studied by chopped and steady-state *J-V* measurements and photocurrent spectroscopic measurements (i.e. external quantum efficiency measurements or IPCE measurements).

3.3.1 Structural characterisation

3.3.1.1 XRD measurement

The X-ray diffraction (XRD) technique is a non-destructive analytical technique which can provide information about the crystallographic structure of materials. In these studies, XRD had been used in order to study structural characterization for extracting information on the material such as type of atoms, crystal orientations and average grain size. It involves directing incident X-rays into a material and using a detector that moves around in a circular path around a sample or vice versa, and measuring the direction and intensities of any resulting diffracted waves. Constructive and destructive interference of the diffracted waves

produce “diffraction patterns” which can provide information regarding the crystal structure of a thin film material [212].

In general, materials with long repeat distances exhibit diffraction at small angles and materials with short repeat distances exhibit diffraction at large angles. Also, crystals with precise periodicities over long distances have sharp diffraction peaks whereas those that contain impurities, internal strains or other defects have broadened, shifted or weakened peaks. The XRD peak locations can be used to calculate the interplanar spacing, *d*, by using Bragg’s Law,

$$n\lambda = 2d \sin\theta \qquad (3-12)$$

Where θ is the Bragg angle which is the angle which satisfies Bragg’Law, λ is the wavelength of the incident X-rays and n is order of the spectra.

The average grain size can be calculated using Scherrer’s Equation:

$$t = \frac{0.9\lambda}{B\cos\theta} \qquad (3-13)$$

Where *B* is Full Width of Half Maximum (FWHM) of a particular peak, *t* is the crystallite size, θ is the Bragg angle and λ is the wavelength of the incident X-rays [213].

The structural studies of the semiconductor films were investigated by an X-ray diffractometer (Bruker D8) (Scanning angle between 20º and 60º)**,** and operated with monochromatic high density Cu Kα **(**wavelength, λ = 0.1542 nm) radiation using a PSD detector. The XRD machine is shown in Fig 3-11.

The crystallinity of the samples was obtained from the ratio of the total integrated intensities scattered by the crystalline and the amorphous fractions. Peak positions and intensities for many materials can be found in International Center Diffraction Data (ICDD) reference databases of powder diffraction files (PDF). The data base is available from the Diffraction equipment manufacturers or from ICDD direct.

Fig. 3-11: Picture of the Bruker D8 XRD system.

3.3.1.2 FEGSEM measurements

Field Emission Gun Scanning electron microscope (FEGSEM) was used in this study in order to measure thickness and surface morphology. The mechanism can be explained as the image is created by scanning the focused electron beam in a raster pattern across the area of the sample. Secondary electrons are then collected by a detector, generating a signal which is displayed on a monitor. The most common imaging mode collects low-energy (<50 eV) secondary electrons that are ejected from the specimen atoms by inelastic scattering interactions with beam electrons. Due to their low energy, these electrons originate within a few nanometers from the sample surface [214,215]. The brightness of the signal depends on the number of secondary electrons reaching the detector. If the beam enters the sample perpendicular to the surface, then the activated region is uniform about the axis of the beam

and a certain number of electrons “escape” from within the sample. As the angle of incidence increases, “the escape” distance of one side of the beam will decrease, and more secondary electrons will be emitted. Thus steep surfaces and edges tend to be brighter than flat surfaces, which results in images with a well-defined, three-dimensional appearance. A general introduction to FEGSEM principles can be found in references [214,215].

FEGSEM was used to determine the surface nanostructure and the thickness of the films using Leo 1530 VP (Carl Zeiss NTS Ltd., Cambridge, UK) field emission gun SEM (FEGSEM) at an accelerating voltage of 5 kV, and a working distance of 6 mm. For the sample preparation, the thin films were cut in two pieces, of which the first part was used to study the thickness and the second part for surface morphology. Then the films were attached to the sample holder by using silver paint concentrate solution between the conducting FTO layer and the holder. Finally, the thin films were coated by gold prior to using a Polaron Emitech SC7640 sputter coater (Quorum Technologies Ltd, West Sussex, UK) and ready to be measured in FEGSEM measurement. The picture of the FEGSEM is shown in Fig. 3-12.

Fig. 3-12: Picture of the FEGSEM.

3.3.2 Optical characterisation

Ultraviolet-visible (UV-Vis) spectrophotometer is a device used to study the interaction between radiation and matter in regards to the wavelength of photons. The interaction can be explained in the following equation;

$$E = \frac{1240}{\lambda} \qquad (3-14)$$

Where E is photon energy (eV), and λ is wavelength (nm). Specifically, it measures visible light and the close-to-visible range of ultraviolet and infrared spectrum ranges. This allows identification of the optical spectroscopy of solids specifically the optical density, absorption, transmittance and reflectance and from this information (by plotting graph) the band gap of the material can be calculated. Basically, UV-Vis spectrophotometer functions with the following elements [216]:

(i) A light source (usually a deuterium lamp for the UV spectral range and a tungsten lamp for the Vis and IR spectral ranges) that is focused on the entrance to a monochromator.

(ii) A monochromator, which is used to select a single frequency (wavelength) from all of those provided by the lamp source and to scan over a desired frequency range.

(iii) A sample holder.

(iv) A light detector (usually a photomultiplier for the UV–Vis range) to measure the intensity of each monochromatic beam after traversing the sample.

(v) A computer, to display and record the absorption spectrum.

The spectral shape of the light after passing through each element has also been sketched in Fig.3-13.

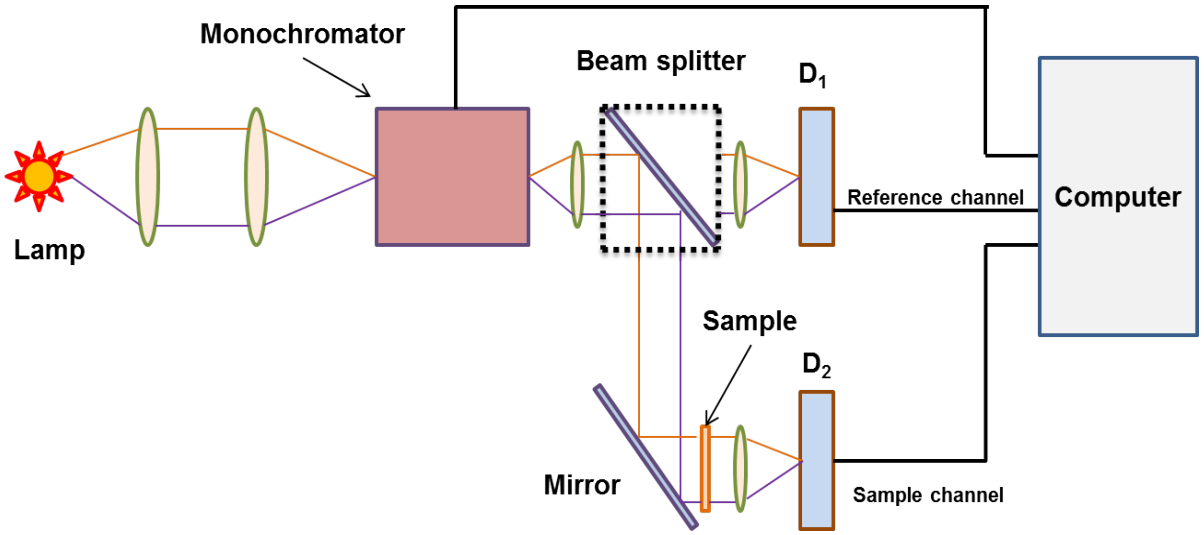

Fig. 3-6: Schematic diagram of a double beam spectrophotometer.

As illustrated in Fig. 3-13, the beam intensity attenuation *dl* travelling through different thickness *dx* can be written as

$$dl = -\alpha l\, dx \qquad (3-15)$$

Where *l* is the light intensity at a distance *x* into the material and α is the absorption coefficient of the material. By integration of equation 3-15, the law known as the Beer-lambert law is obtained which is related to the incoming light intensity and the thickness of the film [216].

$$I = I_o e^{-\alpha x} \qquad (3-16)$$

Where I_o is defined as incident intensity minus the reflection losses at the surface. All three parameters, optical density (OD), absorbance (A) and Transmittance (T) work in different modes for optical spectrophotometers measurement. These parameters are calculated using the following equation, providing that the thickness of the sample is known:

$$OD = log\frac{I_o}{I} \qquad (3-17)$$

$$\alpha = \frac{(OD)}{x \log e} = \frac{2.303\ (OD)}{x} \qquad (3-18)$$

The other two modes have been directly measured by the instrument and can be related using a well-known equation and according to Equation 3-16 the transmittance is determined by

$$T = \frac{I}{I_0} \qquad (3-19)$$

And the absorbance determined by

$$A = 1 - \frac{I}{I_0} \qquad (3-20)$$

That means using Equations 3-19 and 3-20, by measuring the absorbance, the transmittance spectra can be determined or vice versa [216]. However, the equations above are for low optical densities, the optical density spectra are more sensitive hence the absorbance will be very close to the optical density (A ≈ 1 − (1 − OD) = OD) so that the absorbance spectrum displays the same shape as the optical density. At higher optical densities, the absorbance spectrum gives different shapes compared to the actual absorption.

Another optical absorption parameter, which is of relevance when working with optical thin films, is the reflectance. The reflectance provides similar information to the absorption and transmittance via measurement in a different mode. For example an absorption coefficient of a high value such as $10^5 – 10^6$ cm^{-1} can only be measured by using a very thin film sample. According to these, the reflectivity spectra are advantageous due to the singularities in measurement caused by the absorption process. The reflectivity at each frequency is defined by

$$R = \frac{I_R}{I_o} \qquad (3-21)$$

Where I_R is reflected intensity. The reflectance can divided to two different modes such as direct reflectivity and diffuse reflectivity. Direct reflectivity measurements are for well-polished samples at normal incidence but the diffuse reflectivity is generally used for unpolished or powder samples. Fig. 3-14 shows the schematic of diffuse or direct reflectivity [216].

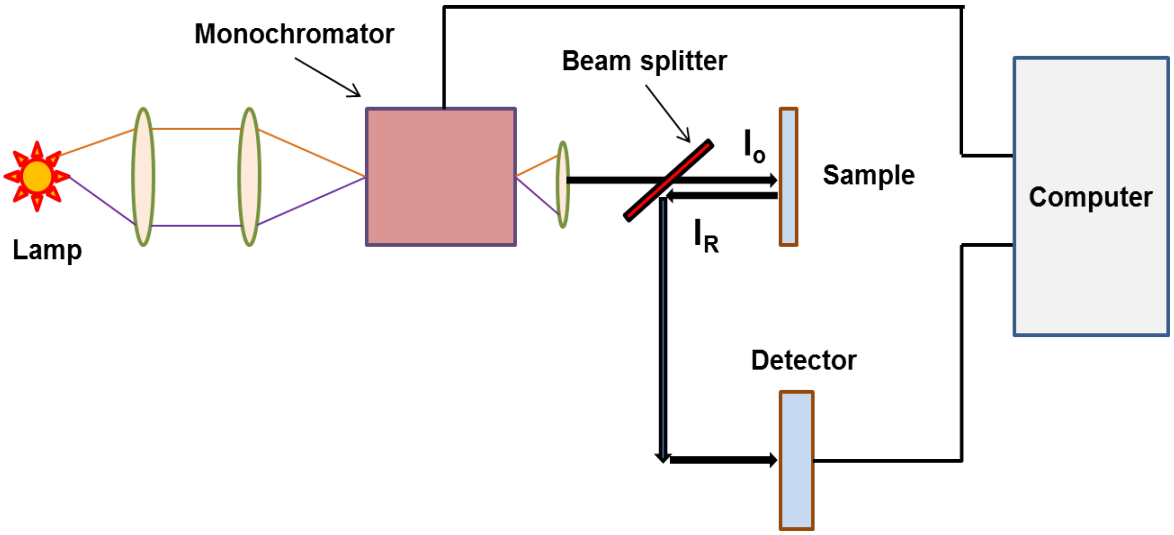

Fig. 3-7: Schematic diagram of reflectance mechanism.

For direct reflectivity measurement, monochromatic light (produced by a lamp and monochromator) is passed through a semitransparent lamina. This lamina deviates the light reflected in the sample towards a detector. For diffuse reflectivity measurements, an integrating sphere (a sphere with a fully reflective inner surface) is used as shown in Fig. 3-15.

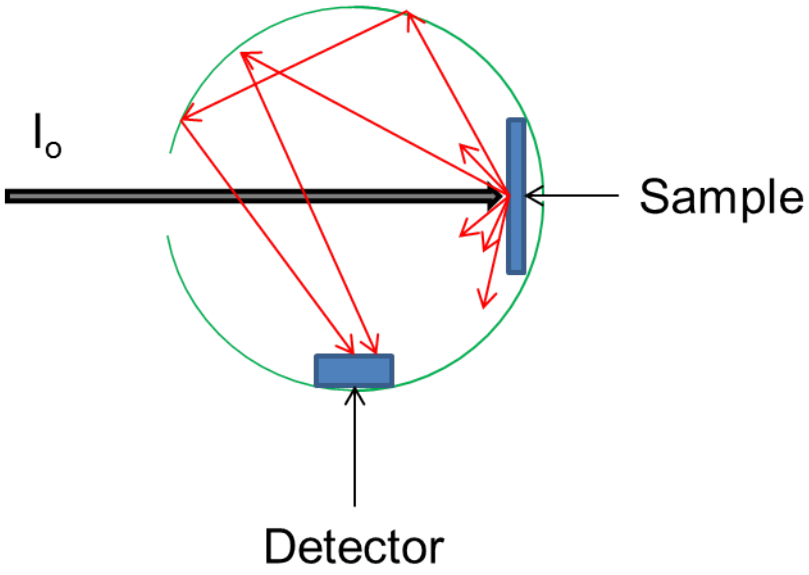

Fig. 3-8: Schematic diagram of an integrating sphere for measuring diffuse reflectivity.

Such a sphere has a pinhole through which the light enters and is transmitted toward the sample. The diffuse reflected light reaches the detector after suffering multiple reflections in the inner surface of the sphere. The integrating spheres can be incorporated as additional instrumentation into conventional spectrophotometers.

In these studies, the absorbance, transmittance and diffuse reflectance of films were measured by using a Lambda 35 Perkin-Elmer UV-Vis spectrophotometer. A bare FTO substrate was used as the reference for absorbance and transmittance and an optical white filter was used as the reference. The completed CSSCs were also studied for optical properties. The scan range was typically 300 – 1100 nm. The instrument is shown in Fig 3-16.

Fig. 3-9: Picture of UV-Visible spectroscopy.

3.3.3 Electrical characterisation

3.3.3.1 Capacitance measurements

Accurate determination of the band edges, flat band potential, donor/acceptor density and type of material are extremely important to understand the solar cell performances. The capacitance measurements are suitable for this because they can be performed under the affected by defects. Other methods such as photocurrent onset and photopotential measurements are less accurate and require higher light intensities [217]. The location of the energies corresponding to the edges of the valence and the conduction bands, of the semiconductor electrode with respect to electrolyte energy level is useful in the selection of suitable electrolyte for optimizing solar cell performance. These are usually found by determination of flat band potential, by measuring the semiconductor electrode capacitance as a function of applied potential. The band-edge positions are derived from capacitance measurements and flat band potentials can be determined by the following Mott-Schottky relations [218];

$$n-type, \frac{1}{{C_{sc}}^2} = \frac{2}{\varepsilon\varepsilon_o e N_d}\left(E - E_{fb} - \frac{kT}{e}\right) \qquad (3-22)$$

$$p-type, \frac{1}{{C_{sc}}^2} = \frac{2}{\varepsilon\varepsilon_o e N_A}\left(E - E_{fb} - \frac{kT}{e}\right) \qquad (3-23)$$

Where the C_{sc} is the capacitance of the space charge region, ε is dielectric constant, ε_o is permittivity of free space, e is the charge, N_d is the donor density, N_A is the acceptor density, E_{fb} called flat band potential, E is potential, k is Boltzmann's constant and T is temperature. By constructing a Mott-Schottky plot from the measurement, the flat band potential and donor/acceptor can be determined from the slope of the graph. Then the energy band edge, E_{vbe} can be determined by [218];

$$E_{vbe} = E_{fb} - kTln\left[\frac{N_d}{N_v}\right] \qquad (3-24)$$

Where E_{vbe} and E_{cbe} are the energies of the valence and conduction band edges, and Nv is the effective density of states in the valence band. From these values, the band gap and band positions can be located. Finally, the conduction band edge E_{cbe} can be calculated from [218];

$$E_{cbe} = E_{vbe} - E_g \qquad (3-25)$$

Where E_{vbe} is the valence band edge and E_g is the band gap of the material. The type of the material (*p* or *n*-type) also can be observed from the slope of the Mott-Schottky plot. The positive slope and the flat band potential towards a more positive value on the graph mean that the material exhibits *p*-type behaviour where holes are the dominant charge carrier. For the negative slope, the value of the flat band potential towards a more negative value mean the material show *n*-type behaviour and the majority charge carrier are electrons.

Capacitance studies were conducted by performing scan rate measurements using microAutoLab type III and computer controlled GPES software. For this, a three-electrode potentiostatic set-up was used, the potential ranges depend on the material being measured. The reference electrode used was Ag/AgCl/3 M KCl, platinum were the counter electrode, and the aqueous solution was the electrolyte in an electrochemical cell with a quartz window. All potentials were expressed against the Ag/AgCl/3 M KCl reference electrode potential.

3.3.4 Performances

3.3.4.1 Current density–voltage *(J–V)*

Current–voltage *(J–V)* measurements of the cells were carried out using a potentiostat (microAutoLab, type III, Windsor Scientific, Berkshire, UK) while the cells were illuminated using an AM 1.5 Class A solar simulator provided by (Solar Light 16S – 300 solar simulator, Solar Light Company Inc., PA, USA), at 1000 $mWcm^{-2}$ light intensity, calibrated by a solar pyranometer PMA2144 Solar Light pyronometre (Solar Light Company Inc., PA, USA) traceable to NPL standard.

J-V performance of semiconductor cathodic solar cells was measured using two-electrode and three-electrode configurations. In two-electrode mode, I^-/I_3^- was used as an electrolyte and sandwiched between the photocathode and Pt counter electrodes. Then the PEC cell was placed perpendicular to the solar simulator source. For the three-electrode configuration the electrode cell was placed in 0.2 M $Eu(NO_3)_3$ electrolyte solution in an electrochemical cell with quartz window where the Ag/AgCl/KCl(3 M) was used as the reference electrode, and a platinum wire as a counter electrode. In the electrochemical cell,

light enters through a quartz window and travels about a 5 mm path length in the electrolyte before illuminating the PEC cell. The PEC cell was illuminated through the electrolyte side and illumination area was measured depend to the cell area. In both mode of configurations steady-state and chopped *J-V* were measured. For the chopped measurements, the light was manually chopped at regular intervals to record dark and photocurrent simultaneously. The potential ranges selected depended on the open circuit voltage of the cell. The cell was studied under dark and illuminated conditions. In order to measure the photocurrent response the illuminated light was chopped every 0.02 V and the scan speed was 0.05 mV/s.

3.3.4.2 Incident Photon-to-Electron Conversion Efficiency (IPCE)

The incident photon-to-electron conversion efficiency (IPCE) at different wavelengths is defined as the number of photo-generated electrons in the external circuit divided by the number of incident photons at a certain wavelength or simply comparing the number of incident photons to the number of electrons produced [219,220].

$$IPCE(\lambda) = \frac{n_{electron}(\lambda)}{n_{photon}(\lambda)} = \frac{qN_{electron}/s}{qN_{photon}/s} = \frac{I(\lambda)}{qN_{photon}/s} \qquad (3-26)$$

The incident power

$$P_{in}(\lambda)(Watt) = P_{in}(\lambda)\left(\frac{Joule}{s}\right) = \frac{N_{photon}}{s}hv = \frac{N_{photon}}{s}\frac{hC_o}{\lambda} \qquad (3-27)$$

With equations 3-28 and 3-29 can be written as

$$IPCE(\lambda) = \frac{I(\lambda)}{\frac{q.P_{in}(\lambda).(\lambda)}{hC_o}} = \frac{I(\lambda)}{P_{in}(\lambda)}\frac{hC_o}{q}\frac{1}{\lambda} \approx \frac{I(\lambda)}{P_{in}(\lambda)} \times \frac{1240}{\lambda(nm)} \qquad (3-28)$$

Where I (λ) correspond to measured current in μA/cm^2, P_{in} (λ) is the output optical power in W/m^2, and λ the wavelength of the incident irradiation in nm. In general, the IPCE is measured under short-circuit conditions and is graphically displayed versus the corresponding wavelength. The IPCE corresponds to the photoresponse or external quantum efficiency.

The experiment setup is shown in Fig. 3-17. IPCE measurements were conducted using a 75 W Xenon lamp connected to a monochromator (TMc300, Bentham Instruments Ltd., Berkshire, UK) and the system was calibrated using a silicon photodiode (Bentham). Photocurrent spectra were measured at a constant potential vs. Ag/AgCl using a combination

of a lock-in amplifier (Bentham 485, Bentham Instruments Ltd., Berkshire, UK) and an in-house built potentiostat. The IPCE spectra of CSSC were recorded at zero bias and were illuminated through the electrode over the 300–1100 nm range, using a chopping frequency of 21 Hz. The cells were measured using two and three electrode as explained in section 3.2.5.

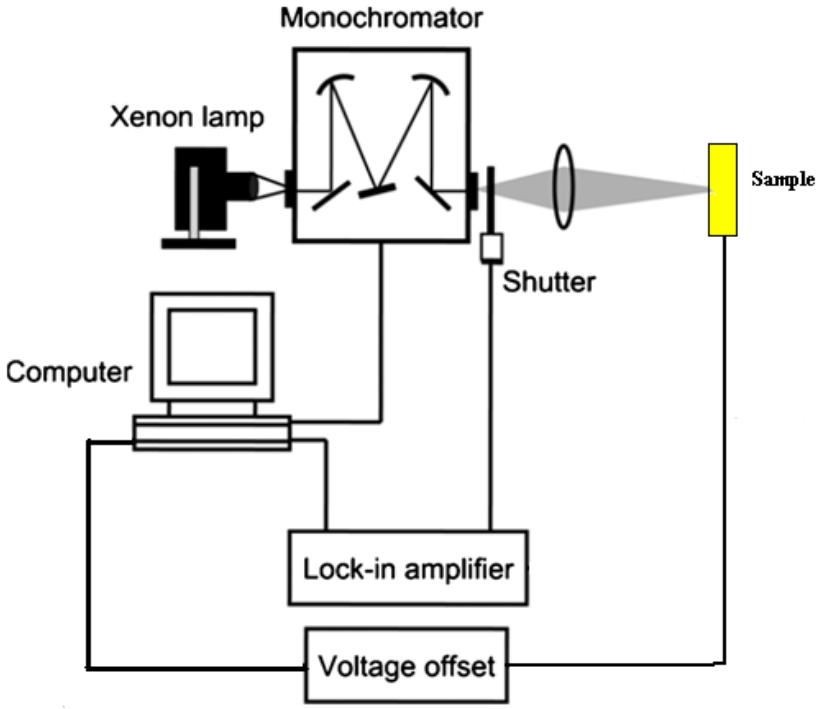

Fig. 3-10: Schematic diagram for IPCE measurement.

Chapter 4: Experimental Results on *p*-CuI and *p*-NiO Photocathodes

4.0 Introduction

In this chapter, the properties and photoelectrochemical performances of two wide band gap *p*-type semiconductor materials used for solar cell construction are presented. The materials are *p*-CuI and *p*-NiO. The studies are focused on their structural, optical, electrical and PEC properties of the electrodes. As discussed in the previous chapter, the CuI electrodes were prepared by electrodeposition and AAD technique whilst the NiO electrodes were prepared by AACVD.

4.1 Electrodeposited CuI electrodes

The CuI films were prepared at room temperature by galvanostatic electrodeposition, using continuous and pulsed methods. The influence of pulsed electrodeposition was compared against the continuous electrodeposition and discussed in this section. As mentioned in chapter 3, the so called continuous electrodeposition was conducted over a period of 15 s and called ED for the simplicity. Pulsed electrodeposition was conducted in four different ways. In the first pulsed electrodeposition, three pulses (each lasting for 5 seconds) were applied and named as PED-1. In the second pulsed electrodeposition, again three pulses were applied in a sequence of 3 s, 6 s and 6 s and it was called PED-2. In the third pulsed electrodeposition, different sequences of four pulses were applied (in the order of 1 s, 3 s, 5 s and 6 s) and it was called PED-3. Finally, in the fourth pulsed electrodeposition, five pulses were applied (each lasting for 3 s) and it was called PED-4. The total deposition time was kept at 15 s in all electrodeposition methods (ED, PED-1, PED-2, PED-3 and PED-4). The properties of the deposited films were characterized by XRD, SEM, capacitance (i.e. Mott-Schottky plots), UV-Vis spectroscopy, *J-V* measurement under AM 1.5 illumination and by photocurrent spectroscopy (i.e. IPCE measurement).

4.1.1 X-ray Diffraction (XRD) analysis

The phase and crystal structure of CuI was determined by conducting XRD studies. The XRD patterns ($20° \leq 2\theta \leq 60°$) of ED and PED (PED-1, PED-2, PED-3 and PED-4) CuI electrodes are given in Fig. 4-1. The peaks corresponding to the conducting FTO substrate are indexed by an asterisk. Apart from the predominant (111) peak at 2θ of 25.6°, no other identifiable CuI peaks are present in the spectra corresponding to both ED and PED CuI electrodes.

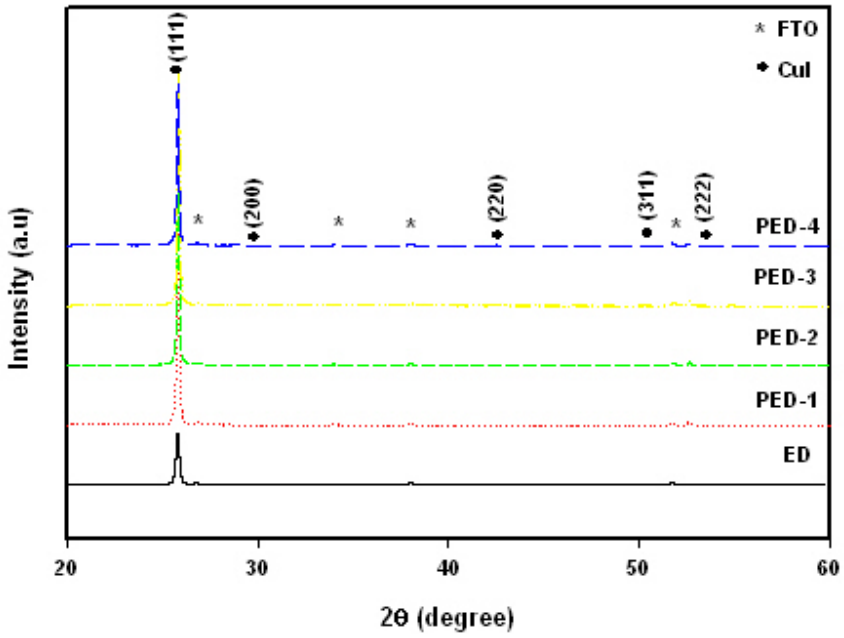

Fig. 4-1: X-ray diffraction patterns of CuI electrodes prepared by using continuous electrodeposition (ED) and pulsed electrodeposition (PED-1, PED-2, PED-3 and PED-4) methods.

The dominant crystallographic reflection (111) and also very low reflection of (200), (220), (311) and (222) which have been attributed to the face-centered cubic (fcc) with γ-phase. According to the growth selection theory, two different growth modes can be considered [221]. The growth is outward if the electrical field lines and the direction of the highest growth rate are the same. However, if the growth perpendicular to the substrate is inhibited, it takes place parallel to the surface and this situation is commonly known as the

lateral growth mode. Previous studies show that materials with a cubic crystal structure, such as ZnSe and CuI, can be electrodeposited particularly on FTO substrates with a strong preferential orientation on (111) direction [222,223]. The CuI films electrodeposited on FTO in the present work have also shown dominant preferential orientation in (111) direction and agrees with observations made by others previously [222]. This could be explained on the basis of lattice match between the CuI (111) plane and the (110) plane of the FTO substrate [224].

The CuI crystallite size was estimated for ED and PED electrodes by using the Scherrer equation (by taking the (111) peak into account in each XRD pattern). They were found to be around 40, 59, 64, 67 and 63 nm for ED and PED-1, PED-2, PED-3 and PED-4 electrodes respectively. It could be suggested that pulsed electrodeposition resulted in increased crystallite sizes. Among the pulsed electrodepositions, PED-1 showed the highest XRD peak intensity as shown in the Fig 4-2.

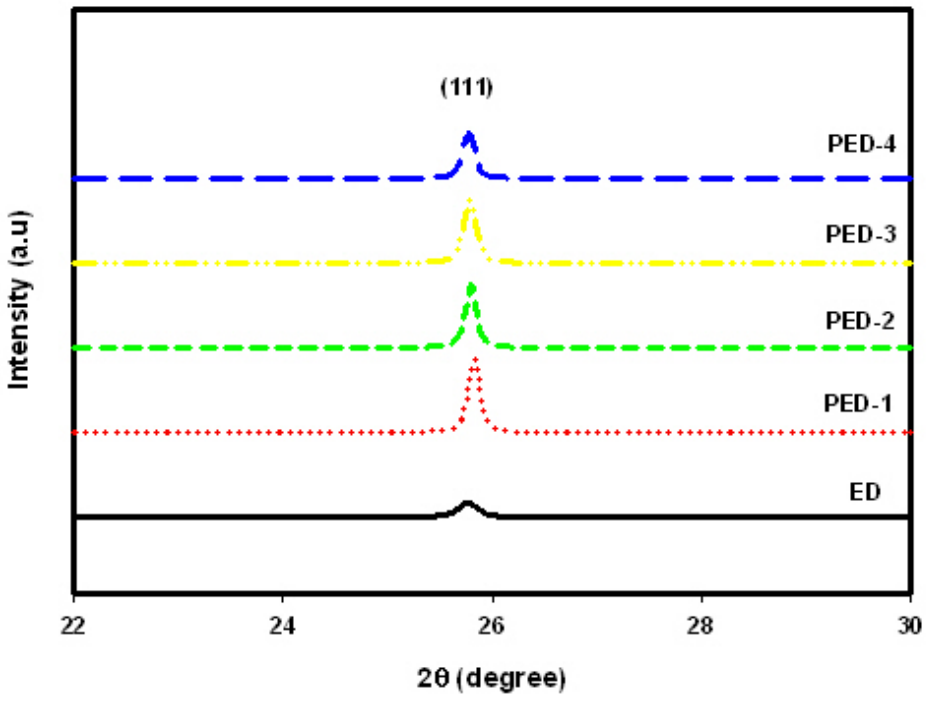

Fig. 4-2: X-ray diffraction patterns of CuI electrodes prepared by using continuous electrodeposition (ED) and pulsed electrodeposition (PED-1, PED-2, PED-3 and PED-4) methods.

This suggests that the cycling time plays an important role in the growth of particles leading to different thicknesses. Among the pulsed methods, PED-1 is the most interesting due to the fact that it produces the highest (111) peak intensity presumably due to the high crystallinity of the CuI electrode prepared by the PED-1 method. Our XRD data were also compared with the data reported by others in previous studies. Sirimanne *et al.* reported the pulse laser deposited CuI with an average crystallite size of 1 μm [225]. Sankapal *et al.* estimated the crystallite size of SILAR and CBD deposited CuI films and they found the crystallite size to be about 50 and 100 nm, respectively [226].

4.1.2 Surface morphology analysis

The surface morphology and cross-section of ED and PED CuI electrodes were studied using FEGSEM. Fig. 4-3 shows FEGSEM topographical images of the surface morphology of the CuI.

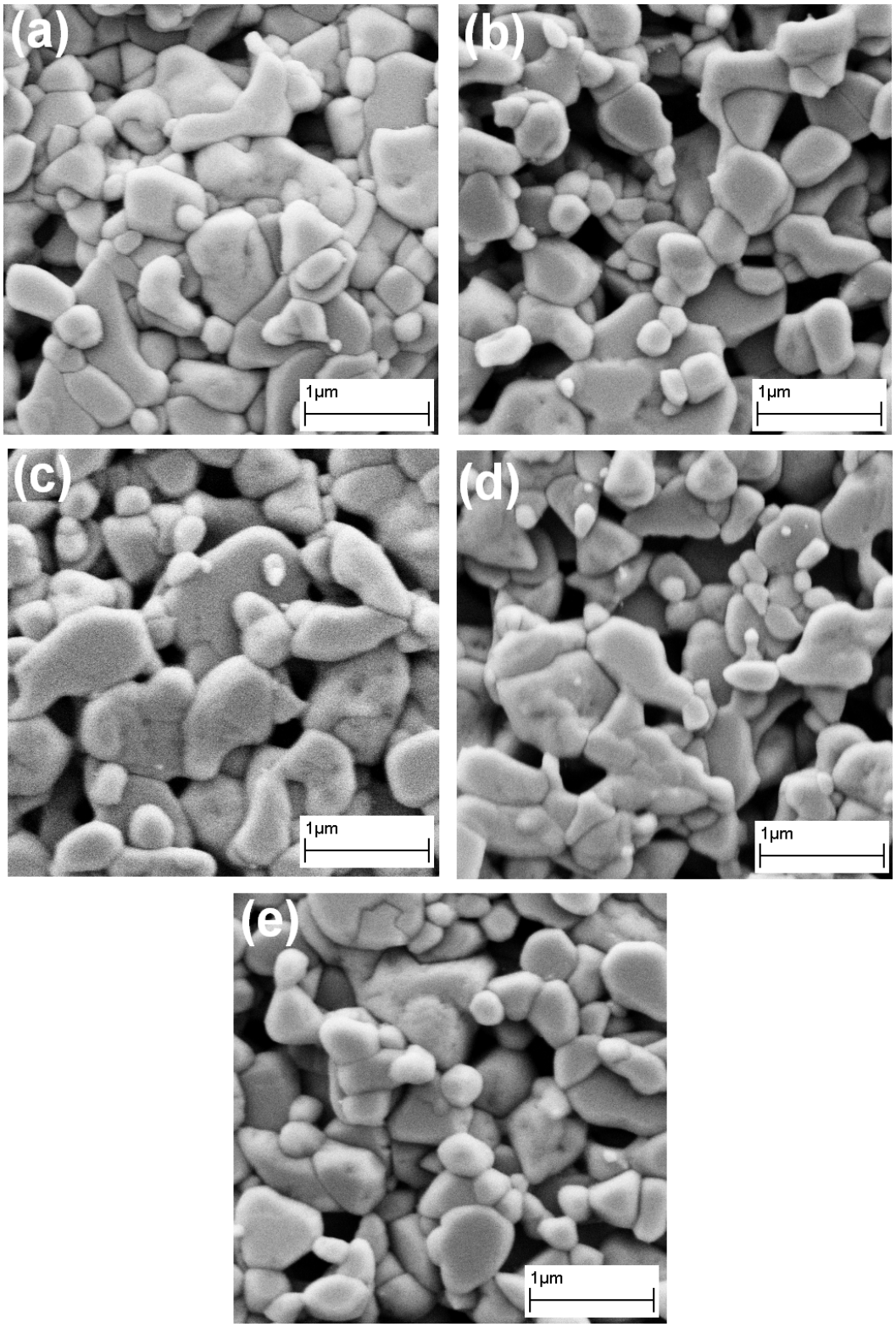

Fig. 4-3: FEGSEM images of CuI electrodes deposited on the FTO glass substrates corresponding to the (a) ED, (b) PED-1, (c) PED-2, (d) PED-3 and (e) PED-4.

Overall, the surface morphology difference between ED and PED CuI electrodes is distinguishable. Relatively small CuI particles are visible and interior voids are frequent in the PED electrode, whereas such features are less frequent in the ED electrode. In other words, the electrode prepared by pulsed electrodeposition resulted in a porous and textured film compared to the ED electrode which produced a relatively compact electrode. As shown in Fig. 4-3, it appears that the repeated nucleation and subsequent particle growth have resulted in a relatively porous CuI microstructure in the PED case. Previous studies have shown that the material's morphology can be controlled by altering the PED parameters. For example, Mathews *et al.* reported that highly porous of SnS films can be prepared on FTO substrate by PED [227]. Baeck *et al.* have shown the deposition of WO_3 with a controlled microstructure by adapting the same technique [228]. The material growth by the electrodeposition method has been described as a five-step nucleation-coalescence mechanism; (i) formation of isolated nuclei, (ii) growth to larger particles, (iii) coalescence of larger particles, (iv) formation of a linked network, and (v) formation of a continuous deposit [227,229].

Particle size calculated from the SEM topography of ED, PED-1, PED-2, PED-3 and PED-4 shows that the average feature sizes of CuI were 670, 360, 510, 440, and 560 nm, respectively. These values are significantly smaller than the individual particle sizes of electrodeposited films reported in the literature (~ 1-3 μm) [222]. The formation of relatively smaller CuI feature size in the PED case can be explained in terms of high nucleation rate with a decrease in the crystallite coalescence. It has been claimed that the nucleation and growth by PED reduces the internal stress that is directly related to crystallite coalescence [228,230]. Formation of relatively small CuI particles suggests that the growth of the new small particle nuclei is more favoured in the PED process. On in contrast, it appears that the growth and coalescence of existing particles forming larger particles are predominant in the ED process. This result agrees with XRD analysis where the PED-1 sample shows highly crystalline phase compared to other pulsed electrodeposited films (PED-2, PED-3 and PED-4) as well as continuous electrodeposited films.

The FEGSEM cross sectional images of CuI electrodes shown in Fig. 4-4 indicate that the thickness of the ED CuI electrode was about 680 nm, whereas the thickness for the samples PED-1, PED-2, PED-3 and PED-4 was estimated to be about 818, 727, 636 and 909 nm, respectively. The mass of CuI films in both ED and PED electrodes found to be identical.

The constant applied charge (0.45 Ccm^{-2}) and the identical mass in each case suggest that the change of the texture within the CuI films may be the origin of this thickness difference.

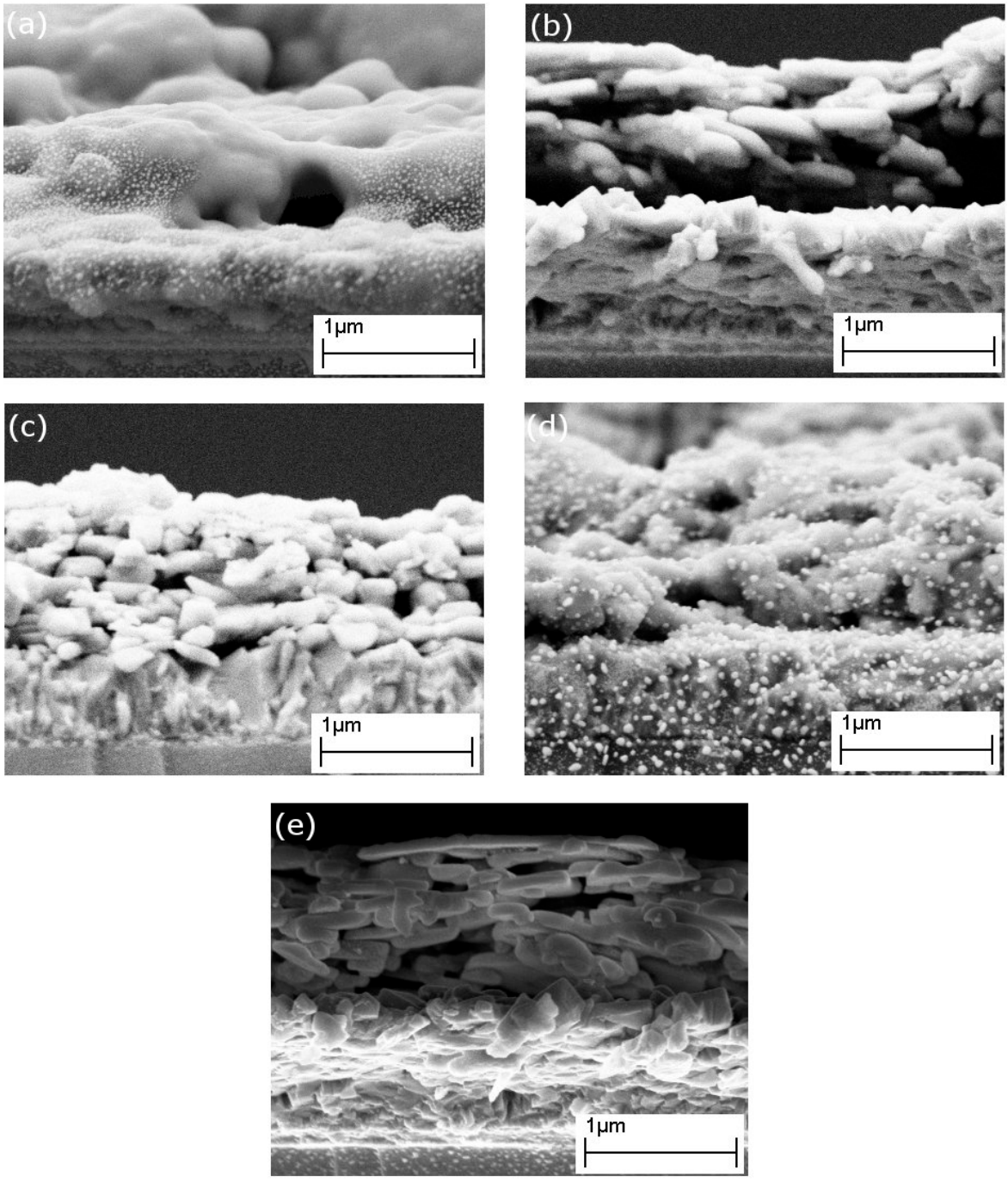

Fig. 4-4: Cross-section of CuI electrodes for samples (a) ED, (b) PED-1, (c) PED-2, (d) PED-3 and (e) PED-4.

4.1.3 Mott-Schottky analysis

To characterize the semiconducting behaviour of the deposited CuI, the Mott-Schottky plots were constructed by conducting capacitance measurements in the range between 0 and 0.25 V (vs. Ag/AgCl/3 M KCl) where the depletion region is forward within the electrode material. The negative slope in the Mott-Schottky plots confirms that CuI is a cathodic semiconductor material (see Fig. 4-5).

The Mott-Schottky analysis can also be used to determine the flat band potential. The flat band potentials derived from the plots are shown in Table 4-1. The shifts in the flat band potential of the electrode towards more positive potentials for PED electrodes compared to that of the ED electrodes indicate the changes in the surface morphology, porosity and crystallinity. For cathodic semiconductors the majority charge carriers are holes. The acceptor density (N_A) for CuI was calculated from the slope of Mott-Schottky plot by taking into account the dielectric constant of CuI which is 4.58 [231]. It was found that the acceptor density varied between 1.13 x 10^{25} m^{-3} to 9.01 x 10^{24} m^{-3} for the CuI electrodes prepared in this study (Table 4-1). The variations in the N_A may be due to the changes in the internal surface area of each electrode. The change of internal surface area is related to the changes in the texture of each electrode resulted by altering the electrodeposition conditions and the material growth.

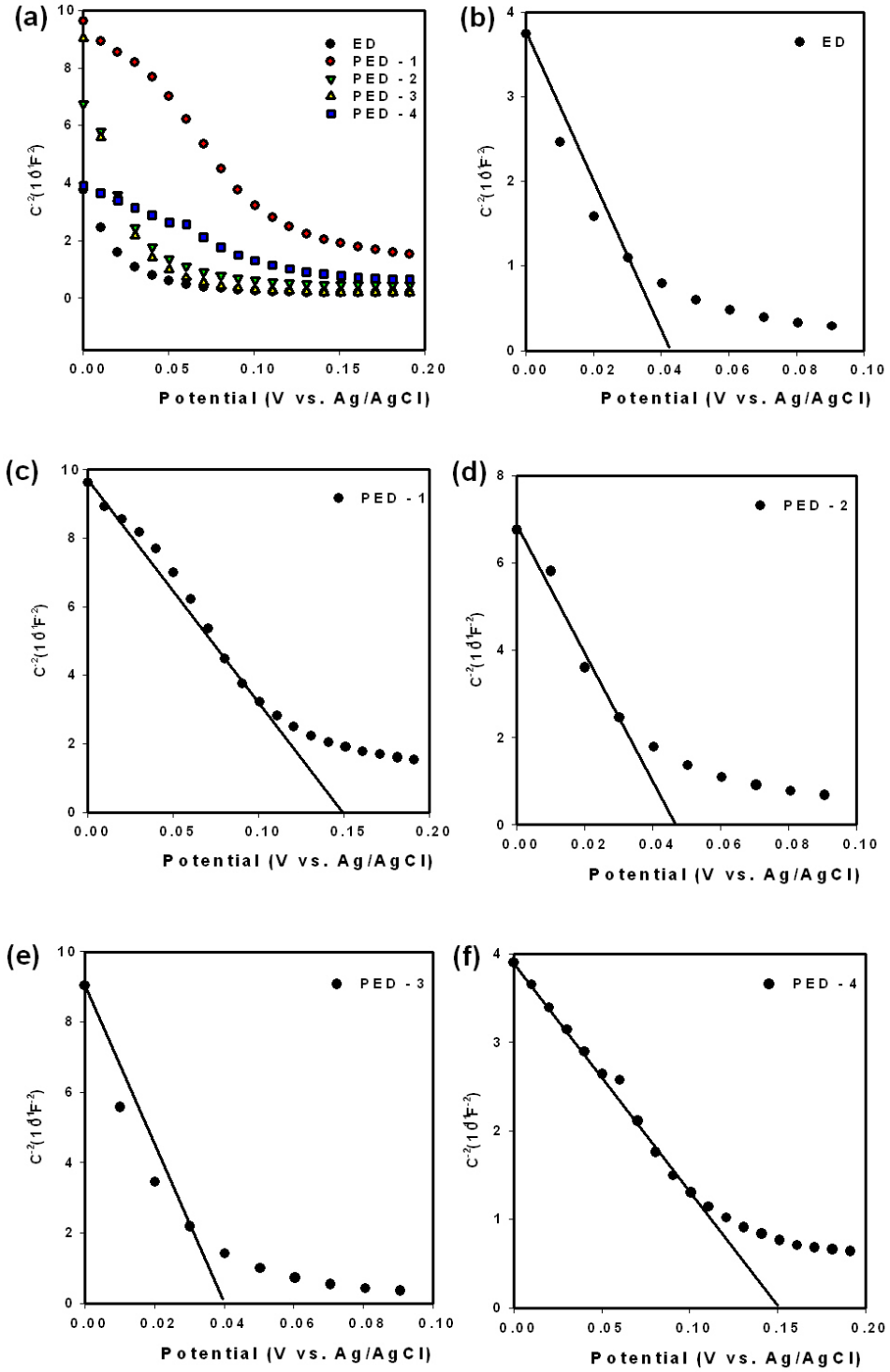

Fig. 4-5: Mott-Schottky plot of CuI electrodes for samples (a) ED, (b) PED-1, (c) PED-2, (d) PED-3 and (e) PED-4.

Table 4-1: The flat band potential and acceptor density calculated from Mott-Schottky plots.

Electrode	**Flat band potential (V vs. Ag/AgCl/3 M KCl)**	**Acceptor density (N_A) (m^{-3})**
ED	0.04	9.01×10^{24}
PED-1	0.14	3.79×10^{24}
PED-2	0.05	7.70×10^{24}
PED-3	0.04	4.41×10^{24}
PED-4	0.15	1.13×10^{25}

4.1.4 Optical absorption properties

The optical absorption spectra of the CuI films deposited on FTO substrates were recorded by using a UV-Vis spectrometer. A bare FTO substrate was used as the background reference in these measurements. The spectra for all CuI films prepared by continuous (ED) and pulsed electrodeposition (PED-1, PED-2, PED-3 and PED-4) were very similar as shown in Fig. 4-6. The absorbance beyond the 430 nm is due to the light scattering nature of the CuI electrodes prepared in this study.

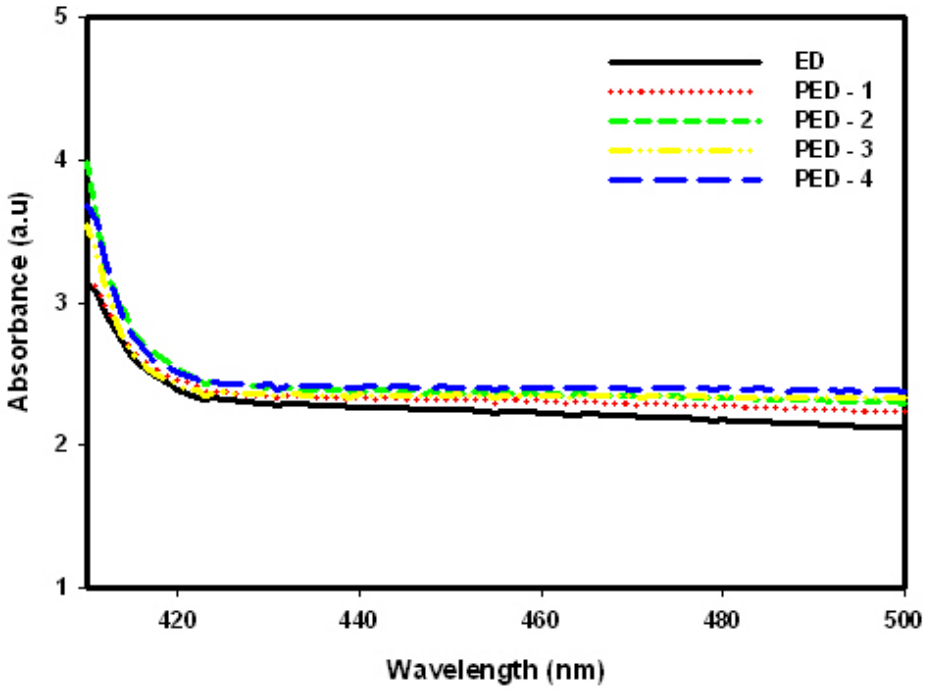

Fig. 4-6: UV-Vis absorption spectra of CuI electrodes for samples (a) ED, (b) PED-1, (c) PED-2, (d) PED-3 and (e) PED-4.

As can be seen in Fig. 4-6 the photoresponse at 420 nm corresponds to the on-set of the band gap excitation and it is in agreement with the previously reported value for a CuI electrode prepared by screen-printing [232].

The optical band gaps of ED, PED-1, PED-2, PED-3 and PED-4 CuI electrodes were calculated from the plots of $(\alpha hv)^2$ versus hv in each case (as shown in Fig. 4-7). According to the extrapolated straight line portion to the energy basis at $\alpha = 0$, the band gaps were estimated and found to be about 2.97 eV. Our estimated band gap value agrees well with the literature reported value (2.98 eV) [232].

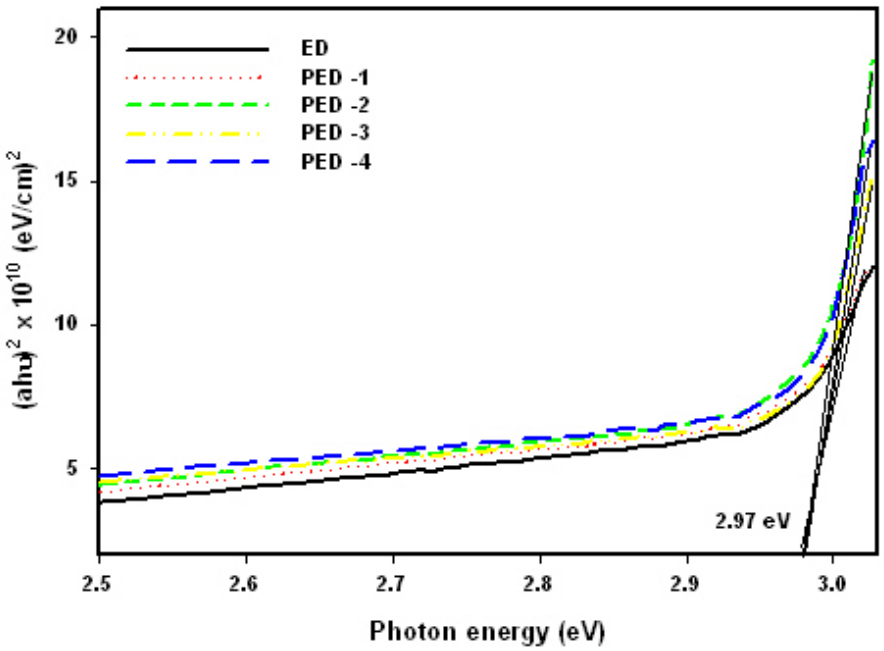

Fig. 4-7: $(\alpha h\nu)^2$ versus hν plots of CuI electrodes for samples (a) ED, (b) PED-1, (c) PED-2, (d) PED-3 and (e) PED-4.

4.1.5 Current-voltage analysis

The current-voltage measurements were conducted for all CuI electrodes under chopped light conditions. The illumination light source is AM 1.5 simulated sunlight. The light was chopped manually in 0.02 V intervals. The current-voltage plots obtained under applied bias voltage between -0.2 and 0.2 V versus the Ag/AgCl/3 M KCl reference electrode potential in 1 M Na_2SO_3 are shown in Fig. 4-8. The strong negative photocurrent observed for all electrodes confirmed that CuI prepared by the electrodeposition method (pulsed and continuous) are cathodic.

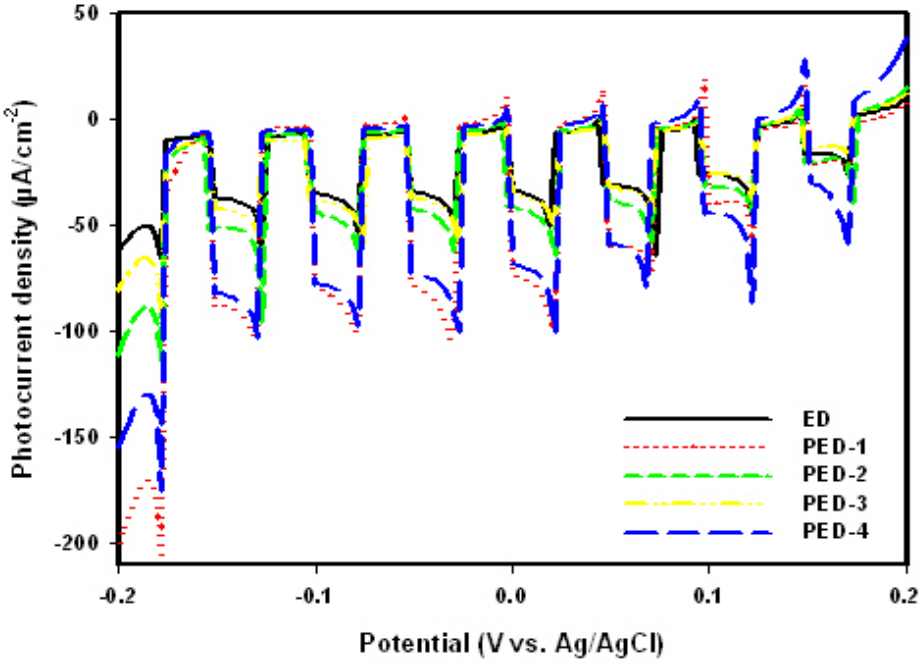

Fig. 4-8: The chopped photocurrent density vs. potential plots recorded in 1 M Na_2SO_3 solution for CuI electrode samples corresponding to (a) ED, (b) PED-1, (c) PED-2, (d) PED-3 and (e) PED-4. The illumination light source is AM1.5 simulated sunlight.

When the electrode is illuminated, electron-hole pairs are generated upon absorption of light by CuI. The charge separation under applied bias and the subsequent collection at the FTO substrate results in the photocurrent. The sharp negative photocurrent pulses that are observed under illumination (following a chopping period which provides the dark current) indicate that a portion of the photogenerated electrons are transferred to the electrolyte and the corresponding holes are moved in the opposite direction to be collected at the FTO substrate. A negligible current was observed for all electrodes in the dark (when the illumination is interrupted). The sharp negative and positive spikes that are seen at relatively low applied bias voltages suggest strong recombination of photogenerated electron-hole pairs in that region. As the applied voltage is gradually shifted in the negative direction, such sharp spikes have disappeared. However, even in that region the photocurrent pulses are associated with a slow decay component.

The comparison of photocurrent density for all CuI electrodes shows that the photocurrent is significantly high in pulsed electrodeposited electrodes compared to that of the continuous electrodeposited counter parts (Fig. 4-8). This observation is in good agreement with the structural characterisation information of CuI electrodes. The PED electrodes in general had more textured matrix, hence relatively high internal surface area. The improved crystallinity in PED electrodes may have also been partly responsible for this behaviour. By improving the surface structure of the electrodes, the photocurrent was enhanced by efficient transport of majority holes towards the film to combine with the electrons transported towards the electrolyte and enter the external circuit before arriving at the back contact of the film.

Fig. 4-9 presents the steady-state photocurrent density results of the CuI electrode in the dark and under illumination. These data agree with the chopped photocurrent results as shown in Fig. 4-8. The dark-current onsets are located in between 0.05 and -0.1 V for all CuI electrodes. The dark-current is negligible for all electrodes over the entire potential window of $-0.2\ V \leq V_{applied} \leq 0.2\ V$. The photocurrent densities of the electrodes were increased gradually when the applied voltage was scanned towards the negative region. In comparison with all samples, the PED–1 electrode prepared by pulsed deposition exhibits the highest photocurrent density. The results obtained at 0 V vs. Ag/AgCl/3 M KCl potential bias were about 75 μAcm^{-2}. The other electrodes, namely ED, PED-2, PED-3 and PED-4, showed photocurrent densities of 32, 42, 30 and 67 μAcm^{-2}, respectively, at 0 V vs. Ag/AgCl/3 M KCl.

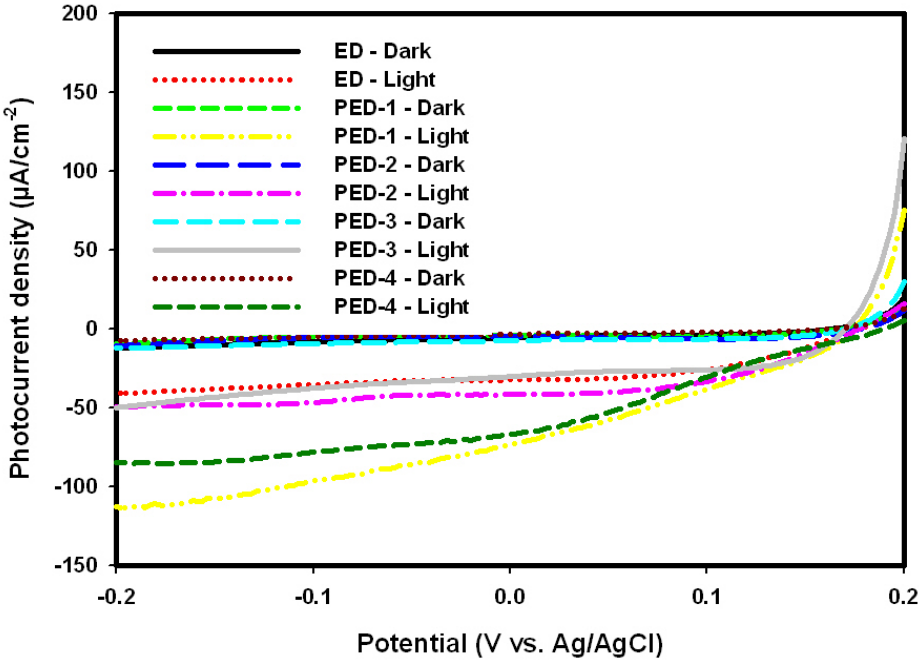

Fig. 4-9: The steady-state of photocurrent density vs. potential measured in 1 M Na_2SO_3 solution for CuI electrode corresponding to samples (a) ED, (b) PED-1, (c) PED-2, (d) PED-3 and (e) PED-4.

4.1.6 Incident Photon to Electron Conversion Efficiency (IPCE)

The monochromatic photocurrent data was recorded and IPCE was calculated in order to understand the external quantum efficiency of CuI electrodes under illumination. The IPCE spectrum for each electrode provides incident photon to electron conversion efficiency at every 5 nm in the wavelength window of 340 – 600 nm. Fig. 4-10 displays IPCE plots for the ED, PED-1, PED-2, PED-3 and PED-4 electrodes in 1 M Na_2SO_3 electrolyte under a cathodic bias (at 0 V vs. Ag/AgCl/3 M KCl). The photocurrent drops at 420 nm, which corresponds to the band gap energy of CuI as shown in Fig. 4-10. The recorded maximum IPCE values are about 2.6, 5.3, 3.5, 2.5 and 5.0 % for the ED, PED-1, PED-2, PED-3 and PED-4 electrode respectively. The IPCE results showed that the CuI films are photoactive and capable of harvesting light in high energy end of the solar spectrum. The IPCE spectra are in agreement with photocurrent density results, where the CuI prepared by pulsed electrodeposition (PED

electrode series) exhibited the higher photocurrent density compared to the continuous-electrodeposition (ED electrode).

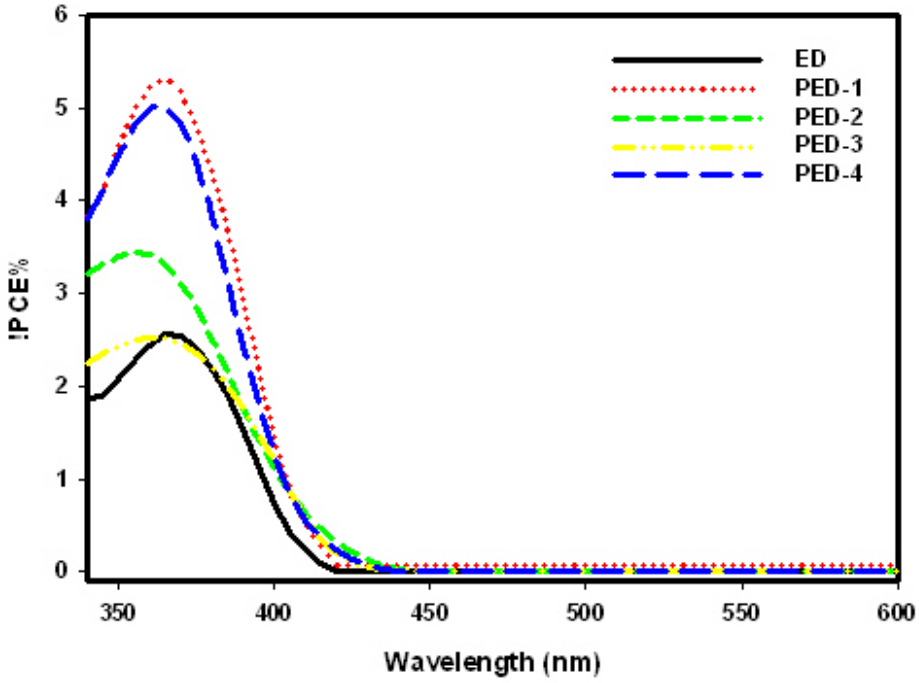

Fig. 4-10: The IPCE spectra for CuI electrode corresponding to samples (a) ED, (b) PED-1, (c) PED-2, (d) PED-3 and (e) PED-4.

4.2 AAD CuI electrode

In an attempt to further enhance the electrode texture morphology and hence the photoelectrochemical performance, the CuI was deposited from an acetonitrile suspension by the AAD technique. The AAD technique has been previously reported by Parkin's group in 2007 to deposit WO_3 thin films from a toluene suspension of WO_3 nanoparticles and Choy's group in 2008 to deposit D, L-lactic acid films [233,234].

4.2.1 X-ray Diffraction (XRD) analysis

The XRD pattern in Fig. 4-11 shows the normalized at $2\theta = 26.6°$ (FTO) X-ray diffraction patterns of CuI electrode prepared by the AAD technique.

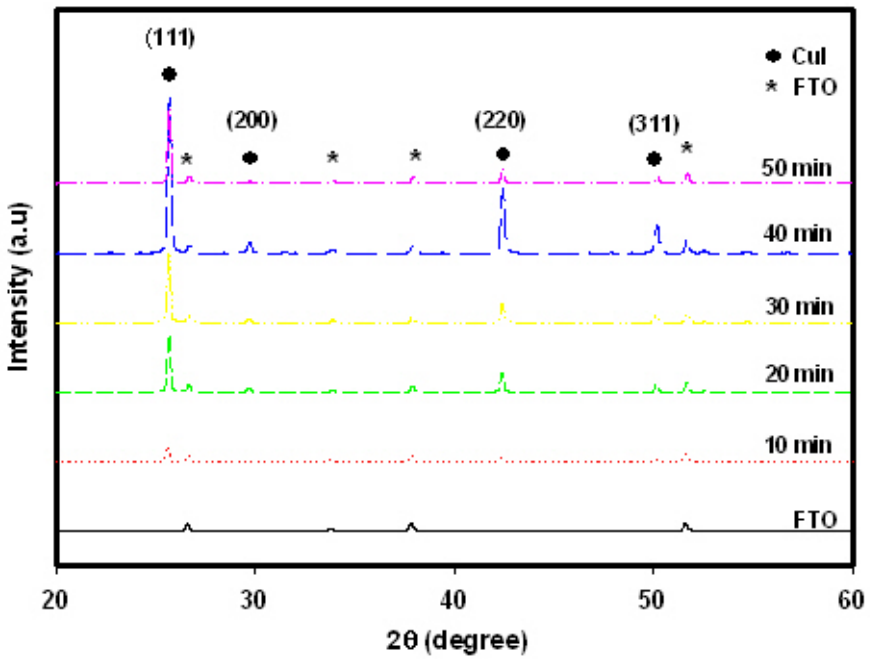

Fig. 4-11: X-ray diffraction patterns of CuI electrode prepared by using AAD method. Electrodes corresponding to 10, 20, 30, 40 and 50 min deposition time.

XRD patterns of electrodeposited CuI electrodes show predominant peak at (111) crystallographic reflection and virtually no other CuI peaks were identifiable. However, in the case of the AAD deposited CuI, in addition to (111) reflection, there are other CuI reflections indicating the polycrystalline nature of AAD CuI electrodes. The reflections were observed at 2θ values of 29.5°, 42.2°and 49.9° correspond to the CuI reflection of (200), (220) and (311), respectively. Despite these noticeable XRD changes for the AAD electrode, the pattern is still significantly dominated by the (111) reflection. The work reported by others shows that the solvent associated chemical deposition techniques generally produce polycrystalline CuI electrodes [233,234]. The average crystallite size of 10, 20, 30, 40 and 50 min deposition times CuI electrode was estimated by the Scherrer equation by taking into account (111) peak and it was found in between 39 and 46 nm as presented in Table 4-1.

Table 4-2: Average crystallite size measured at different 2θ and different deposition times for AAD CuI electrodes.

Deposition time (min)	2θ (25.6°) (nm)	2θ (29.5°) (nm)	2θ (42.2°) (nm)	2θ (49.9°) (nm)	Average crystallite size (nm)
10	43.69	44.87	47.63	47.68	46
20	43.69	41.78	46.22	45.70	44
30	44.01	39.99	44.02	44.29	43
40	40.13	36.50	39.21	41.40	39
50	45.88	47.74	44.62	46.09	46

Notably, in the present work the AAD technique produces electrodes with the smallest average CuI crystallite sizes compared to that of electrodeposited CuI electrodes (i.e. ED and PED electrodes). A search in the literature suggests that the AAD CuI electrode prepared in the present study may consist of the smallest CuI crystallites reported for a thin film electrode to date. This indeed shows the potential of the AAD as a technique to control the crystallite size, texture and morphology.

4.1.2 Surface morphology analysis

Fig. 4-12 illustrates FEGSEM images of CuI films prepared by AAD technique at different deposition times. The high resolution images showed that the small particles had average sizes of 290, 120, 110, 210 and 280 nm for sample 10, 20, 30, 40 and 50 min deposition times, respectively.

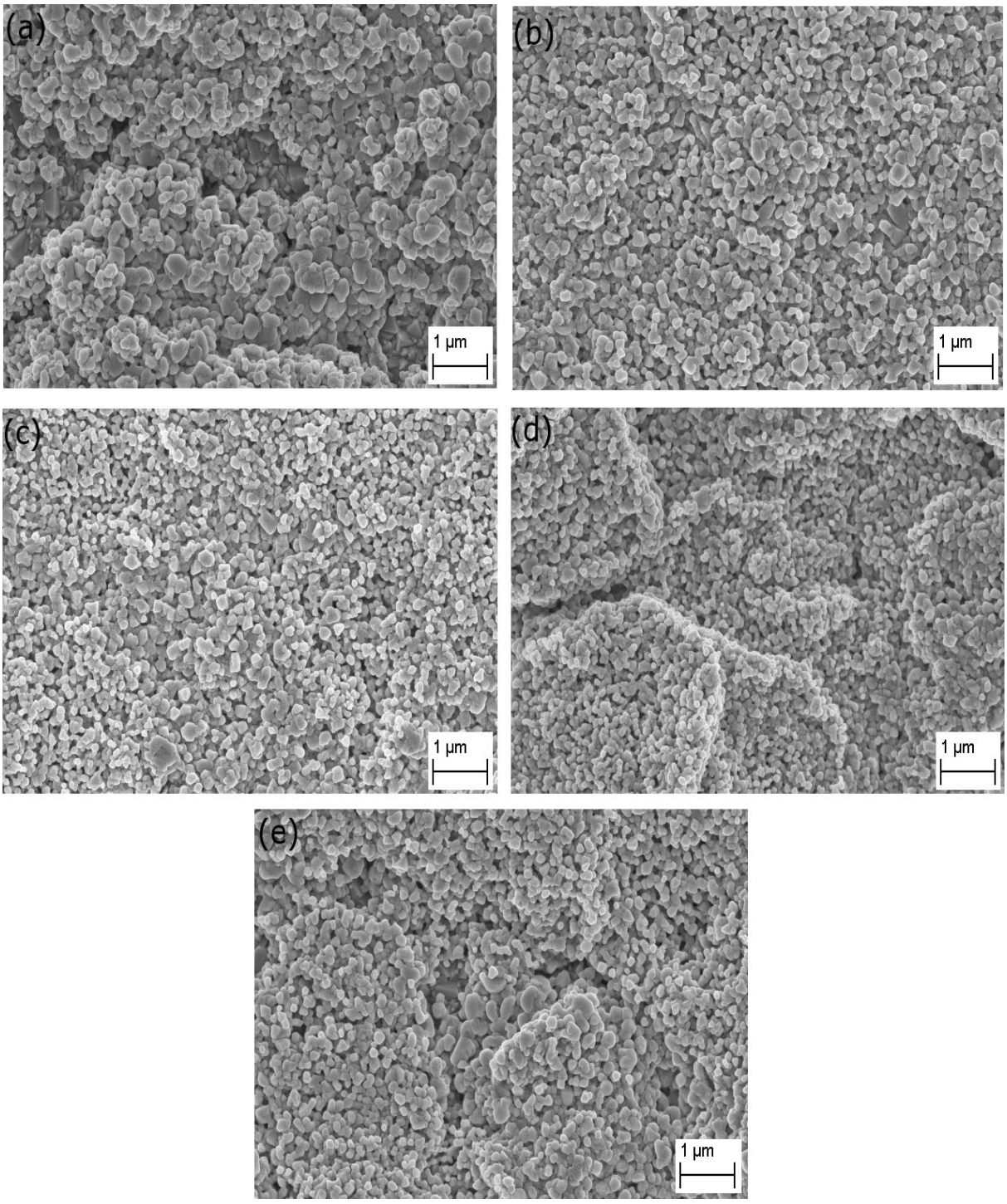

Fig. 4-12: FEGSEM images of CuI deposited by AAD method on FTO substrates (a) 10 min (b) 20 min (c) 30 min (d) 40 min and (e) 50 min deposition.

As shown in Fig. 4-12, the individual CuI particles are fused to each other forming a 3-D matrix. This analysis shows that the aerosol mediated growth technique has the potential to produce electrodes with fine particles by varying deposition parameters such as the flow rate of the carrier gas, precursor concentration and deposition temperature. In the previously reported AAD work by Parkin *et al.*, WO_3 nanoparticles with an average size (radius) between 15-20 nm were used to prepare a suspension of WO_3 in toluene and then transported to the deposition chamber as an aerosol. The features of the resulting WO_3 film contained nanosized particles as well as large agglomerated clusters in the micro meter range [233]. However, in our case, the sizes of CuI particles are uniformly distributed throughout the electrode. This, indeed, demonstrates the flexibility of AAD in which the appropriate control of parameters is capable of producing the desired film texture (i.e. nanostructured). Our recent work [235-237] as well as the work reported by other groups such as O'Brien, Parkin and Choy have already shown that aerosol mediated growth (i.e. AACVD) is a powerful method to obtain textured materials [233,234,238].

As it can be seen in Fig. 4-12(a), the substrate surface was not fully covered by the CuI particles and the particle size was significantly bigger for the relatively short deposition times, However, as the deposition time is gradually increased, the smaller particles (Fig. 4-12(b)) form and fuse together to form a matrix which produces high internal surface area and more porosity. Improvements in the surface morphology of the electrode would result in improving the photoelectrochemical performance of the electrode. After 40 min deposition, the FEGSEM image shows that the film is compact in nature. This is due to the formation of excess CuI particles at relatively longer deposition times (> 40 min).

The average thicknesses of the AAD CuI electrodes were determined from the cross-sectional images shown in Fig. 4-13 and Fig. 4-14.

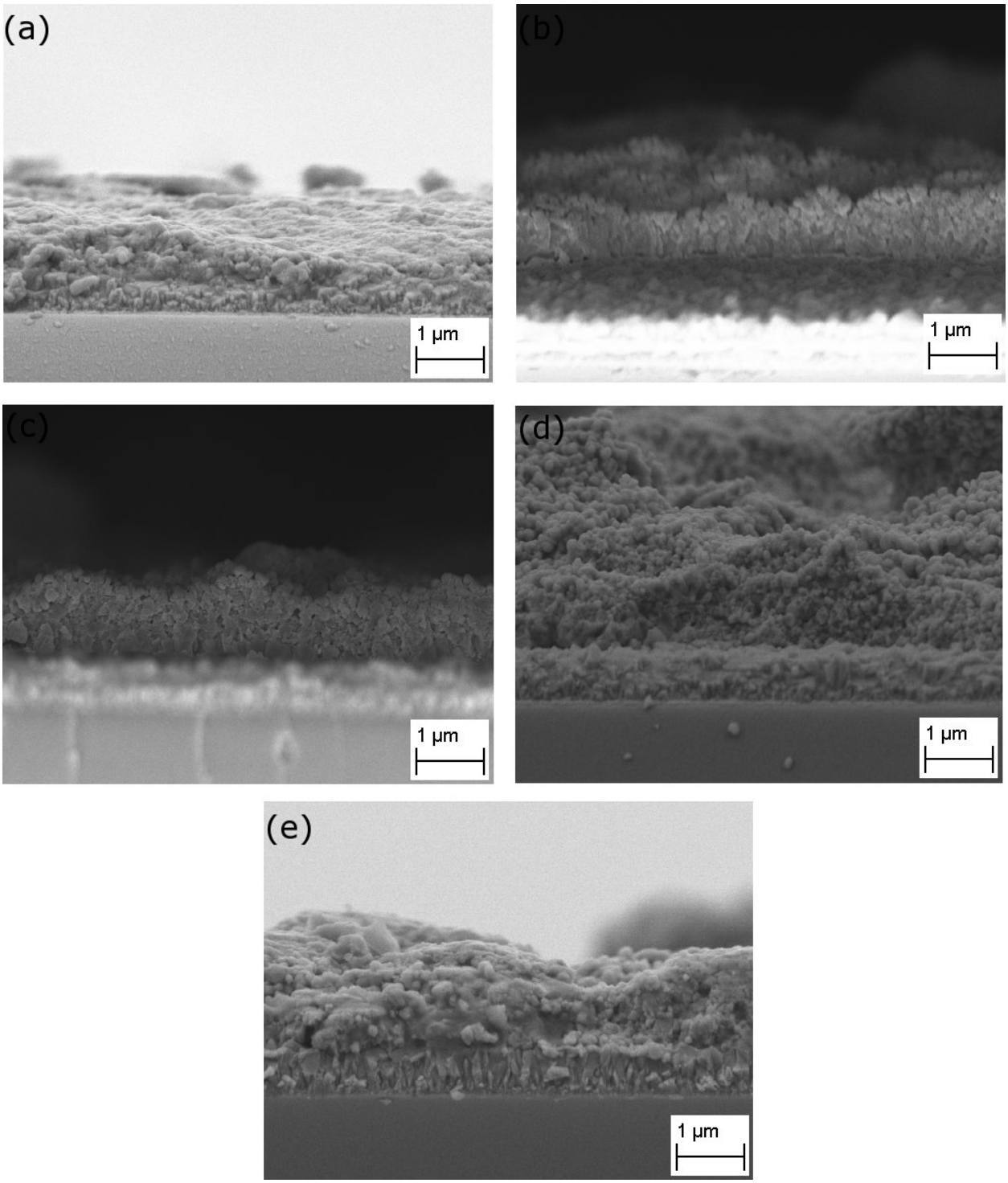

Fig. 4-13: Cross-sectional images of CuI electrode deposited by AAD method on FTO substrates (a) 10 min (b) 20 min (c) 30 min (d) 40 min and (e) 50 min deposition.

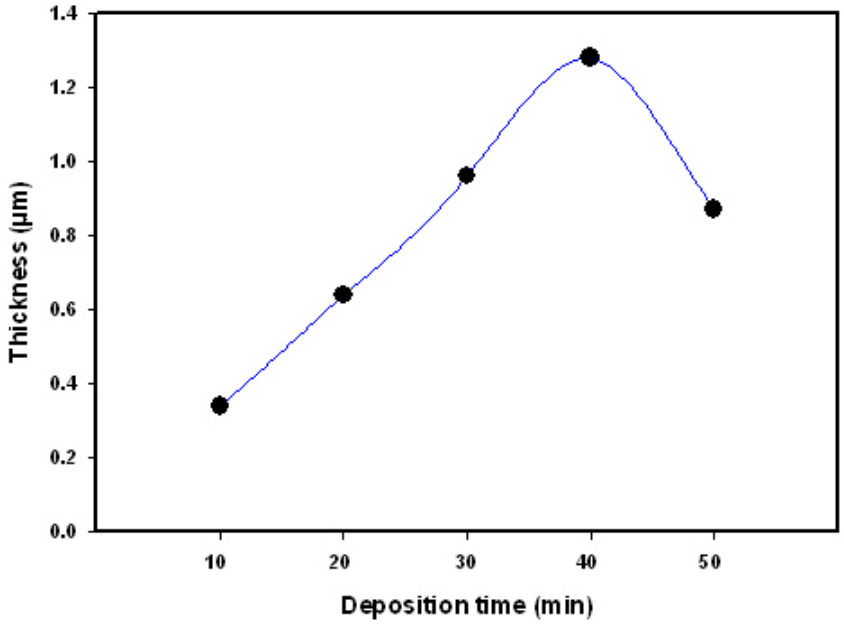

Fig. 4-14: Thickness of CuI deposited by AAD.

The thickness of the CuI films prepared by AAD was estimated to be 0.34, 0.64, 0.96, 1.28 and 0.87 µm for sample 10, 20, 30, 40 and 50 min deposition times, respectively. The deposition rate is calculated to be about 32 nm per min (up to 40 mins deposition time). The cross-section image also shows that the particles are grown and fused to form a matrix which gives a highly porous structure. However, due to the temperature difference, the by-product of CuI is formed on the surface as discussed in the previous paragraph. This can be seen clearly on the 40 min deposition electrode, where the electrode is really thick. Further increases of deposition time to 50 min, resulted in formation of a powder on the surface and a more compact film. It appears that the mechanical strength of CuI film beginning to lose as the deposition time is increased. It is possible that a part of the CuI film is dissolved as a result of this. That could be the reason for the uncharacteristic film thickness observed for the CuI electrodes prepared over a period beyond 40 mins (i.e. 50 mins).

4.1.3 Mott-Schottky analysis

Fig. 4-15 shows the Mott-Schottky plot constructed from capacitance data for a CuI electrode prepared by AAD at different deposition times in 1 M Na_2SO_3 solution under dark conditions. It is well known that the negative slope of the Mott-Schottky plot indicates *p*-type and a positive slope indicates n-type semiconductor behaviour. From the slope of the plots shown, it is concluded that AAD CuI is *p*-type in nature. The variation in the deposition time shows a similar flat band potential around 0.08 V (vs Ag/AgCl/3 M KCl). The values of N_A were estimated to be in between 2.08 x 10^{25} m^{-3} and 4.19 x 10^{24} m^{-3} (see the Table 4-3 below).

Table 4-3: The Flat band potentials and acceptor densities calculated from Mott-Schottky plots.

Electrode deposition time (min)	Flat band potential (V vs. Ag/AgCl/3 M KCl)	Acceptor density (N_A) (m^{-3})
10	0.05	2.08 x 10^{25}
20	0.08	5.57 x 10^{25}
30	0.05	2.08 x 10^{24}
40	0.09	4.19 x 10^{24}
50	0.07	2.12 x 10^{25}

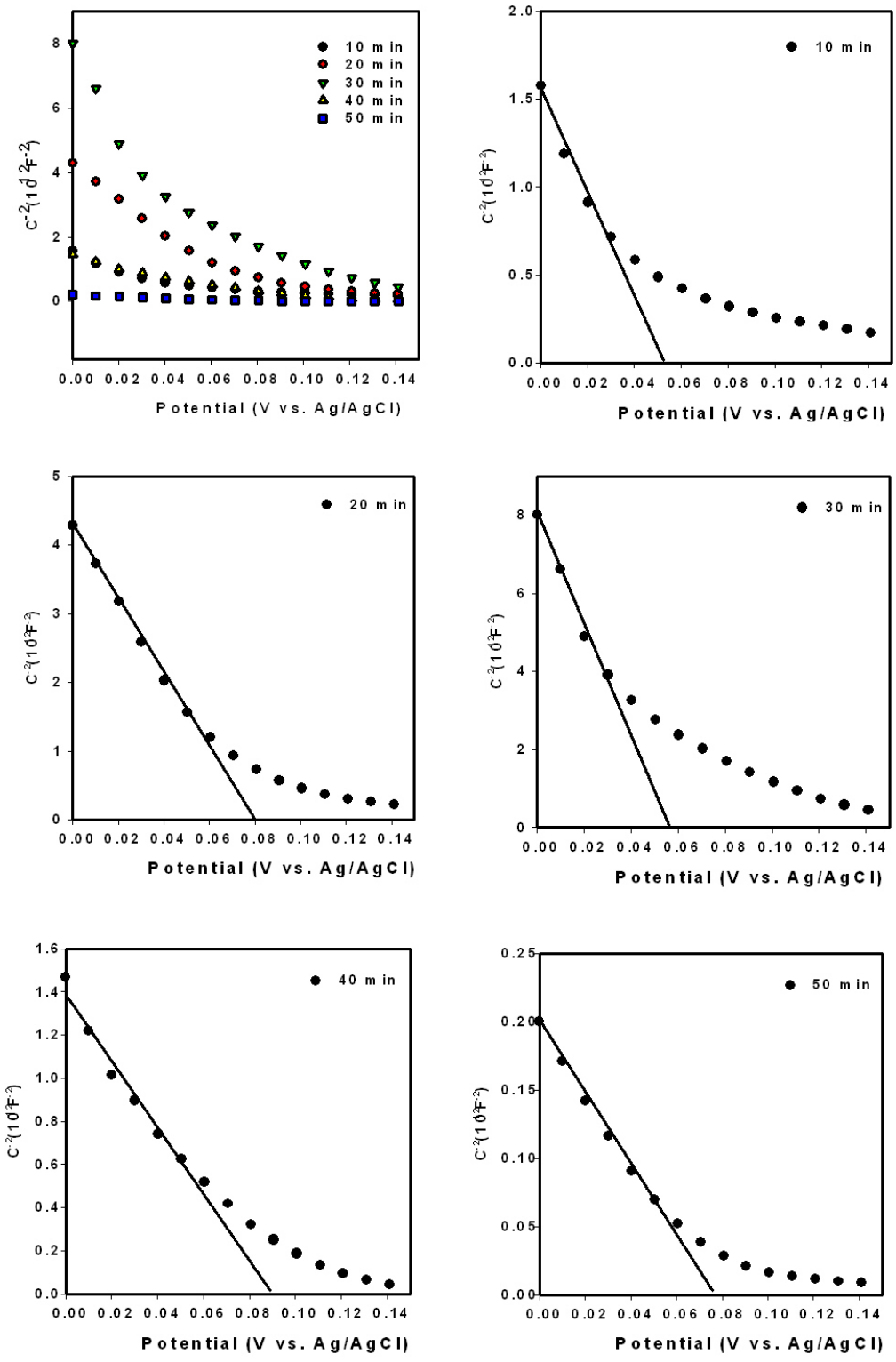

Fig. 4-15: Mott-Schottky plot of CuI electrodes prepared by AAD method with deposition time (a) 10 min (b) 20 min (c) 30 min (d) 40 min and (e) 50 min.

4.1.4 Optical absorption properties

Fig. 4-16 presents the optical absorbance of the CuI electrodes on FTO substrates deposited from different deposition times in the wavelength range of 400–500 nm.

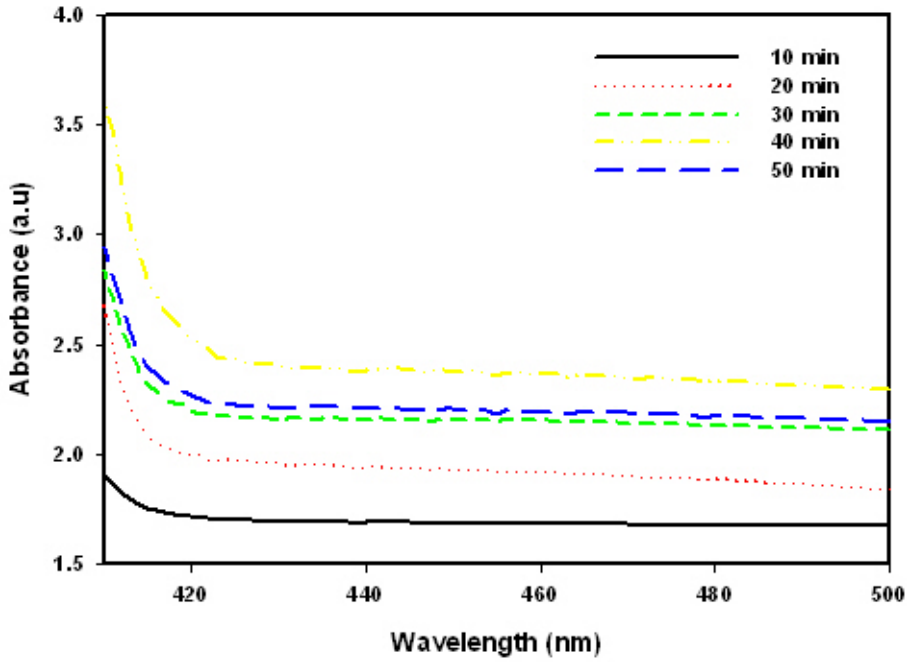

Fig. 4-16: UV-Vis absorption spectra of CuI electrode prepared by AAD method at different deposition times (a) 10 min (b) 20 min (c) 30 min (d) 40 min and (e) 50 min.

The relatively low absorbance observed for these electrodes may be due to their low thickness. It can be seen from Fig. 4-12 (surface morphology) that the substrate was not fully covered by CuI particles and in certain parts of the electrode the bare FTO substrate can be clearly observed. For deposited electrodes at longer deposition times (i.e. 40 min), the spectrum exhibited higher absorbance than for the electrodes deposited at relatively low deposition times. These electrodes have shown highly dense and non-uniform films. However, as the deposition time is further increased beyond 50 mins, the optical absorbance is decreased. This observation agrees with the surface morphology as presented in the Fig. 4-12. The spectrum also shows a sharp absorption edge at 420 nm and it is in good agreement with the previously

reported absorbance behaviour for a CuI electrode prepared by screen-printing method which is an indication of good crystallinity of our electrodes [226].

The direct band gap transition energy value can be deduced from the absorption coefficient vs. photon energy plot. Fig. 4-17 illustrates $(\alpha hv)^2$ vs. hv plot for AAD CuI electrodes.

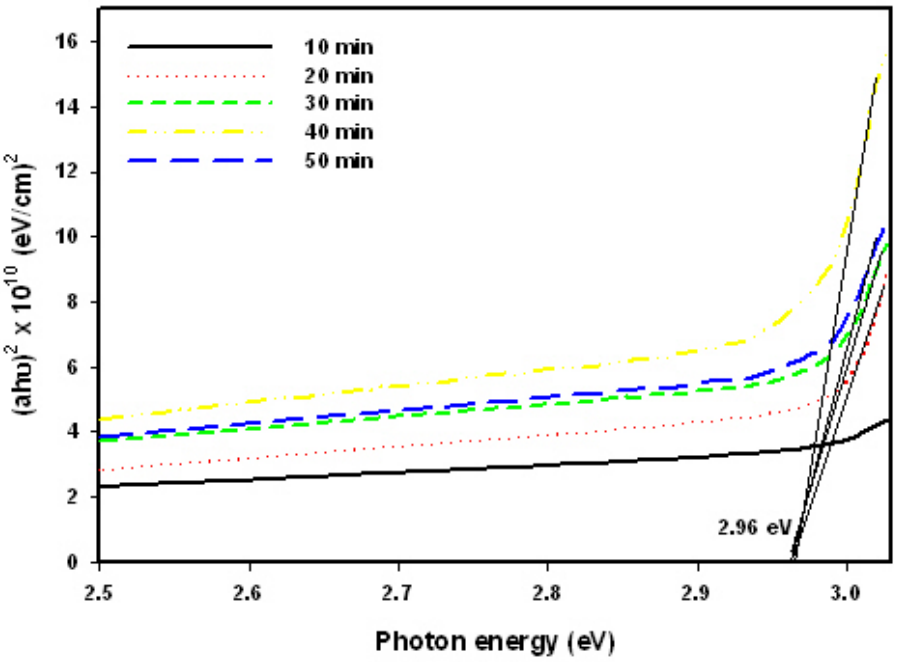

Fig. 4-17: Plot of $(\alpha hv)^2$ versus hv of CuI electrode prepared at different deposition times (a) 10 min (b) 20 min (c) 30 min (d) 40 min and (e) 50 min.

The band gap calculated by extrapolating the linear part of the curve to zero absorption was 2.96 eV for almost all CuI electrodes. The band gap value estimated for AAD CuI electrodes is very similar to the values deduced for the CuI electrodes prepared by the electrodeposition (ED and PED).

4.1.5 Current-voltage analysis

The photocurrent density was measured whilst light was manually chopped. The illumination was kept constant at 1000 $mWcm^{-2}$. The corresponding chopping photocurrent density versus applied potential plots of CuI electrodes are presented in Fig. 4-18.

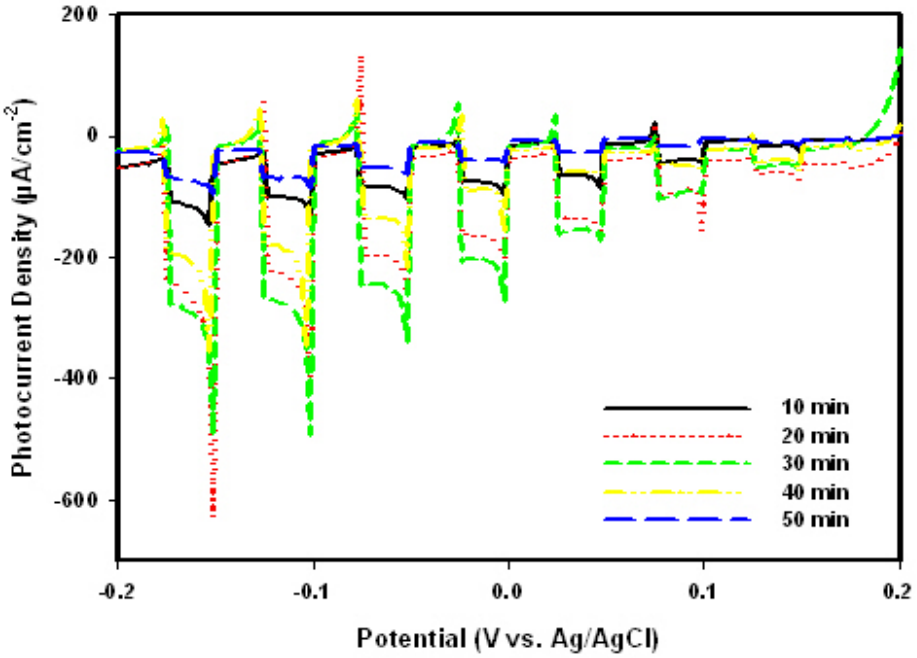

Fig. 4-18: The chopping photocurrent density vs. potential measured in 1 M Na_2SO_3 solution for CuI electrode corresponding to (a) 10 min (b) 20 min (c) 30 min (d) 40 min and (e) 50 min deposition time.

The CuI electrodes were scanned at potentials more positive than -0.2 (V vs. Ag/AgCl/3 M KCl) as potentials more negative than -0.2 can possibly destroy the CuI due to degradation. Evidence for degradation was seen at potentials more negative than -0.2 V in which the colour of the electrode changed from its typical white colour to black and the film peeled off from the FTO substrate. This could be due to the oxidation of CuI to other phases. However, study of degradation products under extreme bias conditions is beyond the scope of the present study.

Strong recombination spikes were observed when the light is interrupted by chopping at every 0.02 V intervals. The spikes observed for AAD electrodes are relatively stronger than

that of ED and PED electrodes indicating high recombination. The photocurrent density at 0 V were about 75, 154, 174, 89 and 33 μAcm^{-2} for AAD CuI electrodes deposited for 10, 20, 30, 40 and 50 min, respectively. The photocurrent density was progressively enhanced as the deposition time was increased until 30 min. Interestingly, for the 20 and 30 min deposited electrodes, the texture is uniform and the individual particles are uniformly distributed. This appears to increase the internal surface area of such electrodes thereby improving the photocurrent density. However, for the AAD CuI electrodes deposited for 40 and 50 mins the photocurrent density is reduced, presumably due to the compact nature and increased thickness of the electrode. This could be due to strong recombination that may take place within the electrodes as the photogenerated electrons and holes are required to travel relatively long distances before they reach the semiconductor/electrolyte interface and FTO substrate, respectively. The 30 mins deposited AAD electrode provides a good compromise between charge recombination and charge separation/transport/collection. In fact, that may be the reason for observation of high photocurrent density for 30 mins deposited AAD electrode. Overall, the AAD CuI electrodes have shown higher photocurrents than the electrodeposited CuI electrodes. The variation of the steady-state photocurrent density has been presented by the *J–V* characteristics shown in the Fig. 4-19.

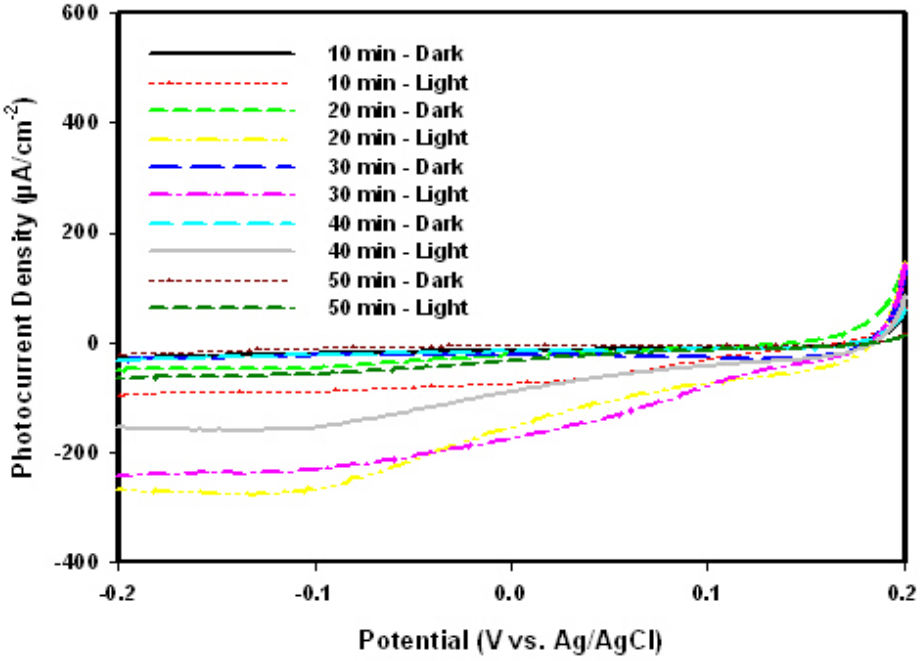

Fig. 4-18: The steady-state photocurrent density vs. applied potential measured in 1 M Na_2SO_3 solution for CuI electrode prepared at (a) 10 min (b) 20 min (c) 30 min (d) 40 min and (e) 50 min deposition.

4.1.6 Incident Photon to Electron Conversion Efficiency (IPCE)

Fig. 4-20 shows the incident photon to electron conversion efficiency (IPCE) spectra of AAD CuI electrodes deposited at different time intervals.

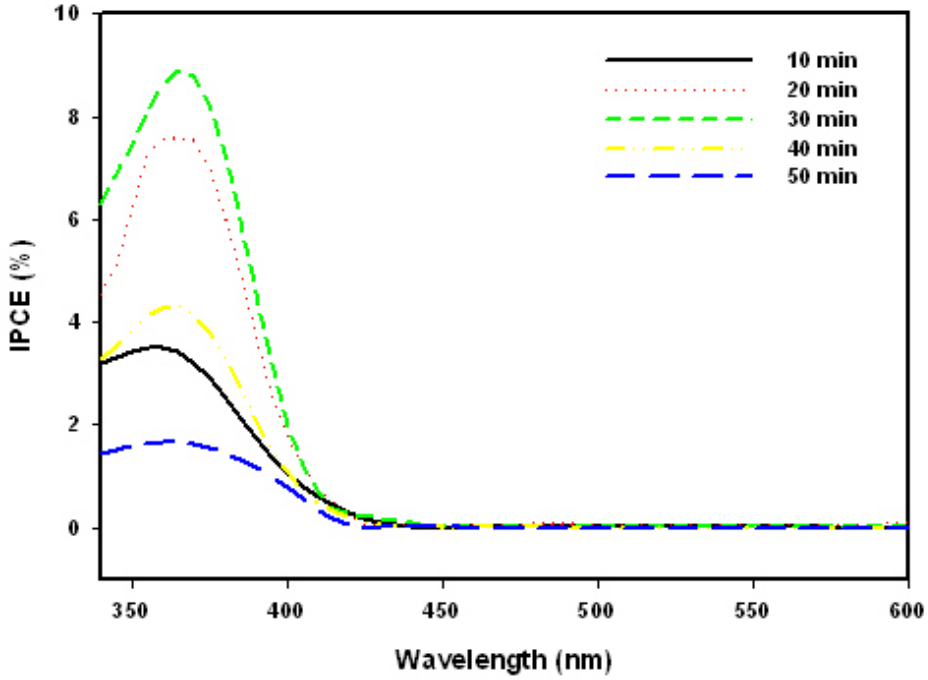

Fig. 4-20: The IPCE spectra for CuI electrode corresponding to the samples (a) 10 min, (b) 20 min, (c) 30 min, (d) 40 min and (e) 50 min.

The photocurrent was observed up to 420 nm, which corresponds to the wavelength of band gap threshold energy (2.96 eV) as shown in Fig. 4-17. The data agree well with the band gap calculated for the same electrode using optical absorbance data. The IPCE spectra showed that the CuI films are photoactive and useful to harvest light in the high energy end of the sunlight. The maximum IPCE were recorded at 365 nm are 3.6, 7.6, 8.9, 4.3 and 1.7% for AAD CuI electrodes corresponding to 10, 20, 30, 40 and 50 min deposition times, respectively.

4.3 AACVD *p*-NiO semiconductor electrode

Nanostructured NiO electrodes were successfully synthesized through a simple one-step approach by employing the AACVD technique. The effect of deposition temperature, carrier gas and solvent on preferred orientation, nanostructure and morphology of the deposited films was investigated in detail. All films deposited exhibited excellent adhesion properties on the FTO substrate as verified by the “scotch tape test” and are stable towards air

and atmospheric moisture. The films deposited in the current work have a range of advantages over the literature reported methods, such as, being a one-step process, having clean deposition and good adhesion to the FTO substrate.

4.3.1 X-ray Diffraction (XRD) analysis

The NiO electrodes deposited by AACVD revealed the crystalline face-centred cubic NiO system with indices of (111), (200) and (220) are formed. The XRD reflection pattern shows no signs of any chemically or pyrolytically produce impurities suggesting that Ni(acac) converts completely to a NiO electrode. Generally, the crystallographic orientation of the NiO film varies with the deposition parameters such as temperature and oxygen content of the deposition chamber. The NiO prepared in the (111) orientation shows the enhanced PEC performance. The desired (111) orientation of NiO was prepared by controlling the temperature as well as the oxygen content of the deposition chamber. The oxygen content of the deposition chamber was controlled by changing the solvent ratio (methanol and toluene) as well as carrier gas ratio (Argon and Air). Comparison of the XRD pattern of the deposited electrodes with the standard ICCD pattern for NiO revealed that the deposited crystalline material is NiO in its cubic form. The deposition solvent and carrier gas play a vital role in the crystallographic orientation in the current NiO electrodes.

4.3.1.1 Effect of temperature on crystallographic orientation

The X-ray diffraction patterns of the films deposited at the substrate temperature from 400 to 500 °C using toluene as a solvent and air as a carrier gas are shown in Fig. 4-21.

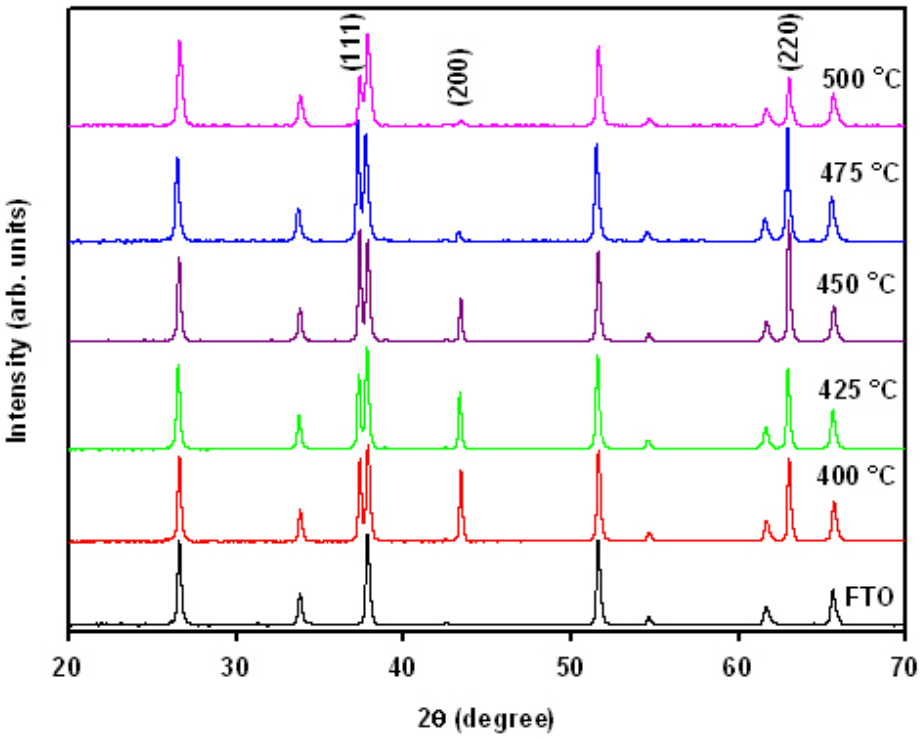

Fig. 4-19: The XRD patterns of the films deposited at different temperatures using 0.1 M solution in toluene and air as a carrier gas.

The crystal structure of NiO films deposited at 400 °C to 425 °C was identified to be (111), (200) and (220). The preferred orientation have changes with an increase in deposition temperature, which indicating the dependence of preferred orientation on temperature. The films deposited at 475 and 500 °C show the preferred orientation have change and the growth of the NiO were identified to be (111) and (220). The deposition temperature above 500 °C cannot be achieved due to the stability of the substrate and premature burning of the aerosol at high temperature.

4.3.1.2 Effect of solvent and carrier gas on crystallographic orientation

Along with the temperature, the effect of oxygen content (solvent and carrier gas) on the crystallographic orientation has been studied in detail. The 475 °C temperature was selected to prepare the preferred (111) oriented film and the oxygen content of the deposition

system was varied by changing the solvent between toluene (non oxygen containing solvent) and methanol (oxygen containing solvent). The oxygen content of the deposition system was also controlled by changing the ratio of carrier gases (argon and air). The X-ray diffraction patterns of the films deposited at the 475 °C from toluene and methanol solution with different ratio of argon to air as carrier gas are shown in Fig. 4-22 and Fig. 4-23, respectively. The X-ray diffraction patterns (Fig. 4-22) of the films deposited using methanol as a solvent and pure argon (100% Ar) as a carrier gas shows a dominant (111) reflection, which indicates a preferred orientation of the NiO crystals along the (111) direction. This preferred orientation of NiO films strongly depends on the oxygen content [239]. The oxygen content in the methanol and argon is relatively small which results in the oxygen deficient (111) growth of NiO film. While a change in the carrier gas from argon to 50:50 mixture of argon and air initiate the dominant growth in the (200) direction which reflects in the suppressing of (111). Further changes in the carrier gas flow to 100% air shows the dominant growth towards (200) than the (111) orientations. The shift of preferred orientation growth from (111) to (200) orientation by changing the carrier gas (oxygen content of the system) is also supported by previously reported NiO films using different deposition techniques [239,240].

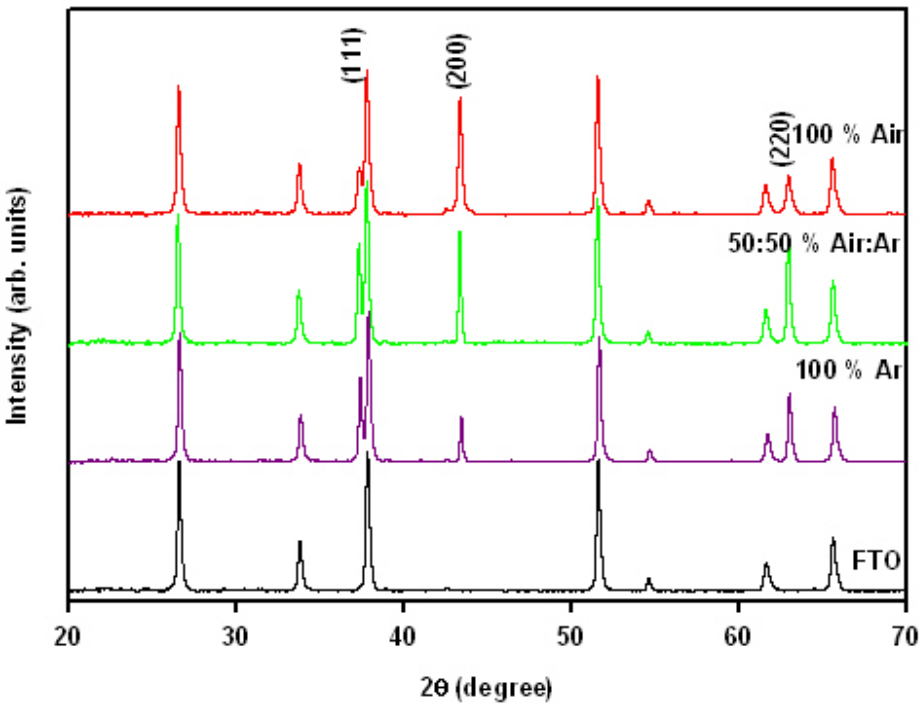

Fig. 4-20: The XRD reflection patterns of the films deposited using different ratio of carrier gas flow from 0.1 M solution in methanol at 475 °C.

In contrast, the films deposited using toluene as deposition solution and argon as a carrier gas under similar conditions show a preferred orientation to (111) direction but the intensity of the NiO reflection is very weak, which may be due to the lower crystallinity of the films. As shown in Fig. 4-23, the preferred orientation sharply changed to (111) with the increase in air content of carrier gas. The films deposited using only air (100% air) shows a strong (111) orientation with better crystallinity. The crystallographic orientation of NiO shows a dependence on the oxygen content of the system as shown in the Fig. 4-24. The ideal preparation conditions, toluene as a solvent and air as a carrier gas for (111) growth has been adopted to study the performance of NiO films.

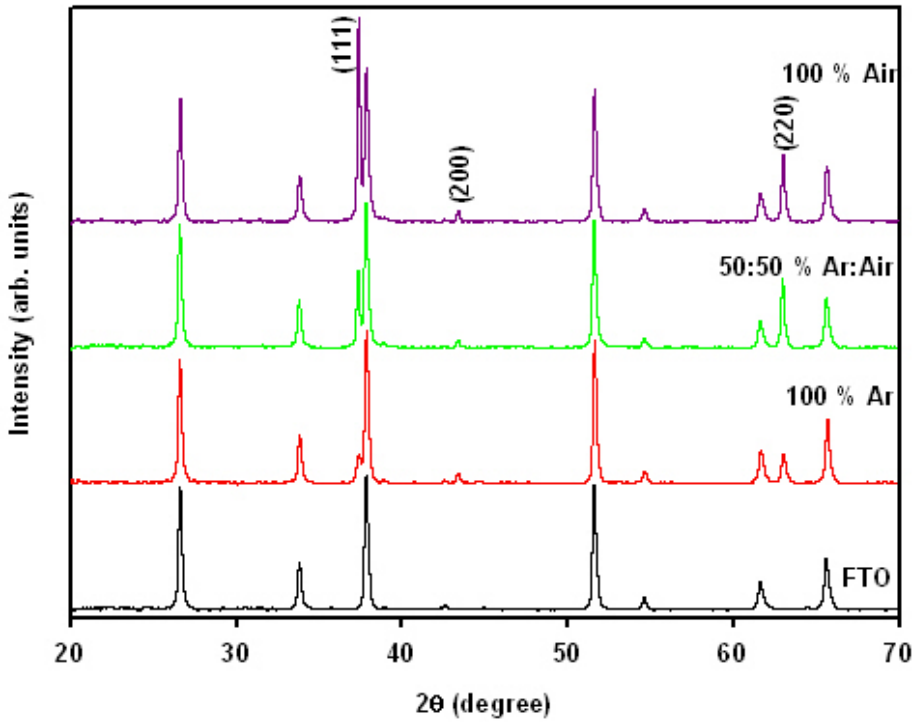

Fig. 4-21: The XRD reflection patterns of NiO films deposited using different ratio of carrier gas flow from 0.1 M solution in toluene at 475 °C.

The decomposition mechanism of the precursor in the deposition chamber of AACVD is always very complicated. The orientation, texture and morphology of the films can be controlled by altering the deposition parameters, which in other words affects the kinetics and thermodynamics of the deposition process. The dependence of preferred orientation on the substrate temperature and on the oxygen content can be explained as follows. In AACVD, the film growth starts with nucleation at the substrate surface. The nucleation and growth is directly dependent on the deposition parameters. The films deposited using toluene solvent and argon as a carrier gas are highly deficient of oxygen and the NiO films are only formed by using only oxygen from the precursor molecule. The films have (111) predominant orientation which is due to less oxygen content and intermediate decomposed material may have high surface energy. On the other hand, films deposited using methanolic solution and air as a carrier gas has a (200) predominant orientation which can be explained on the basis that

decomposition of the precursor due to high oxygen content and NiO formed with low surface energy. This trend is in agreement with other results (using different deposition techniques) reported in the literature [241].

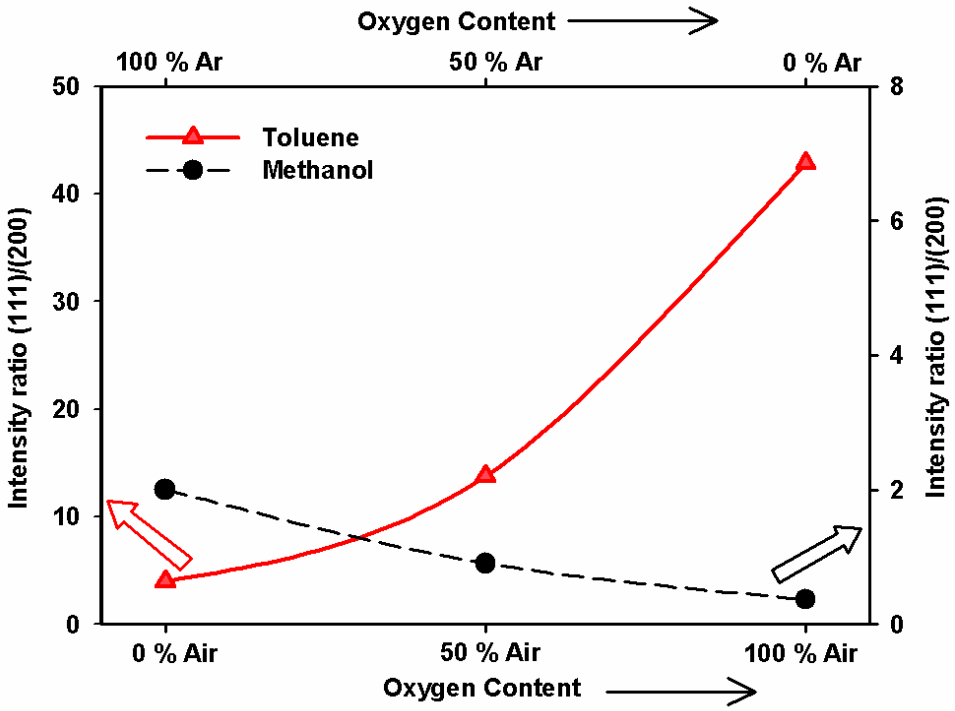

Fig. 4-22: Ratio of (111)/(200) with the increase in oxygen content of the deposition system.

Similarly, the deposition temperature also shows a strong effect on the preferred orientation of NiO films deposited from toluene as a solvent and air as a carrier gas. In the start of the deposition, at relatively low temperature, NiO along with partially decomposed precursor molecules adsorb on the substrate surface and nucleate in random orientations resulting in polycrystalline films. When the substrate temperature increases up to 450 °C or above the preferred orientation gradually changes from polycrystalline to the (111) orientation. At higher substrate temperatures, the deposition of the precursor may almost complete in the gaseous phase and only NiO particles adsorbed on the surface of the substrate and have enough energy to arrange themselves to the (111) orientation. This minimizes the surface free energy of growing NiO. Electrodes with controlled crystallographic orientation have previously been

deposited for bismuth chalcogenides [242] and ZnO [243] using AACVD by tuning the substrate temperature and carrier gas flow rate.

4.3.2 Surface morphology analysis

4.3.2.1 Effect of solvent and carrier gas

The surface morphology and thickness of the films was determined by using FEGSEM and the films deposited under different deposition conditions shows different morphologies. The surface topography of the films deposited using toluene or methanol as solvent and air or argon as a carrier gas are shown in Fig. 4-25 and respective FEGSEM cross-sections are given in Fig. 4-26.

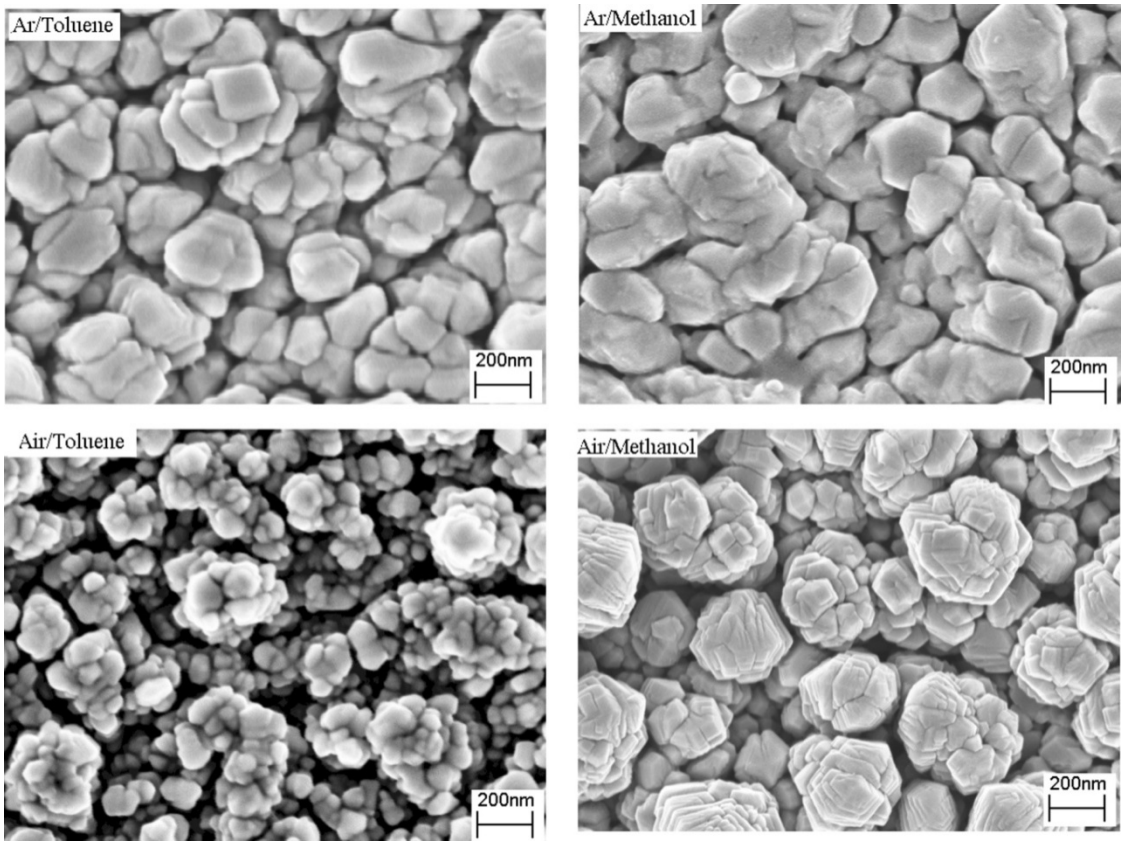

Fig. 4-23: The FEGSEM surface topography of NiO films deposited using Ar and Air as carrier gas using 0.1 M solution in toluene or methanol at 400 °C.

The film densities were not measured. FEGSEM imaging (Fig. 4-25) indicated that films deposited using argon as a carrier gas had the lowest porosity and those deposited using air have comparatively more porosity. FEGSEM was also used to examine the film microstructures. It was observed that changing the deposition conditions dramatically changed the surface microstructure of the film. Fig. 4-25 also indicates that under similar deposition conditions, the film morphology depends upon the oxygen content of the system. The films deposited using argon as carrier gas showed an agglomeration of sub-micrometer particles. The particles acquired a particular shape with well-defined boundaries by replacing argon to air as a carrier gas.

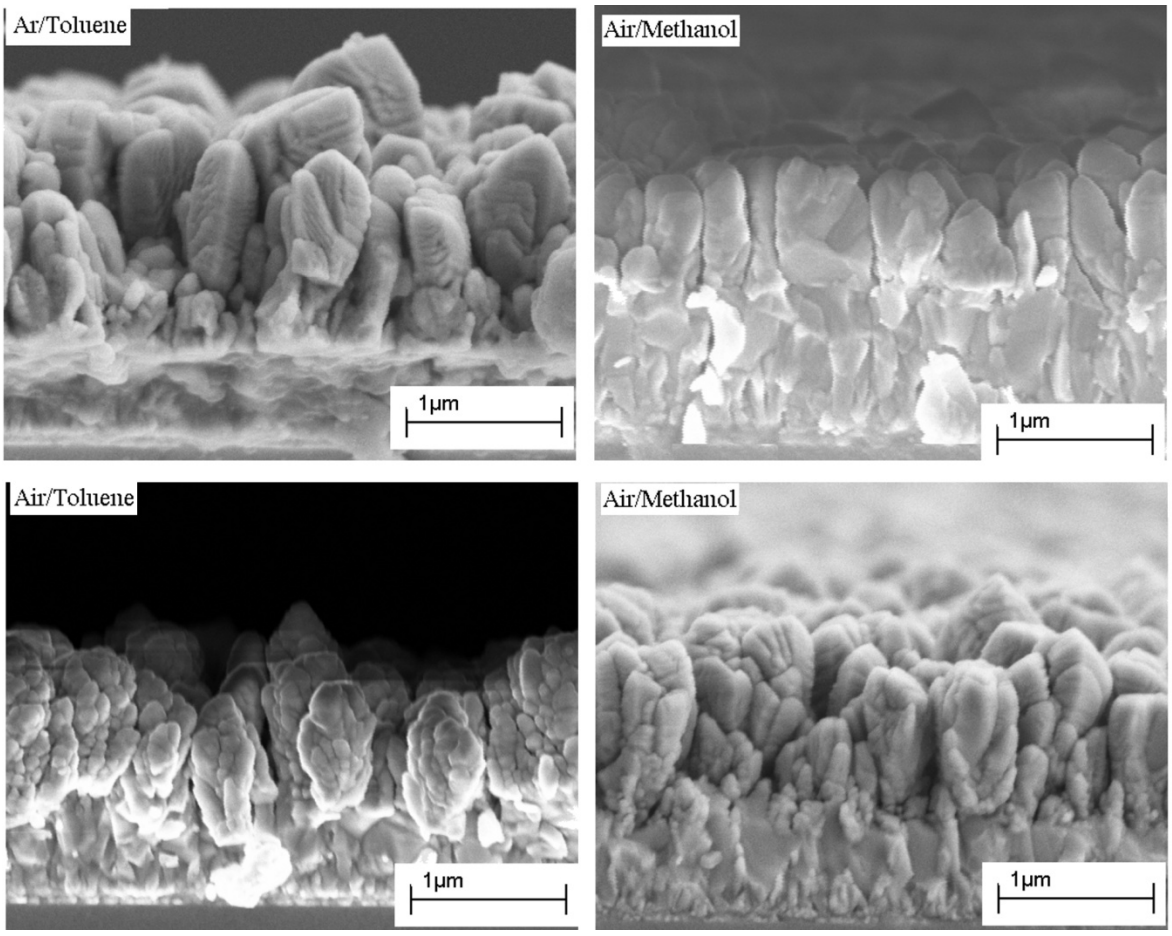

Fig. 4-24: The FEGSEM cross-section of NiO films deposited using Ar and Air as a carrier gas using 0.1 M toluene or methanolic solution at 400 °C.

Similarly, the particle size also changed with the change in oxygen content of the deposition system. Films deposited using air/toluene have particles with size ranging from 15 – 20 nm, while the films deposited from air/methanol system have particle sizes in the range of 35 – 50 nm, which is larger than the air/toluene system. The films deposited Ar/methanol system had a structure somewhere between that of Air/toluene and that of Air/methanol system, while the film deposited from Air/methanol system shows a large cubic crystallites sintered together to form agglomerated structures growing perpendicular to the substrate surface.

4.3.2.2 Effect of temperature

The temperature of the substrate also affects the film morphology and could also be used as a process parameter for controlling the morphology of the NiO film [243]. The effect of temperature on the morphology of the films was studied by depositing films using air as a carrier gas and toluene as a solvent at different substrate temperature. The FEGSEM images in Fig. 4-27 prove the change in films morphology with the change in substrate temperatures.

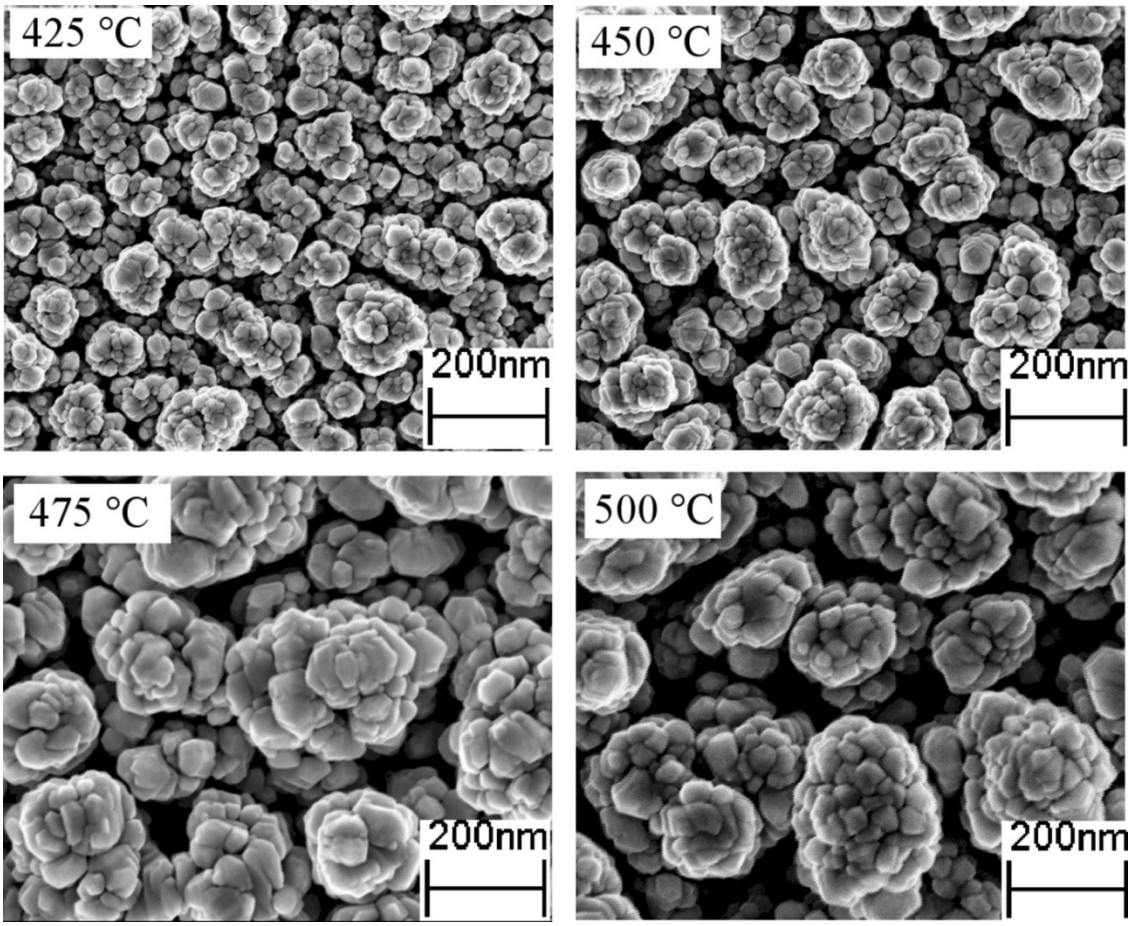

Fig. 4-25: The FEGSEM surface topography of NiO films deposited at 425-500 °C using 0.1 M solution in toluene and air as a carrier gas.

For the granular branched tree structure (cross-section), the precursor molecules were deposited from the aerosol-phase to the substrate and underwent decomposition without any restructuring once deposited. The branched tree structure become a fractal columnar structure with the increase in temperature from 400 °C to 450 °C and the surface morphology of the films became an arrangement of bundles of nanoparticles in flower shape. At this temperature NiO nanoparticles underwent further restructuring and adopted columnar structure with flower-like surface morphology. At relatively higher substrate temperatures (475 °C to 500 °C), we assume that the precursor in vapour-phase was completely decomposed, resulting in the deposition of particles rather than vapour-phase precursor. Thus, the deposition regime shifted from a vapour-particle mixed regime to a particle-dominant regime, and the

morphology changed from fractal columnar structures to well-developed columnar structures (Fig. 4-28).

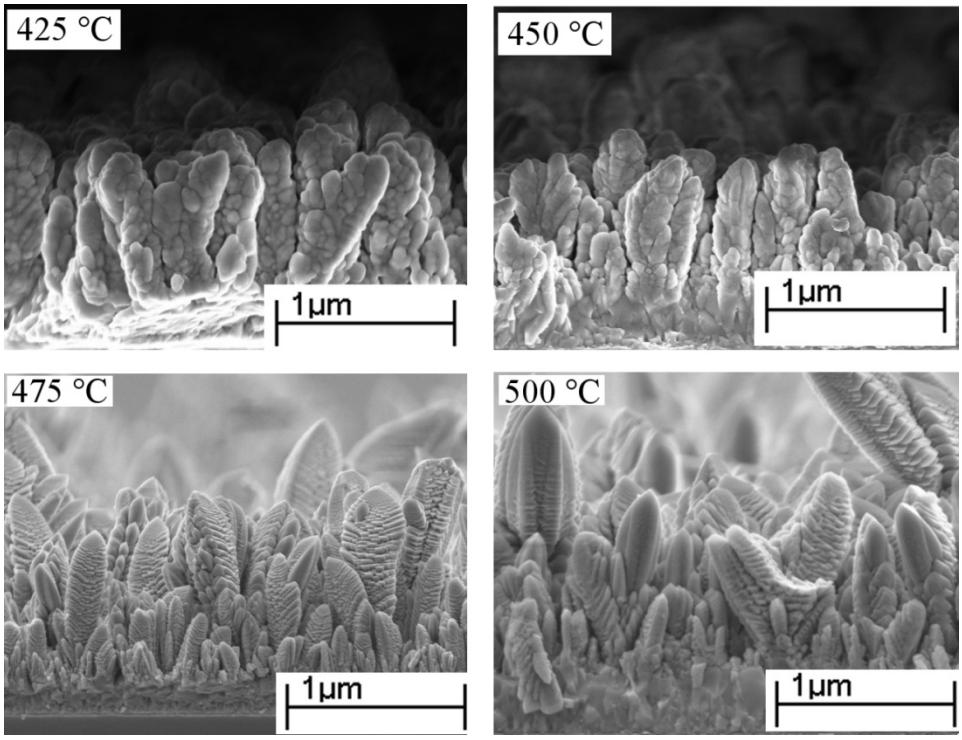

Fig. 4-26: The FEGSEM surface topography of NiO films deposited at 425-500 °C using 0.1 M solution in toluene and air as a carrier gas.

Previous studies showed that the nanorod and columnar structures based films in DSC's have charge transport "tens to hundreds of times faster" than the films with nanoparticles structure [244]. The preferred (111) orientation and columnar structures of the films fabricated at 475 °C makes it a promising photocathode for PEC and DSCs applications. The particle size increases with increase in deposition temperature as shown in Fig. 4-29. Further increase in deposition temperature cannot be achieved due to the stability of FTO at elevated temperature.

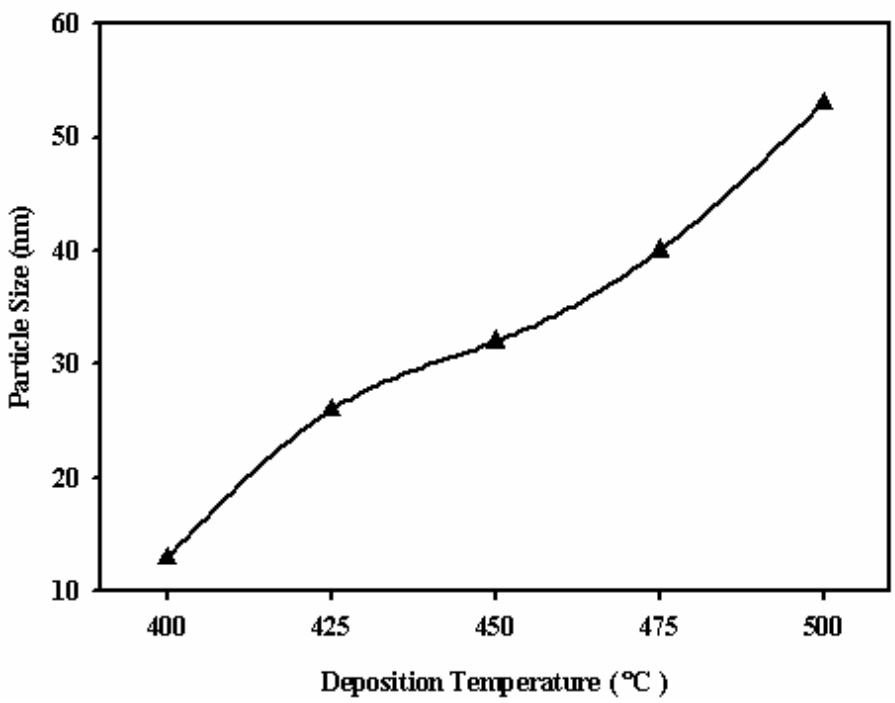

Fig. 4-27: The effect of temperature on particle size of the films deposited using 0.1 M methanolic solution and air as a carrier gas.

The growth rate of NiO electrodes was determined by depositing films under same conditions for different deposition times. Films were deposited for times ranging from 10 to 40 min and thicknesses of the electrodes were calculated from cross sectional FEGSEM images. Fig. 4-30 shows that the films thickness increased smoothly with increase in deposition time. An average deposition rate of 34 nm/min was calculated from the thickness of the films deposited at different deposition times, which shows great control over deposition of NiO electrode through AACVD.

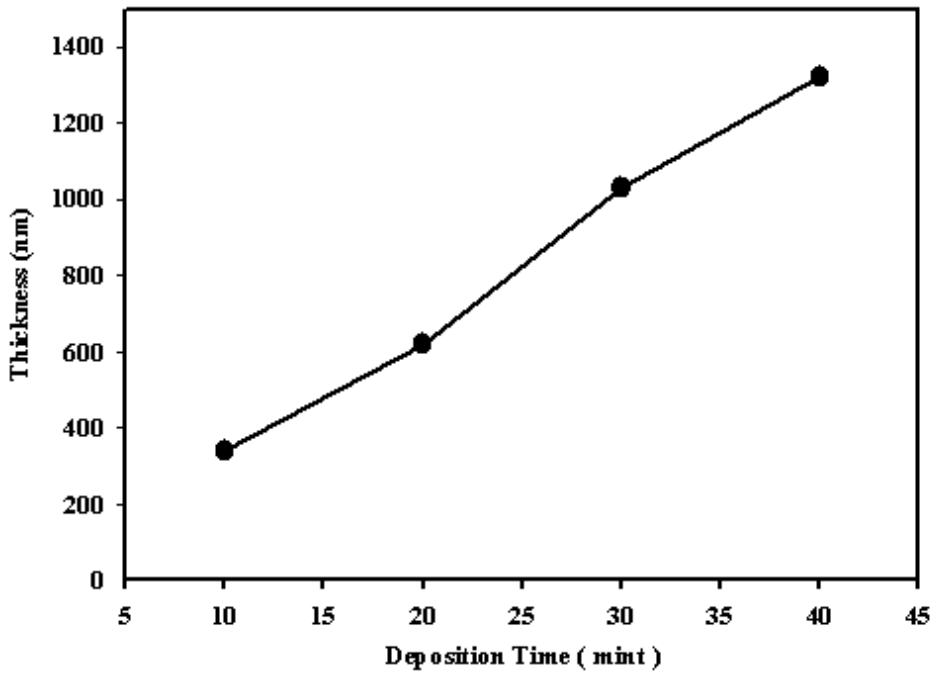

Fig. 4-30: The effect of deposition time on thickness of the NiO films deposited using 0.1 M methanolic solution and air as a carrier gas.

4.3.3 Capacitance analysis

Cyclic voltammograms of nanostructured NiO in aqueous electrolyte (0.2 M $Eu(NO_3)_3$) were measured in a three electrode setup under dark condition at different scan rates. Typical CVs for the electrode prepared at 475 °C are shown in Fig. 4-31 (a).

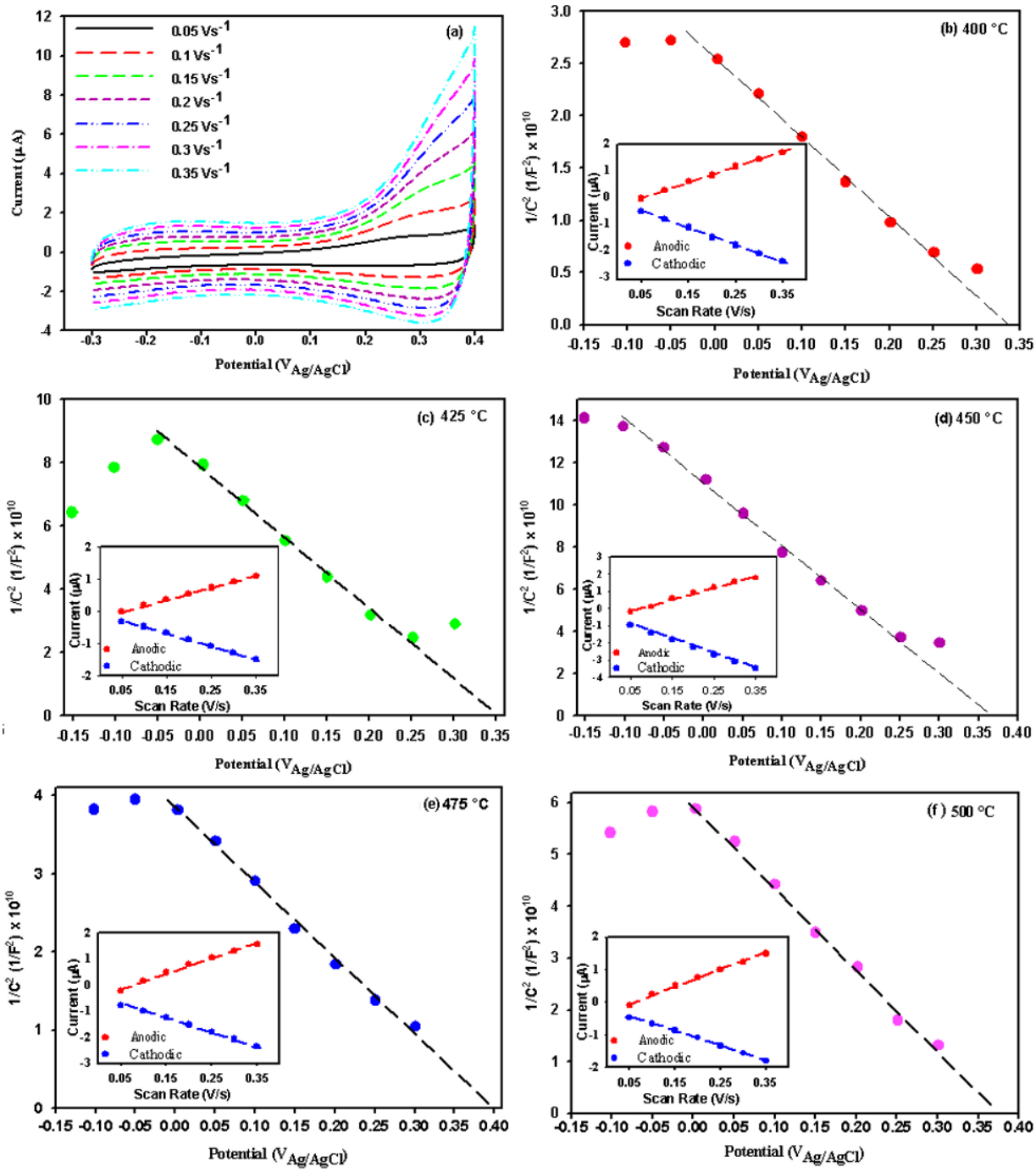

Fig. 4-28: (a) Voltammograms of NiO electrode deposited at 475 °C using 0.1 M solution in toluene and air as a carrier gas measured in 0.2 M $Eu(NO_3)_3$ electrolyte. Scan rates are 0.05, 0.1, 0.15, 0.2, 0.25, 0.3 and 0.35 V s^{-1}. (b-f) Mott−Schottky plot constructed using capacitance data calculated from slope of anodic lines of current vs. scan rate at each potential. Inset; current vs. scan rate plot demonstrates one example for both cathodic and anodic currents at -0.05 V vs. Ag/AgCl/3 M KCl.

The potential range is such that the NiO films are always under depletion conditions; i.e., the applied potential is more negative than the flat band potential (V_{FB}). An intriguing feature of these CVs are that the current is an approximately linear function of the applied potential in the directions of both the forward and the reverse scans. Furthermore, the current at a given potential is linearly dependent on the scan rate (see insets of Fig. 4-31(b-f)). The CVs of NiO electrodes prepared by AACVD in the current work shows no peak due to electrochemical reaction as compared to the previous studies by Boschloo *et al*. [245]. In their study, CVs of NiO films prepared by heating $Ni(OH)_2$ sol-gel shows two strong oxidation reduction peaks due to the conversion of Ni^{II} to Ni^{VI} in (0.2 M KCl + 0.01 m KH_2PO_4 + 0.01 M K_2HPO_4) aqueous electrolyte. The absence of peak due to any electrochemical reaction indicates that the origin of the current is capacitive.

Mott-Schottky plots (Fig. 4-31(b-f)) were constructed using capacitance data calculated from CV measurements. In the absence of interfacial redox reactions, the scan-rate (n) dependence of current can be attributed to charging and discharging of the space charge layer. The CVs collected for a series of scan rates were obtained from plotting the current (i) versus scan rate (n) at selected applied potential. The slope of the line in such a plot is a measure of space charge layer capacitance (C_{SC}) at each potential. The data from the backward scans of the CVs in Fig. 4-31(a) are used to calculate the capacitance, which is presented in a Mott−Schottky plot (i.e., C^{-2} vs V) in Fig. 4-31(b-e). The flatband potential (V_{fb}) is an important characteristic for predicting the PEC properties. From the Mott-Schottky results shown in Fig. 4-31, the flatband potential was estimated by extrapolating the linear part of the Mott−Schottky plots. The flatband potential calculated from Fig. 4-31 agrees with the photocurrent onset potentials (inset of Fig. 4-31).

In energetic terms, the V_{FB} of a semiconductor is an indication of the position of the conduction and valence band energies relative to a reference energy scale or to a redox energy level in the electrolyte. Interactions with the electrolyte depend on the chemical nature of the semiconductor surface, which depends in part on crystallographic termination and V_{FB} can be changed by altering the surface dipole potential [246]. Fig. 4-32 shows the dependence of NiO V_{FB} in 0.2 M $Eu(NO_3)_3$ electrolyte on the relative intensity ratio of (111)/ [(111)+(200)].

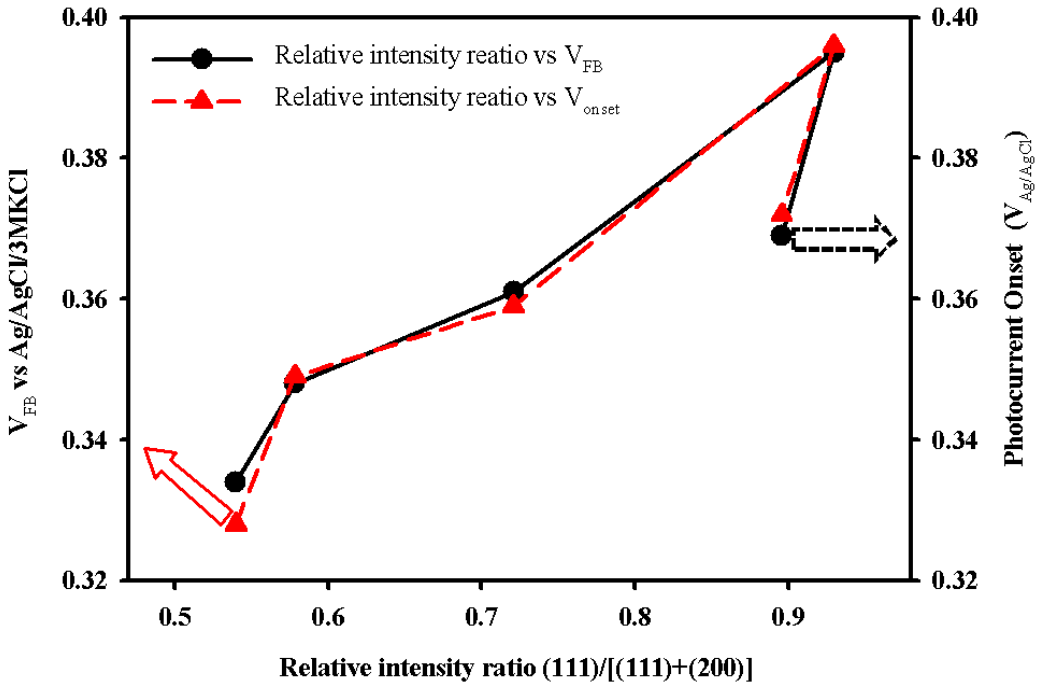

Fig. 4-29: Flat-band potential and photocurrent onset vs. the relative ratio of (111)/ [(111)+(200)] orientation in 0.2 M $Eu(NO_3)_3$ electrolyte.

At low deposition temperatures (400 ^{o}C), the relatively small (111)/ [(111)+(200)] intensity ratio suggest that NiO is preferentially oriented in the (200) plane. According to Fisher [247], the surface of the (200) crystal plane of NiO is a Type I surface in Tasker's scheme [248] which is electrostatically neutral and formed with stoichiometric ratio. As the deposition temperature is increased, the (111)/ [(111)+(200)] intensity ratio gradually rises towards a maximum at 475 ^{o}C, suggesting that NiO is preferentially oriented in the (111) plane, which is a Type III surface in Tasker's scheme. The non-stoichiometric NiO oriented in (111) plane is electrostatically polar and has a dipole moment in the repeat unit perpendicular to the surface. The charged surface of (111) oriented films attract more ions towards the surface and help to ease the redox reaction and should reduce the external bias required to obtain the optimum conditions for PEC water splitting.

4.3.4 Optical absorption analysis

The UV-Vis absorption spectra for NiO electrodes deposited at 475 °C for different deposition time are given in Fig. 4-33.

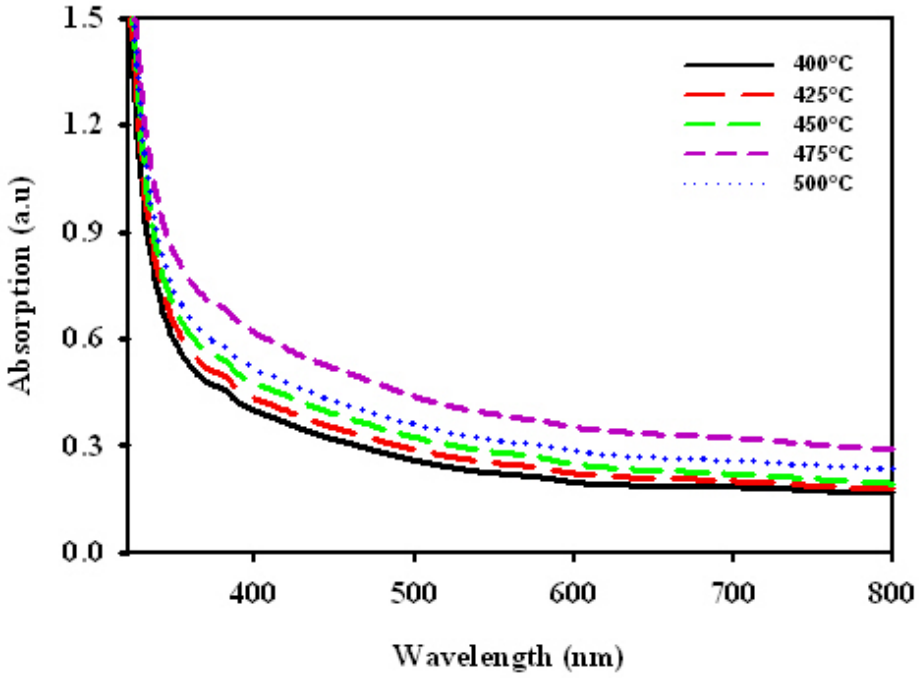

Fig. 4-30: UV-Vis absorption spectra of NiO electrodes deposited at different temperatures.

A strong absorption in the UV range can be attributed to the NiO band gap absorption and the optical band gap energy is determined from the UV-Vis absorption spectra by plotting $(\alpha h\upsilon)^2$ verses photon energy $(h\upsilon)$ (Fig. 4-34), where α is the absorption coefficient, h is Planck's constant and υ is the frequency of the light, and then extrapolating the linear portion of the curve to zero.

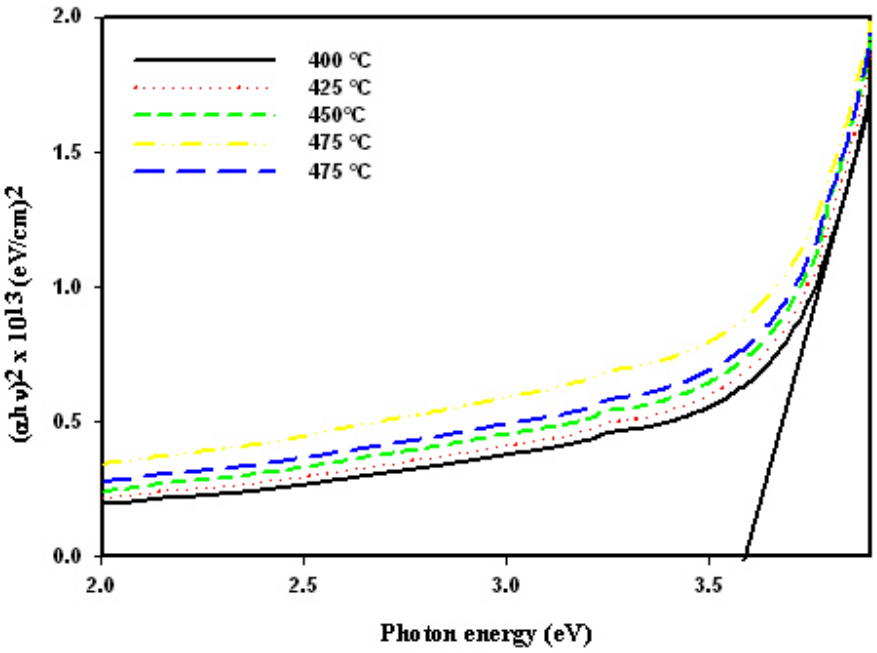

Fig. 4-31: Plot of $(\alpha h\upsilon)^2$ versus $h\upsilon$ of CuI electrodeposited at different temperature.

The linear relation observed for the $(\alpha h\upsilon)^2$vs. $h\upsilon$ plot in the high energy region suggests that the NiO nanostructure is direct band gap semiconductors. The long tail of the absorption spectra observed in the long wavelength region can exist due to the scattered radiation of nickel oxide nanostructure. The estimated band gap energy, 3.65 eV, is in agreement with the band gap reported for NiO (3.6−4.0 eV) [249]. As the films are deposited under similar conditions the crystallinity of the NiO films remains the same and only varies in thickness and in principle, the optical absorption edge and band gap should remain the same. The unchanged absorption edges corresponding to the variation in the film thickness are showing the stoichiometric nature of the films grown by AACVD method.

4.3.5 Current-voltage analysis

The *J*-V plots for NiO electrodes deposited at different temperature are shown in Fig. 4-35(a-e). The current-voltage characteristics under illumination clearly show *p*-type (cathodic) behaviour for NiO electrode. Fig. 4-35(f) shows the influence of the deposition temperature on the photocurrent behaviour. As the deposition temperature increases, up to 475 °C, the photocurrent gradually increases and then decreases with further increase in deposition temperature up to 500 °C. We attribute this decrease in photocurrent density to the increase in particle size and compactness of the film. The J^2-V curves in the insets of Fig. 4-35(a-e) show a shift of photocurrent onset towards more positive potentials with the increase in deposition temperature. The shift is more pronounced for the films deposited at 475 °C (Fig. 4-35(d) inset). The positive shift of the photocurrent onset is due to the preferred (111) plane orientation of the crystallites as well as to the morphology of the electrodes. It seems that the textural properties as well as the degree of crystallographic preferred orientation are the key factors in defining the light harvesting properties.

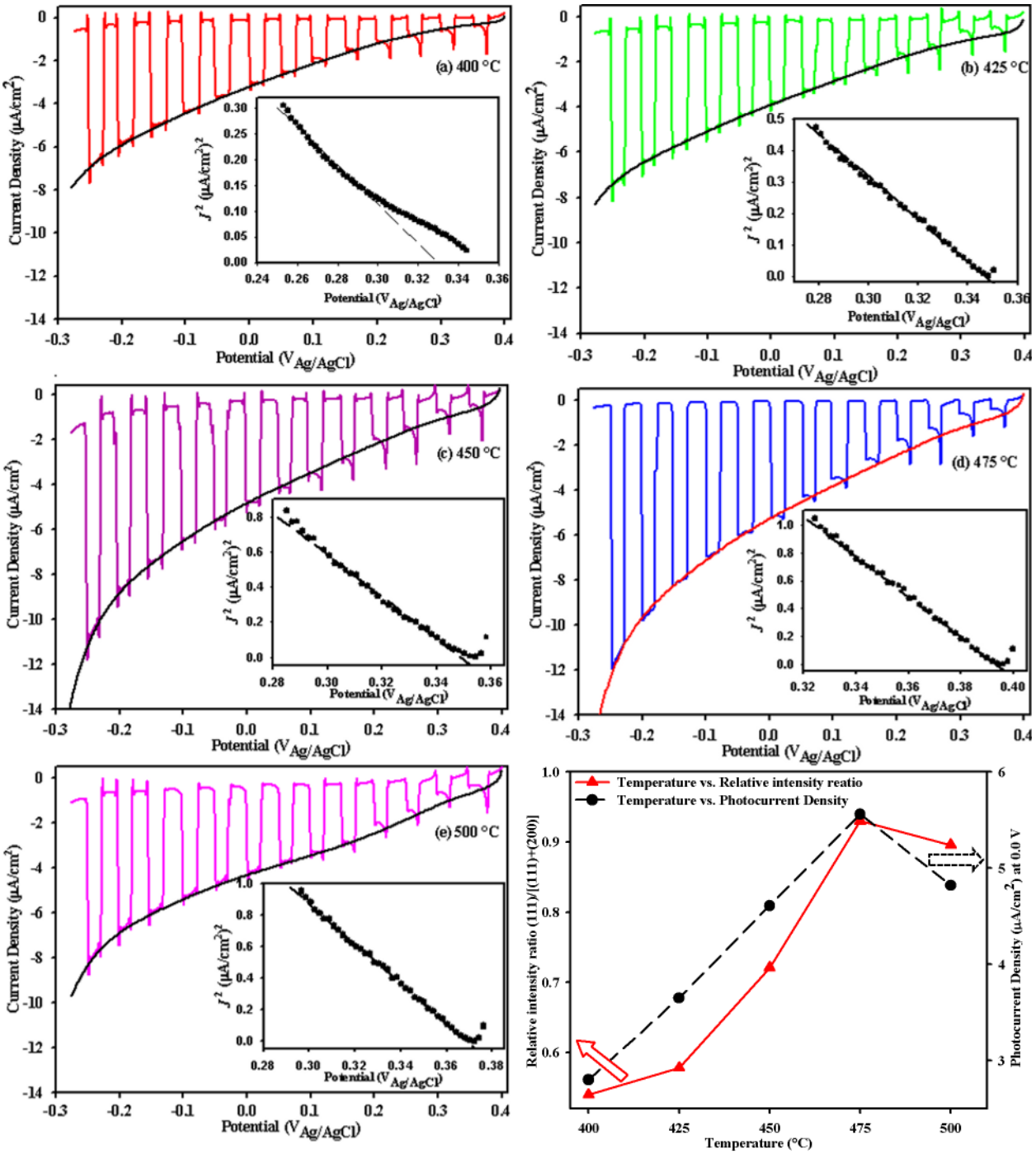

Fig. 4-32: (a-e) Current–voltage characteristics for NiO electrodes deposited at different temperature using 0.1 M solution in toluene and air as a carrier gas. Inset: (a-e) J^2- V plot showing the estimated photocurrent onset potential. (f) Effect of temperature on the photocurrent density. The light was manually chopped to reveal photocurrent and dark current simultaneously.

For comparison, the steady-state *J-V* plots were superimposed on the transient plot in each case. Steady-state and transient *J-V* plots agree well for all electrodes. Generally negligible amount of dark current was observed for all the electrodes in 0.2 M $Eu(NO_3)_3$ electrolyte as compare to the earlier report on NiO [250]. We attributed this to the better quality and complete coverage of FTO surface with NiO for the films deposited by AACVD since the generation of dark current is considered to be a result of incomplete surface coverage of the substrate surface [31]. The electrode deposited at 400 °C is the weakest electrodes in term of PEC performance (Fig. 4-35(a)) and has highest recombination. The transient photocurrent pulses acquire desirable squarer shaped indicating a decrease in recombination with an increase in deposition temperature. In all cases the recombination is relatively high in the positive applied potential region where the space charge width is relatively narrow.

The best NiO photoelectrode is the one prepared at 475 °C having photocurrent density about 5.5 μAcm^{-2} at 0.0 V (vs Ag/AgCl/3 M KCl) under AM1.5 illumination which is the highest reported so far. We attribute this to preferred orientation along the (111) plane. Along with the preferred crystallographic orientation the columnar shaped growth of NiO structures vertical to the substrate also enhanced the transport of the electron. It is well known that the charge transport is "tens to hundreds of times faster" in nanorods and columnar electrodes [251]. For comparison, the photocurrent densities of other electrodes were recorded at the same applied potential (0.0 V vs Ag/AgCl/3 M KCl) and plotted against temperature as shown in Fig. 4-35(f). This suggests that the light harvesting properties of NiO photoelectrodes depend on the fabrication condition which is directly related to the morphology and preferred orientation of electrodes [252].

4.3.6 Incident Photon to Electron Conversion Efficiency (IPCE)

Since the photocurrents produced by NiO electrodes were very small it was very difficult to obtain any measureable IPCE. In order to study the efficiency of the NiO electrode, a DSC cell was constructed and the efficiency of the cell was considered representative of the efficiency of the NiO. The IPCE studies were conducted by sensitizing all electrodes with C343 dye by soaking for 24 h and the electrodes showed impressive improvement which meant that the electrode was suitable to be applied to DSC and semiconductor solar cells. The performance result of the NiO-DSC, such as photocurrent and IPCE, are reported as follows.

4.3.6.1 Application of the NiO electrode to DSCs

To assess the suitability of the above NiO electrodes in the fabrication of dye-sensitized solar cells, we used the coumarin C343, since it proved to be one of the best performing sensitizer among the commercially available dyes and also for straightforward comparisons with other reported *p*-type DSCs [246,253-255]. Dye-sensitized solar cells were constructed using NiO electrodes deposited at different temperatures with thickness of about ~ 1 μm. Sandwich-type solar cells were assembled using C343-sensitized NiO as the working electrode, platinum conducting glass as the counter electrode, and 1.0 M LiI/0.1 M I_2 in acetonitrile as the electrolyte. The open circuit photovoltage (V_{OC}), the short circuit photocurrent (J_{SC}), fill factor (*FF*) and the overall photoconversion efficiency (η) were measured as a function of (111) orientation of the NiO film controlled by deposition temperature. The *J*−*V* characteristics for these solar cells are presented in Fig. 4-36.

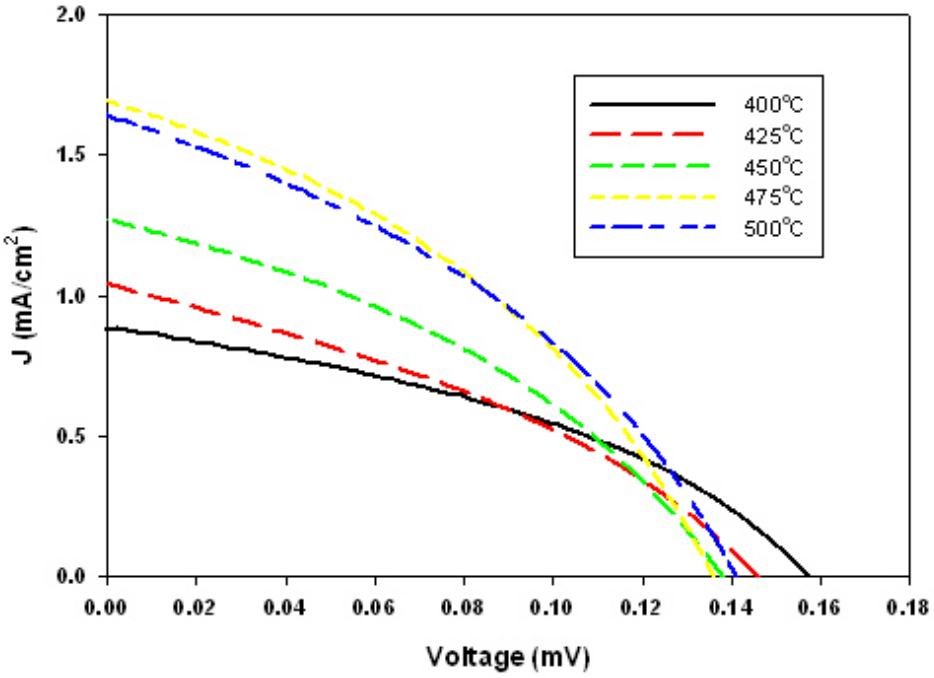

Fig. 4-33: *p*-DSCs characteristics of NiO electrodes deposited at different temperature measured under AM1.5 (1000 Wm^{-2}) illumination. The highly (111) oriented columnar structured NiO electrodes fabricated at 475 °C showed best DSC performance.

The open circuit photovoltage (V_{OC}), the short circuit photocurrent density (J_{SC}), fill factor (*FF*) and efficiency (η) of the electrodes increased with an increase in deposition temperature and the highly (111) oriented films deposited at 475 °C exhibited the highest V_{OC} (135 mV), J_{SC} (1.69 mAcm^{-2}) *FF* (38%) and η (0.087%) reported for C343 sensitized NiO-based solar cells [255-258]. We attribute the increase in V_{OC} and *FF* to the (111) orientation of NiO electrodes which increases with an increase in temperature. The morphology, which consists of interconnected networks of NiO columnar structure, certainly provides an efficient transport of the injected holes to the back conductive FTO electrode. But, most importantly, the preparation of the NiO electrodes by AACVD method is more controllable and reproducible, a feature which is not shared by the other electrode fabrication techniques such as doctor blade.

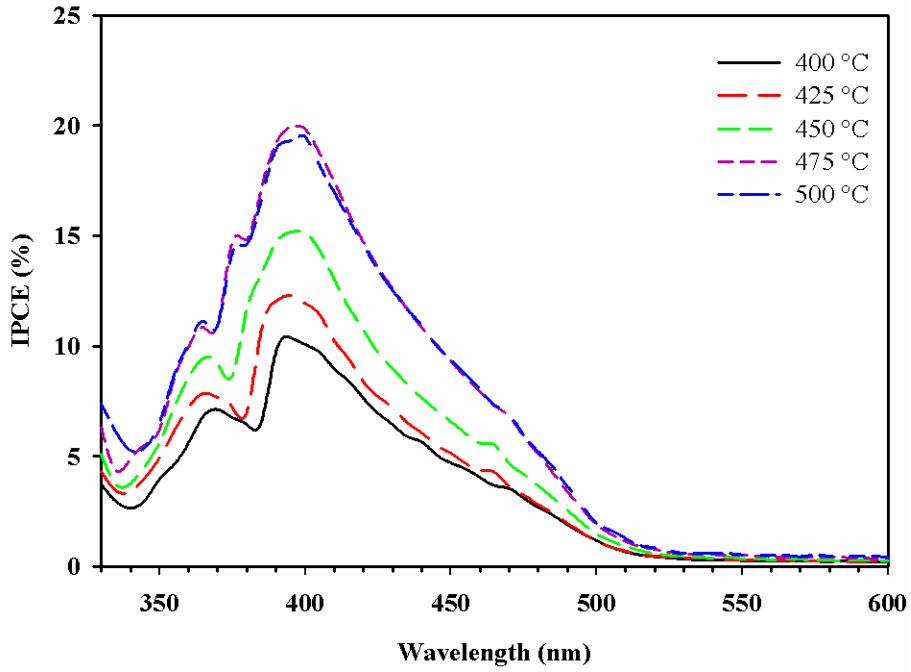

Fig. 4-34: Incident photon-to-current conversion efficiency (IPCE) spectra of C343 for NiO electrode deposited at different temperatures. The highly (111) oriented NiO electrodes grown at 475 °C showing maximum IPCE. Platinum-coated conducting glass (fluorine-doped tin oxide) was used as a counter electrode.

The incident photon-to-current conversion efficiency (IPCE) value also increases with an increase in the (111) orientation controlled by the deposition temperature and the maximum IPCE value of 20 % was obtained for the cell fabricated from the electrode deposited at 475 °C (Fig. 4-37). Significant improvement in the IPCE values are observed from AACVD deposited NiO compared to earlier reports. In comparison with previously reported *p*-type DSCs, high IPCE values were obtained [256,258,259]. The IPCE and other cell parameters given in Table 4-4 are the highest among the reported to the best of our knowledge, for the C343 sensitized NiO *p*-type DSCs. The photovoltaic performances of the solar cells made with these oriented NiO films are higher than those prepared with other techniques. We believe that this new fabrication method of orientation controlled NiO electrodes will be useful for investigating new sensitizers and new electrolytes to design and construct more efficient *p*-DSCs and tandem cell devices.

Table 4-4: IPCE and other cell parameters for NiO DSC.

NiO	V_{oc} **(V)**	J_{SC} **(mAcm^{-2})**	**Fill factor** ***FF***	**Efficiency (%)**	**IPCE (%)**
400 °C	0.157	0.88	0.40	0.055	10.5
425 °C	0.145	1.04	0.36	0.054	12.4
450 °C	0.137	1.27	0.38	0.066	15.3
475 °C	0.135	1.69	0.38	0.087	20.1
500 °C	0.139	1.64	0.38	0.087	19.5

4.4 Conclusions

The preparation and characterisation of two different *p*-type semiconductor materials namely CuI and NiO were discussed in this chapter. They were selected on the basis of their

suitability in solar cell applications as photocathodic materials. The deposition of wide band gap CuI photocathode was successfully achieved by conducting electrodeposition (continuous and pulsed) and AAD method. NiO was also prepared by AACVD method. By altering the surface morphology, porousity, individual particle size of these materials the optical and photoelectrochemical properties of these electrodes were optimised. *p*-NiO is also a very promising cathodic semiconductor electrode material. With further studies, these materials could be used in development of cathodic semiconductor solar cells (CSSC) and solid state cathodic semiconductor solar cells (SS-CSSC). Studies of such solar cells are reported in the following chapters.

Chapter 5: Experimental Results of Photoelectrochemical Cathodic Semiconductor Solar cells

5.0 Photoelectrochemical Cathodic Semiconductor Solar Cells (CSSC)

This chapter presents the characterisation of photosensitised cathodic semiconductor photoelectrodes. Here, the cathodic wide band gap porous electrodes of *p*-CuI and *p*-NiO were photosensitised by incorporating a thin light absorber-layer of *p*-Cu_2S on the surface. The construction of such photosensitised cathodic electrodes is relatively cheap and easy to fabricate. The PEC properties of the CSSC were carried out in both Eu^{3+}/Eu^{2+} and I_3^{-}/I^{-} redox electrolytes.

5.1 FTO/*p*-CuI/Cu_2S photoelectrode

In general, most of the studies conducted to date on PEC solar cells have been centred on semiconductor photoanodes (*n*-type) as the active photoelectrode. Typically, an electroactive cathode such as Pt, C or Au has been used to complete the construction of such cells. When attention was recently turned to new solar cell configurations that are capable of harvesting sunlight beyond the Shockley-Queisser limit for the theoretical maximum efficiency of a single band gap solar cell, work started on incorporation of two photoactive electrodes into a single solar cell (i.e. Tandem solar cell). Such novel concepts led to the renewed interest on development of semiconductor photocathodic materials. With the concept of tandem cells, researchers have been focusing on finding photoactive semiconducting cathodic materials which can be replaced with traditional electroactive cathodes in PEC cells. However, until now, only a few studies have been reported on the sensitization of *p*-type semiconductors due to difficulties such as unavailability of photocathodic semiconductor materials with desired physical and chemical properties and poor stability of known photocathodic semiconductors.

In the present study, *p*-CuI electrodes were used as photoactive wide band gap semiconductor electrodes enabling facilitation as a support for light harvesting materials as well as a hole-collecting phase. *p*-CuI electrodes have been sensitised with Cu_2S. By combining such photosensitised electrodes with a suitable kinetically fast enough electron scavenging redox couple (i.e. Eu^{3+}/Eu^{2+}) construction of CSSC has been completed [260]. Our studies have been focused on optimising various cell components. For example, this study paid particular attention to different deposition times of the Cu_2S photosensitizer on the surface of porous *p*-CuI electrode. PEC performance of such electrodes was compared against that of the bare *p*-CuI electrodes reported in Chapter 4. Here, the samples are referred to as CS-1, CS-2, CS-3, CS-4 and CS-5 which corresponds to 1, 2, 3, 4 and 5 minutes deposition time of Cu_2S respectively as shown in Table 5-1. The AAD and AACVD methods were employed to prepare *p*-CuI and Cu_2S layers, respectively.

Table 5-1: The deposition times of CuI and Cu_2S in the making of photoelectrochemical CuI/Cu_2S CSSC.

Sample	**Deposition Time of CuI (min)**	**Deposition time of Cu_2S (min)**
CS-1	40	1
CS-2	40	2
CS-3	40	3
CS-4	40	4
CS-5	40	5

5.1.1 X-ray Diffraction (XRD) analysis

Fig. 5-1 shows the XRD patterns of bare FTO, the Cu_2S sensitizer and CuI deposited on FTO substrate in the range of 20-60° (corresponding to sample CS-4).

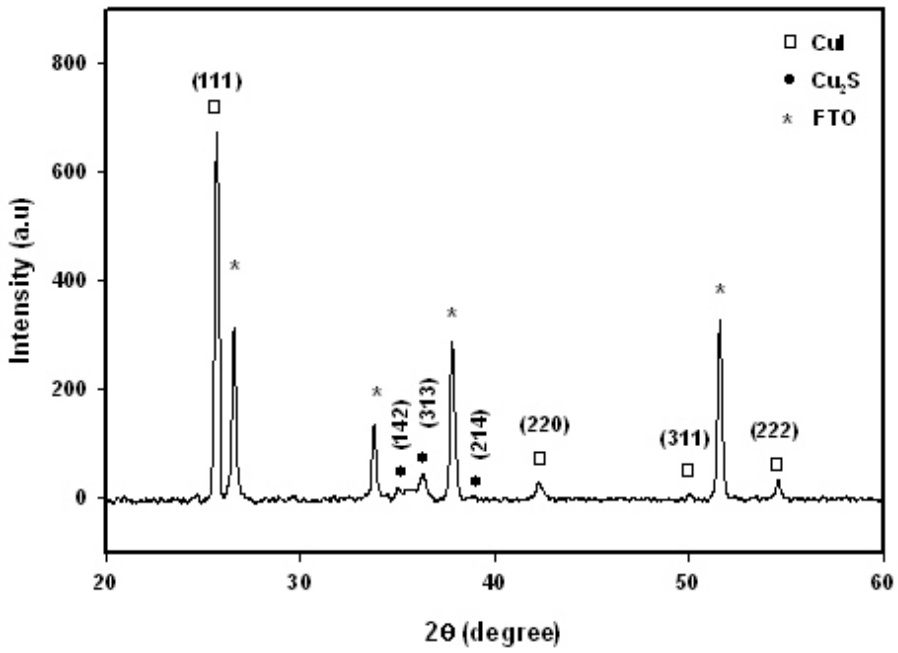

Fig. 5-1: X-ray diffraction patterns of 4 min deposition time Cu_2S on porous *p*-CuI electrode (CS-4).

The CuI consists of face-centred cubic (fcc) structure with γ-phase. As discussed in Chapter 4, the preferred orientation for CuI is along the (111) direction at 25.6°. Similar data were also reported by B.R. Sankapal *et al*.[226]. The deposition of Cu_2S photosensitisizer on *p*-CuI (using the precursor already employed in the literature) caused new XRD reflection peaks in the spectra [75]. The new reflections corresponding to Cu_2S show hexagonal chalcocite crystal structure. However, still the diffraction patterns were largely dominated by the reflections of *p*-CuI and FTO, presumably due to their highly crystalline nature and the relatively high layer thickness (compared to that of Cu_2S). The three small reflections at 35.5°, 35.7° and 38.8° correspond to the (142), (313) and (214) reflections of Cu_2S, respectively. The overall crystallite sizes of Cu_2S were estimated according to Scherer equation and it is found that the crystallite size varies within the range of 18 and 34 nm which were calculated using FWHM of highest peak at 36.5°. These values are much smaller than the literature values reported for Cu_2S films prepared by chemical bath deposition (~60 nm) [261]. The crystallite sizes of Cu_2S

at various thicknesses are recorded in Table 5-2. The results show that the crystallite size increases with increasing the deposition time.

Table 5-2: Crystallite particle size estimated by the strong peak of CuI and Cu_2S at various deposition times of Cu_2S.

Sample	**Strong Peak (°)**	**FWHM (°)**	**Estimated crystallite size (nm)**
CuI	25.6	0.173	49
CS-1	35.7	0.486	18
CS-2	35.7	0.456	19
CS-3	35.7	0.339	26
CS-4	35.7	0.265	33
CS-5	35.7	0.257	34

The diffraction patterns recorded for *p*-CuI/Cu_2S electrodes when the Cu_2S layer thickness is varied by altering the deposition time is illustrated in Fig. 5-2. The patterns show the reduction of preferred orientation of CuI in the (111) direction as the deposition time of Cu_2S is gradually increased. The reflections of Cu_2S become stronger with an increase of the deposition time indicating the incremental growth of Cu_2S on the surface of *p*-CuI.

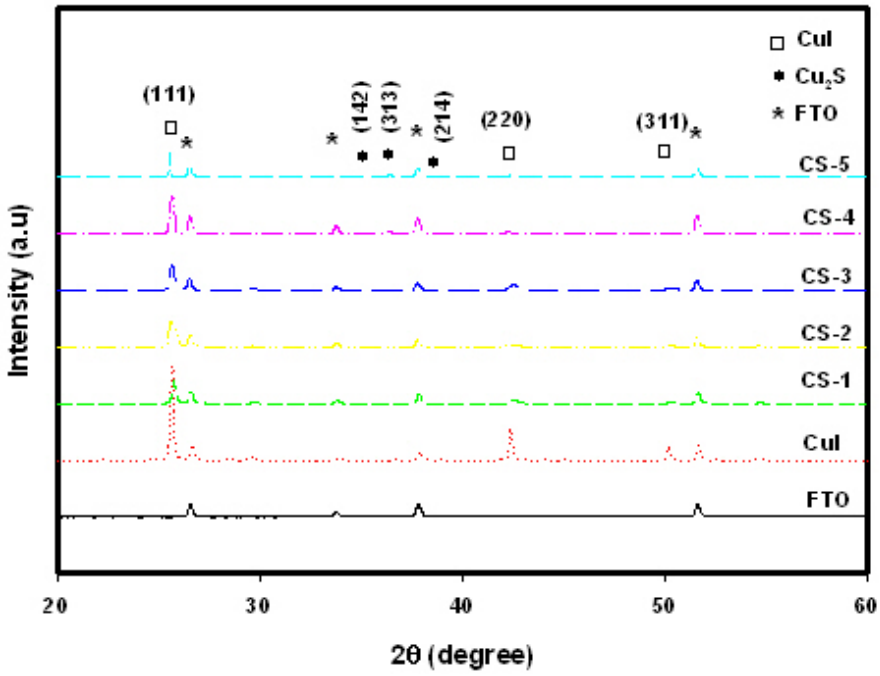

Fig. 5-2: X-ray diffraction patterns of *p*-CuI/Cu_2S electrodes recorded for different Cu_2S deposition times (a) FTO, (b) CuI, (c) CS-1, (d) CS-2, (e) CS-3, (f) CS-4 and (g) CS-5.

5.1.2 Surface morphology analysis

The surface morphology and cross-section of Cu_2S deposited on CuI thin films were studied using FEGSEM. FEGSEM images of the CuI electrodes prepared by AAD method are shown in Fig.5-3 (a) and the rest of the FEGSEM images correspond to various deposition times of Cu_2S on CuI electrodes (Fig. 5-3 (b-f)).

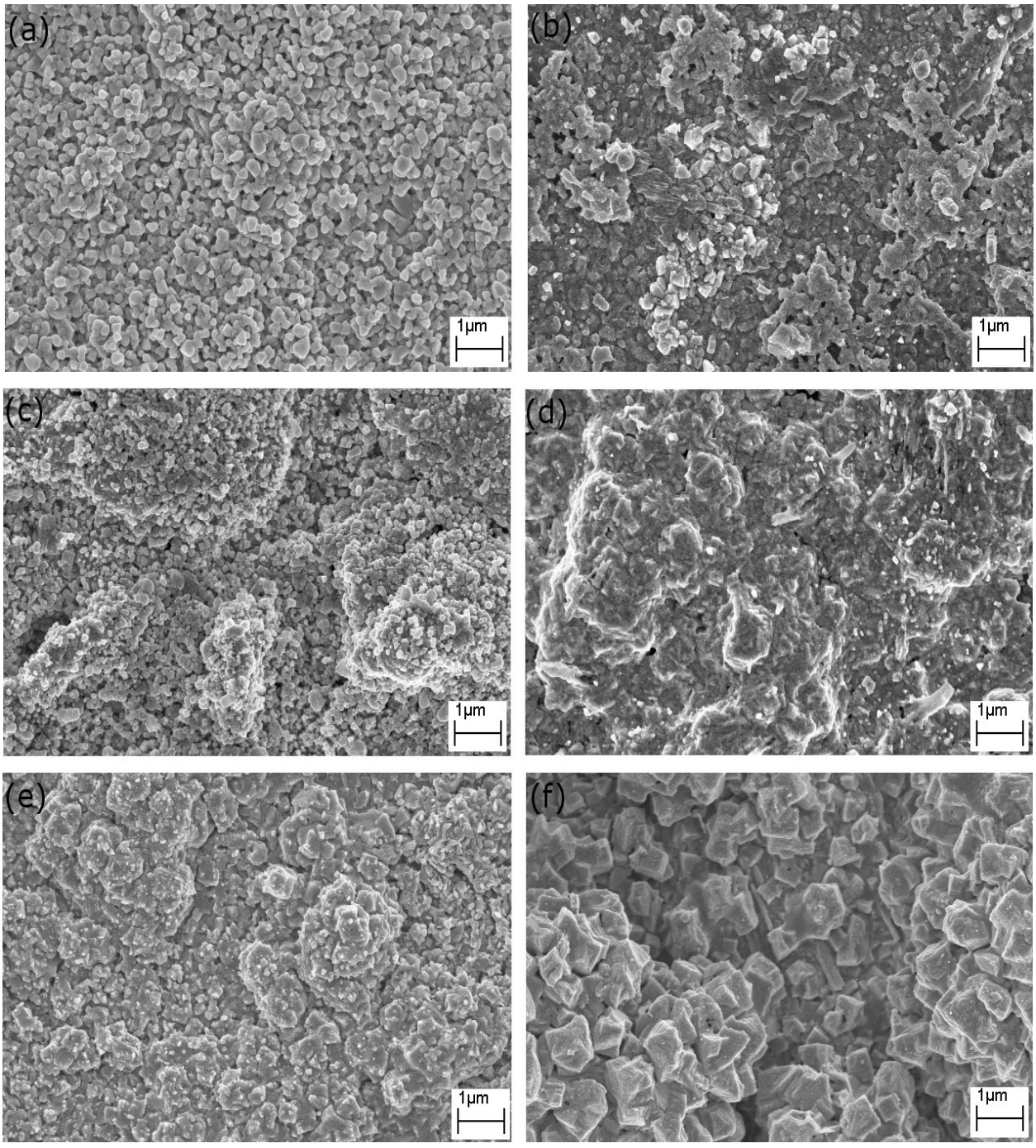

Fig. 5-3: FEGSEM images of bare *p*-CuI electrode and Cu_2S deposited on the CuI substrates corresponding to (a) CuI, (b) CS-1, (c) CS-2, (d) CS-3, (e) CS-4 and (f) CS-5.

As it can be seen from the FEGSEM images, the electrodes are reasonably uniform and relatively crack-free. The surface morphology of porous *p*-CuI electrode consists of fine particles forming a 3-D matrix as shown in Fig.5-3 (a). The nanoparticles have fused together and have grown in a vertical order. This causes formation of pores and clusters on the nano-scale. The individual CuI nano-particles show a good contact between each other. Having such good contacts between individual nanoparticles may result in an improvement in the charge transport properties leading to enhanced PEC performance in photoelectrochemical cell configurations [262]. *p*-CuI electrodes showed a highly porous nano-structure and large internal surface area which is desirable for a better coating of the sensitizing material. As discussed in Chapter 4, the average nano-particle diameters were estimated from the FEGSEM measurement of CuI electrode for 30 min deposition is about 110 nm. This is much larger than the reported values form pulse laser deposition technique (~30 nm) [263].

For the construction of an efficient CSSC, the surface morphology and porosity of the CuI/Cu_2S electrodes are very important. Ideally, a conformal coating with uniform thickness of Cu_2S on the surface of CuI is preferred. However, such a conformal layer can only be achieved by methods such as Atomic Layer Deposition. Such sophisticated methods are beyond our reach. We had to rely on an aero-sol based AACVD method to deposit the Cu_2S in this study. Therefore, it is realistic to expect a patchy and non-uniform coating of Cu_2S on *p*-CuI surface. The purity of each material (i.e. defect free) should also be a vital factor for better photoelectrochemical performance of the electrode. In this work a range of different morphologies were obtained at various deposition times using the same deposition solution as shown in Fig.5-3 (b) to 5-3 (f). Fig. 5-3 (b) shows a small difference of CuI electrode morphology after the deposition of Cu_2S for period of 1 minute (CS-1). This is due to the fact that only a small amount of Cu_2S is deposited during the 1 min deposition time. The XRD spectra presented in the previous section provided the evidence for the presence of Cu_2S on the CuI surface. The particle size of Cu_2S is relatively small compared to that of the CuI (~40 nm) and they exist in discrete fused clusters. Due to the small crystallite size of Cu_2S compared with CuI, the Cu_2S crystallites are capable of penetrating in to the interior of the CuI matrix and make intimate contact with each other. The particle size of Cu_2S particles increase with deposition time. For various thicknesses of the Cu_2S deposited is illustrated in the Fig. 5-4.

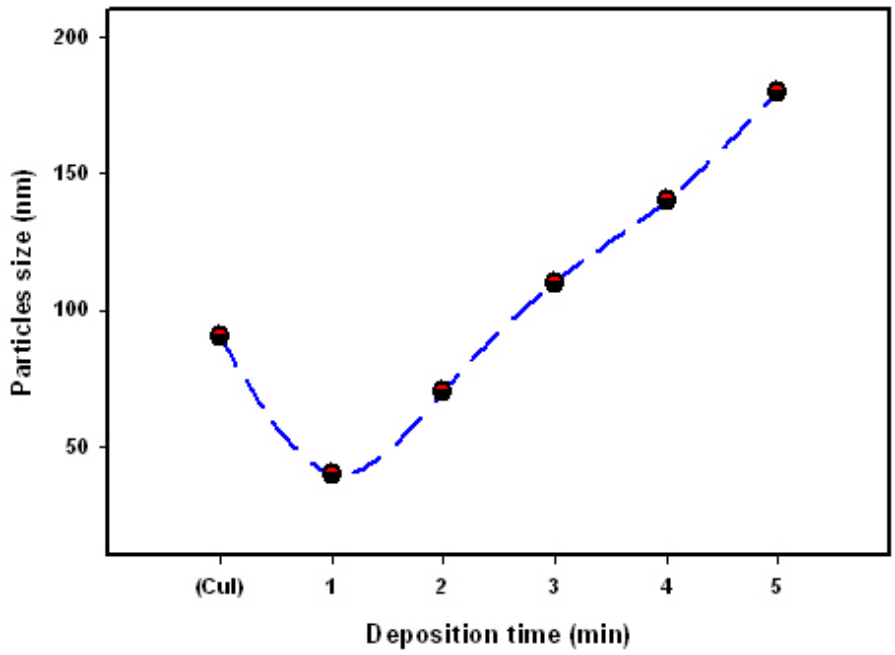

Fig. 5-4: Estimated particles size of Cu_2S and at various deposition times of Cu_2S coated on the CuI surface.

When the deposition time is increased to 2 min (CS-2), the Cu_2S particles fuse and is coated over the entire surface of CuI, forming a layer of Cu_2S. This coating of Cu_2S may have improved the contact between CuI and Cu_2S and hence increased the PEC performance of the electrode. The average particle size of Cu_2S was also increased with further increase of the deposition time (Fig. 5-4). For this electrode, the crystallite size of Cu_2S is estimated to be about 70 nm, which is greater than that of Cu_2S for the 1 minute deposited electrode (CS-1). The crystallite size increased linearly against the deposition time as illustrated in Fig.5-4. This indicates that as the deposition time is increased the particle growth has continued rather than further agglomeration of smaller particles. Furthermore, when the deposition time is increased up to 4 min (CS-4), the electrode appeared to be more uniform and the particles merge together. This is expected to increase the PEC performance of the electrode. However, after 5 min deposition time (CS-5) the deposition leads to form a compact surface layer which could result in poor PEC performance.

Fig. 5-5 shows the cross section images of bare and Cu_2S coated CuI electrodes. The thickness was measured at various cross-sectional locations in each electrode and an average value was calculated. Such calculation is necessary for analysis as the coating of Cu_2S wasn't uniform over the surface of CuI. This average coating thickness value was considered in the subsequent data analysis of this study. The thickness of the CuI electrode was estimated to be 1 μm as seen from the cross-section SEM image of the bare CuI electrode in Fig.5-5 (a). The cross-sectional image of bare CuI also further confirms that the individual CuI particles are grown in such a way that they cluster together making a textured and high aspect ratio surface. Such a textured film is preferred for the photosensitisation of CuI electrode by an appropriate light-absorber material layer (Cu_2S in this case). In the Fig.5-5, the individual CuI particles seem to have grown in the vertical direction from the FTO substrate. The reason for such growth is not well understood. We believe that the aero-sol flow in the heated zone as well as temperature profile may be responsible for it. The cross section of Cu_2S coated CuI electrodes were also studied by the FEGSEM. Fig.5-5 (b) to (f) shows the Cu_2S coating on the surface of CuI as the growth time is gradually increased.

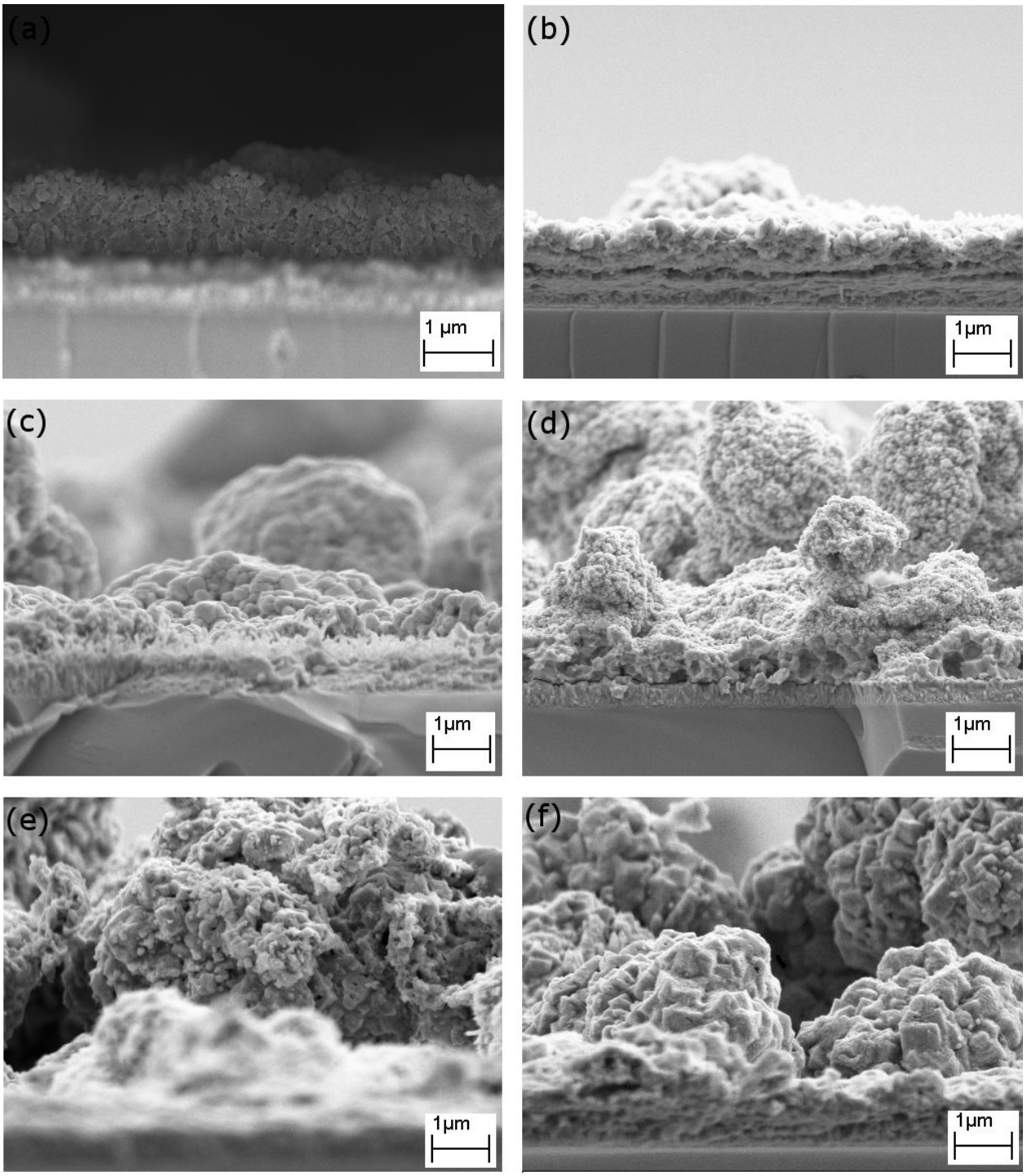

Fig. 5-5: Cross-sectional images of bare CuI electrode and Cu_2S coated CuI electrodes corresponding to different deposition times (a) CuI, (b) CS-1, (c) CS-2, (d) CS-3, (e) CS-4 and (f) CS-5.

When the deposition time is increased the Cu_2S layer gradually becomes thicker. The thickness of the Cu_2S and the deposition rate was estimated from FEGSEM images. The analysis suggests that the deposition rate was ~28 nm/min. The relationship between Cu_2S deposition time and film thickness is illustrated in Fig.5-6. It is nearly linear for the period of 1 – 5 min deposition time. The deposition of Cu_2S did not continue longer than 5 mins as the photoelectrochemical performance of cells were poor.

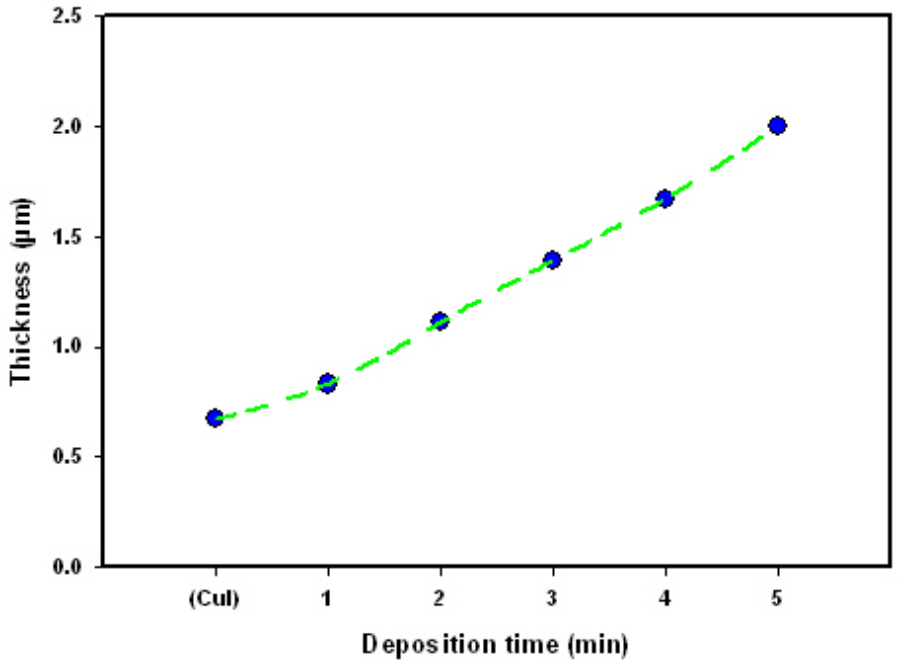

Fig. 5-6: The deposition times of Cu_2S vs. the electrode thickness (analysed from SEM images).

5.1.3 Optical absorption analysis

Fig. 5-7 shows the absorption spectra of CuI and CuI/Cu_2S electrodes recorded at room temperature. As shown in the figure, the absorption threshold for CuI is about 420 nm, which agrees with the previously reported values for CuI electrodes prepared by screen-printing [264]. The background absorbance beyond the steep absorbance at 420 nm suggests the light scattering nature of bare CuI electrode. As it can be seen from the plot, beyond the absorption threshold (at 420 nm), there is a steep slope clearly indicating the formation of Cu_2S on the

CuI surface. There is some evidence for the light scattering as well [265]. The SEM images provide necessary evidence for it. The abrupt change in absorbance at 420 nm in the absorption spectrum originates from light absorption and the excitation of electrons from the valence band to the conduction band [265]. Furthermore, it is apparent that the absorption threshold of CuI/Cu_2S electrodes is around 570 nm whereas it was around 420 nm for bare CuI electrode. The shifts in the absorption edge suggest that the decrease of optical band gap with the presence of Cu_2S layer.

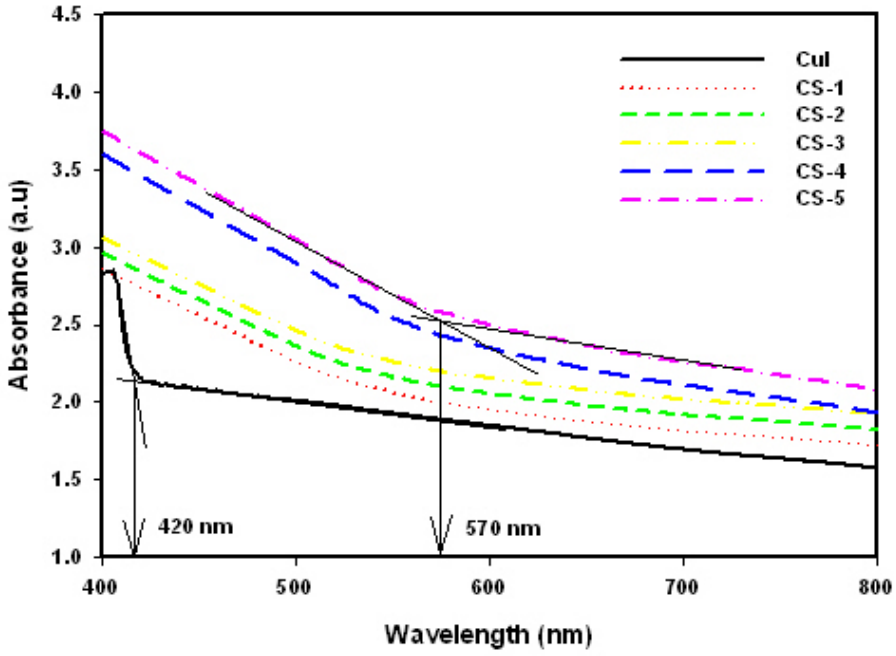

Fig. 5-7: Optical absorption spectra of bare CuI and CuI/Cu_2S electrodes.

To discuss the band gap behaviour of all electrodes investigated here, their band gap was evaluated by constructing Tauc plots. Before constructing Tauc plots, the optical absorbance measurements of the band gap of Cu_2S electrodes was calculated using the relationship of $(\alpha h\nu)=B(h\nu-E_g)^n$, in which α is the light adsorption coefficient, B is constant, $h\nu$ is the photon energy, the exponent n equals 1/2 for direct band gap materials. As shown in

Fig.5-8, the direct band gap energy of the CuI electrode was evaluated as 2.96 eV from the Tauc plot. This value agrees with the previously reported values indicated in Chapter 4 [264].

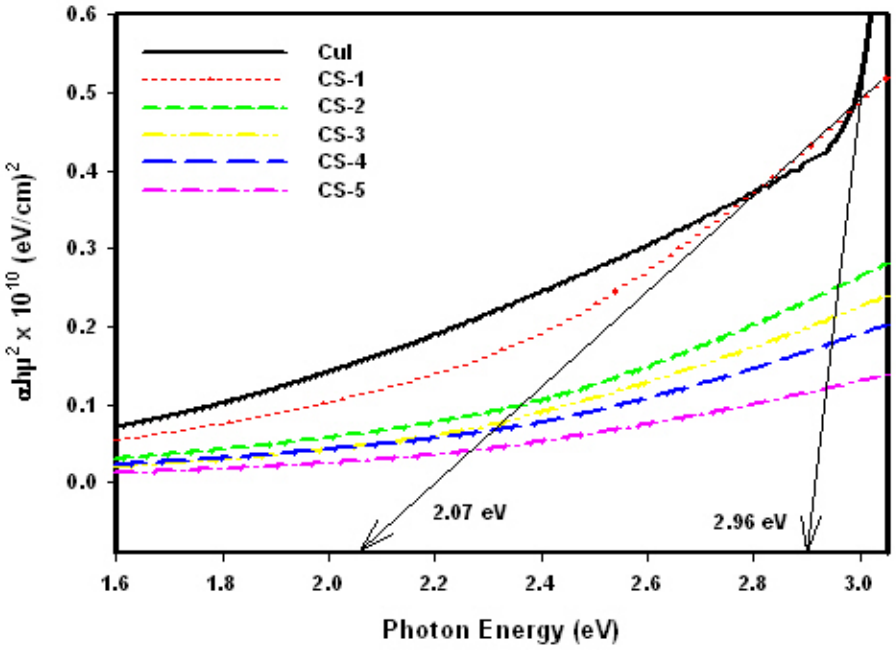

Fig. 5-8: Plot of $(\alpha hv)^2$ versus hv of CuI electrode and CuI/Cu_2S electrodes.

According to the Tauc plot of CuI/Cu_2S electrode in Fig. 5-8, the intercept of photon energy was determined as the direct band gap of Cu_2S. When the deposition time of Cu_2S is increased from 1 min to 5 min, the direct band gap was varied from 2.07 eV to 2.25 eV, which was comparable with the band gap of Cu_2S thin film reported by S.V. Bagul *et al.* [266] and F. Zhuge *et al.* [267] (2.48 eV and 2.74 eV), however, the observed band gap for the electrodes is much larger than the reported values. A sharp slope of the optical absorption feature is obtained, indicating a good homogeneity in the shape and size of the particles as well as low defect density near to the band edge [261].

5.1.4 Current-voltage analysis

In this work the cathodic semiconductor sensitised solar cells have been constructed and studied. CuI has been used as the wide band gap semiconductor that facilitates the light

absorbing Cu_2S layer and collecting holes. The *J-V* data was obtained in the potential range of -0.2 to 0.3 V (vs Ag/AgCl).

To demonstrate the PEC performance of CuI and Cu_2S, the measurements were conducted in 0.2 M europium nitrate (Eu^{2+}/Eu^{3+}) aqueous electrolyte (pH ~2.9). For *p*-type semiconductor materials, relatively negative redox potentials (compared to hole quasi Fermi level) give rectifying contacts, while relatively positive redox potentials produce poor rectifying contacts. Therefore, high photovoltages can be obtained with relatively large negative redox potential containing electrolytes [268]. Therefore, PEC properties of CuI was examined using the Eu^{2+}/Eu^{3+} redox couple, which has a more negative standard redox potential (– 5.05 eV vs. vacuum) compared to the iodide/triiodide (I^-/I_3^-) redox couple (-4.44 V vs. vacuum) [74,77]. The redox reactions of Eu^{2+}/Eu^{3+} couple can be explained as follows;

$$Eu^{3+} + e^- \leftrightarrow Eu^{2+} \quad \text{(reduction)} \qquad (1)$$

$$Eu^{2+} \leftrightarrow Eu^{3+} - e^- \quad \text{(oxidation)} \qquad (2)$$

Fig. 5-9 and 5-10 shows the steady-state and chopping photocurrent density of the CuI and CuI/Cu_2S electrode in Eu^{2+}/Eu^{3+} redox electrolyte.

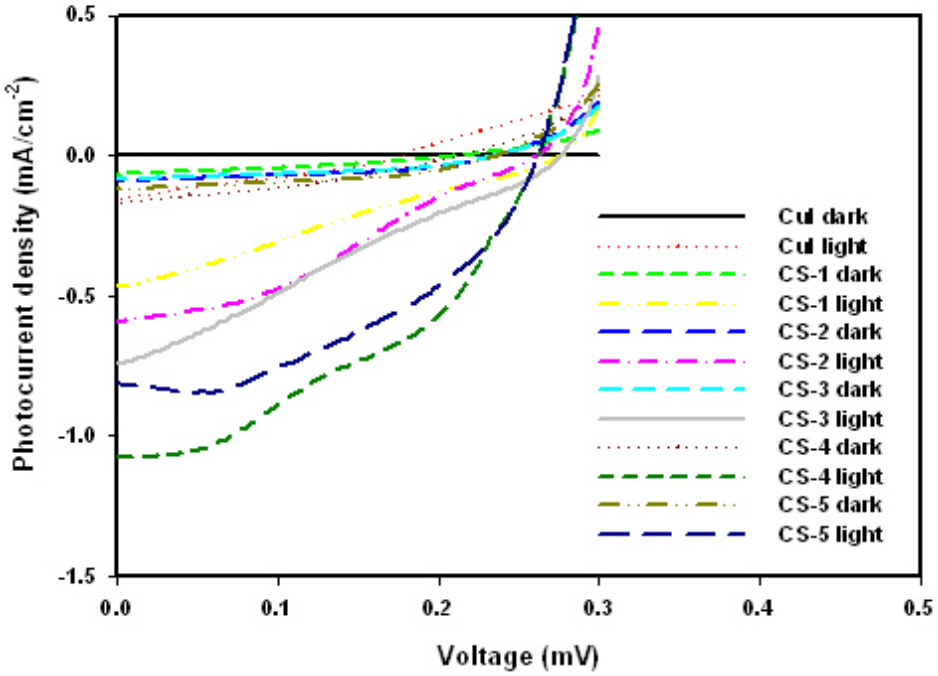

Fig. 5-9: Current-voltage (*J-V*) curves for CuI, CS-1, CS-2, CS-3, CS-4 and CS-5.

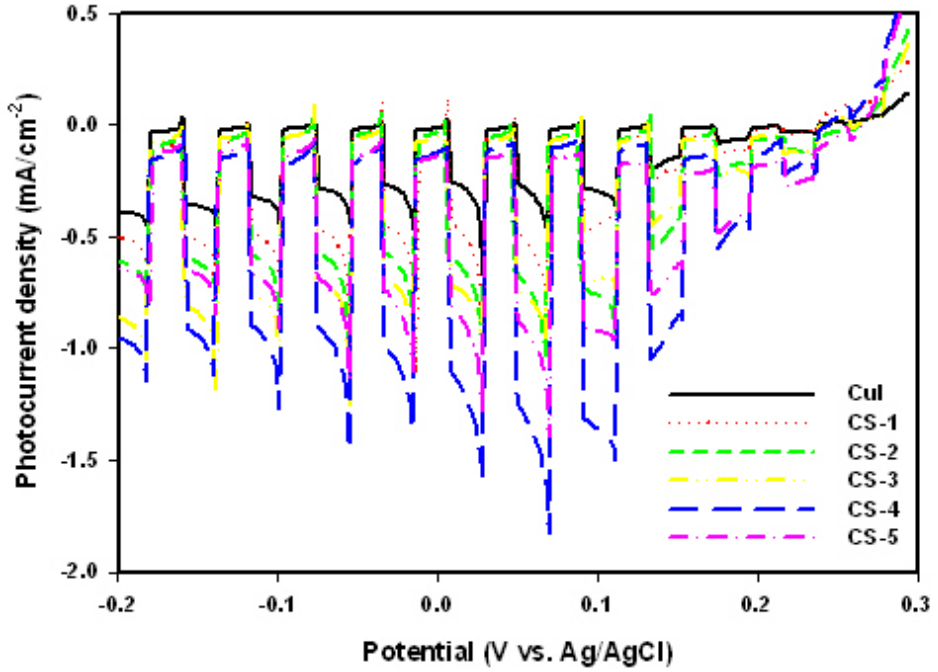

Fig. 5-10: Chopped Current-voltage (*J-V*) curves for CuI, CS-1, CS-2, CS-3, CS-4 and CS-5.

As the bias potential is increased towards more negative values, the photocurrent under illumination becomes more negative and it is confirmed that CuI is a *p*-type semiconductor and CuI/Cu_2S is a cathodic type photoelectrochemical solar cell. As the potential swept in the opposite direction, the cathodic photocurrent decreased because the band bending is lowered and the rate of electron-hole recombination is increased as a result [269]. Increasing the bias potential further in the negative direction shows that the cathodic photocurrent was reduced above the potential of -0.2 V (vs Ag/AgCl). This is due to the influence of CuI characterisation. When the potential is applied in the presence of light, photogenerated electron and hole pairs are generated and separated in the space charge region of the electrode. The transfer of electrons at the electrode/electrolyte interface will result in excessive photogenerated majority carrier holes in the semiconductor. In other words, at the electrode/electrolyte interface the electron will transfer from electrode to the electrolyte due to the difference in energy level as illustrated in Fig. 5-11. The result is a cathodic photocurrent.

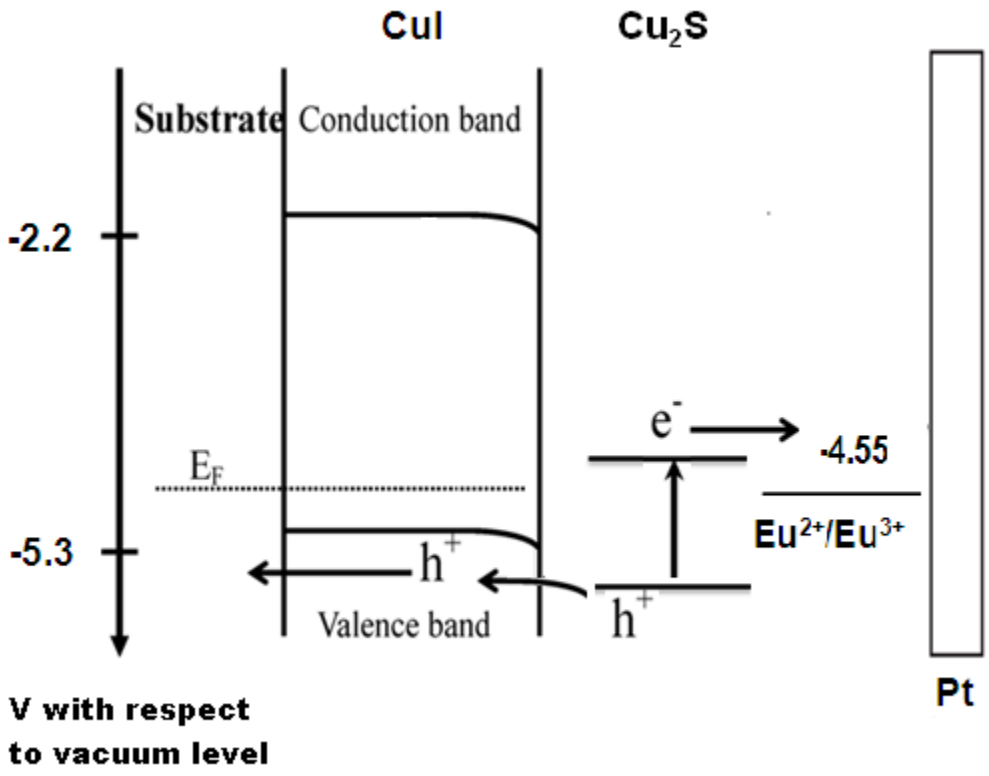

Fig. 5-11: Schematic of cathodic electrode/electrolyte junction.

The electrode showed a relatively negligible dark current due to the uniform nature of CuI electrodes. This also suggests the absence of shunting due to reasonably uniform and good coverage of CuI on FTO surface. The high internal surface area associated with the nanoparticles electrode provides a large contact area between the electrolyte/electrode interface hence relatively high photocurrent. From the steady-state current-voltage plots of bare CuI and CuI/Cu_2S in Fig. 5-9 a number of other important device parameters have also been obtained and summarised in Table 5-3. Fig. 5-10, the results show less recombination (less spike) which leads to increase the performance of the cells. This can be related to the better surface coverage of Cu_2S on the NiO layer which can avoid the contact between the FTO and the films.

Table 5-3: *J-V* characteristics of cathodic semiconductor sensitised solar cells under one sun condition.

	V_{oc} (mV)	J_{SC} (mAcm^{-2})	Fill Factor (FF)	efficiency (%)
CuI	0.18	-0.16	0.28	0.008
CS-1	0.28	-0.47	0.24	0.032
CS-2	0.26	-0.59	0.32	0.048
CS-3	0.28	-0.74	0.25	0.051
CS-4	0.26	-1.08	0.41	0.12
CS-5	0.26	-0.81	0.46	0.097

The characteristic PEC values such as the short-circuit current density (J_{sc}), fill factors (*FF*), open circuit voltages (V_{oc}), and the overall energy conversion efficiency (η) were obtained for the bare CuI electrode and they were 1.08 mAcm^{-2} vs. Ag/AgCl/3 M KCl, 0.41, 0.263 V and 0.12% respectively. The relatively high PEC performance of the CuI electrode is

very encouraging. It is due to several factors such as the fast electron scavenger (Eu^{2+}/Eu^{3+}) redox couple containing electrolyte, large internal surface area of the electrode, and the uniformity of the electrode.

As indicated in the absorbance and FEG-SEM studies, the gradual increase of the Cu_2S layer thickness led to an increase in the photocurrent density of the electrode. Fig. 5-12 summarizes the photocurrent density of CuI and CuI/Cu_2S at different deposition times of Cu_2S at 0 V (vs. Ag/AgCl).

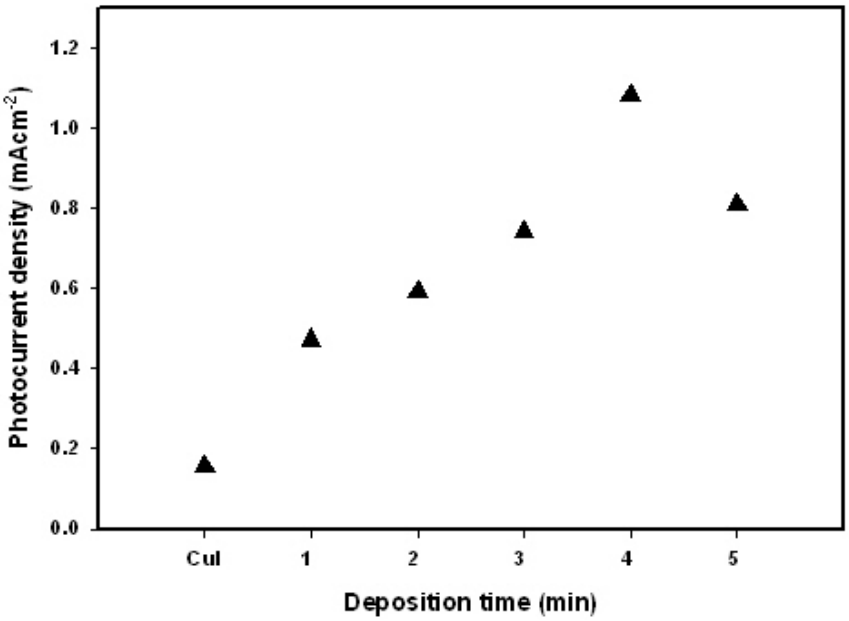

Fig. 5-12: The steady-state photocurrent density of CuI/Cu_2S electrodes at different deposition time of Cu_2S. The photocurrent density of CuI is included as the reference in the plot.

The results given in Fig. 5-11 clearly show that the photocurrent density of the CuI/Cu_2S electrodes is much larger than that of the CuI electrode. This is due to the CuI photosensitisation process which extends the spectral response of the device towards the more visible region (i.e from 420 to 570 nm as shown in Fig. 5.7). The photosensitisation (charge generation in Cu_2S and subsequent transfer mechanism) at the CuI/Cu_2S interface can be illustrated as follows [270,271].

$Cu_2S/CuI + h\upsilon \rightarrow Cu_2S^*/CuI$ (excitation) (3)

$Cu_2S^*/CuI \rightarrow Cu_2S^{\bullet-}/CuI\ (+)$ (charge separation) (4)

$Cu_2S^{\bullet-}/CuI\ (+) + Eu^{3+} \rightarrow Cu_2S/CuI\ (+) + Eu^{2+\bullet-} + e^-$ (absorber regeneration) (5)

According to this scheme, the Cu_2S absorbs the visible light (Equation 3) and generates electron/hole pairs (Equation 4). Then the holes are injected to the CuI before being collected at the FTO substrate and the absorber is reduced. Further, the oxidized species (Eu^{3+}) of electrolyte reacts to the reduced absorber and is regenerated to its ground state (Equation 5). At the same time, electrons leaving the conduction band are injected to the electrolyte at the interface. Finally the Eu^{3+} is regenerated at the counter electrode, completing the cycle.

5.1.5 Incident Photon to Electron Conversion Efficiency (IPCE)

The IPCE measurements were carried out to further study the photo-response of bare CuI and CuI/Cu_2S electrodes with different Cu_2S deposition times as shown in Fig. 5-13.

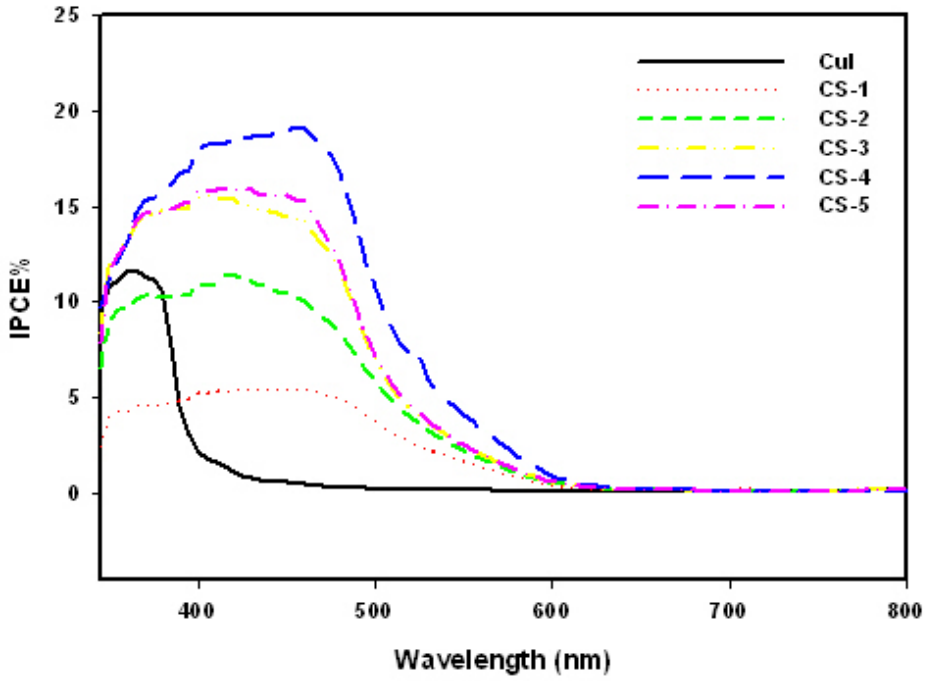

Fig. 5-13: IPCE curves for bare CuI and CuI/Cu_2S electrodes at various deposition times.

As Fig. 5-13 shows, the spectrum edge has shifted to the visible region with the increase of Cu_2S deposition. The bare CuI electrode gives a spectrum edge of 365 nm, whereas deposition of Cu_2S moves the spectrum edge near to 480 nm. These changes of the spectrum edges of the electrodes are well matched with UV-Vis absorption data in Fig 5-7. As indicated, the bare CuI electrodes exhibited the maximum IPCE of 11.6% at 365 nm. The IPCE spectra of Cu_2S sensitized CuI electrodes showed a systematic increase as the Cu_2S layer thickness is gradually increased. The best IPCE was recorded for the CuI/Cu_2S electrode that corresponds to 4 min Cu_2S deposition time. This trend correlates well with the steady-state photocurrent-voltage data (Fig.5-11). Further increase of Cu_2S deposition time results in a low IPCE. This could be due to the increase of recombination that take place in thicker Cu_2S layer upon illumination. The maximum IPCE achieved for the 4 mins Cu_2S deposited CuI/Cu_2S electrode is about 19.2% at 456 nm.

5.2 FTO/NiO/Cu_2S

The conversion efficiency of NiO photocathodes can be improved by replacing the sensitised dye with an inorganic semiconductor sensitizer [272,273]. The advantages of inorganic semiconductors as sensitizers are the high extinction coefficients which improve the light absorption. Construction of band gap energies for appropriate arrangement of the valence band edges and makes possible higher hole efficiency and smaller hole transport resistance for quicker charge transport [274]. This chapter describes the preparation, characterization and PEC performance of Cu_2S sensitized NiO electrodes compared to the bare NiO electrodes. The NiO electrodes and the Cu_2S coatings were deposited by AACVD method and I_3^-/I^- electrolyte was used in order to study the PEC properties of Cu_2S-sensitised NiO solar cells. Studies have been focused on different deposition times of Cu_2S sensitizer on the surface of NiO, and the results have been compared to the highest performance obtained for a bare NiO electrode (reported in Chapter 4). The samples have been named NS-1, NS-2, NS-3, NS-4 and NS-5 corresponding to the 1, 2, 3, 4 and 5 minutes of deposition times as shown in the Table 5-4.

Table 5-4: The deposition times of CuI and Cu_2S in the making of photoelectrochemical CuI/Cu_2S CSSC.

Sample	**Deposition Time of CuI (min)**	**Deposition time of Cu_2S (min)**
NS-1	40	1
NS-2	40	2
NS-3	40	3
NS-4	40	4
NS-5	40	5

5.2.1 X-ray Diffraction (XRD) analysis

The NiO/Cu_2S electrode was studied by varying the Cu_2S deposition time. The phase and crystallinity of the bare NiO and NiO/Cu_2S electrodes were characterised by the X-ray diffraction studies. Fig. 5-14 presents the XRD patterns of NiO/Cu_2S electrodes at various Cu_2S deposition times.

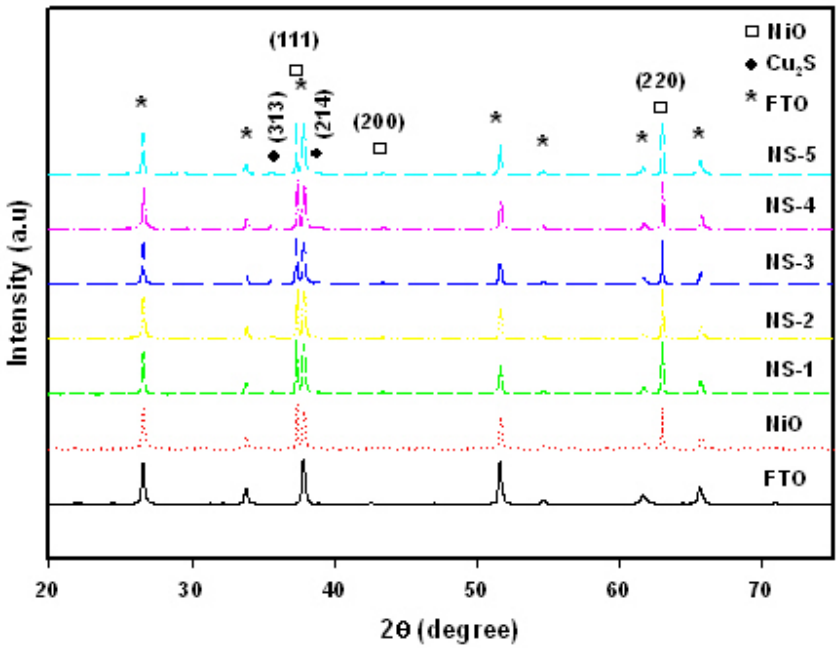

Fig. 5-14: XRD patterns of a bare NiO and as deposited Cu_2S (on NiO) against the deposition time.

The XRD spectrum of bare NiO electrode shows the crystalline nature of the NiO film. As previously discussed, well-defined reflections of NiO can be seen at 37.20° 43.20° and 62.87°. Two reflections belonging to the Cu_2S can be identified at 36.4° and 38.8° corresponding to the (313) and (214) reflections of Cu_2S [92]. The corresponding peak positions for NiO and Cu_2S are in good agreement with previously reported values [275]. For the sensitized layer, reflections of the Cu_2S were well matched to the patterns of hexagonal chalcocite Cu_2S. However, the spectra are dominated by the reflections of NiO and FTO. This could be due to their highly crystalline nature and relatively thick layers (compared to that of Cu_2S). Both of the reflections can be clearly seen in the spectra shown in Fig. 5-15 which arise from sample NS-4.

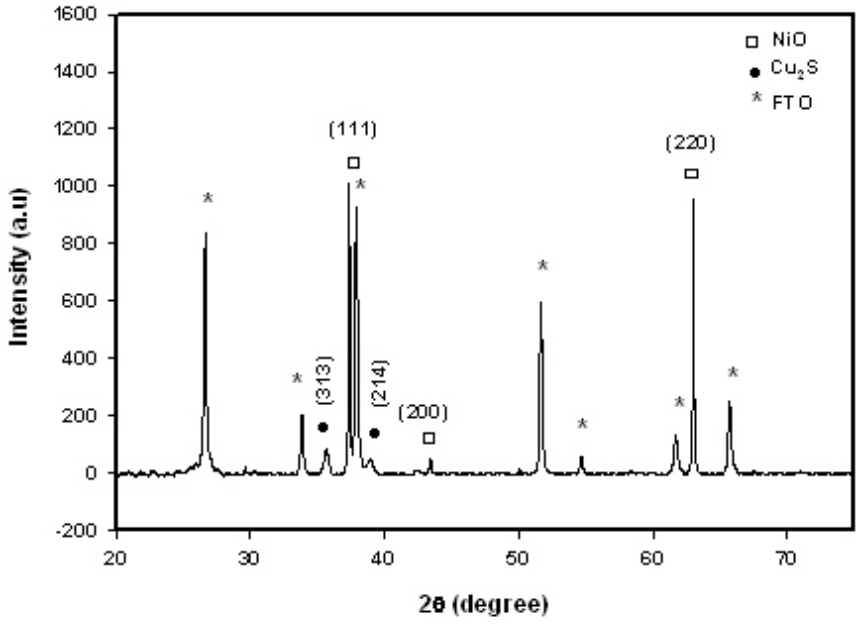

Fig. 5-15: XRD pattern of NiO/Cu_2S electrode (NS-4).

Further information about Cu_2S crystallite sizes were gathered from FWHM obtained from the highest 35.7° reflection. The crystallite size was calculated using the Scherrer equation. These values are much smaller than the literature values of Cu_2S films prepared by chemical bath deposition [261] (~60 nm). The crystallite sizes of Cu_2S at various thicknesses are recorded in Table 5-5. The results show that there was no significant effect of deposition time on the crystallite size and all the films showed crystallite size of about 20-30 nm.

Table 5-5: Crystallite size estimated using the strongest reflections of NiO and Cu_2S at various thicknesses. The XRD peaks used to make this estimation are 35.7°.

Sample	Strong reflection (°)	FWHM (°)	Estimated crystallite size (nm)
NiO	37.2	0.17	49
NS-1	35.7	0.37	24
NS-2	35.7	0.45	20
NS-3	35.7	0.38	23
NS-4	35.7	0.36	25
NS-5	35.7	0.30	30

5.2.2 Surface morphology analysis

The morphology of bare and Cu_2S sensitised NiO electrodes were examined by FEGSEM. The surface topographical images of bare NiO and Cu_2S sensitised NiO electrodes at various deposition times are shown in Fig. 5-16. The same structure of NiO for all electrodes indicated that the electrodes were prepared under the same conditions. The overall images suggested that the electrodes were relatively uniform, free from pinholes, cracks and rich in highly porous surfaces. Such high porous surfaces are necessary for the solar cells constructed in the present study and have been elaborated in detail in the following section.

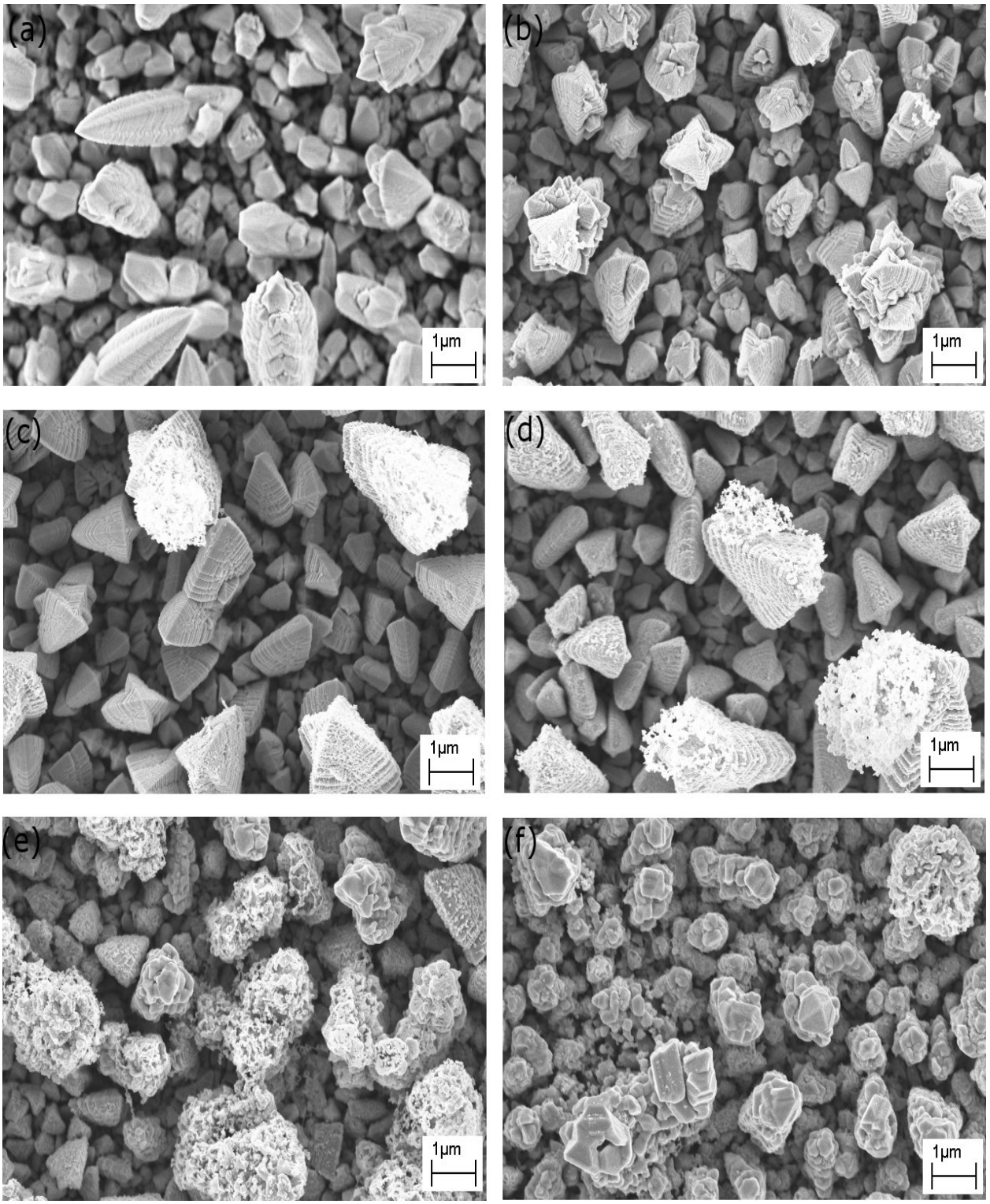

Fig. 5-16: FEGSEM images of bare NiO electrode and Cu_2S deposited NiO electrodes (a) NiO, (b) NS-1, (c) NS-2, (d) NS-3, (e) NS-4 and (f) NS-5.

Fig. 5-16 (a) represents the porous NiO electrode deposited for a period of 40 min (the details of NiO deposition were already discussed in chapter 4). The electrode is highly porous as well as having a large surface area and is well adhered to the FTO substrate which fulfils the requirement of PEC solar cell operation. The large internal surface area of the porous NiO electrode allows for the deposition of enough fine Cu_2S particles to ensure a complete coverage on the NiO surface in order to photosensitise NiO. From the cross sectional SEM images, it is clear that Cu_2S crystallites are grown vertically on FTO glass substrates (see Fig.5-17).

Fig. 5-16 (b) – (f) shows the surface morphologies of as deposited Cu_2S on the NiO electrode at different deposition times. In the case of relatively short deposition time (Fig. 5-16 (b) and (c)), not many Cu_2S particles were observed on NiO suggesting a poor surface coverage of Cu_2S. As the deposition time is gradually increased, the nucleation and number of particles formed on the NiO surface is increased. After 4 mins deposition time a fully covered layer of Cu_2S can be seen on top of the NiO (see Fig. 5-16 (e)). The Cu_2S particles also show good contact with the NiO particles. Such intimate contact is essential for transfer of photogenerated charges to the NiO electrode [276]. However after 5 minutes deposition time (Fig. 5-16 (f)), the Cu_2S layer became relatively thick and exhibited compact nature and particles were seen fused each other. Due to this reason the PEC performance of the electrode was expected to be low [276].

The average particle size of Cu_2S is found to be (40 nm). As discussed in section 4.3.2.2, the average particle size of NiO is about 50 nm. Because the Cu_2S particles are smaller than that of NiO, they were capable of penetrating in to the interior of NiO matrix and make intimate contacts with NiO surface thereby providing necessary NiO/Cu_2S interface in a large area that enable the photosensitisation of NiO. In fact, this is evident from the photoelectrochemical studies (see section 5.2.4 below).

The cross-sectional images of bare NiO electrode and as deposited NiO/Cu_2S electrodes are illustrated in the Fig. 5-17.

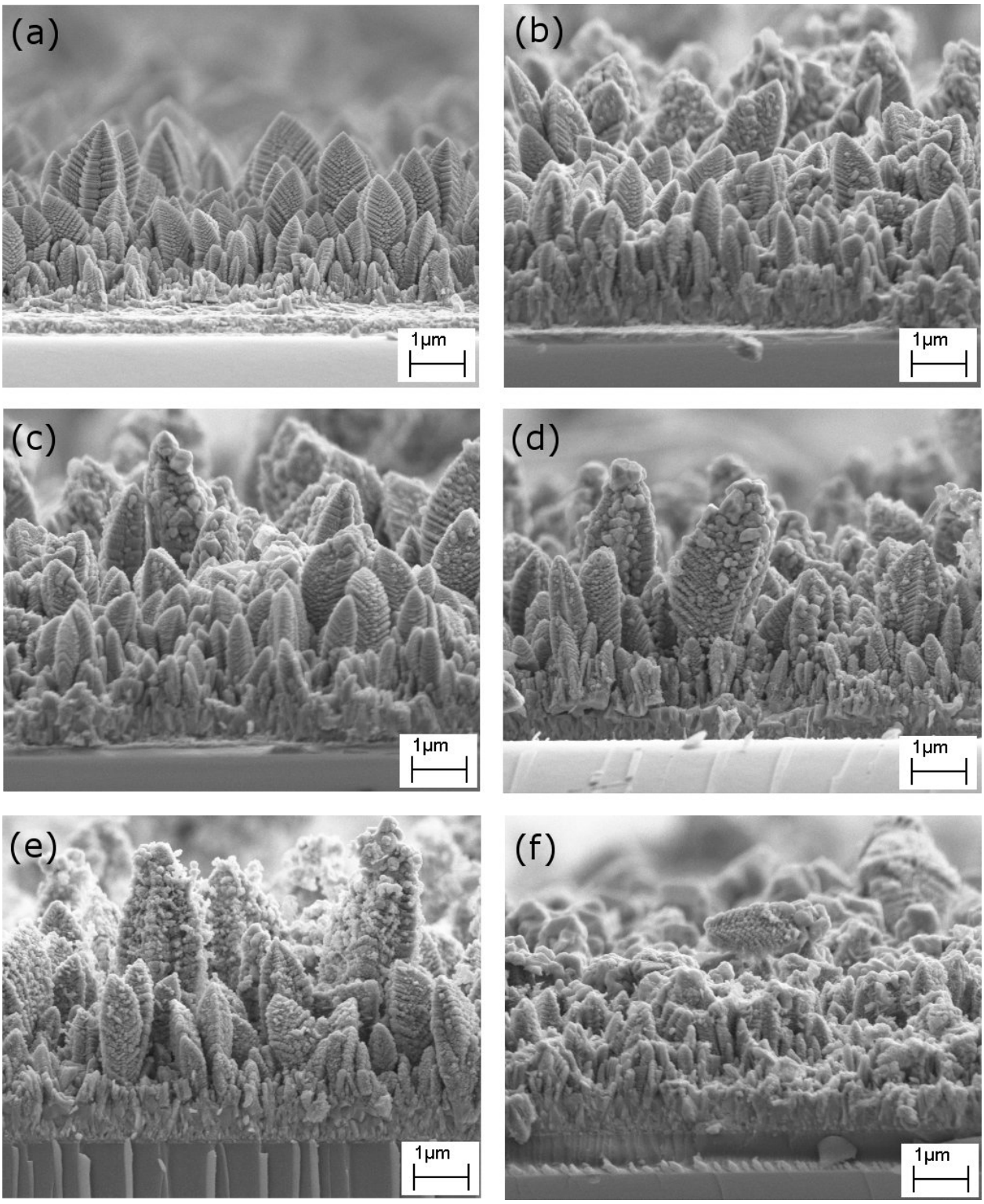

Fig. 5-17: Cross-sectional images of NiO and Cu_2S deposited electrodes corresponding to various deposition times (a) NiO, (b) NS-1, (c) NS-2, (d) NS-3, (e) NS-4 and (f) NS-5.

The surface topographical and cross-sectional images illustrate clearly the Cu_2S over coated layer. The Cu_2S crystallites are very small in size and form a thin layer on the NiO surface. The Cu_2S layer seems to have made a good contact with individual NiO particles. For the NS-4 electrode, it shows a complete coverage of Cu_2S. In fact, the NS-4 electrode shows the highest photoelectrochemical performance (see section 5.2.4). When the Cu_2S deposition was continued further (i.e. for 5 mins), the NiO film appeared to be fractured. Certain NiO particles have disintegrated from the film. This may be due to the high flow rate of carrier gas and at relatively long deposition times. The result indicates that by increasing the deposition time over 5 minutes does not yield good NiO/Cu_2S electrodes to construct photoelectrochemical cell. In fact, such electrodes are photoelectrochemically poor, structurally weak, appeared to have lost the porosity and hence have relatively low electrode internal surface area.

5.2.3 UV-visible optical absorption

As reported in the literature, the optical properties of the thin films are strongly dependant on their morphologies [277]. For example, the porousity of films may increase the light scattering. The UV-Vis absorption spectra of the bare NiO film as well as, as synthesised Cu_2S on the NiO electrode (NiO/Cu_2S) were illustrated in Fig. 5-18. The absorption spectra of the electrodes were measured at room temperature in the wavelength range 300 – 800 nm. It can be seen that the morphological changes of the NiO/Cu_2S electrodes were followed by some changes in the UV-Vis spectra. It appears that due to the considerable difference in morphology associated with NiO and Cu_2S nanoparticles, the optical properties have varied. It is well known that the absorption of the electrodes increases with the increase of film thickness linearly according to the beer-lambert low. However, the Beer-Lambert law only follows for the compact films. In this case, the absorption increases with the thickness, but as mentioned in section 5.2.2 due to fracturing of electrodes (i.e. reducing the film thickness), the absorption was slightly dropped for the NS-5 sample.

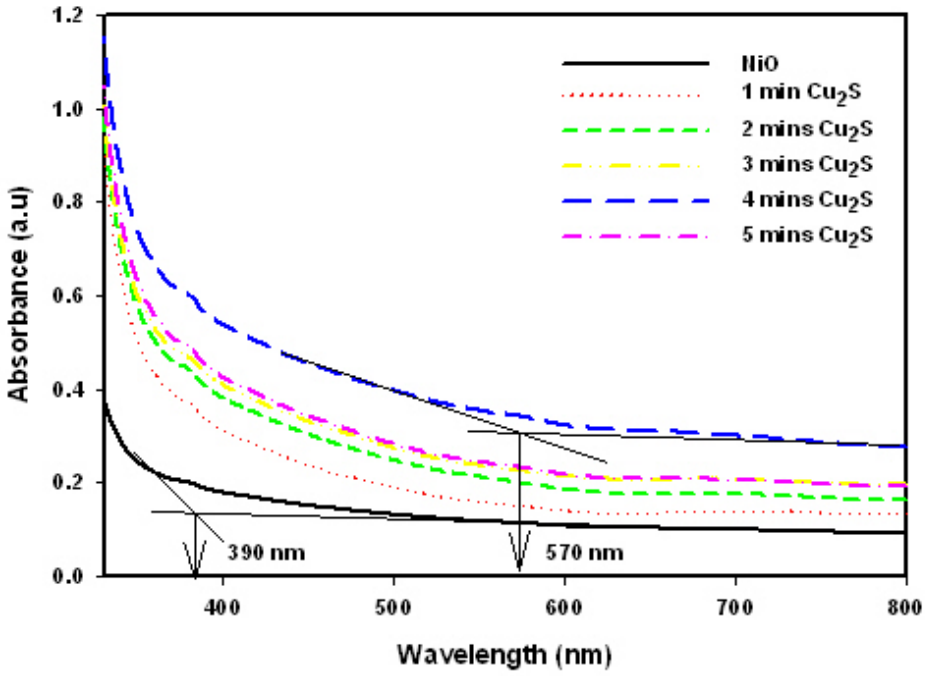

Fig. 5-18: Optical absorption spectra of bare NiO electrode and NiO/Cu_2S electrodes deposited for different growth periods (i.e. 1- 5 mins).

The strong absorption threshold at 390 nm observed for NiO electrode is due to band-to-band excitation of NiO [278,279]. The background absorbance beyond the 570 nm for the NiO is due to the defect and inter emerge of two materials at the interface. The gradual broadening the UV-Vis spectra suggests the presence of Cu_2S on NiO. This behaviour was continued as the deposition time is gradually increased. As discussed earlier in this thesis, the band broadening occurs due to structural change that originates with the photosensitisation process [277,280]. It is evident from Fig. 5.18 that the absorption threshold position of NiO/Cu_2S electrodes have shifted to 570 nm. This can be clearly seen by comparing the bare NiO and the 1 min Cu_2S deposited sample (NS-1). However, the optical band gap energy is difficult to determine in this study due to the difficulties in measuring the thickness of Cu_2S formed on the surface of the NiO electrodes. This difficulty is associated with the textured nature of the electrodes.

5.2.4 Current-voltage analysis

Fig. 5-19 and 5-20 presents the current-voltage characteristics of photosensitised NiO/Cu_2S electrodes under illumination. The NiO/Cu_2S prepared at different Cu_2S deposition times were subjected to this study along with the bare NiO electrode.

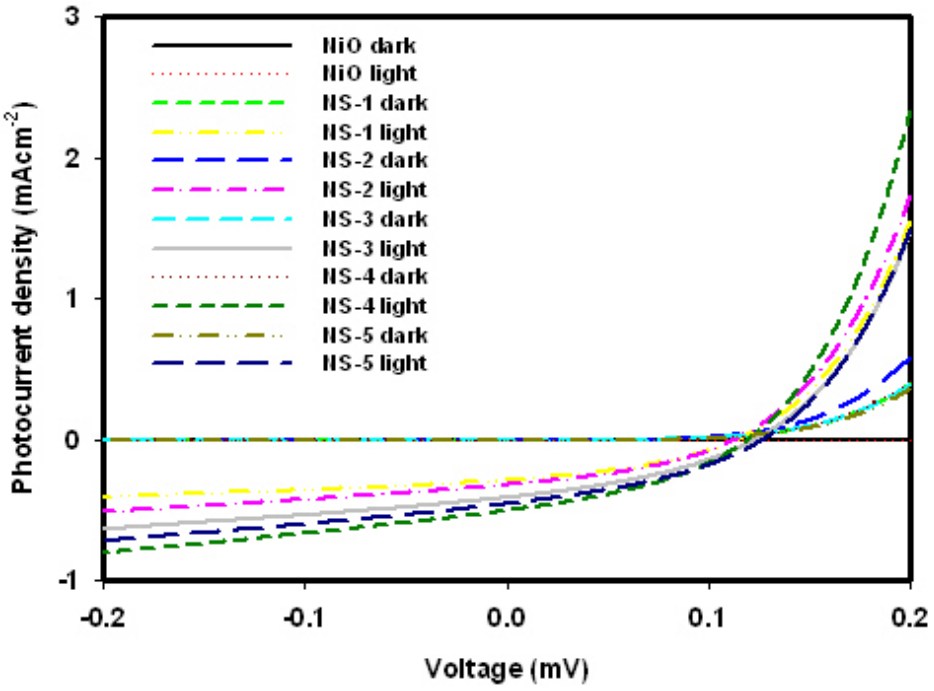

Fig. 5-19: Current-voltage (*J-V*) curves for CuI, NS-1, NS-2, NS-3, NS-4 and NS-5.

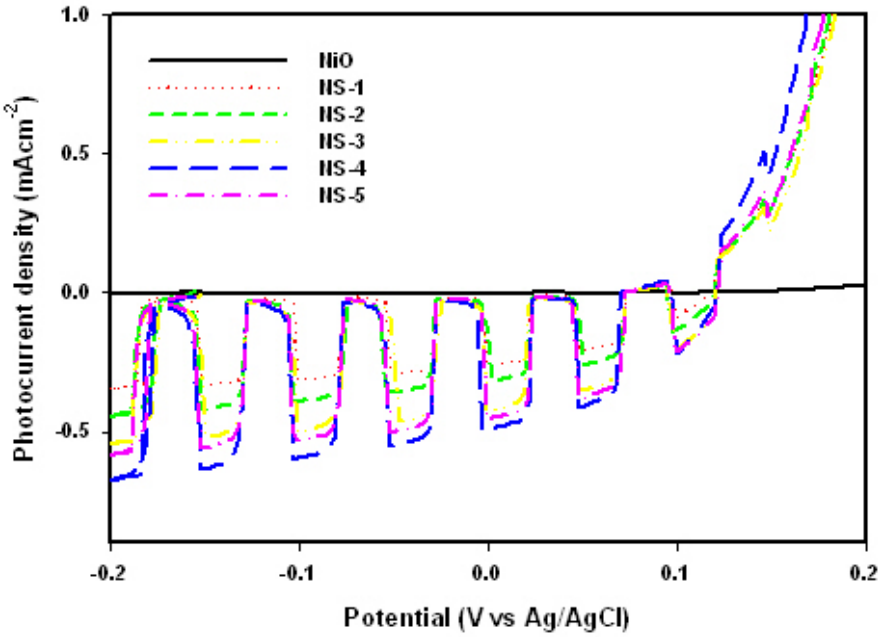

Fig. 5-20: Chopped Current-voltage (*J-V*) curves for CuI, NS-1, NS-2, NS-3, NS-4 and NS-5.

The sign of photocurrents is a signature of determining the difference between the anodic and cathodic sensitized solar cells. In this case, the cathodic photocurrent was found in the presence of I^-/I_3^- electrolyte with a Pt counter electrode. The data recorded are superior to the previously reported best data for such a device presented by J.H. Rhee *et al.* [75]. Here the NiO and Cu_2S were prepared by using doctor blade and spray pyrolysis respectively. From Fig. 5-20, the results show less recombination which leads to increase the performance of the cells. This can be related to the better surface coverage of Cu_2S on the NiO layer which can avoid the contact between the FTO and the films. The photoelectrochemical performances of the devices constructed in this study are presented in Table 5-6.

Table 5-6: *J-V* characteristics of photosensitised NiO cathodic solar cells under one sun condition. Here, the photosensitiser material is Cu_2S.

	V_{oc} (V)	J_{SC} (mAcm^{-2})	Fill Factor (*FF*)	Efficiency (%)
NS-1	0.12	0.29	0.35	0.012
NS-2	0.12	0.33	0.34	0.013
NS-3	0.12	0.42	0.35	0.018
NS-4	0.12	0.51	0.36	0.022
NS-5	0.13	0.46	0.36	0.021

The results reported herein present the device performance, which emphasizes the importance of sensitizers for cathodic semiconductor sensitised solar cells. The device performances for various deposition times of Cu_2S on NiO electrodes were evaluated by the cell parameters such as V_{oc}, J_{sc}, FF and η. The bare NiO electrode without sensitizer gave the lowest photocurrent, as expected. In this study, the highest photoelectrochemical performance for a NiO/Cu_2S solar cell was recorded for the sample NS-4 which had a V_{oc} of 0.12 V, J_{sc} of 0.5 mAcm^{-2}, FF of 0.36 and η of 0.022%. The data indicate that gradual improvement of photoelectrochemical performance with the increase of the Cu_2S deposition time. This can be related to the improvements in the surface coverage of the NiO/Cu_2S electrode, where full coverage is obtained with relatively longer deposition times (i.e. 4 mins). However, at above 5 min deposition times, the NiO/Cu_2S electrode seems to have lost the porosity leading to a reduction in the surface area as observed in Fig.5.16. Fig. 5-21 shows the summary of the variation of the photocurrent densities with the sensitizer deposition time recorded at 0 V (vs. Ag/AgCl).

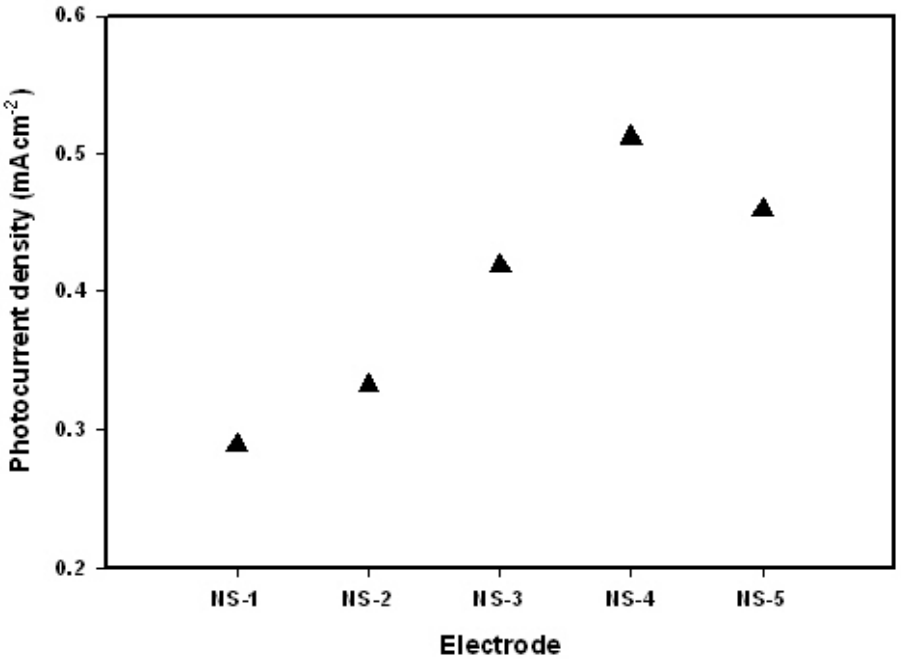

Fig. 5-21: Photocurrent density of bare NiO and NiO /Cu_2S electrodes at different deposition times of Cu_2S.

On the basis of the above results, the charge transfer mechanism related to photosensitisation of NiO can be proposed as follows [271,281-284];

In this case, the absorber (Cu_2S) absorbs the light (*hv*) supplied from 1 sun illumination,

$Cu_2S/NiO + h\upsilon \rightarrow Cu_2S^*/NiO$ (excitation) (6)

Then, charge separation occurs, which produce electron/hole pairs. The photogenerated holes in the valence band of Cu_2S are transferred to the valence band of CuI and the Cu_2S is reduced.

$Cu_2S^*/CuI \rightarrow Cu_2S^{\bullet -}/CuI\ (+)$ (charge separation) (7)

The photoexcited electrons in the conduction band of Cu_2S were captured by the oxidised species in the electrolyte and it is the desired path for a working solar cell. The reduced Cu_2S will react with the oxidized species (I_3^-) of electrolyte and regenerate its ground state.

$Cu_2S^{\bullet-}$/CuI (+) + I_3^- → Cu_2S/CuI (+) + $I_2^{\bullet-}$+I^- (absorber regeneration) (8)

As reported in the literature [285,286], the $I_2^{\bullet-}$ would be generated the same way as with common TiO_2- based DSCs. After oxidation, the absorber can react with NiO to give second hole or disproportionation,

$2I_2^{\bullet-} \rightarrow I^- + I_3^-$ (disproportionation) (9)

Or be oxidized at the anode

$I_2^{\bullet-} \rightarrow e^- + I_2$ (oxidize) (10)

Or regenerate I_3^-

$I_2 \rightarrow I^- + I_3^-$ (regeneration) (11)

And regeneration of I_3^- at the counter electrode

$3I^- \rightarrow I_3^- + 2e^-$ (regenerate) (12)

The regeneration of I_3^- species at the counter electrode completes the charge cycle. As a result, it is believed that the device performance could be greatly improved by optimizing the hole collector electrode (in this case NiO) and the semiconducting light absorber layer (in this case Cu_2S), as well as the charge transport properties of the redox electrolyte. The schematic of the cathodic photosensitised solar cell is illustrated in Fig. 5-22.

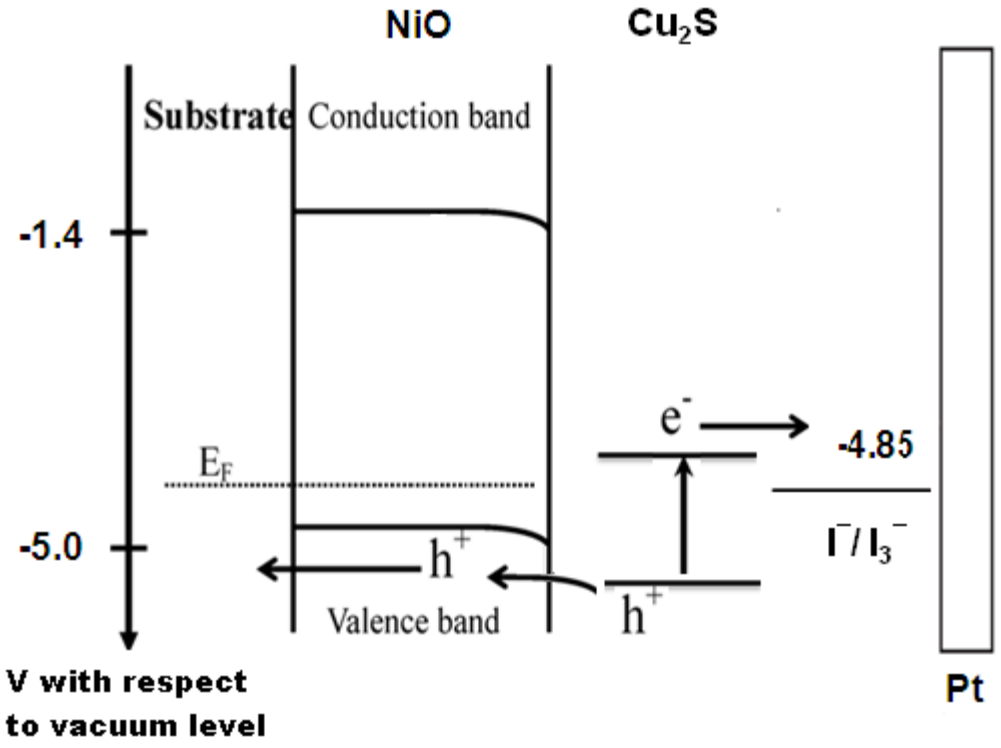

Fig. 5-22: The schematic of mechanism for NiO/Cu_2S characterisation.

5.2.5 Incident Photon to Electron Conversion Efficiency (IPCE)

The IPCE spectra of Cu_2S sensitized NiO and bare NiO electrodes are shown in Fig. 5-23. The bare NiO electrode exhibits almost 0% at 330 nm and the Cu_2S sensitised NiO electrode present greater IPCE at wavelengths below 800 nm. The highest IPCE obtained in this study was ~7.6% at 400 nm for the NS-4 electrode. The IPCE was gradually increased as the thickness of Cu_2S increased up to 4 mins Cu_2S deposition time. Further increase of Cu_2S reduced the device performance and IPCE. This may be due to charge recombination which is due to the increase in thickness of the Cu_2S layer. The IPCE spectra are consistent with the absorption spectrum of NiO/Cu_2S electrode (Fig. 5-18). Therefore, the results suggest that holes are injected from the valence band of Cu_2S to the valence band of NiO.

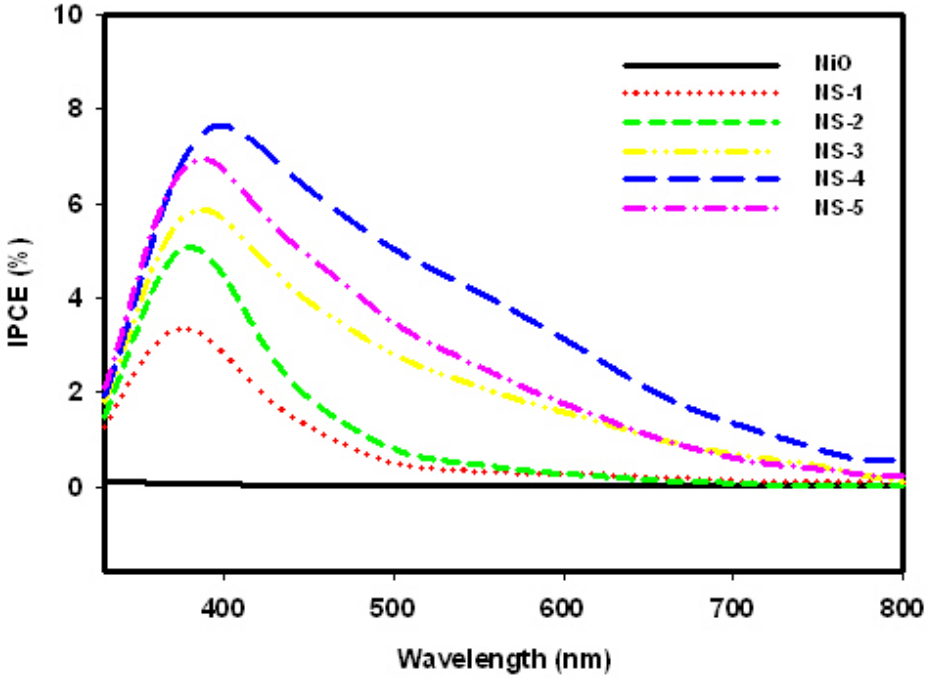

Fig. 5-23: IPCE curves for NiO and NiO/Cu_2S at difference deposition time.

5.3 Conclusions

This chapter presents the successful deposition of Cu_2S on the surface of CuI and NiO electrodes. The deposited Cu_2S acts as an efficient sensitizer for *p*-type CuI and NiO cathodic semiconductor solar cells. The photocurrent density values are found to be 1.0 and 0.6 $mAcm^{-2}$ for the CuI/Cu_2S and NiO/Cu_2S electrodes, respectively. It was shown that the photosensitised cathodic semiconductor solar cells can be employed to fabricate SS-CSSC which is discussed in Chapter 6.

Chapter 6: Experimental Results of Solid State Cathodic Semiconductor Solar cells

6.0 Solid state cathodic semiconductor solar cells (SS-CSSC)

Up until now no reports have been published in the literature on solid-state cathodic semiconductor solar cells (SS-CSSC). By extending the photosensitisation of cathodic semiconductor concept, a fully solid-state cathodic semiconductor solar cell has been constructed in this doctoral study. The SS-CSSCs were constructed by sensitising both CuI and NiO wide band gap semiconductors using a Cu_2S light absorber. Fe_2O_3 was used as the electron transporting material in the SS-CSSC configuration. The SS-CSSCs constructed using CuI and NiO cathodic wide band gap semiconductors can be given as FTO/CuI/Cu_2S/Fe_2O_3/Pt and FTO/NiO/Cu_2S/Fe_2O_3/Pt respectively. This chapter provides construction details of SS-CSSC and material, optical and *J-V* characterisation results.

6.1 FTO/CuI/Cu_2S/Fe_2O_3/Pt

In chapter 5, it was mentioned that the Eu^{3+}/Eu^{2+} redox couple was used as the electrolyte for the PEC measurements of cathodic semiconductor sensitised photoelectrodes (i.e. CuI/Cu_2S). The Eu^{3+}/Eu^{2+} redox couple has fast charge transfer kinetics and is suitable to be employed in the PEC characterisation of cathodic semiconductor sensitised photoelectrodes such as CuI/Cu_2S. Our electrodes studied in contact with Eu^{3+}/Eu^{2+} redox couple in wet liquid-junction PEC cell have shown excellent PEC performance for a CSSC. However, due to the volatile nature of the organic solvent and sealing difficulties, the wet liquid-junction PEC cells would not be suitable for long term applications, due to evaporation of the solvent [287]. Therefore, replacing the wet liquid-junction by employing an *n*-type semiconductor as an electron collector is considered to be a sensible approach to address the above mentioned technological issues. In this section the SS-CSSC based on (CuI/Cu_2S/Fe_2O_3) has been introduced, cell construction and characterisation details have been discussed. For the

fabrication of SS-CSSC, CuI and Cu_2S have been prepared by the methods as discussed in chapters 4 and 5. In order to construct a working cell, Fe_2O_3 was used as the *n*-type electrode collecting phase. After selecting the best performing CuI/Cu_2S, Fe_2O_3 was then deposited on the top layer (the Cu_2S layer coated on CuI electrode) by using the AACVD method. Details of the AACVD method have been discussed in chapter 3. The study focuses on different layers of Fe_2O_3 on the CuI/Cu_2S electrode.

6.1.1 X-ray Diffraction (XRD) analysis

The XRD patterns shown in Fig. 6-1 are that of the complete SS-CSSC (CuI/Cu_2S/Fe_2O_3) at different deposition times of Fe_2O_3.

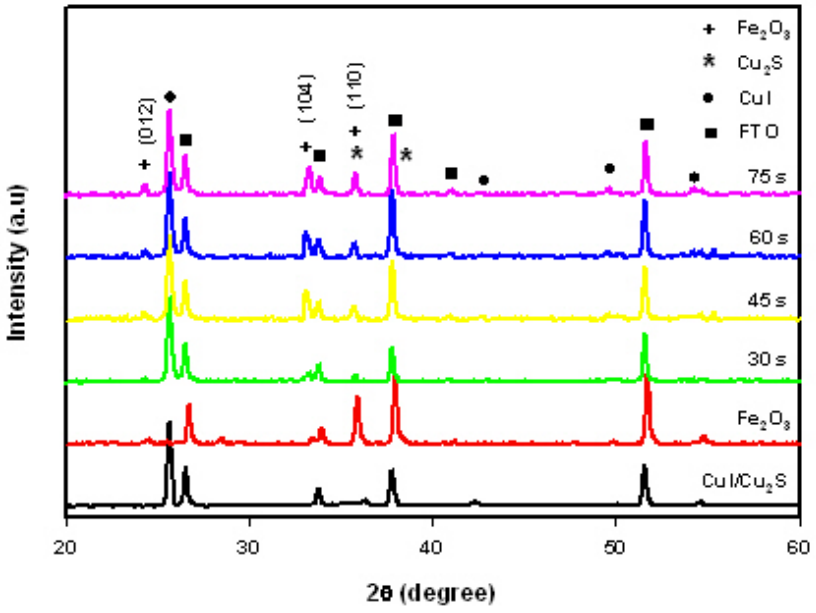

Fig. 6-1: XRD spectra of Fe_2O_3 electrode, CuI/Cu_2S electrode and CuI/Cu_2S/Fe_2O_3 cell corresponding to the various deposition times of Fe_2O_3.

All the existing reflections in spectra can be identified as those of CuI, Cu_2S and Fe_2O_3, and impurities cannot be detected by XRD exist in the complete cell as well as the bare Fe_2O_3 and CuI/Cu_2S electrodes. The strong reflection for the bare thin film of Fe_2O_3 is (110) indicating the growing direction of the thin film prepared by AACVD as reported in the literature [288].

In addition, the other relatively weak reflections obtained correspond to the (012) and (104) reflections.

6.1.3 Optical absorption analysis

The UV-Vis absorption spectra of Fe_2O_3 coated CuI/Cu_2S electrodes are shown in Fig. 6-2 and 6-3.

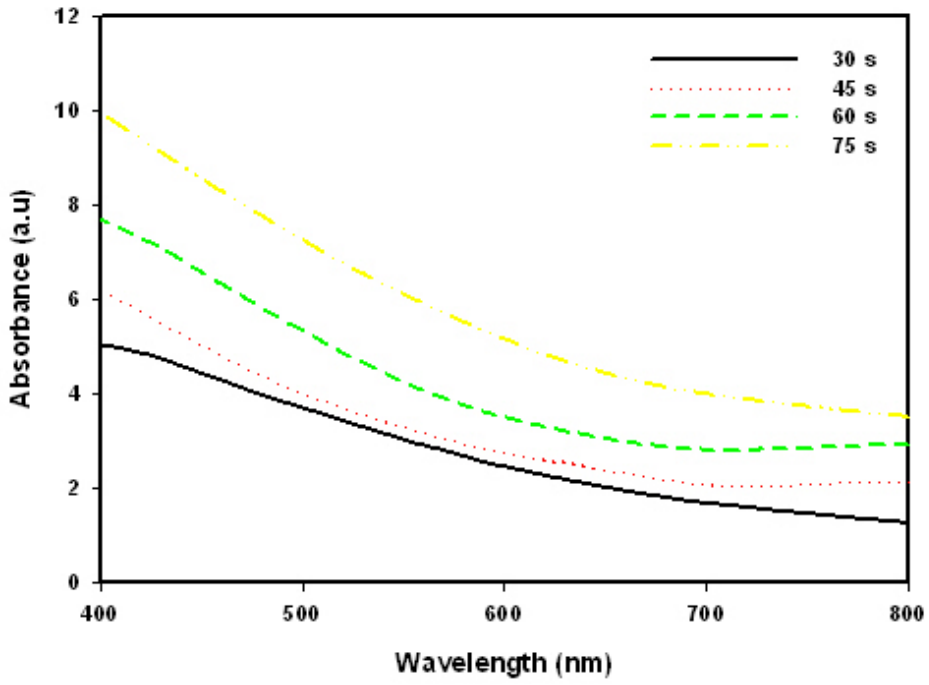

Fig. 6-2: Absorbance spectra of CuI/Cu_2S/Fe_2O_3 cell corresponding to the various deposition times of Fe_2O_3 on CuI/Cu_2S.

The effect of the deposition time of Fe_2O_3 (that will act as an electron collector in the SS-CSSC) on device performance was determined. The absorption spectrum of SS-CSSC shows that it absorbs in the UV region and its absorbance is extended to the visible light range up to 590 nm. This agrees with the literature where the Fe_2O_3 absorbs light up to 590 nm, which corresponds to a band gap of around 2.1 eV [289,290]. The results of the spectra suggest that all the electrodes exhibit similar absorption intensity which is due to the band gap absorption

in Fe_2O_3. In other words, it is not possible to distinguish the contributions of the CuI and Cu_2S at 420 and 570 nm in the absorbance spectra.

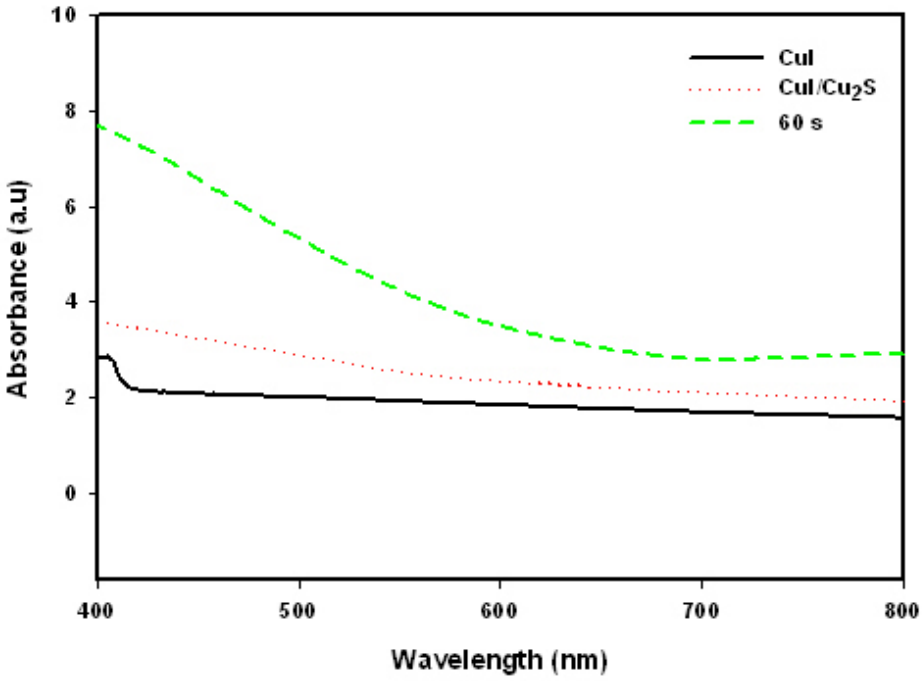

Fig. 6-3: Absorbance spectra for bare CuI electrode, CuI/Cu_2S electrode and complete SS-CSSC corresponding to the 60 s deposition time of Fe_2O_3.

6.1.4 Current-voltage analysis

The main objective of this study is to investigate the feasibility of fabricating SS-CSSC. Hence testing the PEC properties of the device is paramount. Fig. 6-4 illustrates the illumination current voltage behaviour for the different deposition times of Fe_2O_3 SS-CSSC devices.

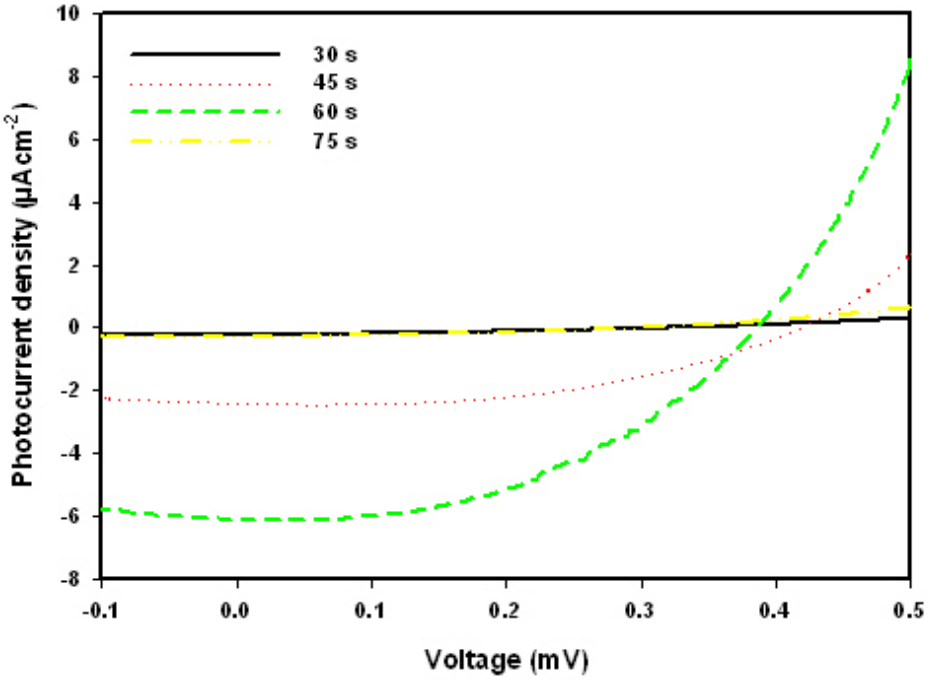

Fig. 6-4: *J-V* characteristics of CuI/Cu_2S/Fe_2O_3 cell corresponding to the various deposition times of Fe_2O_3.

The SS-CSSC cell made from 60 s Fe_2O_3 deposition exhibit the best solid state performance compared to the other deposition times. As shown in Table 6-1, the short-circuit current density (J_{sc}) of 6 μAcm^{-2}, open circuit-voltage (V_{oc}) of 0.38 V and a fill factor (*FF*) of 0.47, resulting in overall efficiency η of 0.0011% have been recorded. As deposited, the J_{sc} increases with the amount of Fe_2O_3, which can be attributed to an enhanced absorption of the incident light and charge separation [291]. The V_{oc} slightly increases from 0.26 V (PEC) up to 0.38 V which agrees with the V_{oc} estimated by plotting band energy as shown in Fig 6-5. The band energy diagram indicates that the V_{oc} is supposed to be less than 0.5 V. The maximum V_{oc} achieved in this study is about 0.42 V for 45 s deposition time.

Table 6-*1*: The PV parameters of SS-CSSC measured based on CuI/Cu_2S/Fe_2O_3 cell performance corresponding to the various deposition times of Fe_2O_3.

Time deposition (s)	V_{oc} **(mV)**	J_{SC} **(µAcm^{-2})**	**Fill Factor (FF)**	**Efficiency (%)**
30	0.31	-0.23	0.34	2.4 x 10^{-5}
45	0.42	-2.42	0.48	4.9 x 10^{-4}
60	0.39	-6.08	0.47	1.1 x 10^{-3}
75	0.30	-0.28	0.36	3.0 x 10^{-5}

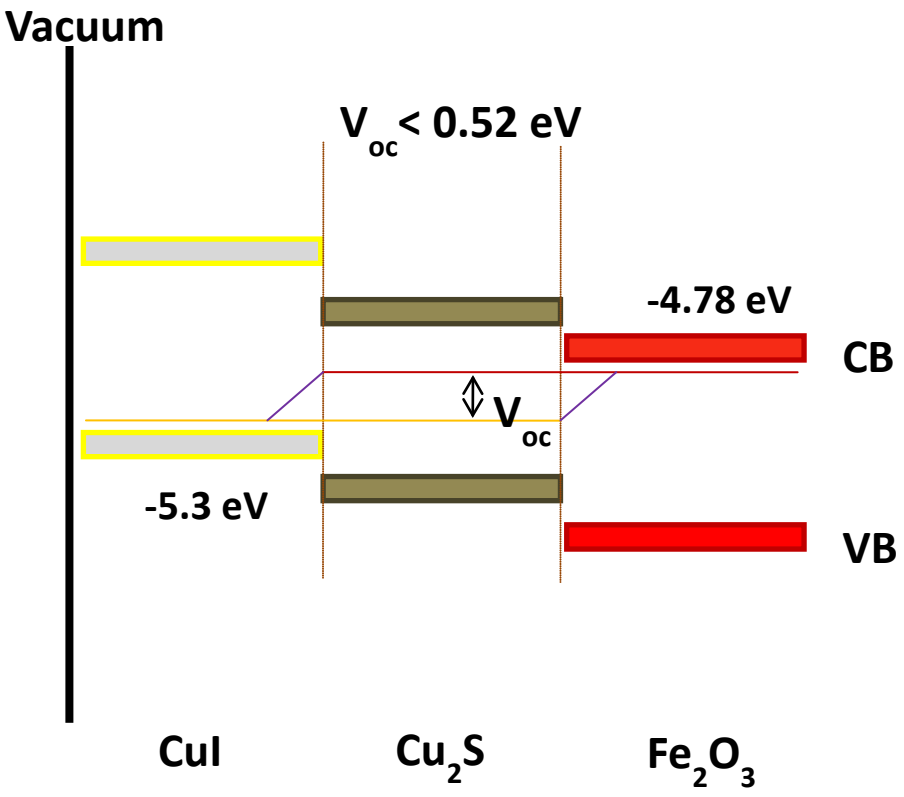

Fig. 6-5: Energy band diagram of the CuI/Cu_2S/Fe_2O_3 cell.

The fill factor (FF) increases as the deposition time is increased. The variation of FF suggests a limitation in the built-in electric field [292] which comes from the fixed hole collector (CuI) and absorber layer (Cu_2S) deposition conditions. The decrease of FF is partly compensated by the increase of J_{sc}. The highest efficiency recorded in this study is about 0.0011% for 60 s deposition time. Overall, from this set of data, it can be concluded that the thickness (amount of Fe_2O_3) of the bottom cell is very important for the total current of the SS-CSSC, which will affect the performance of the cell.

The current voltage measurements also have been carried out in dark conditions as illustrated in Fig. 6-6.

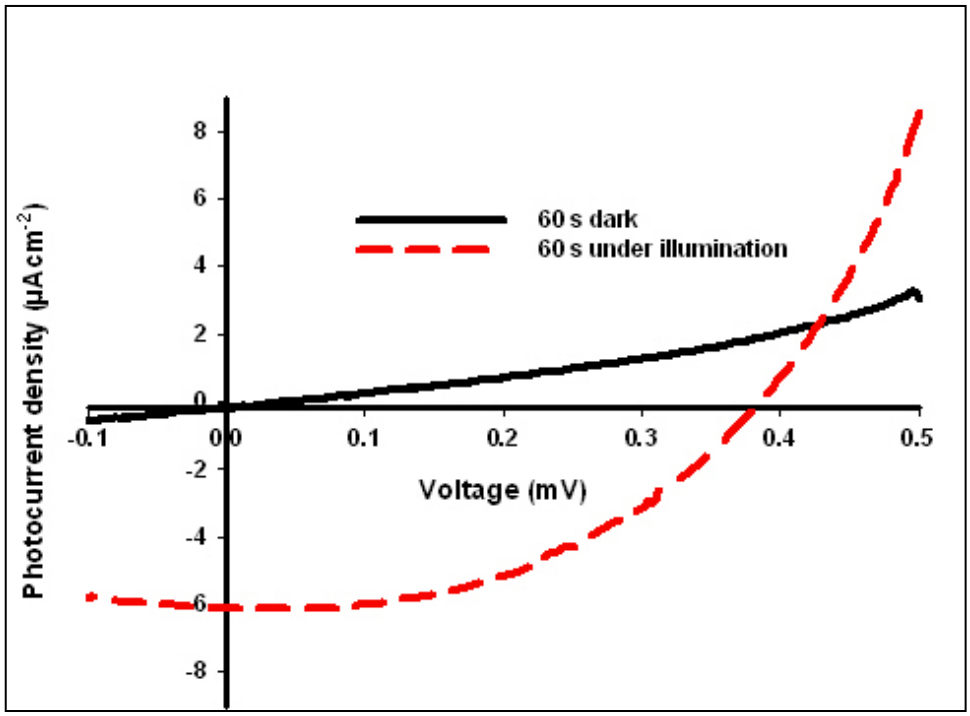

Fig. 6-6: Dark and under illumination of *J-V* characterization of CuI/Cu_2S/Fe_2O_3cell corresponding to the 60 s deposition time of Fe_2O_3.

The result shows that the dark current exhibited linear *J-V* characteristic of the contact between Pt and the electrode indicating an ohmic behaviour. This means without the light the SS-CSSC is not forming any junction which can generate electron hole pairs. The ohmic behaviour is in agreement with the poor solar cells performance [293]. However, under

illumination the rectifying behaviour for the cell was attributed to the junction formation and charge separation [294].

As can be seen in the results, the photocurrent density is lower if compared to the CSSC, as presented in chapter 5. Although the current is generated and collected, the photocurrent density of SS-CSSC remains very poor due to the electrical contact between Cu_2S and Fe_2O_3 layer (poor metal-metal contact). The second reason may be due to the *p*-type behaviour which is governed by the holes as the majority charge carriers. The minority charge carrier will inject easily in the presence of electrolyte. The electrolyte (electron scavenger), the electron can move faster and produce appropriate amounts of photocurrent density. In this situation less recombination will happen. The third possible reason may be due to the very close gap between the conduction bands of Cu_2S and Fe_2O_3. Because of the close energy band gap different, only a small amount of electrons from the excited state of Cu_2S will be injected to the Fe_2O_3 as shown in Fig. 6-5. The gap difference between these two is 0.34 eV.

6.2 FTO/NiO/Cu_2S/Fe_2O_3/Pt

Solid state solar cells based on FTO/ NiO/Cu_2S/Fe_2O_3/Pt have been constructed using a series of different deposition times of Fe_2O_3. The SS-CSSC have been fabricated by using AACVD method.

6.2.1 X-ray Diffraction (XRD) analysis

The XRD patterns of Fe_2O_3, NiO/Cu_2S and the complete cell at different deposition times of Fe_2O_3 are illustrated in Fig. 6-7.

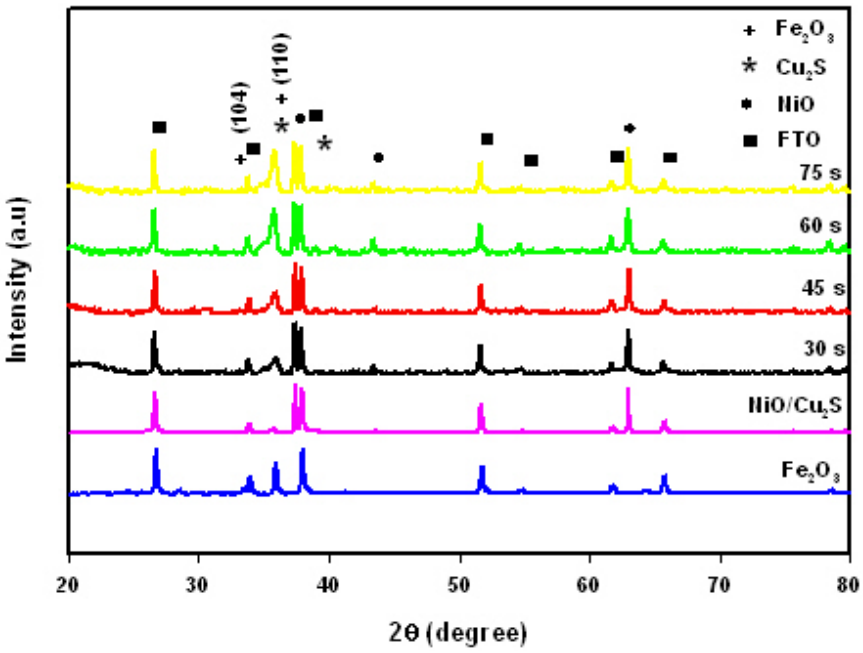

Fig. 6-7: XRD spectra of Fe_2O_3 electrode, NiO/Cu_2S electrode and NiO/Cu_2S/Fe_2O_3 cell corresponding to the various deposition times of Fe_2O_3.

All the reflections can be indexed to the four different materials, namely FTO, NiO, Cu_2S and Fe_2O_3 and no other detectable materials exist. After depositing the Fe_2O_3 layer on the surface of the NiO/Cu_2S electrode, the characteristic (104) and (110) reflections of Fe_2O_3 were detected. The XRD pattern shows that the Fe_2O_3 particles are growing in the (110) direction and the reflection becomes stronger as the deposition time is increased hence the overlapping Cu_2S peaks become very difficult to identify.

6.2.3 Optical absorption analysis

The UV-Visible spectra for the complete SS-CSSC based on FTO/NiO/Cu_2S/Fe_2O_3/Pt electrodes are illustrated in Fig. 6-8. The increase in deposition time of Fe_2O_3 caused an increase in light absorption.

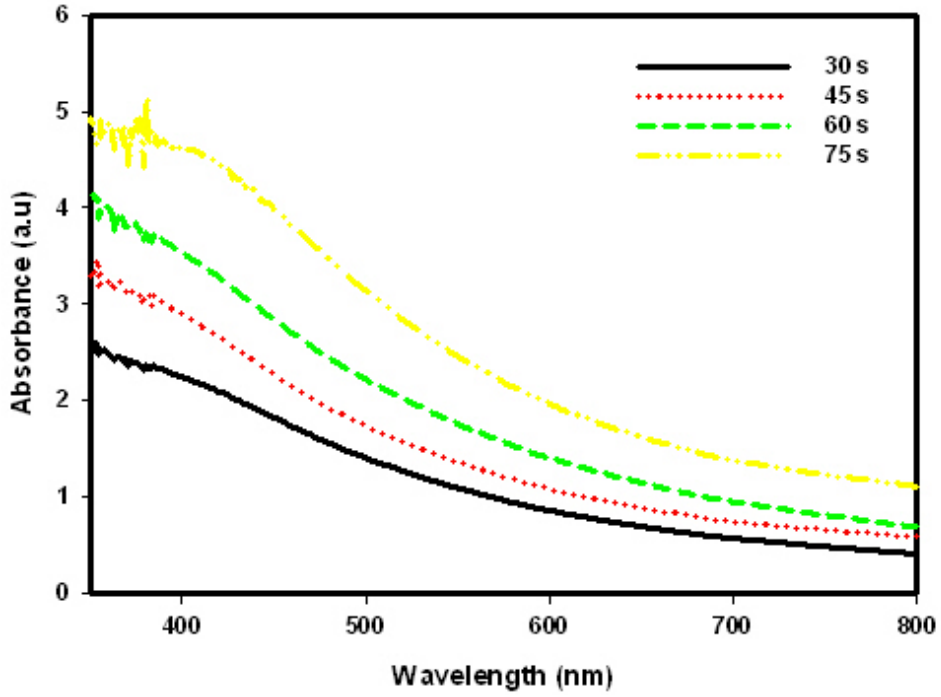

Fig. 6-8: Absorbance spectra of NiO/Cu_2S/Fe_2O_3 cell corresponding to the various deposition times of Fe_2O_3.

The spectra for the bare NiO, NiO/Cu_2S and the complete SS-CSSC (as shown as 60 s in the graph) are plotted together in order to study the difference between the electrode absorption. The NiO/Cu_2S electrode shows improved absorption after coating with a Fe_2O_3 layer as shown in Fig. 6-9 compared to the bare NiO electrode which only absorbs in the UV region.

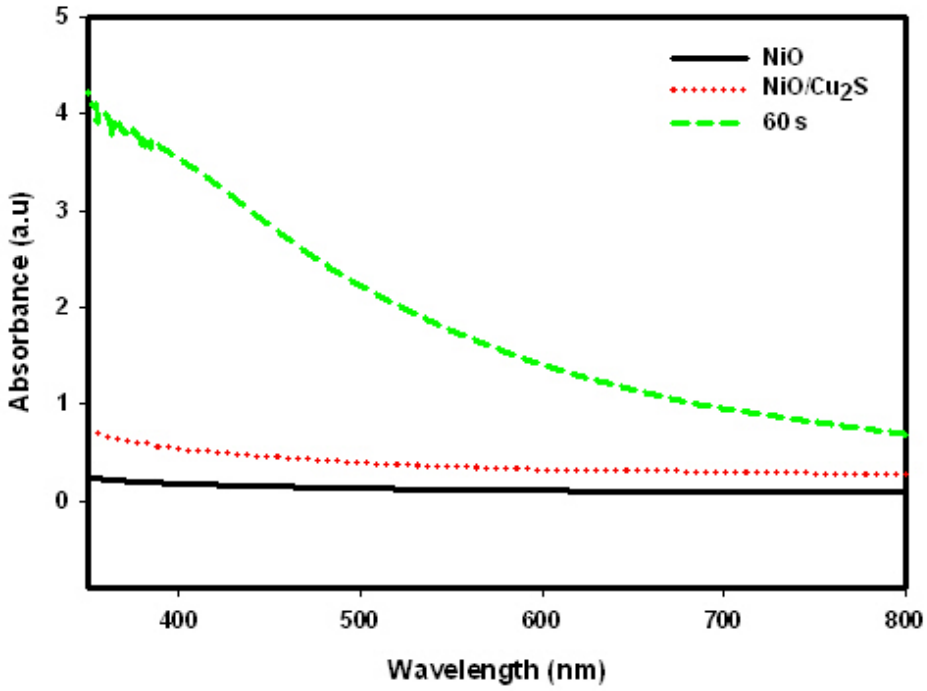

Fig. 6-9: Absorbance spectra for bare NiO electrode, NiO/Cu_2S electrode and complete SS-CSSC corresponding to the 60 s deposition time of Fe_2O_3.

6.2.4 Current-voltage analysis

The *J-V* characteristics of the SS-CSSC fabricated corresponding to the different deposition times of Fe_2O_3 are shown in Fig. 6-10.

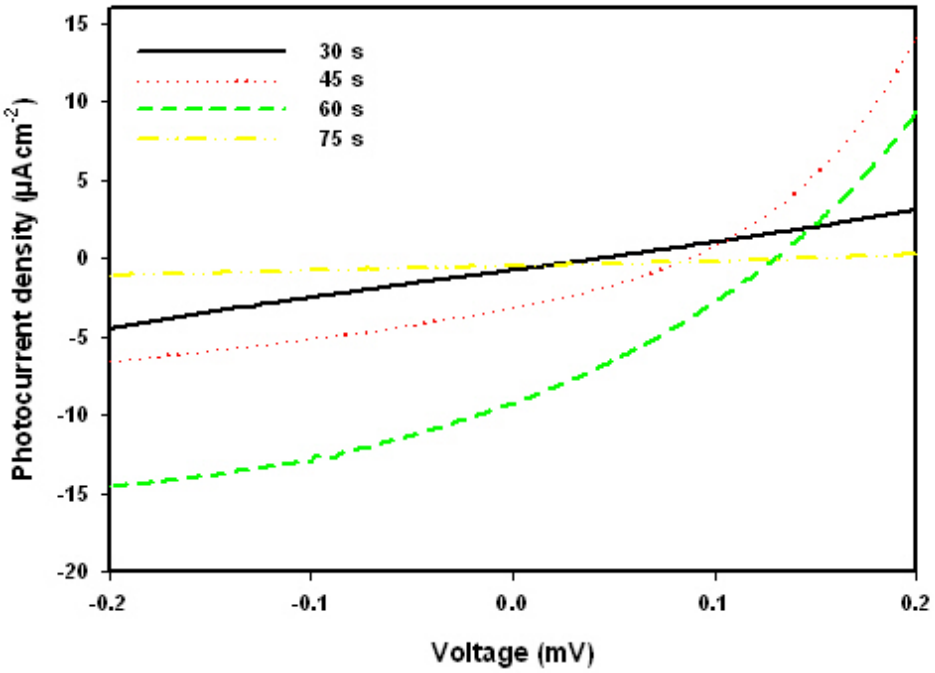

Fig. 6-10: *J-V* characteristics of NiO/Cu_2S/Fe_2O_3 cell corresponding to the various deposition times of Fe_2O_3.

The corresponding photovoltaic parameters extracted from the curves, as well as photovoltage estimated in open circuit conditions, are reported in Table 6-2.

Table 6-*2*: The PV parameters of SS-CSSC measured based on $NiO/Cu_2S/Fe_2O_3$ cell performance corresponding to the various deposition times of Fe_2O_3.

Deposition time (s)	V_{oc} **(V)**	J_{SC} **(μAcm^{-2})**	**Fill Factor (*FF*)**	**Efficiency (%)**
30	0.04	-0.76	0.25	7.6×10^{-6}
45	0.09	-3.67	0.23	7.8×10^{-5}
60	0.13	-9.37	0.29	3.6×10^{-4}
75	0.14	-0.48	0.30	2.1×10^{-5}

At relatively low deposition time (30 s), the *J-V* curves exhibited characteristics very far from the ideal rectifying behaviour. Although some current is generated and collected, the PV effect remains very poor (looks like ohmic behaviour) due to the small amount of Fe_2O_3, which led to the leakages of charge carrier which can cause higher recombination and also lead to high series resistance [295]. The increase in the film thickness, i.e. deposition time, significantly improves the device performance. The shape of the graph shows rectifying behaviour which indicates an improved SS-CSSC. As shown in Table 6-2, the short-circuit current density (J_{sc}) of 9 μAcm^{-2}, open circuit-voltage (V_{oc}) of 0.13 V and a fill factor (FF) of 0.29, resulting in overall efficiency η of 0.0004 % have been recorded. For the cell where the deposition time of Fe_2O_3 is increased up to 75 s, the performance of the cell was found to be reduced. This is due to the high amount of Fe_2O_3, which led to an increased thickness of the cell. By increasing the thickness of the Fe_2O_3, the path that the electron has to travel before reaching the Pt contact will increase and these phenomena will lead to charge recombination, where the performance of the cell will reduce gradually [296]. These results indicate that the thickness of the Fe_2O_3 plays an important role in the fabrication of the ideal SS-CSSC. Compared to the SS-CSSC based on CuI as reported in Table 6-1, the SS-CSSC based on NiO exhibited higher photocurrent density. This is due to the nature of the inherent properties of CuI itself as superior to that of NiO in terms of suitability for this specific cell composition.

For example, the valence band of the NiO is lower compared to that of CuI as illustrated in Fig 6-11.

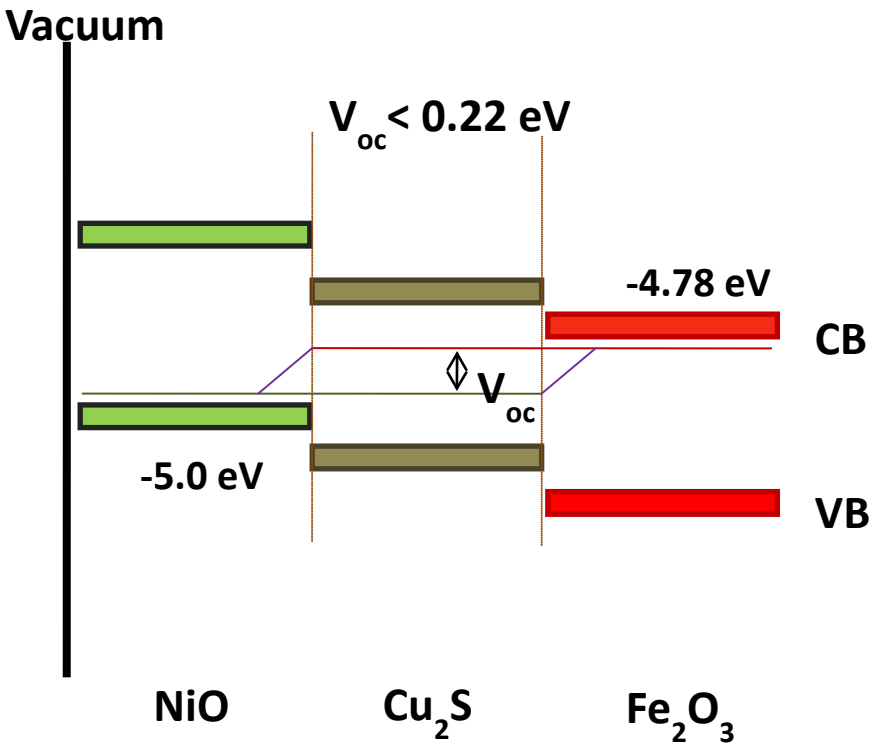

Fig. 6-11: Energy band diagram of NiO/Cu_2S/Fe_2O_3 cell.

According to Fig. 6-11, the V_{oc} of the cell is estimated to be less than 0.22 V and it agrees with the V_{oc} achieved in the cell measured and recorded as shown in Table 6-2. The maximum V_{oc} achieved is about 0.14 V which is the highest value reported. As mentioned above, a smaller V_{oc} would lead to reduced performance of the cell. The other parameter that affects the V_{oc} is the dark current. This is due to the increase in dark current reducing the V_{oc} of the cell [297]. Fig. 6-12 shows the *J*-*V* measured photocurrent density under dark and illumination for the best performing of the SS-CSSC.

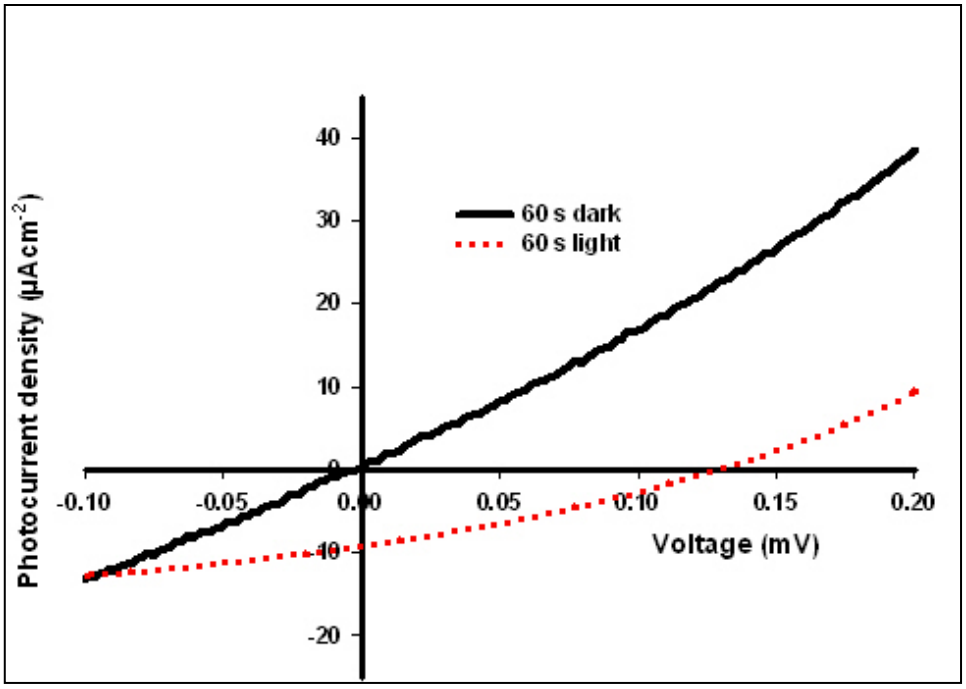

Fig. 6-12: Dark and under illumination *J-V* characterization of NiO/Cu_2S/Fe_2O_3 cell corresponding to the 60 s deposition time of Fe_2O_3.

As a result the dark current obtained in this study indicated ohmic behaviour where it crosses at 0 V potential. This can be explained by the band energy level of the material at the interface being in equilibrium [298]. The Fermi energy of Cu_2S interface (corresponding to the free energy of electrons in this film after thermalisation) equilibrates with the potential of the valence band NiO resulting in zero output voltage. Under these conditions, the SS-CSSC is effectively insulating, so no photocurrent can be observed. In contrast, in the presence of light the hole injection to the NiO conduction band and the excited state electron in the conduction band of Cu_2S were injected to the conduction band of Fe_2O_3, resulting in the cell becoming conductive. This is due to the shift in the Fermi level under irradiation which increases the free energy of injected electrons and is responsible for the generation of the photovoltage in the external circuit [295].

6.3 Conclusion

The overall results achieved in this chapter confirmed our initial expectations that SS-CSSC based on the *p*-type semiconductor material can be constructed. The absorbance extended up to 590 nm, which is due to the incorporation of Fe_2O_3. Under illumination the SS-CSSC shows very low performance of 6 and 9 μAcm^{-2} for $CuI/Cu_2S/Fe_2O_3$ and $NiO/Cu_2S/Fe_2O_3$ cell, respectively. This indicates that both of these cells do not function very well but still show current flow due to hole injection. This may be due to the lack of contact between the absorber and electron collector.

Chapter 7: Conclusions and future work

7.0 Conclusions and future work

7.1 Conclusions

A key question in the development and operation of SS-CSSC is, 'what is the operation mechanism of the solid-state cathodic semiconductor solar cell (SS-CSSC)?' In addition, further questions, such as: 'is it possible to make SS-CSSC and what are the strategies leading us to prove that it works?' need to be answered. The work in this project was aimed at answering these questions. The key objective of the current thesis was to prove and develop a cathodic semiconductor sensitised solar cell. We have succeeded in constructing both wet liquid-junction based cathodic semiconductor sensitised photoelectrochemical cell as well as a complete solid-state cathodic semiconductor sensitised solar cell. The results provide a range of new and original findings. However, the present performance of SS-CSSC is still far lower than a respectable power output from a solar cell (The photocurrent density of a few $mAcm^{-2}$ and the photovoltage of about 600 -700 mV could be a respectable target). The key conclusions conducted within this doctoral project are summarised in this section of the thesis.

The CuI electrodes were deposited on FTO substrates by electrodeposition (ED and PED) as well as by AAD technique and the detailed discussion of it is presented in chapter 4. As far as we are aware, this doctoral thesis is the first report on the preparation of CuI films by the PED and AAD techniques. Individual features in PED electrodes are relatively smaller than that of ED electrodes indicating an improved electrode texture. The AAD electrode had fine individual features and high texture compared to both ED and PED electrodes. Average crystallite size estimated based on XRD data shows a similar trend. The orientation of both ED and PED electrodes were predominant in the (111) direction. Despite the dominant (111) peak, a number of other CuI peaks were also identified for the AAD electrode, indicating its polycrystalline nature. The AAD electrode shows the highest reported photocurrent density for a CuI electrode under AM1.5 illumination indicating the effect of its fine individual features, improved texture and high internal surface area. The AAD CuI electrode showed a significant dark current at relatively negative potentials whereas it was negligible for both ED and PED

CuI electrodes. The cause for the dark current in AAD electrode was found to be the existence of shunting paths through the direct contact between FTO/electrolyte.

A robust system involving AACVD has been developed in order to grow nanostructured NiO electrodes on FTO coated glass substrates. The XRD and FEGSEM data showed that the orientation, crystallite size and morphology of NiO electrodes can be controlled. Studies of chopped *J-V* (current-voltage) characteristics show a direct relation between (111) preferential orientation and the cathodic photocurrent density. The electrodes deposited at 475°C have demonstrated the best photocurrent density of 5.5 μA cm^{-2} at 0.0 V vs. Ag/AgCl/3 M KCl as reported for a bare NiO photocathode. IPCE studies conducted by sensitizing all the electrodes with C343 dye has shown that the best IPCE occurred for nanostructured electrodes constructed at 475 °C (~20%). The trend of IPCE data recorded for dye sensitized NiO electrodes correlate well with the trend that was observed in chopped current-voltage studies of bare NiO electrodes. This work suggests that if a dye with better light absorbing properties in the red region is employed to sensitise the NiO electrodes that are preferentially oriented in the (111) direction, the light harvesting efficiency of the photocathode in the red region can be improved.

Chapter 5 describes the successful fabrication of CuI and NiO electrodes with Cu_2S as the light harvesting material in cathodic semiconductor sensitised solar cells. The photosensitised CuI and NiO electrodes were tested with the Eu^{2+}/Eu^{3+} and I_3^-/I^- redox couple electrolytes respectively. The UV-Visible absorption studies suggested that the photocathodes exhibited enhanced absorption and extended the absorption threshold up to 570 nm in the visible region of solar spectra by incorporating the light absorber material Cu_2S. The PEC performances of CuI/Cu_2S and NiO/Cu_2S electrodes were greater than the bare CuI and NiO electrodes confirming the photosensitisation. It is clear that both CuI and NiO porous electrodes sensitized by Cu_2S can be used for fabricating complete solid-state solar cells (SS-CSSC). Under illumination the external monochromatic efficiency (IPCE) achieved is reasonably high for the cathodic sensitized solar which was around ~19 and ~7% for the CuI/Cu_2S and NiO/Cu_2S electrodes respectively.

The final part of this work (Chapter 6) presents the fabrication of SS-CSSC based on the CuI/Cu_2S and NiO/Cu_2S electrodes incorporating Fe_2O_3 as the electron collector. Fe_2O_3

was selected as the electron conducting media considering its band energy positions (comparable to that of CuI/Cu_2S and NiO/Cu_2S). However, we are aware that it is not the best material in terms of light absorbance properties. The light absorbance of the device was extended to 590 nm, which is due to the incorporation of Fe_2O_3. The CuI and NiO were used as the *p*-type materials and Fe_2O_3 was used as *n*-type material Cu_2S was used as the light absorber layer. The results achieved confirmed our initial expectations that the SS-CSSC can be constructed, although the power efficiency values are still low. Under illumination, the SS-CSSC shows very low photocurrent density of ~ 6 and ~ 9 μAcm^{-2} for CuI/Cu_2S/Fe_2O_3 and NiO/Cu_2S/Fe_2O_3 solar cells respectively, indicating both of these cells need further improvements. This may be due to the poor contacts between the individual interfaces (i.e. the light absorber and electron collector contact). It is believed that high photocurrent and efficiency can also be achieved by changing the electron collector from the semiconductor material to an electron conducting polymer which will improve the contact to the Cu_2S layer. Finally, if the SS-CSSC can be further improved to a respectable light to electricity generation performance, it will give new hope of fabricating tandem cells thereby offering further opportunities and avenues to construct new generation solar cells.

7.2 Future work

One of the problems in the fabrication of SS-CSSC is their low efficiency. This is partly due to the fact that majority charge carriers of the primary photoelectrodes are holes, compared to that of the anodic solid-state semiconductor sensitised solar cells where the majority charge carriers are electrons. However, SS-CSSC research has attracted much attention due to the application in tandem solar cells which absorb a wide range of sunlight compared to that of the single junction solar cells. This work demonstrates that such devices can be prepared by using simple and low cost methods. The development and improvement of the SS-CSSC is still at early stage compared to the other solid state solar cells, however, their efficiencies are suitable to be applied in tandem solar cells because photoactive cathodic side will generate more holes in order to complete the reduction and oxidation inside the redox mediator which led improve the performance of the solar cell. Further optimization in the fabrication of SS-CSSC is necessary. When it comes to further work and improvements in SS-CSSC, one may want to consider the following factors in order to achieve high efficiencies:

- Optimization of the hole collector morphology by controlling the particle size distribution to avoid pinholes and hence obtain a large surface area. This will allow lighter adsorption, high mobility of hole transfer and increase the surface coverage of the absorbing material.
- Optimization of the absorber materials by using suitable band gap materials with high light absorption. This is due to the absorption of the light being a very important parameter to enhance light trapping and charge separation in the system.
- Development of new suitable band gap n-type materials from inorganic semiconductor materials or electron conducting polymers. The material must be photoactive, have high mobility electron transfer and must easily adsorb on the absorber layer.
- Optimization of the electrolyte by increasing the electron transport in the redox couple and choosing a suitable redox potential electrolyte for CSSC.

However, the fabrication of the SS-CSSC based on inorganic semiconductor really depends on the improvement of the particles size synthesis. The main problem in the fabrication of SS-CSSC is finding materials with suitable band gaps, synthesis methods and reproducibility. However, if all the problems are considered and appropriate actions are taken, there are no reasons for SS-CSSC to not be able to match the efficiencies of the other type of solid state devices and at the same time improve the device stability.

Chapter 8: Dissemination

8.0 Dissemination of Results

The results founds during this PhD have been dissemination to other members of the scientific community through presentation at conference and groups meeting. Below are the list of conferences and meetings where the results have been published.

8.1 Conference and meeting

2009 Poster Presentation, Great Western Regional Electrochemistry Meeting, Bath.

2009 Poster Presentation, Electrochem 2009, Royal Society of Chemistry, Manchester.

2010 Oral Presentation, Midlands Electrochemistry Meeting, Leicester.

8.2 Articles in Preparation

1. Asif Ali Tahir, M.A. Mat-Teridi, S.Senthilarasu, K.G. Upul Wijayantha, "Enhanced Solar Energy Conversion Efficiency of *p*-NiO Photocathode by Controlling the Crystallographic Orientation".
2. K.G. Upul Wijayantha, M.A. Mat-Teridi, "Enhanced Photoelectrochemical Properties of Copper Iodide by Manipulating the Electrode Texture".

Chapter 9: References

9.0 References

[1] Mark Jaccard, Sustainable Fossil Fuels: The Unusual Suspect in the Quest for Clean and Enduring Energy, First edition ed., Cambridge University Press, Cambridge, New York, Melbourne, Madrid, Cape Town, Singapore, São Paulo, 2006.

[2] J. Chevalier M., The New Energy Crisis: Climate, Economics and Geopolitics, First edition ed., Palgrave Macmillan, United Kingdom, United State of America, 2009.

[3] T. Markvart, L. Castaner, Practical Handbook of Photovoltaics Fundamentals and Applications, First Edition ed., Elsevier, United Kingdom, United State of America, Japan, 2003.

[4] A. Luque, S. Hegedus, Handbook of Photovoltaic Science and Engineering, First Edition ed., Wiley, USA, Germany, Australia, Singapore, Canada, 2003.

[5] B. Oregan, M. Gratzel, A Low-Cost, High-Efficiency Solar-Cell Based on Dye-Sensitized Colloidal TiO_2 Films, Nature 353 (1991) 737-740.

[6] R. Konenkamp, P. Hoyer, A. Wahi, Heterojunctions and devices of colloidal semiconductor films and quantum dots, Journal of Applied Physics 79 (1996) 7029-7035.

[7] C. Chen, M. Wang, J. Li, N. Pootrakulchote, L. Alibabaei, C. Ngoc-le, et al., Highly Efficient Light-Harvesting Ruthenium Sensitizer for Thin-Film Dye-Sensitized Solar Cells, ACS Nano 3 (2009) 3103-3109.

[8] R. Tena-Zaera, M.A. Ryan, A. Katty, G. Hodes, S. Bastide, C. Lévy-Clément, Fabrication and characterization of ZnO nanowires/CdSe/CuSCN eta-solar cell, Comptes Rendus Chimie 9 (2006) 717-729.

[9] M.K. Nazeeruddin, A. Kay, I. Rodicio, R. Humphry-Baker, E. Mueller, P. Liska, et al., Conversion of light to electricity by cis-X2bis(2,2'-bipyridyl-4,4'-dicarboxylate)ruthenium(II)

charge-transfer sensitizers (X = Cl-, Br-, I-, CN-, and SCN-) on nanocrystalline titanium dioxide electrodes, J. Am. Chem. Soc. 115 (1993) 6382-6390.

[10] D. Wei, Dye Sensitized Solar Cells, International Journal of Molecular Sciences 11 (2010) 1103-1113.

[11] R. Dharmadasa, K.G.U. Wijayantha, A.A. Tahir, ZnO–SnO2 composite anodes in extremely thin absorber layer (ETA) solar cells, J Electroanal Chem 646 (2010) 124-132.

[12] C. Lévy-Clément, A. Katty, S. Bastide, F. Zenia, I. Mora, V. Munoz-Sanjose, A new CdTe/ZnO columnar composite film for Eta-solar cells, Physica E: Low-dimensional Systems and Nanostructures 14 (2002) 229-232.

[13] D. Anca, TiO2 thin layers with controlled morphology for ETA (extremely thin absorber) solar cells, Thin Solid Films 511–512 (2006) 195-198.

[14] J. Hernández-Borja, Y.V. Vorobiev, R. Ramírez-Bon, Thin film solar cells of CdS/PbS chemically deposited by an ammonia-free process, Solar Energy Mater. Solar Cells 95 (2011) 1882-1888.

[15] R. Tena-Zaera, A. Katty, S. Bastide, C. Lévy-Clément, B. O'Regan, V. Muñoz-Sanjosé, ZnO/CdTe/CuSCN, a promising heterostructure to act as inorganic eta-solar cell, Thin Solid Films 483 (2005) 372-377.

[16] T. Hsueh, Y. Chen, S. Chang, S. Wang, C. Hsu, Y. Lin, et al., ZnO nanowire-based CO sensors prepared on patterned ZnO:Ga/SiO_2/Si templates, Sensors Actuators B: Chem. 125 (2007) 498-503.

[17] M.A. Gondal, Q.A. Drmosh, Z.H. Yamani, T.A. Saleh, Synthesis of ZnO2 nanoparticles by laser ablation in liquid and their annealing transformation into ZnO nanoparticles, Appl. Surf. Sci. 256 (2009) 298-304.

[18] Y.F. Zhu, G.H. Zhou, H.Y. Ding, A.H. Liu, Y.B. Lin, Y.W. Dong, Synthesis and characterization of highly-ordered ZnO/PbS core/shell heterostructures, Superlattices and Microstructures 50 (2011) 549-556.

[19] S. Chu, W. Water, J. Liaw, Influence of postdeposition annealing on the properties of ZnO films prepared by RF magnetron sputtering, Journal of the European Ceramic Society 23 (2003) 1593-1598.

[20] J. Bandara, H. Weerasinghe, Solid-state dye-sensitized solar cell with p-type NiO as a hole collector, Solar Energy Mater. Solar Cells 85 (2005) 385-390.

[21] M. Green A., Solar Cells Operating Principles, Technology, and System Application, First Edition ed., Prentice-Hall, Inc., United States of America, 1982.

[22] M.A. Green, Photovoltaic principles, Physica E: Low-dimensional Systems and Nanostructures 14 (2002) 11-17.

[23] D.M. Chapin, C.S. Fuller, G.L. Pearson, A new silicon p-n junction photocell for converting solar radiation into electrical power [3], J. Appl. Phys. 25 (1954) 676-677.

[24] F. Meillaud, A. Shah, C. Droz, E. Vallat-Sauvain, C. Miazza, Efficiency limits for single-junction and tandem solar cells, Solar Energy Mater. Solar Cells 90 (2006) 2952-2959.

[25] J. Zhao, A. Wang, M.A. Green, F. Ferrazza, 19.8% efficient "honeycomb" textured multicrystalline and 24.4% monocrystalline silicon solar cells, Appl. Phys. Lett. 73 (1998) 1991-1993.

[26] M. Green A., Third Generation Photovoltaics: Advanced Solar Energy Conversion, First Edition ed., Springer, Berlin, Heidelberg, New York, 2003.

[27] M.A. Green, K. Emery, Y. Hishikawa, W. Warta, E.D. Dunlop, Solar cell efficiency tables (Version 38), Prog Photovoltaics Res Appl 19 (2011) 565-572.

[28] National Renewable Energy Laboratory (NREL), The Best Research Efficiencies of Solar Cells, 2012 (2012).

[29] O. Schultz, S.W. Glunz, G.P. Willeke, Multicrystalline silicon solar cells exceeding 20% efficiency, Prog Photovoltaics Res Appl 12 (2004) 553-558.

[30] 27.6% Conversion Efficiency a New Record for Single-Junction Solar Cells Under 1 Sun Illumination. Proceedings, 37th IEEE Photovoltaic Specialist Conference, Seattle, June 2011; 2011 (2011).

[31] I. Repins, M.A. Contreras, B. Egaas, C. DeHart, J. Scharf, C.L. Perkins, et al., 19·9%-efficient ZnO/CdS/CuInGaSe2 solar cell with 81·2% fill factor, Prog Photovoltaics Res Appl 16 (2008) 235-239.

[32] I. Mora-Sero, S. Gimenez, F. Fabregat-Santiago, E. Azaceta, R. Tena-Zaera, J. Bisquert, Modeling and characterization of extremely thin absorber (eta) solar cells based on ZnO nanowires, Phys.Chem.Chem.Phys. 13 (2011) 7162-7169.

[33] A. Nattestad, A.J. Mozer, M.K.R. Fischer, Y.-. Cheng, A. Mishra, P. Bauerle, et al., Highly efficient photocathodes for dye-sensitized tandem solar cells, Nat Mater 9 (2010) 31-35.

[34] P. Qin, H. Zhu, T. Edvinsson, G. Boschloo, A. Hagfeldt, L. Sun, Design of an Organic Chromophore for P-Type Dye-Sensitized Solar Cells, J. Am. Chem. Soc. 130 (2008) 8570-8571.

[35] J. Bandara, H. Weerasinghe, Solid-state dye-sensitized solar cell with p-type NiO as a hole collector, Solar Energy Mater. Solar Cells 85 (2005) 385-390.

[36] J.S. Blakemore, Solid State Physics, 2nd edition ed., Cambridge University Press, Cambridge, 1985.

[37] P. Hofmann, Solid State Physics : an introduction, Wiley-VCH, Weinheim, 2008.

[38] H.O. Finklea, Semiconductor electrodes, Elsevier 1986.

[39] S.M. Sze, Semiconductor Devices: Physics and Technology, Wiley, New York ; Chichester, 1985.

[40] J. Nelson, The Physics of Solar Cells, First Edition ed., Imperial College Press, United Kingdom, 2003.

[41] F. Meillaud, A. Shah, C. Droz, E. Vallat-Sauvain, C. Miazza, Efficiency limits for single-junction and tandem solar cells, Solar Energy Mater. Solar Cells 90 (2006) 2952-2959.

[42] Atmospheric-Pressure-Spray, Chemical-Vapor-Deposited Thin-Film Materials Being Developed for High Power-to-Weight-Ratio Space Photovoltaic Applications, 2011 (2002).

[43] R. B.S., Enhancing the performance of silicon solar cells via the application of passive luminescence conversion layers, Solar Energy Mater. Solar Cells 90 (2006) 2329-2337.

[44] A. De Vos, Calculation of the maximum attainable efficiency of a single heterojunction solar cell, Energy Conversion 16 (1976) 67-78.

[45] D.J. Friedman, Progress and challenges for next-generation high-efficiency multijunction solar cells, Current Opinion in Solid State and Materials Science 14 (2010) 131-138.

[46] H. Li, R.L. Stolk, C.H.M. van der Werf, R.H. Franken, J.K. Rath, R.E.I. Schropp, Optimization of n–i–p protocrystalline SiGe:H thin film solar cells for application in thin film multijunction solar cells, J. Non Cryst. Solids 352 (2006) 1941-1944.

[47] S.R. Kurtz, J.M. Olson, P. Faine, The difference between standard and average efficiencies of multijunction compared with single-junction concentrator cells, Solar Cells 30 (1991) 501-513.

[48] T. Yamaguchi, Y. Uchida, S. Agatsuma, H. Arakawa, Series-connected tandem dye-sensitized solar cell for improving efficiency to more than 10%, Solar Energy Mater. Solar Cells 93 (2009) 733-736.

[49] M. Yanagida, N. Onozawa-Komatsuzaki, M. Kurashige, K. Sayama, H. Sugihara, Optimization of tandem-structured dye-sensitized solar cell, Solar Energy Mater. Solar Cells 94 (2010) 297-302.

[50] W. Shockley, H.J. Queisser, Detailed Balance Limit of Efficiency of p-n Junction Solar Cells, J. Appl. Phys. 32 (1961) 510-519.

[51] C.H. Henry, Limiting efficiencies of ideal single and multiple energy gap terrestrial solar cells, J. Appl. Phys. 51 (1980) 4494-4500.

[52] A. Martí, G.L. Araújo, Limiting efficiencies for photovoltaic energy conversion in multigap systems, Solar Energy Mater. Solar Cells 43 (1996) 203-222.

[53] R.R. King, D.C. Law, K.M. Edmondson, C.M. Fetzer, G.S. Kinsey, H. Yoon, et al., 40% efficient metamorphic GaInP/GaInAs/Ge multijunction solar cells, Appl. Phys. Lett. 90 (2007) 183516.

[54] S.P. Bremner, M.Y. Levy, C.B. Honsberg, Analysis of tandem solar cell efficiencies under AM1.5G spectrum using a rapid flux calculation method, Prog Photovoltaics Res Appl 16 (2008) 225-233.

[55] R.D. Rugescu, Solar Energy, Intech, Vukovar, Croatia, 2010.

[56] C.A.N. Fernando, A. Kitagawa, M. Suzuki, K. Takahashi, T. Komura, Photoelectrochemical properties of rhodamine-C18 sensitized p-CuSCN photoelectrochemical cell (PEC), Solar Energy Mater. Solar Cells 33 (1994) 301-315.

[57] J. He, H. LindstrÃm, A. Hagfeldt, S. Lindquist, Dye-Sensitized Nanostructured p-Type Nickel Oxide Film as a Photocathode for a Solar Cell, The Journal of Physical Chemistry B 103 (1999) 8940-8943.

[58] F. Vera, R. Schrebler, E. Muñoz, C. Suarez, P. Cury, H. Gómez, et al., Preparation and characterization of Eosin B- and Erythrosin J-sensitized nanostructured NiO thin film photocathodes, Thin Solid Films 490 (2005) 182-188.

[59] A. Nattestad, M. Ferguson, R. Kerr, Y. Cheng, U. Bach, Dye-sensitized nickel(II)oxide photocathodes for tandem solar cell applications, Nanotechnology 19 (2008) 295304.

[60] S. Mori, S. Fukuda, S. Sumikura, Y. Takeda, Y. Tamaki, E. Suzuki, et al., Charge-Transfer Processes in Dye-Sensitized NiO Solar Cells, The Journal of Physical Chemistry C 112 (2008) 16134-16139.

[61] P. Qin, H. Zhu, T. Edvinsson, G. Boschloo, A. Hagfeldt, L. Sun, Design of an Organic Chromophore for P-Type Dye-Sensitized Solar Cells, J. Am. Chem. Soc. 130 (2008) 8570-8571.

[62] S. Sumikura, S. Mori, S. Shimizu, H. Usami, E. Suzuki, Photoelectrochemical characteristics of cells with dyed and undyed nanoporous p-type semiconductor CuO electrodes, J. Photochem. Photobiol. A. 194 (2008) 143-147.

[63] J.H. Rhee, Y.H. Lee, P. Bera, S.I. Seok, Cu_2S-deposited mesoporous NiO photocathode for a solar cell, Chemical Physics Letters 477 (2009) 345-348.

[64] L. Lepleux, B. Chavillon, Y. Pellegrin, E. Blart, L. Cario, S. Jobic, et al., Simple and Reproducible Procedure to Prepare Self-Nanostructured NiO Films for the Fabrication of P-Type Dye-Sensitized Solar Cells, Inorg. Chem. 48 (2009) 8245-8250.

[65] E. Gibson A., A. Smeigh L., P. Le Loic, J. Fortage, G. Boschloo, E. Blart, et al., A p-Type NiO-Based Dye-Sensitized Solar Cell with an Open-Circuit Voltage of 0.35 V, Angewandte Chemie International Edition 48 (2009) 4402-4405.

[66] P. Qin, J. Wiberg, E.A. Gibson, M. Linder, L. Li, T. Brinck, et al., Synthesis and Mechanistic Studies of Organic Chromophores with Different Energy Levels for p-Type Dye-Sensitized Solar Cells, The Journal of Physical Chemistry C 114 (2010) 4738-4748.

[67] S.H. Kang, K. Zhu, N.R. Neale, A.J. Frank, Hole transport in sensitized CdS-NiO nanoparticle photocathodes, Chem.Commun. 47 (2011) -.

[68] K. Tennakone, G.R.R.A. Kumara, A.R. Kumarasinghe, K.G.U. Wijayantha, P.M. Sirimanne, A dye-sensitized nano-porous solid-state photovoltaic cell, Semiconductor Science and Technology 10 (1995) 1689.

[69] K. Tennakone, G.R.R.A. Kumara, I.R.M. Kottegoda, V.P.S. Perera, G.M.L.P. Aponsu, Nanoporous n- TiO_2/selenium/p-CuCNS photovoltaic cell, J. Phys. D 31 (1998) 2326.

[70] B. O'Regan, F. Lenzmann, R. Muis, J. Wienke, A Solid-State Dye-Sensitized Solar Cell Fabricated with Pressure-Treated P25 TiO_2 and CuSCN: Analysis of Pore Filling and IV Characteristics, Chemistry of Materials 14 (2002) 5023-5029.

[71] C. Zhang, K. Wang, L. Hu, F. Kong, L. Guo, Improved performance of solid-state dye-sensitized solar cells with p/p-type nanocomposite electrolyte, J. Photochem. Photobiol. A. 189 (2007) 329-333.

[72] K.L. Chopra, P.D. Paulson, V. Dutta, Thin-film solar cells: an overview, Prog Photovoltaics Res Appl 12 (2004) 69-92.

[73] K. Tennakone, G.R.R.A. Kumara, I.R.M. Kottegoda, K.G.U. Wijayantha, V.P.S. Perera, A solid-state photovoltaic cell sensitized with a ruthenium bipyridyl complex, J. Phys. D 31 (1998) 1492.

[74] A. Nattestad, M. Ferguson, R. Kerr, Y. Cheng, U. Bach, Dye-sensitized nickel(II)oxide photocathodes for tandem solar cell applications, Nanotechnology 19 (2008) 295304.

[75] J.H. Rhee, Y.H. Lee, P. Bera, S.I. Seok, Cu2S-deposited mesoporous NiO photocathode for a solar cell, Chemical Physics Letters 477 (2009) 345-348.

[76] Y. Xu, M.A.A. Schoonen, The absolute energy positions of conduction and valence bands of selected semiconducting minerals, Am. Mineral. 85 (2000) 543-556.

[77] J.J. Scragg, P.J. Dale, L.M. Peter, Towards sustainable materials for solar energy conversion: Preparation and photoelectrochemical characterization of Cu_2ZnSnS_4, Electrochemistry Communications 10 (2008) 639-642.

[78] M. Grätzel, Dye-sensitized solar cells, Journal of Photochemistry and Photobiology C: Photochemistry Reviews 4 (2003) 145-153.

[79] B. Li, L. Wang, B. Kang, P. Wang, Y. Qiu, Review of recent progress in solid-state dye-sensitized solar cells, Solar Energy Mater. Solar Cells 90 (2006) 549-573.

[80] F. Odobel, L. Le Pleux, Y. Pellegrin, E. Blart, New Photovoltaic Devices Based on the Sensitization of p-type Semiconductors: Challenges and Opportunities, Acc. Chem. Res. 43 (2010) 1063-1071.

[81] Basic Prinsiples of photovoltaics, 2011 (2008).

[82] Walfried Plieth, Electrochemistry for Materials Science, First edition ed., Elsevier Science, Amsterdam, Boston, Heidelberg, London, New York, Oxford Paris, San Diego, San Francisco, Singapore, Sydney, Tokyo, 2008.

[83] P. M., S. M., Fundamentals of Electrochemical Deposition, second edition ed., Wiley, New York, 1998.

[84] C. Xu, M.J. Hampden-Smith, T.T. Kodas, Aerosol-assisted chemical vapor deposition (AACVD) of silver, palladium and metal alloy ($Ag_{1-x}Pd_x$, $Ag_{1-x}Cu_x$ and $Pd_{1-x}Cu_x$) Films, Adv Mater 6 (1994) 746-748.

[85] X. Hou, K.-. Choy, Processing and Applications of Aerosol-Assisted Chemical Vapor Deposition, Chemical Vapor Deposition 12 (2006) 583-596.

[86] A.A. Tahir, K.G.U. Wijayantha, S. Saremi-Yarahmadi, M. Mazhar, V. McKee, Nanostructured α-Fe_2O_3 Thin Films for Photoelectrochemical Hydrogen Generation, Chemistry of Materials 21 (2009) 3763-3772.

[87] R.G. Palgrave, I.P. Parkin, Aerosol Assisted Chemical Vapor Deposition Using Nanoparticle Precursors: A Route to Nanocomposite Thin Films, J. Am. Chem. Soc. 128 (2006) 1587-1597.

[88] K.L. Choy, Chemical vapour deposition of coatings, Progress in Materials Science 48 (2003) 57-170.

[89] U. Qureshi, C. Blackman, G. Hyett, I.P. Parkin, Tungsten Oxide and Tungsten Oxide-Titania Thin Films Prepared by Aerosol-Assisted Deposition Use of Preformed Solid Nanoparticles, European Journal of Inorganic Chemistry 2007 (2007) 1415-1421.

[90] J.L. Garcia-Miquel, Q. Zhang, S.J. Allen, A. Rougier, A. Blyr, H.O. Davies, et al., Nickel oxide sol–gel films from nickel diacetate for electrochromic applications, Thin Solid Films 424 (2003) 165-170.

[91] L.G. Hubert-Pfalzgraf, Some trends in the design of homo- and heterometallic molecular precursors of high-tech oxides, Inorganic Chemistry Communications 6 (2003) 102-120.

[92] J.H. Rhee, Y.H. Lee, P. Bera, S.I. Seok, Cu_2S-deposited mesoporous NiO photocathode for a solar cell, Chemical Physics Letters 477 (2009) 345-348.

[93] W. Bührer, W. Hälg, Crystal structure of high-temperature cuprous iodide and cuprous bromide, Electrochim. Acta 22 (1977) 701-704.

[94] K. Tennakone, G.R.R.A. Kumara, I.R.M. Kottegoda, V.P.S. Perera, G.M.L.P. Aponsu, K.G.U. Wijayantha, Deposition of thin conducting films of CuI on glass, Solar Energy Mater. Solar Cells 55 (1998) 283-289.

[95] J.X.M. Zheng-Johansson, I. Ebbsjö, R.L. McGreevy, A molecular dynamics study of ionic conduction in CuI. I. Derivation of the interionic potential from dynamic properties, Solid State Ionics 82 (1995) 115-122.

[96] J.X.M. Zheng-Johansson, R.L. McGreevy, A molecular dynamics study of ionic conduction in CuI. II. Local ionic motion and conduction mechanisms, Solid State Ionics 83 (1996) 35-48.

[97] P.M. Sirimanne, M. Rusop, T. Shirata, T. Soga, T. Jimbo, Characterization of CuI thin films prepared by different techniques, Mater. Chem. Phys. 80 (2003) 461-465.

[98] W. Sekkal, A. Zaoui, Monte Carlo study of transport properties in copper halides, Physica B: Condensed Matter 315 (2002) 201-209.

[99] Z. Zheng, A. Liu, S. Wang, B. Huang, K.W. Wong, X. Zhang, et al., Growth of highly oriented (110) gamma-CuI film with sharp exciton band, J. Mater. Chem. 18 (2008) 852-854.

[100] J.X.M. Zheng-Johansson, I. Ebbsjö, R.L. McGreevy, A molecular dynamics study of ionic conduction in CuI. I. Derivation of the interionic potential from dynamic properties, Solid State Ionics 82 (1995) 115-122.

[101] H. Kang, R. Liu, K. Chen, Y. Zheng, Z. Xu, Electrodeposition and optical properties of highly oriented γ-CuI thin films, Electrochim. Acta 55 (2010) 8121-8125.

[102] L. Yang, Z. Zhang, S. Fang, X. Gao, M. Obata, Influence of the preparation conditions of TiO2 electrodes on the performance of solid-state dye-sensitized solar cells with CuI as a hole collector, Solar Energy 81 (2007) 717-722.

[103] H. Sakamoto, S. Igarashi, K. Niume, M. Nagai, Highly efficient all solid state dye-sensitized solar cells by the specific interaction of CuI with NCS groups, Organic Electronics In Press, Uncorrected Proof.

[104] A. Konno, T. Kitagawa, H. Kida, G.R. Asoka Kumara, K. Tennakone, The effect of particle size and conductivity of CuI layer on the performance of solid-state dye-sensitized photovoltaic cells, Current Applied Physics 5 (2005) 149-151.

[105] G.R.A. Kumara, S. Kaneko, M. Okuya, K. Tennakone, Fabrication of Dye-Sensitized Solar Cells Using Triethylamine Hydrothiocyanate as a CuI Crystal Growth Inhibitor, Langmuir 18 (2002) 10493-10495.

[106] E. Cariati, J. Bourassa, Luminescence response of the solid state polynuclear copper(I) iodide materials [CuI(4-picoline)] to volatile organic compounds, Chem.Commun. (1998) 1623-1624.

[107] E. Cariati, X. Bu, P.C. Ford, Solvent- and Vapor-Induced Isomerization between the Luminescent Solids [CuI(4-pic)]4 and [CuI(4-pic)]a z (pic = methylpyridine). The Structural Basis for the Observed Luminescence Vapochromism, Chemistry of Materials 12 (2000) 3385-3391.

[108] M. Vitale, P.C. Ford, Luminescent mixed ligand copper(I) clusters (CuI)n(L)m (L=pyridine, piperidine): thermodynamic control of molecular and supramolecular species, Coord. Chem. Rev. 219-221 (2001) 3-16.

[109] P.M. Sirimanne, T. Soga, T. Jimbo, Identification of various luminescence centers in CuI films by cathodoluminescence technique, J Lumin 105 (2003) 105-109.

[110] X. Xie, Y. Chen, D. Ma, Enantioselective Arylation of 2-Methylacetoacetates Catalyzed by CuI/trans-4-Hydroxy-l-proline at Low Reaction Temperatures, J. Am. Chem. Soc. 128 (2006) 16050-16051.

[111] M. Niu, H. Fu, Y. Jiang, Y. Zhao, Copper-catalyzed addition of H-phosphine oxides to alkynes forming alkenylphosphine oxides, Chem.Commun. (2007) 272-274.

[112] C.G. Oliveri, N.C. Gianneschi, S.T. Nguyen, C.A. Mirkin, C.L. Stern, Z. Wawrzak, et al., Supramolecular Allosteric Cofacial Porphyrin Complexes, J. Am. Chem. Soc. 128 (2006) 16286-16296.

[113] A. Pfitzner, M.F. Bräu, J. Zweck, G. Brunklaus, H. Eckert, Phosphorus Nanorods Two Allotropic Modifications of a Long-Known Element, Angewandte Chemie International Edition 43 (2004) 4228-4231.

[114] Y. Yang, X. Li, B. Zhao, H. Chen, X. Bao, Nano-particulate CuI film formed on porous copper substrate by iodination, Chemical Physics Letters 387 (2004) 400-404.

[115] T. Tanaka, K. Kawabata, M. Hirose, Transparent, conductive CuI films prepared by rf-dc coupled magnetron sputtering, Thin Solid Films 281-282 (1996) 179-181.

[116] P.M. Sirimanne, M. Rusop, T. Shirata, T. Soga, T. Jimbo, Characterization of transparent conducting CuI thin films prepared by pulse laser deposition technique, Chemical Physics Letters 366 (2002) 485-489.

[117] G.S. Hsiao, M.G. Anderson, S. Gorer, D. Harris, R.M. Penner, Hybrid Electrochemical/Chemical Synthesis of Supported, Luminescent Semiconductor Nanocrystallites with Size Selectivity: Copper(I) Iodide, J. Am. Chem. Soc. 119 (1997) 1439-1448.

[118] K. Tennakone, A.R. Kumarasinghe, P.M. Sirimanne, G.R.R.A. Kumara, Chlorophyll-sensitized microporous cuprous iodide photocathode, J. Photochem. Photobiol. A. 91 (1995) 59-61.

[119] B.R. Sankapal, E. Goncalves, A. Ennaoui, M.C. Lux-Steiner, Wide band gap p-type windows by CBD and SILAR methods, Thin Solid Films 451-452 (2004) 128-132.

[120] D. Kim, M. Nakayama, O. Kojima, I. Tanaka, H. Ichida, T. Nakanishi, et al., Thermal-strain-induced splitting of heavy- and light-hole exciton energies in CuI thin films grown by vacuum evaporation, Phys.Rev.B 60 (1999) 13879-13884.

[121] B. Sasi, K.G. Gopchandran, Nanostructured mesoporous nickel oxide thin films, Nanotechnology 18 (2007) 115613.

[122] C.R.H. Bahl, S. MÃ¸rup, Varying the exchange interaction between NiO nanoparticles, Nanotechnology 17 (2006) 2835.

[123] D. Adler, J. Feinleib, Electrical and Optical Properties of Narrow-Band Materials, Phys.Rev.B 2 (1970) 3112-3134.

[124] S. Makhlouf, M. Kassem, M. Abdel-Rahim, Particle size-dependent electrical properties of nanocrystalline NiO, J. Mater. Sci. 44 (2009) 3438-3444.

[125] F.J. Morin, Electrical Properties of NiO, Phys.Rev. 93 (1954) 1199-1204.

[126] P. Puspharajah, S. Radhakrishna, A. Arof, Transparent conducting lithium-doped nickel oxide thin films by spray pyrolysis technique, J. Mater. Sci. 32 (1997) 3001-3006.

[127] Mark Winter, Nickel Oxide, 2011 (2010).

[128] V. Biju, M. Abdul Khadar, DC conductivity of consolidated nanoparticles of NiO, Mater. Res. Bull. 36 (2001) 21-33.

[129] S.A. Makhlouf, Electrical properties of NiO films obtained by high-temperature oxidation of nickel, Thin Solid Films 516 (2008) 3112-3116.

[130] E. Antoini, Sintering of $Li_xMi_{1a-x}O$ solid solutions at 1200Â°C, J. Mater. Sci. 27 (1992) 3335-3340.

[131] J. He, H. Lindstrm, A. Hagfeldt, S. Lindquist, Dye-Sensitized Nanostructured p-Type Nickel Oxide Film as a Photocathode for a Solar Cell, The Journal of Physical Chemistry B 103 (1999) 8940-8943.

[132] S.A. Makhlouf, K.M.S. Khalil, Humidity sensing properties of NiO/Al_2O_3 nanocomposite materials, Solid State Ionics 164 (2003) 97-106.

[133] S. Yamada, T. Yoshioka, M. Miyashita, K. Urabe, M. Kitao, Electrochromic properties of sputtered nickel-oxide films, J. Appl. Phys. 63 (1988) 2116-2119.

[134] H. Yamane, M. Kobayashi, Differential type giant magnetoresistive memory using spin-valve film with a NiO pinning layer, J. Appl. Phys. 83 (1998) 4862-4868.

[135] H. Sato, T. Minami, S. Takata, T. Yamada, Transparent conducting p-type NiO thin films prepared by magnetron sputtering, Thin Solid Films 236 (1993) 27-31.

[136] G.A. Niklasson, C.G. Granqvist, Electrochromics for smart windows: thin films of tungsten oxide and nickel oxide, and devices based on these, J.Mater.Chem. 17 (2007) 127-156.

[137] K. Liu, M.A. Anderson, Porous Nickel Oxide/Nickel Films for Electrochemical Capacitors, J. Electrochem. Soc. 143 (1996) 124-130.

[138] Poizot, P., Laruelle, S., Grugeon, S., Dupont, L., Tarascon,J.-M., Nano-sized transition-metal oxides as negative-electrode materials for lithium-ion batteries, Nature 407 (2000) 496-499.

[139] D. Wang, R. Xu, X. Wang, Y. Li, NiO nanorings and their unexpected catalytic property for CO oxidation, Nanotechnology 17 (2006) 979.

[140] X. Wang, J. Song, L. Gao, J. Jin, H. Zheng, Z. Zhang, Optical and electrochemical properties of nanosized NiO via thermal decomposition of nickel oxalate nanofibres, Nanotechnology 16 (2005) 37.

[141] J. Velevska, M. Ristova, Electrochromic properties of NiOx prepared by low vacuum evaporation, Solar Energy Mater. Solar Cells 73 (2002) 131-139.

[142] D.A. Wruck, M. Rubin, Structure and Electronic Properties of Electrochromic NiO Films, J. Electrochem. Soc. 140 (1993) 1097-1104.

[143] C. Natarajan, H. Matsumoto, G. Nogami, Improvement in Electrochromic Stability of Electrodeposited Nickel Hydroxide Thin Film, J. Electrochem. Soc. 144 (1997) 121-126.

[144] A. Šurca, B. Orel, B. Pihlar, P. Bukovec, Optical, spectroelectrochemical and structural properties of sol-gel derived Ni-oxide electrochromic film, J Electroanal Chem 408 (1996) 83-100.

[145] K.-. Min, M. Kim, Y.-. You, S.S. Lee, Y.K. Lee, T.-. Chung, et al., NiO thin films by MOCVD of Ni(dmamb)2 and their resistance switching phenomena, Surface and Coatings Technology 201 (2007) 9252-9255.

[146] J. Kang, S. Rhee, Chemical vapor deposition of nickel oxide films from $Ni(C_5H_5)_2/O_2$, Thin Solid Films 391 (2001) 57-61.

[147] M. Utriainen, M. Kröger-Laukkanen, L. Niinistö, Studies of NiO thin film formation by atomic layer epitaxy, Materials Science and Engineering B 54 (1998) 98-103.

[148] Tachiki, M., Hosomi, T., Kobayashi,T., Room-temperature heteroepitaxial growth of NiO thin films using pulsed laser deposition, Japanese Journal of Applied Physics, Part 1: Regular Papers and Short Notes and Review Papers 39 (2000) 1817-1820.

[149] W. Wang, Y. Itoh, I.W. Lenggoro, K. Okuyama, Nickel and nickel oxide nanoparticles prepared from nickel nitrate hexahydrate by a low pressure spray pyrolysis, Materials Science and Engineering: B 111 (2004) 69-76.

[150] L. Kumari, W.Z. Li, C.H. Vannoy, R.M. Leblanc, D.Z. Wang, Vertically aligned and interconnected nickel oxide nanowalls fabricated by hydrothermal route, Crystal Research and Technology 44 (2009) 495-499.

[151] Y. Wang, Y. Zhang, H. Liu, S. Yu, Q. Qin, Nanocrystalline NiO thin film anode with MgO coating for Li-ion batteries, Electrochim. Acta 48 (2003) 4253-4259.

[152] F. Zhang, Y. Zhou, H. Li, Nanocrystalline NiO as an electrode material for electrochemical capacitor, Mater. Chem. Phys. 83 (2004) 260-264.

[153] W. Xing, F. Li, Z. Yan, G.Q. Lu, Synthesis and electrochemical properties of mesoporous nickel oxide, J. Power Sources 134 (2004) 324-330.

[154] B. Huang, G. Chen, F. Li, Q. Yu, K. Hu, Study of NiO cathode modified by rare earth oxide additive for MCFC by electrochemical impedance spectroscopy, Electrochim. Acta 49 (2004) 5055-5068.

[155] L. Berkat, L. Cattin, A. Reguig, M. Regragui, J.C. Bernède, Comparison of the physico-chemical properties of NiO thin films deposited by chemical bath deposition and by spray pyrolysis, Mater. Chem. Phys. 89 (2005) 11-20.

[156] F. Vera, R. Schrebler, E. Muñoz, C. Suarez, P. Cury, H. Gómez, et al., Preparation and characterization of Eosin B- and Erythrosin J-sensitized nanostructured NiO thin film photocathodes, Thin Solid Films 490 (2005) 182-188.

[157] M. Page, O. Niitsoo, Y. Itzhaik, D. Cahen, G. Hodes, Copper sulfide as a light absorber in wet-chemical synthesized extremely thin absorber (ETA) solar cells, Energy Environ.Sci. 2 (2009) 220-223.

[158] F. Zhuge, X. Li, X. Gao, X. Gan, F. Zhou, Synthesis of stable amorphous Cu_2S thin film by successive ion layer adsorption and reaction method, Mater Lett 63 (2009) 652-654.

[159] J.J. Loferski, J. Shewchun, S.D. Mittleman, E.A. DeMeo, R. Arnott, H.L. Hwang, et al., Cathodoluminescence characteristics of Cu_2S films produced by different methods, Solar Energy Materials 1 (1979) 157-169.

[160] D.F.A. Koch, R.J. McIntyre, The application of reflectance spectroscopy to a study of the anodic oxidation of cuprous sulphide, Journal of Electroanalytical Chemistry and Interfacial Electrochemistry 71 (1976) 285-296.

[161] M. Ashry, S.A. Fayek, Radiation effects on fabricated Cu_2S/CdS heterojunction photovoltaic cells, Renewable Energy 23 (2001) 441-450.

[162] R.L.N. Chandrakanthi, M.A. Careem, Preparation and characterization of CdS and Cu_2S nanoparticle/polyaniline composite films, Thin Solid Films 417 (2002) 51-56.

[163] G. Liu, T. Schulmeyer, J. Brötz, A. Klein, W. Jaegermann, Interface properties and band alignment of Cu_2S/CdS thin film solar cells, Thin Solid Films 431-432 (2003) 477-482.

[164] R. del Ro, D. Basaure, R. Schrebler, H. Gmez, R. Crdova, Anodic Electrosynthesis of a Thin Film of Cu2S on a Gold Electrode. A Voltammetric, Nanoelectrogravimetric, and I/t Transient Study, The Journal of Physical Chemistry B 106 (2002) 12684-12692.

[165] Orci, Copper (I) sulfide, 2011 (2011).

[166] P.K. Nair, M.T.S. Nair, Chemically deposited SnS-Cu x S thin films with high solar absorptance: new approach to all-glass tubular solar collectors, J. Phys. D 24 (1991) 83.

[167] H. Lee, S.W. Yoon, E.J. Kim, J. Park, In-Situ Growth of Copper Sulfide Nanocrystals on Multiwalled Carbon Nanotubes and Their Application as Novel Solar Cell and Amperometric Glucose Sensor Materials, Nano Letters 7 (2007) 778-784.

[168] T. Sakamoto, H. Sunamura, H. Kawaura, T. Hasegawa, T. Nakayama, M. Aono, Nanometer-scale switches using copper sulfide, Appl. Phys. Lett. 82 (2003) 3032-3034.

[169] L. Huang, P.K. Nair, M.T.S. Nair, R.A. Zingaro, E.A. Meyers, Interfacial Diffusion of Metal Atoms during Air Annealing of Chemically Deposited ZnS-CuS and PbS-CuS Thin Films, J. Electrochem. Soc. 141 (1994) 2536-2541.

[170] J.-. Chung, H.-. Sohn, Electrochemical behaviors of CuS as a cathode material for lithium secondary batteries, J. Power Sources 108 (2002) 226-231.

[171] A. Galdikas, A. Mironas, V. Strazdiene, A. Setkus, I. Ancutiene, V. Janickis, Room-temperature-functioning ammonia sensor based on solid-state CuxS films, Sensors Actuators B: Chem. 67 (2000) 76-83.

[172] M.T.S. Nair, P.K. Nair, SnS-Cu x S thin film combination: a desirable solar control coating for architectural and automobile glazings, J. Phys. D 24 (1991) 450.

[173] I. Grozdanov, Electroconductive copper selenide films on transparent polyester sheets, Synth. Met. 63 (1994) 213-216.

[174] N.K. Allouche, T. Ben Nasr, C. Guasch, N. Kamoun Turki, Optimization of the synthesis and characterizations of chemical bath deposited Cu_2S thin films, Comptes Rendus Chimie 13 (2010) 1364-1369.

[175] I.P. Parkin, Solid state metathesis reaction for metal borides, silicides, pnictides and chalcogenides: ionic or elemental pathways, Chem. Soc. Rev. 25 (1996) 199-207.

[176] S. Schneider, J.R. Ireland, M.C. Hersam, T.J. Marks, Copper(I) tert-Butylthiolato Clusters as Single-Source Precursors for High-Quality Chalcocite Thin Films:Film Growth and Microstructure Control, Chemistry of Materials 19 (2007) 2780-2785.

[177] L. Isac, A. Duta, A. Kriza, S. Manolache, M. Nanu, Copper sulfides obtained by spray pyrolysis — Possible absorbers in solid-state solar cells, Thin Solid Films 515 (2007) 5755-5758.

[178] M. Xin, K. Li, H. Wang, Synthesis of CuS thin films by microwave assisted chemical bath deposition, Appl. Surf. Sci. 256 (2009) 1436-1442.

[179] C.N.R. Rao, K.P. Kalyanikutty, The Liquid-Liquid Interface as a Medium To Generate Nanocrystalline Films of Inorganic Materials, Acc. Chem. Res. 41 (2008) 489-499.

[180] K. Wang, G. Li, J. Li, Q. Wang, J. Chen, Formation of Single-Crystalline CuS Nanoplates Vertically Standing on Flat Substrate, Crystal Growth & Design 7 (2007) 2265-2267.

[181] T. Kuzuya, K. Itoh, M. Ichidate, T. Wakamatsu, Y. Fukunaka, K. Sumiyama, Facile synthesis of nearly monodispersed copper sulfide nanocrystals, Electrochim. Acta 53 (2007) 213-217.

[182] J. Johansson, J. Kostamo, M. Karppinen, L. Niinisto, Growth of conductive copper sulfide thin films by atomic layer deposition, J.Mater.Chem. 12 (2002) 1022-1026.

[183] C. Fischer, H. Muffler, M. Ba, T. Kropp, A. Schnmann, S. Fiechter, et al., Spray-Ion Layer Gas Reaction (ILGAR) Novel Low-Cost Process for the Deposition of Chalcopyrite Layers up to the Micrometer Range for Photovoltaic Applications, The Journal of Physical Chemistry B 107 (2003) 7516-7521.

[184] K. Sivula, F. Le Formal, M. Grätzel, Cover Picture: Solar Water Splitting: Progress Using Hematite (α-Fe_2O_3) Photoelectrodes (ChemSusChem 4/2011), ChemSusChem 4 (2011) 417-417.

[185] M. Aronniemi, J. Lahtinen, P. Hautojarvi, Characterization of iron oxide thin films, Surf. Interface Anal. 36 (2004) 1004-1006.

[186] F.L. Souza, K.P. Lopes, P.A.P. Nascente, E.R. Leite, Nanostructured hematite thin films produced by spin-coating deposition solution: Application in water splitting, Solar Energy Mater. Solar Cells 93 (2009) 362-368.

[187] Y. Xu, M.A.A. Schoonen, The absolute energy positions of conduction and valence bands of selected semiconducting minerals. Journal of the Mineralogical Society of America, 85 (2000) 543 - 556.

[188] A.L. Stroyuk, I.V. Sobran, S.Y. Kuchmiy, Photoinitiation of acrylamide polymerization by Fe_2O_3 nanoparticles, J. Photochem. Photobiol. A. 192 (2007) 98-104.

[189] Iron Oxide, 2011 (2010).

[190] A.S. Teja, P. Koh, Synthesis, properties, and applications of magnetic iron oxide nanoparticles, Progress in Crystal Growth and Characterization of Materials 55 (2009) 22-45.

[191] S.S. Shinde, R.A. Bansode, C.H. Bhosale, K.Y. Rajpure, Physical properties of hematite α-Fe 2 O 3 thin films: application to photoelectrochemical solar cells, Journal of Semiconductors 32 (2011) 013001.

[192] X. Gou, G. Wang, J. Park, H. Liu, J. Yang, Monodisperse hematite porous nanospheres: synthesis, characterization, and applications for gas sensors, Nanotechnology 19 (2008) 125606.

[193] J. Chen, L. Xu, W. Li, X. Gou, α-Fe2O_3 Nanotubes in Gas Sensor and Lithium-Ion Battery Applications, Adv Mater 17 (2005) 582-586.

[194] Z. Sun, H. Yuan, Z. Liu, B. Han, X. Zhang, A Highly Efficient Chemical Sensor Material for H2S: α-Fe_2O_3 Nanotubes Fabricated Using Carbon Nanotube Templates, Adv Mater 17 (2005) 2993-2997.

[195] M. Hermanek, R. Zboril, I. Medrik, J. Pechousek, C. Gregor, Catalytic Efficiency of Iron(III) Oxides in Decomposition of Hydrogen Peroxide: Competition between the Surface Area and Crystallinity of Nanoparticles, J. Am. Chem. Soc. 129 (2007) 10929-10936.

[196] I. Cesar, A. Kay, J.A. Gonzalez Martinez, M. Gratzel, Translucent Thin Film Fe_2O_3 Photoanodes for Efficient Water Splitting by Sunlight: Nanostructure-Directing Effect of Si-Doping, J. Am. Chem. Soc. 128 (2006) 4582-4583.

[197] L.-. Zhong, J.-. Hu, H.-. Liang, A.-. Cao, W.-. Song, L.-. Wan, Self-Assembled 3D Flowerlike Iron Oxide Nanostructures and Their Application in Water Treatment, Adv Mater 18 (2006) 2426-2431.

[198] P. Wu, W. Wang, Y. Huang, H. Sheu, Y. Lo, T. Tsai, et al., Porous Iron Oxide Based Nanorods Developed as Delivery Nanocapsules, Chemistry A European Journal 13 (2007) 3878-3885.

[199] K.L. Hardee, A.J. Bard, Semiconductor Electrodes, J. Electrochem. Soc. 123 (1976) 1024-1026.

[200] K.L. Hardee, A.J. Bard, Semiconductor Electrodes, J. Electrochem. Soc. 124 (1977) 215-224.

[201] A.M. Redon, J. Vigneron, R. Heindl, C. Sella, C. Martin, J.P. Dalbera, Differences in the optical and photoelectrochemical behaviours of single-crystal and amorphous ferric oxide, Solar Cells 3 (1981) 179-186.

[202] Curran, J.S., Gissler,W., Different Photoelectrochemical Behavior of Sintered and Flame-Oxidize Fe_2O_3, J. Electrochem. Soc. 126 (1979) 56-59.

[203] A. Duret, M. GrÃtzel, Visible Light-Induced Water Oxidation on Mesoscopic α-Fe_2O_3 Films Made by Ultrasonic Spray Pyrolysis, The Journal of Physical Chemistry B 109 (2005) 17184-17191.

[204] A. Kay, I. Cesar, M. GrÃtzel, New Benchmark for Water Photooxidation by Nanostructured α-Fe_2O_3 Films, J. Am. Chem. Soc. 128 (2006) 15714-15721.

[205] J.A. Glasscock, P.R.F. Barnes, I.C. Plumb, N. Savvides, Enhancement of Photoelectrochemical Hydrogen Production from Hematite Thin Films by the Introduction of Ti and Si, The Journal of Physical Chemistry C 111 (2007) 16477-16488.

[206] H. Miyake, H. Kozuka, Photoelectrochemical Properties of Fe_2O_3-Nb_2O_5 Films Prepared by Sol-Gel Method, The Journal of Physical Chemistry B 109 (2005) 17951-17956.

[207] H.E. Prakasam, O.K. Varghese, M. Paulose, G.K. Mor, C.A. Grimes, Synthesis and photoelectrochemical properties of nanoporous iron (III) oxide by potentiostatic anodization, Nanotechnology 17 (2006) 4285.

[208] H.L. Sanchez, H. Steinfink, H.S. White, Solid solubility of Ge, Si, and Mg in Fe_2O_3 and photoelectric behavior, Journal of Solid State Chemistry 41 (1982) 90-96.

[209] R.K. Quinn, R.D. Nasby, R.J. Baughman, Photoassisted electrolysis of water using single crystal α-Fe2O3 anodes, Mater. Res. Bull. 11 (1976) 1011-1017.

[210] C. Sanchez, K.D. Sieber, G.A. Somorjai, The photoelectrochemistry of niobium doped α-Fe_2O_3, Journal of Electroanalytical Chemistry and Interfacial Electrochemistry 252 (1988) 269-290.

[211] A.A. Tahir, K.G.U. Wijayantha, S. Saremi-Yarahmadi, M. Mazhar, V. McKee, Nanostructured α-Fe_2O_3 Thin Films for Photoelectrochemical Hydrogen Generation, Chemistry of Materials 21 (2009) 3763-3772.

[212] B. Fultz, J. Howe, Transmission Electron Microscopy and Diffractometry of Materials, 3rd Edition ed., Springer, Berlin, Heidelberg, New York, 2008.

[213] H. B. Bob, Two-dimensional X-ray diffraction, First edition ed., John Wiley & Sons, Inc., Hoboken, New Jersey, 2009.

[214] J. Goldstein I., C. Lyman E., D. Newbury E., E. Lifshin, P. Echlin, L. Sawyer, et al., Scanning Electron Microscopy and X-Ray Microanalysis, 3rd Edition ed., Kluwer Academic/Plenum publisher, New York Boston, Dordrecht, London, Moscow, 2003.

[215] P. Echlin, Handbook of Sample Preparation for Scanning Electron Microscopy and X-Ray Microanalysis, First edition ed., Springer, New York, 2009.

[216] J. Sole G., L. Bausa E., D. Jaque, An Introduction to the Optical Spectroscopy of Inorganic Solids, First edition ed., John Wiley & Sons Ltd, West Sussex England, 2005.

[217] C.A. Koval, P.R. Segar, Photoelectrochemical reduction of a copper(I) complex to copper metal by hot electrons at p-InP, J. Am. Chem. Soc. 111 (1989) 2004-2010.

[218] H. Finklea O., Semiconductor Electrodes, First edition ed., Elsevier Science, Amsterdam, Oxford, New York, Tokyo, 1988.

[219] X.-. Guo, Y.-. Luo, Y.-. Zhang, X.-. Huang, D.-. Li, Q.-. Meng, Study on the effect of measuring methods on incident photon-to-electron conversion efficiency of dye-sensitized solar cells by home-made setup, Rev. Sci. Instrum. 81 (2010).

[220] X. Guo, Y. Luo, C. Li, D. Qin, D. Li, Q. Meng, Can the incident photo-to-electron conversion efficiency be used to calculate short-circuit current density of dye-sensitized solar cells, Current Applied Physics In Press, Corrected Proof.

[221] R. A.K.N., Preferred orientations in nickel electro-deposits: I. The mechanism of development of textures in nickel electro-deposits, Journal of Electroanalytical Chemistry (1959) 6 (1963) 141-152.

[222] H. Kang, R. Liu, K. Chen, Y. Zheng, Z. Xu, Electrodeposition and optical properties of highly oriented γ-CuI thin films, Electrochim. Acta 55 (2010) 8121-8125.

[223] Y.G. Gudage, N.G. Deshpande, A.A. Sagade, R. Sharma, Room temperature electrosynthesis of ZnSe thin films, J. Alloys Compounds 488 (2009) 157-162.

[224] X. Chan, J.R. Jennings, M.A. Hossain, K.K.Z. Yu, Q. Wang, Characteristics of p-NiO Thin Films Prepared by Spray Pyrolysis and Their Application in CdS-sensitized Photocathodes, J. Electrochem. Soc. 158 (2011) H733-H740.

[225] P.M. Sirimanne, M. Rusop, T. Shirata, T. Soga, T. Jimbo, Characterization of transparent conducting CuI thin films prepared by pulse laser deposition technique, Chemical Physics Letters 366 (2002) 485-489.

[226] B.R. Sankapal, E. Goncalves, A. Ennaoui, M.C. Lux-Steiner, Wide band gap p-type windows by CBD and SILAR methods, Thin Solid Films 451-452 (2004) 128-132.

[227] N.R. Mathews, H.B.M. Anaya, M.A. Cortes-Jacome, C. Angeles-Chavez, J.A. Toledo-Antonio, Tin Sulfide Thin Films by Pulse Electrodeposition: Structural, Morphological, and Optical Properties, J. Electrochem. Soc. 157 (2010) H337-H341.

[228] S.H. Baeck, T. Jaramillo, G.D. Stucky, E.W. McFarland, Controlled Electrodeposition of Nanoparticulate Tungsten Oxide, Nano Lett. 2 (2002) 831-834.

[229] P. Shen, N. Chi, K. Chan, Morphology of electrodeposited WO studied by atomic force microscopy, J.Mater.Chem. 10 (2000) 697-700.

[230] C.C. Nee, W. Kim, R. Weil, Pulsed Electrodeposition of Ni-Mo Alloys, J. Electrochem. Soc. 135 (1988) 1100-1103.

[231] G.S. Hsiao, M.G. Anderson, S. Gorer, D. Harris, R.M. Penner, Hybrid Electrochemical/Chemical Synthesis of Supported, Luminescent Semiconductor Nanocrystallites with Size Selectivity: Copper(I) Iodide, J. Am. Chem. Soc. 119 (1997) 1439-1448.

[232] C. Hsu, H. Chung, A. Kumar Senthil, J. Zen, Novel Preparation and Photoelectrochemical Properties of γ-CuI Semiconductor Nanocrystallites on Screen-Printed Carbon Electrodes Electroanalysis 17 (2005) 1822-1827.

[233] U. Qureshi, C. Blackman, G. Hyett, I.P. Parkin, Tungsten Oxide and Tungsten Oxide-Titania Thin Films Prepared by Aerosol-Assisted Deposition - Use of Preformed Solid Nanoparticles, European Journal of Inorganic Chemistry 2007 (2007) 1415-1421.

[234] X. Hou, K. Choy, J. Yan, Deposition of biodegradable poly (d,l-lactic acid) films using aerosol-assisted method, Surface and Coatings Technology 202 (2008) 5175-5179.

[235] A.A. Tahir, K.G.U. Wijayantha, Photoelectrochemical water splitting at nanostructured ZnFe2O4 electrodes, J. Photochem. Photobiol. A. 216 (2010) 119-125.

[236] R. Dharmadasa, A.A. Tahir, K.G.U. Wijayantha, Single Step Growth and Characterization of Zinc Oxide, Tin Oxide, and Composite ($Zn_xSn_{1-x}O_y$) Nanoplate and Nanocolumn Electrodes, J Am Ceram Soc (2011) no-no.

[237] A.A. Tahir, K.G.U. Wijayantha, S. Saremi-Yarahmadi, M. Mazhar, V. McKee, Nanostructured α-Fe_2O_3 Thin Films for Photoelectrochemical Hydrogen Generation, Chem. Mater. 21 (2009) 3763-3772.

[238] A. Panneerselvam, M.A. Malik, P. O'Brien, M. Helliwell, The Aerosol-Assisted CVD of Silver Films from Single-Source Precursors, Chemical Vapor Deposition 15 (2009) 57-63.

[239] Y. Ni, Z. Jin, Y. Fu, Electrodeposition of p-Type CuSCN Thin Films by a New Aqueous Electrolyte With Triethanolamine Chelation, J Am Ceram Soc 90 (2007) 2966-2973.

[240] S. Nandy, B. Saha, M. Mitra, K. Chattopadhyay, Effect of oxygen partial pressure on the electrical and optical properties of highly (200) oriented p-type $Ni_{1-x}O$ films by DC sputtering, J. Mater. Sci. 42 (2007) 5766-5772.

[241] H.W. Ryu, G.P. Choi, W.S. Lee, J.S. Park, Preferred orientations of NiO thin films prepared by RF magnetron sputtering, J. Mater. Sci. 39 (2004) 4375-4377.

[242] J. Waters, D. Crouch, J. Raftery, P. O'Brien, Deposition of Bismuth Chalcogenide Thin Films Using Novel Single-Source Precursors by Metal-Organic Chemical Vapor Deposition, Chem. Mater. 16 (2004) 3289-3298.

[243] M.R. Waugh, G. Hyett, I.P. Parkin, Zinc Oxide Thin Films Grown by Aerosol Assisted CVD, Chemical Vapor Deposition 14 (2008) 366-372.

[244] A.B.F. Martinson, J.E. McGarrah, M.O.K. Parpia, J.T. Hupp, Dynamics of charge transport and recombination in ZnO nanorod array dye-sensitized solar cells, Phys.Chem.Chem.Phys. 8 (2006) 4655-4659.

[245] G. Boschloo, A. Hagfeldt, Spectroelectrochemistry of Nanostructured NiO, J Phys Chem B 105 (2001) 3039-3044.

[246] A. Nattestad, M. Ferguson, R. Kerr, Y. Cheng, U. Bach, Dye-sensitized nickel(II)oxide photocathodes for tandem solar cell applications, Nanotechnology 19 (2008) 295304.

[247] F. Craig A.J, Molecular dynamics simulations of reconstructed NiO surfaces, Scr. Mater. 50 (2004) 1045-1049.

[248] P.W. Tasker, The stability of ionic crystal surfaces, Journal of Physics C: Solid State Physics 12 (1979) 4977.

[249] F. Odobel, L. Le Pleux, Y. Pellegrin, E. Blart, New Photovoltaic Devices Based on the Sensitization of p-type Semiconductors: Challenges and Opportunities, Acc. Chem. Res. 43 (2010) 1063-1071.

[250] G. Boschloo, D. Fitzmaurice, Spectroelectrochemistry of Highly Doped Nanostructured Tin Dioxide Electrodes, J Phys Chem B 103 (1999) 3093-3098.

[251] R. Dharmadasa, K.G.U. Wijayantha, A.A. Tahir, ZnO–SnO2 composite anodes in extremely thin absorber layer (ETA) solar cells, J Electroanal Chem 646 (2010) 124-132.

[252] L. Zhang, Y. Wang, H. Cheng, W. Yao, Y. Zhu, Synthesis of Porous Bi2WO6 Thin Films as Efficient Visible-Light-Active Photocatalysts, Adv Mater 21 (2009) 1286-1290.

[253] P. Qin, H. Zhu, T. Edvinsson, G. Boschloo, A. Hagfeldt, L. Sun, Design of an Organic Chromophore for P-Type Dye-Sensitized Solar Cells, J. Am. Chem. Soc. 130 (2008) 8570-8571.

[254] A. Morandeira, G. Boschloo, A. Hagfeldt, L. Hammarstrom, Coumarin 343-NiO Films as Nanostructured Photocathodes in Dye-Sensitized Solar Cells: Ultrafast Electron Transfer, Effect of the I3-/I- Redox Couple and Mechanism of Photocurrent Generation, J. Phys. Chem. C 112 (2008) 9530-9537.

[255] M. Borgstrm, E. Blart, G. Boschloo, E. Mukhtar, A. Hagfeldt, L. Hammarstrm, et al., Sensitized Hole Injection of Phosphorus Porphyrin into NiO: Toward New Photovoltaic Devices, J Phys Chem B 109 (2005) 22928-22934.

[256] S. Mori, S. Fukuda, S. Sumikura, Y. Takeda, Y. Tamaki, E. Suzuki, et al., Charge-Transfer Processes in Dye-Sensitized NiO Solar Cells, J. Phys. Chem. C 112 (2008) 16134-16139.

[257] L. Lepleux, B. Chavillon, Y. Pellegrin, E. Blart, L. Cario, S. Jobic, et al., Simple and Reproducible Procedure to Prepare Self-Nanostructured NiO Films for the Fabrication of P-Type Dye-Sensitized Solar Cells, Inorg. Chem. 48 (2009) 8245-8250.

[258] A. Morandeira, G. Boschloo, A. Hagfeldt, L. Hammarstrm, Photoinduced Ultrafast Dynamics of Coumarin 343 Sensitized p-Type-Nanostructured NiO Films, J Phys Chem B 109 (2005) 19403-19410.

[259] H. Zhu, A. Hagfeldt, G. Boschloo, Photoelectrochemistry of Mesoporous NiO Electrodes in Iodide/Triiodide Electrolytes, J. Phys. Chem. C 111 (2007) 17455-17458.

[260] R.C. Alkire, D.M. Kolb, J. Lipkowski, Photoelectrochemical Materials and Energy Conversion Processes, John Wiley & Sons, Germany, 2011.

[261] N.K. Allouche, T. Ben Nasr, C. Guasch, N. Kamoun Turki, Optimization of the synthesis and characterizations of chemical bath deposited Cu2S thin films, Comptes Rendus Chimie 13 (2010) 1364-1369.

[262] S. Sun, L. Gao, Y. Liu, Enhanced dye-sensitized solar cell using graphene-TiO[sub 2] photoanode prepared by heterogeneous coagulation, Appl. Phys. Lett. 96 (2010) 083113.

[263] P.M. Sirimanne, M. Rusop, T. Shirata, T. Soga, T. Jimbo, Characterization of transparent conducting CuI thin films prepared by pulse laser deposition technique, Chemical Physics Letters 366 (2002) 485-489.

[264] C. Hsu, H. Chung, A.S. Kumar, J. Zen, Novel Preparation and Photoelectrochemical Properties of γ-CuI Semiconductor Nanocrystallites on Screen-Printed Carbon Electrodes, Electroanalysis 17 (2005) 1822-1827.

[265] B.R. Sankapal, E. Goncalves, A. Ennaoui, M.C. Lux-Steiner, Wide band gap p-type windows by CBD and SILAR methods, Thin Solid Films 451-452 (2004) 128-132.

[266] S.V. Bagul, S.D. Chavhan, R. Sharma, Growth and characterization of CuxS (x=1.0, 1.76, and 2.0) thin films grown by solution growth technique (SGT), Journal of Physics and Chemistry of Solids 68 (2007) 1623-1629.

[267] F. Zhuge, X. Li, X. Gao, X. Gan, F. Zhou, Synthesis of stable amorphous Cu_2S thin film by successive ion layer adsorption and reaction method, Mater Lett 63 (2009) 652-654.

[268] T. Yohannes, O. Inganäs, All-solid-state photoelectrochemical energy conversion with the conjugated polymer poly[3-(4-octylphenyl)-2,2′-bithiophene], Synth. Met. 107 (1999) 97-105.

[269] C.M. McShane, K. Choi, Photocurrent Enhancement of n-Type Cu_2O Electrodes Achieved by Controlling Dendritic Branching Growth, J. Am. Chem. Soc. 131 (2009) 2561-2569.

[270] I. Robel, V. Subramanian, M. Kuno, P.V. Kamat, Quantum Dot Solar Cells. Harvesting Light Energy with CdSe Nanocrystals Molecularly Linked to Mesoscopic TiO_2 Films, J. Am. Chem. Soc. 128 (2006) 2385-2393.

[271] P. Qin, J. Wiberg, E.A. Gibson, M. Linder, L. Li, T. Brinck, et al., Synthesis and Mechanistic Studies of Organic Chromophores with Different Energy Levels for p-Type Dye-Sensitized Solar Cells, J. Phys. Chem. C 114 (2010) 4738-4748.

[272] X. Chan, J.R. Jennings, M.A. Hossain, K.K.Z. Yu, Q. Wang, Characteristics of p-NiO Thin Films Prepared by Spray Pyrolysis and Their Application in CdS-sensitized Photocathodes, J. Electrochem. Soc. 158 (2011) H733-H740.

[273] J.H. Rhee, Y.H. Lee, P. Bera, S.I. Seok, Cu_2S-deposited mesoporous NiO photocathode for a solar cell, Chemical Physics Letters 477 (2009) 345-348.

[274] S.H. Kang, K. Zhu, N.R. Neale, A.J. Frank, Hole transport in sensitized CdS-NiO nanoparticle photocathodes, Chem.Commun. 47 (2011) 10419-10421.

[275] I. Hotovy, J. Huran, L. Spiess, Characterization of sputtered NiO films using XRD and AFM, J. Mater. Sci. 39 (2004) 2609-2612.

[276] E. Ghadiri, N. Taghavinia, S.M. Zakeeruddin, M. Gratzel, J. Moser, Enhanced Electron Collection Efficiency in Dye-Sensitized Solar Cells Based on Nanostructured TiO_2 Hollow Fibers, Nano Lett. 10 (2010) 1632-1638.

[277] A.I. Inamdar, A.C. Sonavane, S.K. Sharma, H. Im, P.S. Patil, Nanocrystalline zinc oxide thin films by novel double pulse single step electrodeposition, J. Alloys Compounds 495 (2010) 76-81.

[278] G. Boschloo, D. Fitzmaurice, Spectroelectrochemistry of Highly Doped Nanostructured Tin Dioxide Electrodes, J Phys Chem B 103 (1999) 3093-3098.

[279] X. Wang, J. Song, L. Gao, J. Jin, H. Zheng, Z. Zhang, Optical and electrochemical properties of nanosized NiO via thermal decomposition of nickel oxalate nanofibres, Nanotechnology 16 (2005) 37.

[280] A. Morandeira, G. Boschloo, A. Hagfeldt, L. Hammarstrm, Photoinduced Ultrafast Dynamics of Coumarin 343 Sensitized p-Type-Nanostructured NiO Films, J Phys Chem B 109 (2005) 19403-19410.

[281] A. Morandeira, J. Fortage, T. Edvinsson, L. Le Pleux, E. Blart, G. Boschloo, et al., Improved Photon-to-Current Conversion Efficiency with a Nanoporous p-Type NiO Electrode by the Use of a Sensitizer-Acceptor Dyad, J. Phys. Chem. C 112 (2008) 1721-1728.

[282] A. Morandeira, G. Boschloo, A. Hagfeldt, L. Hammarstrom, Coumarin 343 NiO Films as Nanostructured Photocathodes in Dye-Sensitized Solar Cells: Ultrafast Electron Transfer, Effect of the I_3^-/I^- Redox Couple and Mechanism of Photocurrent Generation, J. Phys. Chem. C 112 (2008) 9530-9537.

[283] A. Morandeira, G. Boschloo, A. Hagfeldt, L. Hammarstrm, Photoinduced Ultrafast Dynamics of Coumarin 343 Sensitized p-Type-Nanostructured NiO Films, J Phys Chem B 109 (2005) 19403-19410.

[284] M. Borgstram, E. Blart, G. Boschloo, E. Mukhtar, A. Hagfeldt, L. Hammarstram, et al., Sensitized Hole Injection of Phosphorus Porphyrin into NiO: Toward New Photovoltaic Devices, J Phys Chem B 109 (2005) 22928-22934.

[285] C. Bauer, G. Boschloo, E. Mukhtar, A. Hagfeldt, Interfacial Electron-Transfer Dynamics in Ru(tcterpy)(NCS)3-Sensitized TiO2 Nanocrystalline Solar Cells, J Phys Chem B 106 (2002) 12693-12704.

[286] L.M. Peter, Characterization and Modeling of Dye-Sensitized Solar Cells, J. Phys. Chem. C 111 (2007) 6601-6612.

[287] C. Lee, P. Chen, R. Vittal, K. Ho, Iodine-free high efficient quasi solid-state dye-sensitized solar cell containing ionic liquid and polyaniline-loaded carbon black, J.Mater.Chem. 20 (2010) 2356-2361.

[288] A.A. Tahir, K.G.U. Wijayantha, S. Saremi-Yarahmadi, M. Mazhar, V. McKee, Nanostructured α-Fe_2O_3 Thin Films for Photoelectrochemical Hydrogen Generation, Chem. Mater. 21 (2009) 3763-3772.

[289] Z. Zhang, C. Boxall, G.H. Kelsall, Photoelectrophoresis of colloidal iron oxides 1. Hematite (α-Fe_2O_3), Colloids Surf. Physicochem. Eng. Aspects 73 (1993) 145-163.

[290] R.R. Rangaraju, A. Panday, K.S. Raja, M. Misra, Nanostructured anodic iron oxide film as photoanode for water oxidation, J. Phys. D 42 (2009) 135303.

[291] G. Wang, Y. Ling, D.A. Wheeler, K.E.N. George, K. Horsley, C. Heske, et al., Facile Synthesis of Highly Photoactive α-Fe_2O_3-Based Films for Water Oxidation, Nano Lett. 11 (2011) 3503-3509.

[292] Z. Xiao-Dan, Z. Xin-Xia, X. Sheng-Zhi, L. Quan, W. Chang-Chun, S. Jian, et al., Micromorph tandem solar cells: optimization of the microcrystalline silicon bottom cell in a single chamber system, Chinese Physics B 20 (2011) 108801.

[293] S. Dongaonkar, J.D. Servaites, G.M. Ford, S. Loser, J. Moore, R.M. Gelfand, et al., Universality of non-Ohmic shunt leakage in thin-film solar cells, J. Appl. Phys. 108 (2010) 124509.

[294] G. Michael, Dye-sensitized solar cells, Journal of Photochemistry and Photobiology C: Photochemistry Reviews 4 (2003) 145-153.

[295] A.J.N. M.D. Archer, Nanostructured and photoelectrochemical systems for solar photon conversion, 1st ed., Imperial Collage press, Singapore, 2008.

[296] F. Liu, J. Nunzi, Air stable hybrid inverted tandem solar cell design, Appl. Phys. Lett. 99 (2011) 063301.

[297] A. Stanley, B. Verity, D. Matthews, Minimizing the dark current at the dye-sensitized TiO2 electrode, Solar Energy Mater. Solar Cells 52 (1998) 141-154.

[298] G. A. Somorjai, Y. Li, Introduction to Surface Chemistry and Catalysis, 2nd ed., John Wiley and Sons, United State of America, 2010.